Structural Response to Deflagration-to-Detonation Transition Events in a Tube

F. Pintgen and J. E. Shepherd
Graduate Aeronautical Laboratories
California Institute of Technology
Pasadena, CA 91125

Explosion Dynamics Laboratory Report FM2005-005

August 18, 2005
Revised March 30, 2020.

Abstract

In the current report, the structural response of a tube structure to a deflagration-to-detonation transition (DDT) event is analyzed. Laboratory experiments were carried out at pressure (0.1 MPa) and temperature (300°C). Simultaneous pressure and hoop strain measurements were obtained along the tube wall for various O_2/C-ratios mixtures, determining the loading profile and structural response in the slow and fast combustion regime.

Following the description of the experimental setup, the experimental results are presented. Within the analysis section of this report, the extent of the thermal stress induced by the combustion event is discussed. The thermal stresses where found to significantly contribute to the structural loading in the slow combustion regime. Finally, a design guideline based on the concept of the dynamic load factor is proposed, which allows estimation of the peak strain based on the calculated Chapman-Jouguet detonation pressure.

Contents

1 Introduction

The purpose of the present study is to evaluate the potential for a particular type of explosion hazard, deflagration-to-detonation transition (DDT). The main focus of the present study is the structural response of a tube to the DDT event and builds on previous work Pintgen and Shepherd (2003) conducted in our laboratories. Previous work investigated the potentially hazardous conditions for combustion wave acceleration, high-speed flame propagation, and DDT. Three DDT criteria have been considered: cell size λ, expansion ratio σ, and critical run-up distance. While these considerations, together with experimental pressure measurements, gave an estimate of the potentially hazardous operating conditions, the structural response to the tube in case of a DDT event has not yet been studied. The experiments in our laboratory are carried out at an initial pressure of $P_0 = 1$ bar and $T_0 =$ 300 K, the results have to be scaled to industrial facility conditions. The detailed pressure measurements and simultaneous structural response measurements via strain gauges are also used to develop methods and models for interpreting the large-scale experiments. The first part of this report discusses briefly the experimental setup. A more detailed description is found in Pintgen and Shepherd (2003). We present the results of our detailed pressure and structural response measurements, which were conducted at $P_0 = 1$ bar and $T_0 = 300$ K. We then present a simplified model showing how to scale the laboratory results to reactor conditions via the determination of a dynamic load factor. This enables us to make an an estimate of the structural response based on the detonation pressure, which can be calculated for reactor conditions.

2 Experimental Set-up

All experiments were carried out at initial pressure of $P_0 = 1$ bar and initial temperature of $T_0 = 300$ K. The CH_4-O_2 mixture composition was varied from $0.6 \leq O_2/C \leq 1.2$. A tube with a length of 1.25 m and inner diameter 127 mm was used for the experiments (Fig. 1). The tube had a wall thickness of 12 mm and could be equipped with obstacles of different spacing and blockage ratio. The obstacles are mounted on four 1/2-in threaded rods which are attached to the end flange on the ignition side (see Fig.2).

The mixture was ignited by applying a voltage of 10 V (at a current of 9.5 A) to a

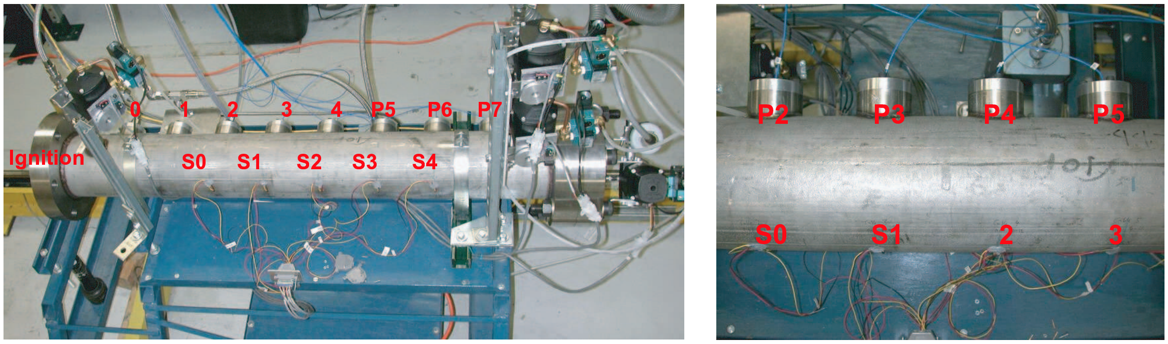

a) b)

Figure 1: Experimental set-up. a) 8 Pressure transducer ports ($P0$-$P7$) and 5 strain gauges ($S0$-$S4$). Ignition flange is to the left. b) Top view: Pressure transducers and strain gauges are mounted opposite each other.

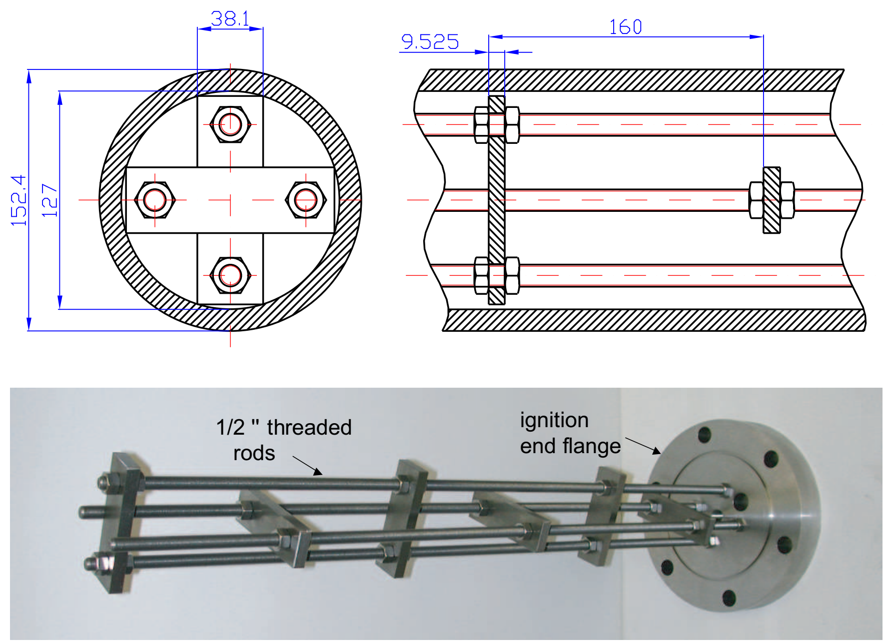

Figure 2: Top: Drawing of an obstacle pair mounted in the tube, units are given in mm. The blockage ratio is 0.37 and the obstacle spacing is 1.25 D. Bottom: Photograph of obstacle assembly outside the tube.

glow plug (Bosch 0-250-202-051) which was mounted in the center of one of the flanges at the end of the tube. Depending on the O_2/C-ratio of the mixture, the ignition occurred within 17 seconds from the time the voltage was applied. The glow plug characteristics were quantified using a pyrometer measuring the surface temperature of the glow plug over time for different applied voltages (Fig. 3). The ignition temperature for the mixture regime studied is approximately 1000°C.

The facility was modified from the one previously described in Pintgen and Shepherd

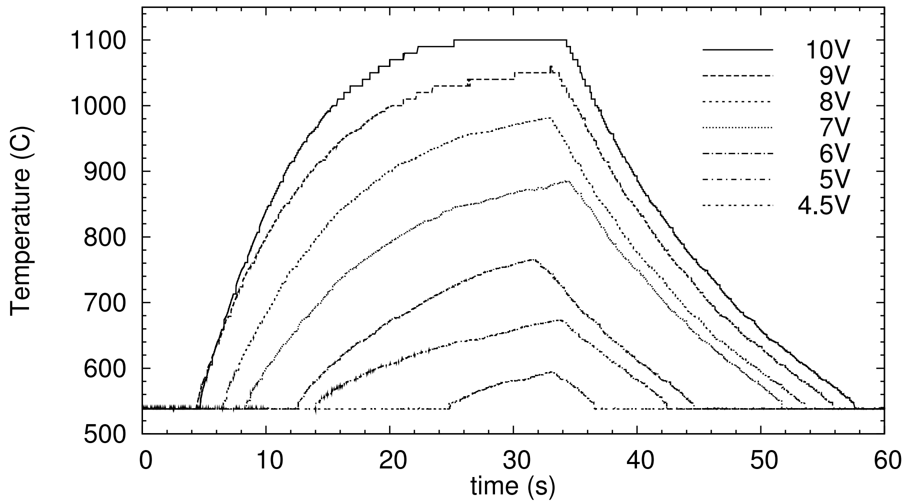

Figure 3: Pyrometer temperature measurements of glow plug surface temperature for various fixed voltages applied. The voltage was applied from time $t = 0$ for approximately 30 seconds.

(2003) to allow for detailed pressure measurements along the tube sidewall. The eight pressure transducer ports (P_0-P_7) were welded onto the tube sidewall and spaced at a distance of 127 mm. The pressure transducers were mounted in plugs that fit snugly within the ports, and the sensitive surface of the transducers was flush with the interior surface of the tube. Transducer port P_0 is located 117 mm from the inner surface of the ignition flange (Fig 1a). During an experiment, the tube is equipped with six pressure transducers, and the remaining two pressure transducer ports are capped with plugs. As the peak pressure measured varied over several orders of magnitude in the various combustion regimes, piezoelectric pressure transducer (PCB) models 113A24 and 113A23 were used which have a dynamic range of 69 bar and 1034 bar, respectively. The useful over-range is given as double the dynamic range.

A set of five strain gauges (S_0-S_4) was mounted on the outer tube surface, opposite to the pressure transducer ports P_2-P_6 (Fig 1b). Prior to the mounting of the strain gauges, the tube surface was polished and finished with 500-grit sandpaper to allow for proper bounding of the gauges to the tube. The strain gauges of type CEA-06-032UW-120 (Vishay Measurements Group, Micro-Measurements Division) have a uni-axial strain gauge pattern and are oriented to measure the hoop strain of the tube. The gauges are operated with an excitation voltage of 10 V in the quarter bridge mode using the built-in 120 Ω dummy gauges of the signal conditioning amplifiers (Type 2310A, Vishay Measurements Group, Micro-Measurements Division). Depending on the peak strain in the experiment, the amplification factors for the strain gauge signals were varied from 500 to 10000 in order to employ the full range of the data acquisition system ($\pm$10V). The bridge circuits are balanced prior to the ignition event.

The pressure and strain histories were recorded with a 12-bit data acquisition system sampling all channels with a maximum frequency of 2.5 MHz. The data acquisition system was triggered by the rising edge of the pressure transducer signal closest to the ignition flange.

Two series of experiments were conducted: one series without obstacles, and one with six obstacles with a blockage ratio of 37%. The obstacles were 10 mm thick plates of 38 mm width, spaced 160 mm apart with alternating horizontal or vertical orientation extending completely across the inner tube wall (see Fig. 2). This obstacle configuration was found to be close to the optimum setup in terms of flame acceleration and DDT from experimental studies by Lee et al. (see OECD 2000) in H_2-air mixtures and was used in the previous study Pintgen and Shepherd (2003).

3 Experimental Results

A total of 49 experiments was conducted, 38 were with the obstacle laden tube (BR=0.37) and 11 were without obstacles (BR=0). For a complete list of the experiments and the pressure and strain histories, see Appendix A and B. The parameter varied in each experimental series was the O_2/C-ratio; the initial pressure and temperature were kept constant at $T_0 =$ 300 K and $P_0 = 1$ bar.

3.1 With Obstacles

The transition point from the slow to the fast combustion regime determined by previous experiments of Pintgen and Shepherd (2003) was confirmed to take place at O_2/C=0.85 for BR=0.37 and at O_2/C=1 for BR=0, whereas the slow combustion regime is observed for O_2/C-ratios smaller than the transition point. First, the experimental results of the experiments with obstacles ($BR = 0.37$) are described.

3.1.1 Slow combustion regime

Representative pressure traces for the slow (sub-sonic) combustion regime are shown in Fig. 4. The pressure rises are nearly simultaneous throughout the tube. The peak pressure (0.5 MPa) is observed to be less than the calculated constant volume explosion pressure (P_{CV}=1.3 MPa), a consequence of the very slow flame propagation and the simultaneous cooling of the hot products inside the tube. In the slow combustion regime, the peak strain was measured to be on the order of 20–30 μ (Fig. 4b). As for the pressure transducers, a simultaneous rise is observed for the strain gauge signals throughout the tube. The highest

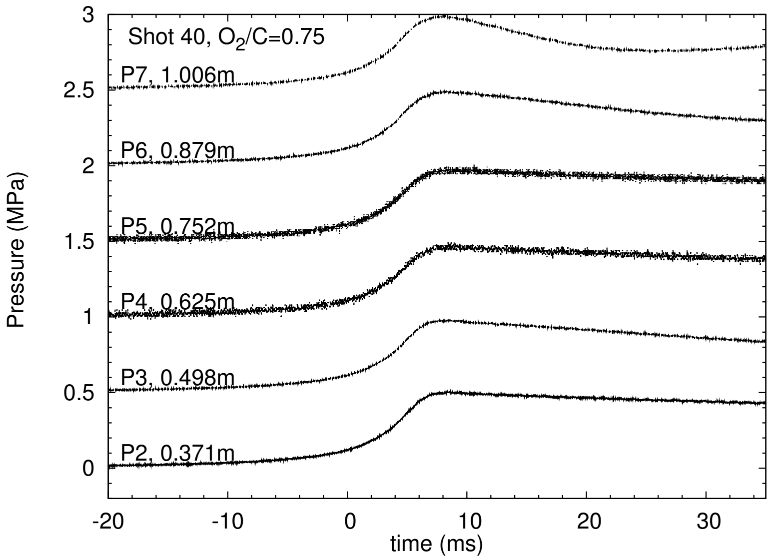

a)

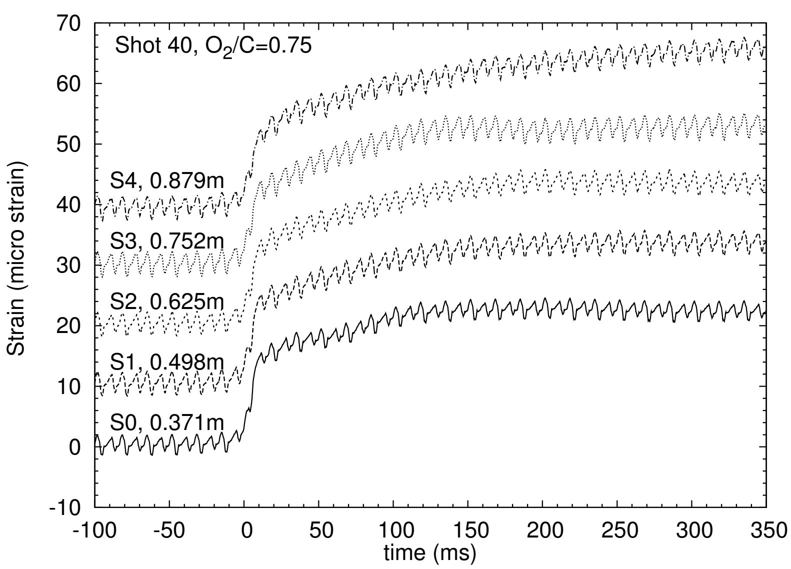

b)

Figure 4: Pressure (a) and strain histories (b) of shot 40, O_2/C=0.75, BR=0.37. Slow combustion regime.

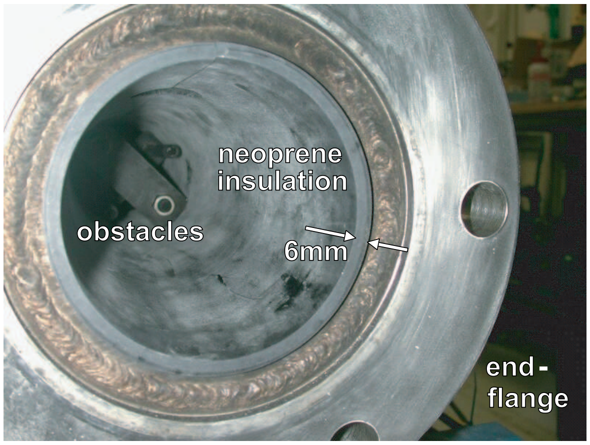

a)

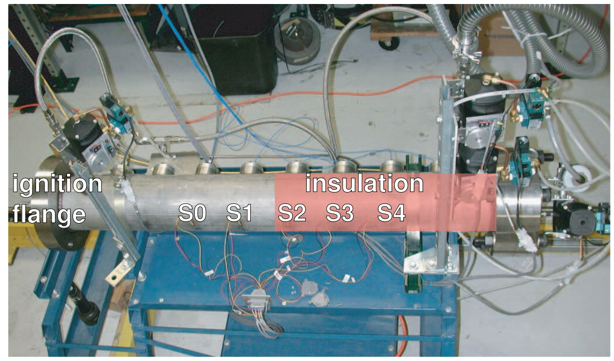

b)

Figure 5: a) Thermal insulation layer of 0.6 mm neoprene sheet on the inside of the tube. View into tube in the direction of the ignition-flange with end-flange removed. b) A 0.6 m long tube section was equipped with insulation. Strain gauges $S2$, $S3$, and $S4$ are not affected by thermal stresses.

amplification factor of 10000 had to be used to allow for the acquisition of the 100 μV peak signal resulting from the small peak strain. Despite careful shielding of the cable, a small amount of noise is visible for these very low signal experiments. The amplitude of the present noise in terms of the strain is approximately 3 μ. As the noise signal is observed prior to the ignition event, the signal is clearly not an effect of the tube oscillation but is electrical signal contamination with a frequency of approximately 120 Hz. For these very low signal experiments the presence of the noise required signal filtering for the precise determination of the peak strain.

Note that the strain measured on the tube outer surface in the slow combustion regime is not only originating from the high pressure inside the tube but also from thermal stresses. Heat transfer is taking place from the hot combustion products to the inner tube wall. This creates thin layer of heated metal on the inside of the tube. The thermal expansion of this layer creates a strain, which can be measured on the outer surface. The colder outer layer does not expand thermally but experiences strain from the expanding hot inner layer. This effect, known as thermal stress, contributes additionally to the hoop strain on the outer surface. To differentiate between the stresses originating from the internal pressure loading and the ones arising from the thermal loading, part of the tube was thermally insulated. A 6 mm thick neoprene layer was placed on the inside of the tube covering a 0.6 m long section of the tube over the entire circumference, (Fig.5). The tube section of strain gauges $S2$, $S3$, and $S4$ is, therefore, not affected by thermal stresses for this particular experiment. Shots 45 to 49 are equipped with the thermal insulation layer. All other experiments have been

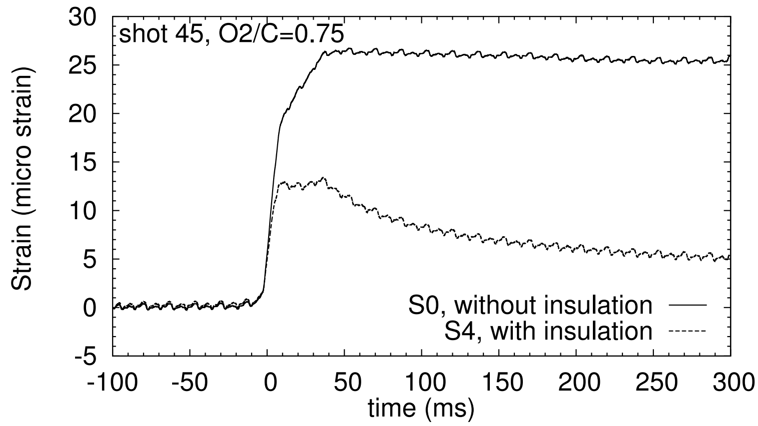

a)

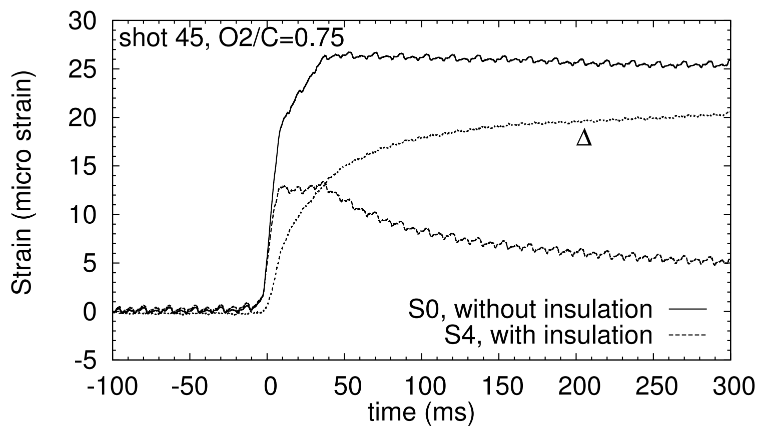

b)

Figure 6: a) Strain measurements in section without ($S0$) and with ($S4$) thermal insulation. b) The difference is the thermally induced strain Δ on outer tube surface.

carried out without any insulation.

The insulation dramatically influences the strain measurements in the slow combustion regime (Fig. 6a). The peak strain measurements including thermal stresses are, for an O_2/C-ratio of 0.75 up to a factor of 2.3 higher. The thermal loading signal can be isolated by taking the difference Δ (Fig. 6b) between the strain gauge signal $S0$ which includes internal pressure and thermal loading and the signal of strain gauge $S4$ which includes only the pressure loading. The characteristic rise time of the thermal loading signal is approximately 50 ms and dominates the long time observation. An analytical estimation of the thermal stresses can be made with a simplified model. To do this, the characteristic penetration depth h of the heat into the inner tube layer and a characteristic temperature increase ΔT of that layer must be known (Fig. 7a). From the experimental observations, the characteristic time scale t_c of the heat transfer was determined to be approximately 50 ms. From the one-dimensional

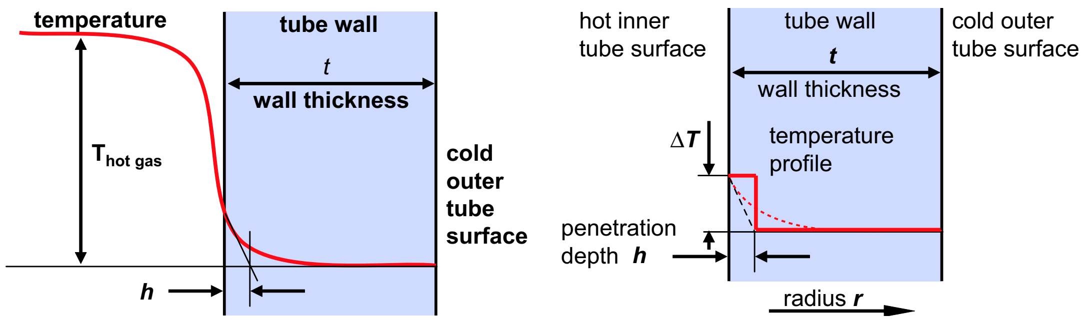

a) b)

Figure 7: a) Thermal penetration depth into inner tube surface. b) Square wave approximation of temperature profile on the inner tube surface.

heat equation, the penetration depth is given as $h = \sqrt{\kappa t_c}$, where κ is the thermal diffusivity of steel. Given $\kappa_{steel} = 3.5 \cdot 10^{-6}$ m^2/s, the penetration depth h can be determined to be $h = 0.4$ mm. The temperature profile ideally has the form of the error function but is approximated here by a square-wave (Fig. 7b). This simplified situation corresponds to an inner tube layer of thickness h which is in temperature ΔT above the outer shell of the tube.

A model to derive the thermal stresses for a square temperature profile is to assume the tube to be separated into a warm, thin inner and a cold, thick outer shell; both are initially at the same tube temperature T_{out}. The outer radius of the inner shell and the inner radius of the outer shell are both r_c, the center radius. The inner shell is then heated up to $T_{out} + \Delta T$ and its outer radius r_{oI} expands to $r_{oI} = r_c + (\alpha r_c \Delta T)$. The shells are assumed to remain in contact at their interface, and the outer radius of the inner shell r_{oI} will decrease by Δr_{oI}. Correspondingly, the inner radius of the outer shell r_{iO} will expand by Δr_{iO}. The boundary conditions of displacement and normal stress (pressure) have to be matched at the interface. The displacement of the outer radius of the inner tube Δr_{oI} and inner radius of the outer tube Δr_{iO} are given from thick cylindrical shell theory by:

$$\Delta r_{oI} = \frac{P_{if}\, r_c \left({r_c}^2 + {r_i}^2\right)}{E\left(r_c^2 - r_i^2\right)} \tag{1}$$

$$\Delta r_{iO} = \frac{P_{if}\, r_c \left(r_c^2 + r_o^2\right)}{E\left(-{r_c}^2 + {r_o}^2\right)}, \tag{2}$$

where P_{if} is the pressure at the interface. Note that a positive displacement is defined in the outside direction and P_{if} acts as internal pressure on the outer shell and as external load on the inner shell. The displacement condition to be matched is then given by $\Delta r_{iO} - \Delta r_{oI} =$

Δr_c, which enables, together with Eqs. 1 and 2, the determination of the interface pressure

$$P_{if} = \frac{\Delta r_c \, E \, \left({r_c}^2 - {r_i}^2\right) \left({r_c}^2 - {r_o}^2\right)}{2 \, {r_c}^3 \, \left({r_i}^2 - {r_o}^2\right)}. \tag{3}$$

The stress $\sigma_{\theta\theta}$ and strain ϵ_θ on the tube's outer surface are then given by

$$\begin{aligned} \sigma_{\theta\theta} &= \frac{2 P_{if} r_c^2}{r_o^2 - r_c^2} \\ &= \frac{\alpha \, \Delta T \, E \, \left({r_c}^2 - {r_i}^2\right)}{{r_o}^2 - {r_i}^2} \qquad (4) \\ \epsilon_\theta &= \sigma_{\theta\theta}/E \\ &= \frac{\alpha \, \Delta T \, \left({r_c}^2 - {r_i}^2\right)}{{r_o}^2 - {r_i}^2}. \qquad (5) \end{aligned}$$

As $h \ll r_i$, this can be further simplified using $r_c^2 - r_i^2 = (r_i + d)^2 - r_i^2 \approx 2 r_i h$, which leads to

$$\sigma_{\theta\theta} = \frac{\alpha \, \Delta T \, E \, 2 r_i h}{{r_o}^2 - {r_i}^2}. \tag{6}$$

A more sophisticated model can be used to check this result and extend it to the calculation of the thermally induced stress for arbitrary temperature profiles. The thermally induced hoop stress $\sigma_{\theta\theta}$ at a radial position r for an arbitrary temperature profile $\tau(r)$ is given (Noda et al., 2002) by

$$\sigma_{\theta\theta}(r) = \alpha E \left(\frac{1}{r^2} \int_{r_i}^{r_o} \tau(r) r \, dr + \frac{r^2 + r_i^2}{r^2 (r_o^2 - r_i^2)} \int_{r_i}^{r_o} \tau(r) r \, dr - \tau(r) \right), \tag{7}$$

where α is the coefficient of thermal expansion ($9.6 \cdot 10^{-6}$ K^{-1}), E is the Young's modulus (210 GPa), $\tau(r)$ is the temperature profile as a function of radius, and r_i and r_o are the inner and outer tube radius respectively. Setting $r = r_o$, the thermally induced stress on the outer surface simplifies Eq.7 to

$$\sigma_{\theta\theta}(r = r_o) = \alpha E \left(\frac{2}{r_o^2 - r_i^2} \int_{r_o}^{r_o} \tau(r) r \, dr - \tau(r_o) \right). \tag{8}$$

Using the temperature at the outer radius as a reference temperature for $\tau(r)$ and defining $\tau(r)$ as the temperature difference with respect to the temperature of the outer tube surface, the last term can be neglected since $\tau(r_o) = 0$. The thermal stresses are governed by the integral term of Eq. 8. The thermal stress on the outer surface is directly proportional to $\int_{r_i}^{r_o} \tau(r) \, r \, dr$. This integral, in turn, is directly proportional to the thermal energy content Q

	steel	hot gas
ρ[kg/m^3]	8238	0.917
k[W/(m K)]	13.4	0.5
c_p[J/(kg K)]	468	2934

Table 1: Thermal properties of steel and hot combustion products assuming constant volume combustion.

T[K]	P[bar]	u_g[MJ/kg]	$\epsilon_{\theta \text{ thermal}}$ [μ strain]
2327	13.4	-1.97	0
1500	8.6	-3.85	10
1000	4.9	-6.16	22
500	1.7	-9.21	38
300	1.0	-9.49	39

Table 2: Gas pressure P, specific internal energy u_g, and calculated (Eq. 12) thermally induced strain during the cool down process from the constant volume combustion state (T_{CV}=2327 K).

per unit tube length

$$2\pi c\rho \int_{r_a}^{r_b} \tau(r)\, r\, dr = Q, \tag{9}$$

where c is the specific heat capacity of the tube and ρ is the density of the tube. Therefore, regardless of the specific temperature profile, the thermal stress on the outer tube surface is governed by only the total thermal energy content of the tube

$$\sigma_{\theta\theta}(r = r_o) = \frac{\alpha E}{2\pi c\rho} \frac{2}{r_o^2 - r_i^2} Q, \tag{10}$$

For the square-wave temperature profile $Q = 2\pi c\rho r_i \Delta T$, the simplified model, Eq. 6, agrees with the results derived above

$$\sigma_{\theta\theta}(r = r_o) = \alpha E \frac{2 r_i h \Delta T}{r_o^2 - r_i^2}. \tag{11}$$

The fact that the thermal stress does not depend on the specific temperature profile within the tube simplifies the problem, as the thermal stress at a given time depends only on the total energy transferred from the hot gas to the tube wall up to that time. In order to estimate the thermally induced stress, an energy balance between the hot gas and the inner shell has to be considered. The constant volume combustion temperature for a O_2/C=0.75 mixture at $P_0 = 1$ bar was calculated to be T_{CV}=2327 K and the constant volume combustion pressure P_{CV}=13.3 bar using `stanjan` Reynolds (1986). The specific heat capacity depends on the gas temperature. The specific internal energy u was calculated for several temperatures during the cool-down process (Table. 2). The energy balance between the heat-affected inner tube shell and the hot gas initially at temperature T_{CV} cooling to T_{cool} is

$$\begin{aligned} \Delta E_{gas} &= \Delta E_{tube}, \\ \rho_g V g \ (u_g(T_{CV}) - u_g(T_{cool})) &= Ql, \end{aligned} \tag{12}$$

where $l = 1.25$ m is the tube length, u_g and ρ_g are the specific energy and density of the gas, respectively, and V is the volume of the tube. Assuming a square-wave temperature profile leads to

$$\rho_g V g \ (u_g(T_{CV}) - u_g(T_{cool})) = \rho_s 2\pi r_i h l \Delta T. \tag{13}$$

The heat transfer to the end flanges and obstacles are neglected in this simplified analysis. Assuming cooling to $T_{cool} = 1000\ K$ ($\Delta U = 4.2$ MJ/kg) results in a thermally induced stress and strain of $\sigma_{\theta\theta}$=4.6 MPa and ϵ_θ=22 μ. For a square-wave temperature assumption with $h = 0.4$ mm, this leads to ΔT=79 K. This is in good agreement with the thermal stresses of 20μ measured experimentally (Fig. 6b). Note that for long times, all excess energy in the gas will be transferred to the tube walls. The expected strain for $T_{cool} = 300$ K and long times based on this model is 39 μ. The discrepancies between the results and the model can be explained by the limited data recording time and the simplifications of the analysis. The thermal stresses influence the determination of the peak strain only in the slow combustion regime for two reasons. In the fast combustion regime, the time scale of the peak pressure loading is much shorter ($\approx 100\ \mu s$) than the characteristic time scale of the thermal loading ($\approx$ 100 ms). Only in the slow combustion regime are the time scale of the pressure rise and the thermal loading comparable. Furthermore, the thermal loading is negligible in the fast combustion regime because the peak strain caused by the pressure loading is up to 40 times higher than that caused by thermal stresses. The strain caused by the thermal loading is too small and occurs too late to influence the peak strain measurements in the fast combustion regime.

In general, the strain measured on the outer surface is also a function of the overall tube temperature. When the tube temperature is increased uniformly over the throughout the wall thickness, the entire tube expands uniformly and no thermal stresses are induced. Nevertheless, the strain resulting from the thermal expansion is detected by the strain gauges. In this case, there is thermally induced strain without thermally induced stress. For the analysis shown above, the outer surface temperature was taken as the reference temperature for the assumed temperature profile within the tube ($\tau(r = r_o) = 0$). The temperature on the outer surface of the tube increases in the experimental setup during a series of ten shots

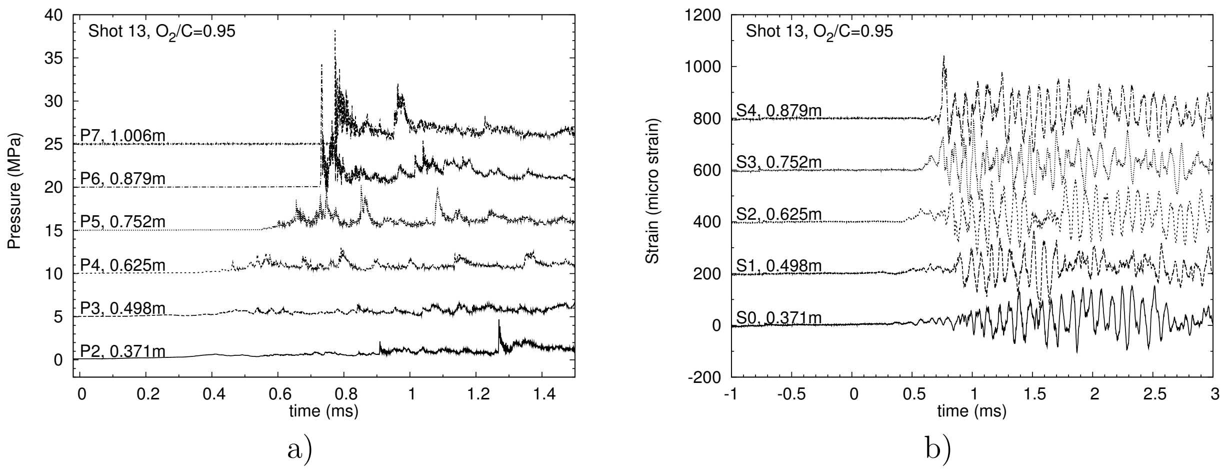

Figure 8: a) Pressure traces for fast combustion regime, Shot 13, O_2/C=0.95. b) Strain gauge histories for fast combustion regime, Shot 13, O_2/C=0.95.

approximately up to 32° C, 10° above room temperature. This effect does not influence the strain gauge measurements over a series of experiments for two reasons. The strain gauge circuits are balanced prior to each experiment and the gas temperature of the hot combustion products is large compared to the slight increase of the tube temperature, causing a negligible effect on the heat transfer rate from the gas to the tube.

3.1.2 Fast combustion regime

The transition to the fast combustion regime is near O_2/C=0.85, and the detonation onset occurs near the end flange due to the reflection of compression waves (Pintgen and Shepherd, 2003). With increasing O_2/C-ratio, the DDT event takes place further away from the end wall. For O_2/C=0.95, the transition point can be determined from pressure traces to be at approximately 0.88 m from the ignition flange (Fig. 8a). The sharp jump in pressure observed on transducer $P6$ and the magnitude of the peak pressure indicates that the transition to detonation has taken place close to $P6$ (Fig. 8a). The peak pressure measured is 14 MPa and approximately five times larger than the calculated Chapman-Jouguet (CJ) pressure of 3.1 MPa. The measured strain transient has two parts (Fig. 8b). For early times a deflagration precursor can be observed. The precursor is more pronounced for the strain gauges close to the ignition flange. Once the transition to detonation has taken place, the traveling wave excites flexural modes in the tube; peak strains of 200-300μ were measured. The shock traveling toward the ignition end is evident on the strain gauge histories.

Increasing the O_2/C-ratio further shifts the detonation transition point toward the ignition flange and, for O_2/C=1.05, the transition event is taking place in the tube center (Fig. 9a). On the pressure traces, one can clearly observe the peak pressure of the transition

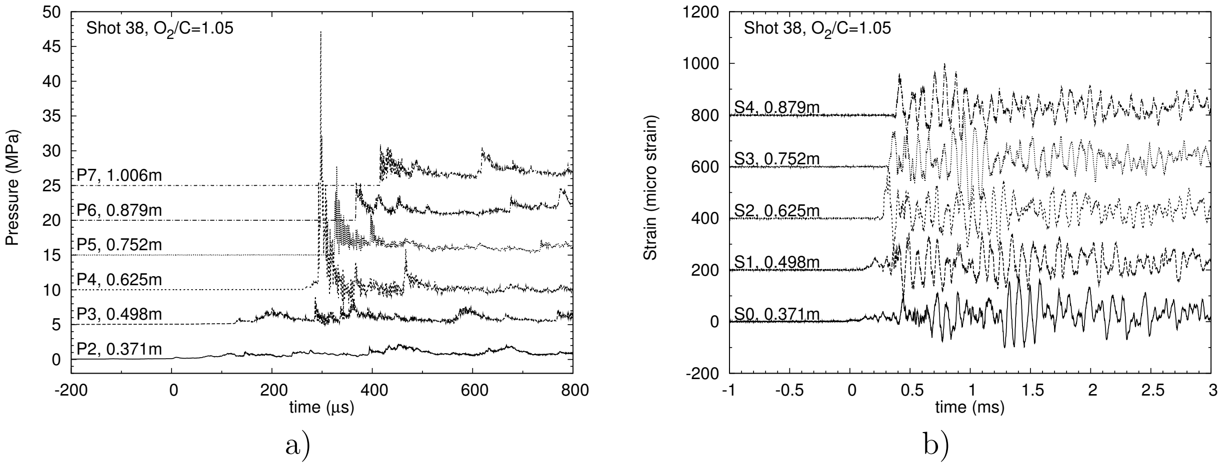

Figure 9: a) Pressure traces for fast combustion regime, Shot 38, O_2/C=1.05. b) Strain gauge histories for fast combustion regime, Shot 38, O_2/C=1.05.

event ($P4_{max} = 37$ MPa), approximately ten times higher than the CJ-pressure. Once the transition has taken place, the detonation is propagating as a CJ-detonation into the remaining section of the unburned mixture. The peak pressure measured for $P6$ and $P7$ is close to the calculated CJ-pressure of 3 MPa (Fig. 9a). On the strain histories, the wave propagation from the center results in the flexural waves being created first at the tube middle and moving outward, Fig. 9b. No precursor can be observed for strain gauges downstream of the transition point.

The different combustion regimes occurring for varying O_2/C-ratio can be best seen when plotting the peak pressure observed as a function of the O_2/C-ratio (Fig. 10a). For O_2/C$\leq$ 0.8, the peak pressure is below the calculated constant volume combustion pressure P_{CV}, indicating an event in the slow combustion regime. This can be explained by significant heat transfer to the tube walls taking place while the flame is slowly propagating along the tube. This leads to a decrease in the temperature of the hot combustion products and a reduced peak pressure. This effect is reduced for the experiments in which the tube was thermally shielded since the heat transfer to the tube walls is delayed, leading for the same O_2/C-ratio to a higher peak pressure than for the experiment without insulation (Fig. 10a). For O_2/C$\geq$ 0.85, the peak pressures observed are larger than the calculated CJ-pressure P_{CJ} and, for O_2/C$\geq$ 0.9, larger than the calculated reflected pressure of a CJ-detonation. Maximum peak pressures of 60 MPa were measured, whereas the typical value in the event of a DDT was found to be on the order of 15 MPa. The peak strain is drastically increasing with increasing O_2/C-ratio, from 25 μ up to over 300 μ for O_2/C$\geq$ 0.85, Fig. 10b. Compared to the slow combustion regime, this corresponds to a factor of ten increase in strain due to the DDT event. The representative value for the peak strain is on the order of 250 μ.

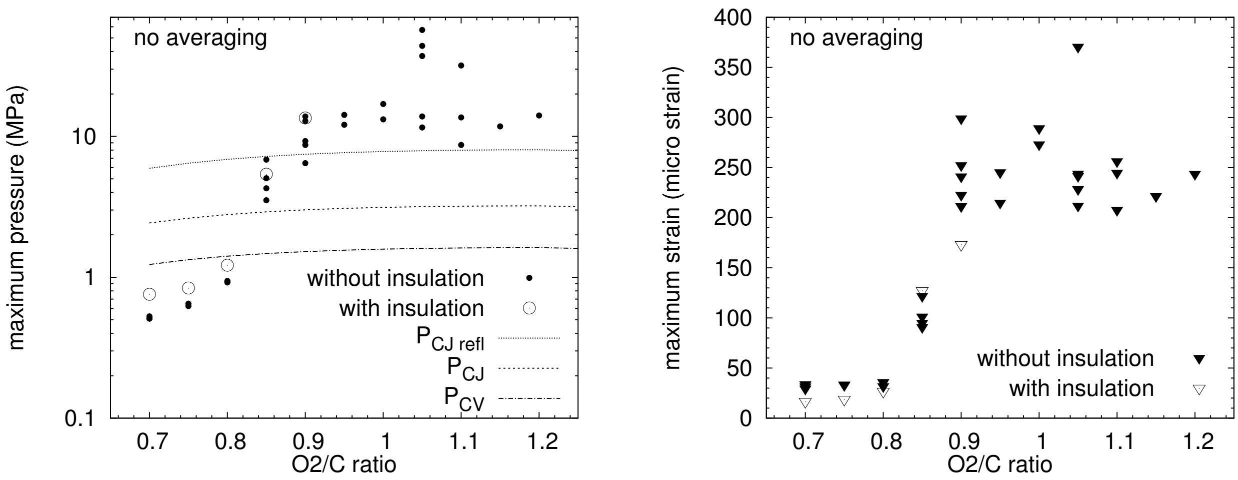

a) b)

Figure 10: Peak pressure (a) and peak strain (b) observed as a function of the O_2/C-ratio. All experiments were conducted at $T_0 = 300$ K, $P_0 = 1$ bar, $BR = 0.37$.

3.2 Without Obstacles

The results of experiments conducted with no obstacles in the tube ($BR = 0$) are similar to the cases of $BR = 0.37$. The transition point from slow to fast combustion regime is shifted to O_2/C=1. The peak pressures observed in the slow combustion regime are close to P_{CV} (Fig. 11a). In the fast combustion regime, O_2/C$\geq$ 1.05, the peak pressures are approximately the reflected CJ-pressure of 8 MPa. The measured peak strains in the slow combustion regime are of the order of 50 μ and, in the fast combustion regime, approximately 250 μ. Note that the results presented in the preceding two sections were not obtained for the operating conditions of the reactor. Both the scale of the reactor and the initial conditions (T_0, P_0) are different from the Caltech test conditions. In order to allow for a scale-up of the results obtained in the Caltech experiments to the actual reactor, the concept of the dynamic load factor is used as discussed in the next section.

4 Dynamic Load Factor

The dynamic load factor Φ is a simple method used to account for the affect of loading history and rates and relates the maximum stress to the maximum load. It is defined as the ratio of the actual peak stress to the static response stress based on the peak load. In the case of a tube of inner and outer radius of r_i and r_o, respectively, the dynamic load factor

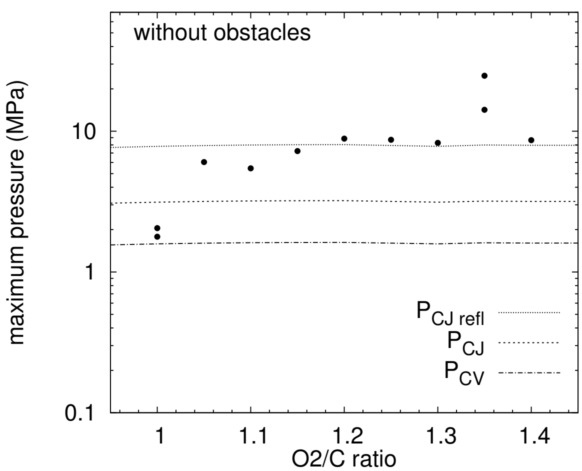

a)

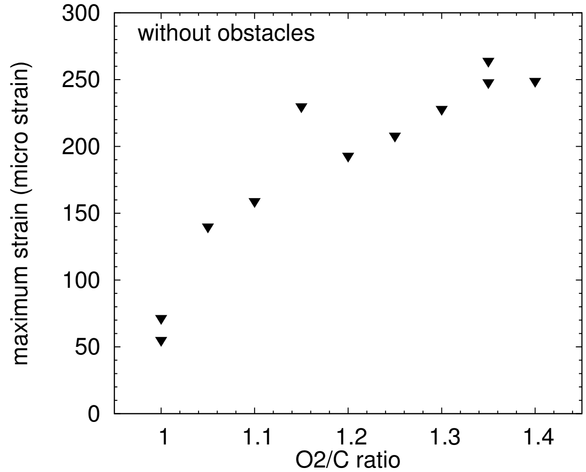

b)

Figure 11: Measured peak pressure (a) and peak strain (b) as a function of the O_2/C-ratio. All experiments were conducted at $T_0 = 300$ K, $P_0 = 1$ bar, $BR = 0$.

for the hoop strain can be written as

$$\Phi = \frac{\sigma_{measured}}{\sigma_{calc,Ppeak}} = \frac{\sigma_{measured}}{P_{peak} 2r_i^2/(r_o^2 - r_i^2)}, \tag{14}$$

$$\tag{15}$$

or, assuming a thin tube,

$$\Phi \approx \frac{\sigma_{measured}}{P_{peak} R/t}, \tag{16}$$

where $\sigma_{measured}$ is the peak stress inferred from measured peak strain, and $\sigma_{calc,Ppeak}$ is the stress which was calculated assuming the static loading of the tube with the measured peak pressure. For static and quasi-static loading, $\Phi = 1$ per definition. As long as the characteristic structural response time τ_c is much smaller than the time τ to increase the load up to the peak load P, the loading regime is quasi-static (Fig. 12). In the sudden loading regime, the load is applied as a step function. For an ideal step function loading, the dynamic load factor $\Phi = 2$. For the impulsive loading regime the dynamic load factor $\Phi < 2$, and the exact value of Φ depends on the impulse profile and duration compared to τ_c.

For the present test, the dynamic load factor Φ was calculated based on Eq. 14 and the the peak strain and peak pressure shown in Fig. 10 and 11. For the slow combustion regime (O_2/C$\leq$ 0.80) and BR=0.37, the dynamic load factor is up to $\Phi = 3$ for the experiments without the thermal insulation and $\Phi \approx 1$ for all thermally shielded experiments (Fig. 13)a.

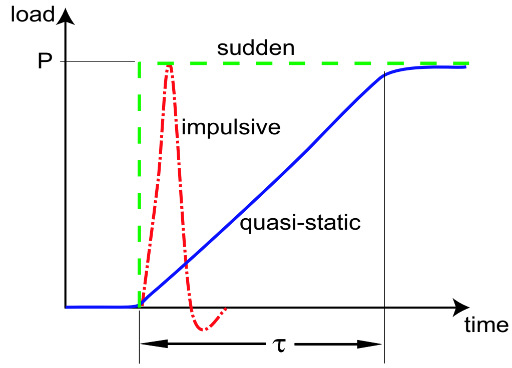

Figure 12: Different loading regimes sketched as tube load versus time.

This shows that, in the slow combustion regime, the pressure loading can be treated as quasi-static loading. The high values for Φ for the non-thermally-insulated experiments are caused by the additional thermal stresses contributing to $\sigma_{measured}$ (Eq. 14). In the determination of Φ, the thermal stress is not accounted for since only loading due to pressure is assumed for the calculation of $\sigma_{calc,Ppeak}$ (Eq. 14). For the fast combustion regime (O_2/C$\geq$ 0.85), the dynamic load factor varies between 0.5 and 1.8 (Fig. 13a). The scatter is mainly caused by the range of peak pressures measured (Fig. 10a). As the DDT event and the associated peak pressure is fairly local, the true peak pressure of the DDT event might not be captured since the pressure transducers are spaced by 12 cm and located only on one tube side of the tube. If the DDT event is taking place closer to the side the strain gauges are mounted on, the pressure wave will have already decayed slightly before being detected by the pressure transducer. The scatter in the peak strain is modest (Fig. 10b). This could be associated with the fact that the flexural waves travel along the tube walls without significant decay compared to the localized pressure wave of the DDT event, which decays fairly quickly over distance. Two-dimensional numerical simulations of the structural response are currently being carried out to further investigate this issue.

For the experimental series without obstacles ($BR = 0$), Φ varies between 0.5 and 1.5 (Fig. 13b). All experiments without obstacles were carried out without thermal insulation. The experimental series for $BR = 0$ was not extended as far in the slow combustion regime as the one for $BR = 0.37$. Therefore, the thermal loading effect on the determination of Φ is not as pronounced on the plot for the series without obstacles (Fig. 13b). The highest values for Φ were observed for the lowest value of O_2/C=1, for which the peak strain is lowest and the thermal loading has the largest influence on Φ.

In order to estimate the peak strain on the tube outer surface from the measured peak pressure, a dynamic load factor of $\Phi = 2$ seems an appropriate upper bound in the fast combustion regime. Based on the experiments conducted so far, a static loading with double

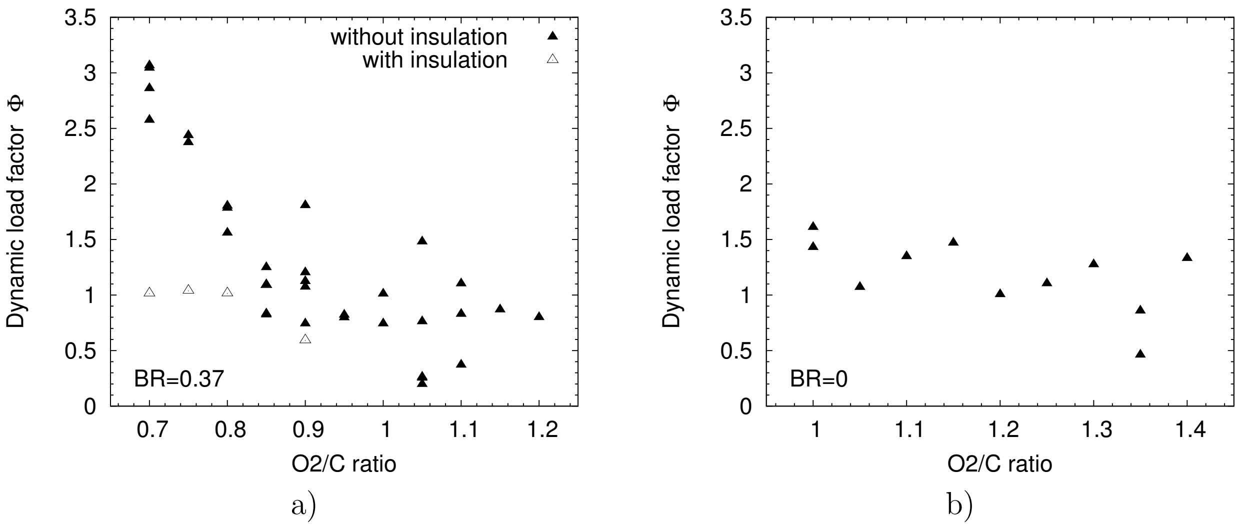

Figure 13: Dynamic load factor Φ as a function of O_2/C-ratio. a) $BR = 0.37$. b) $BR = 0$, no thermal insulation.

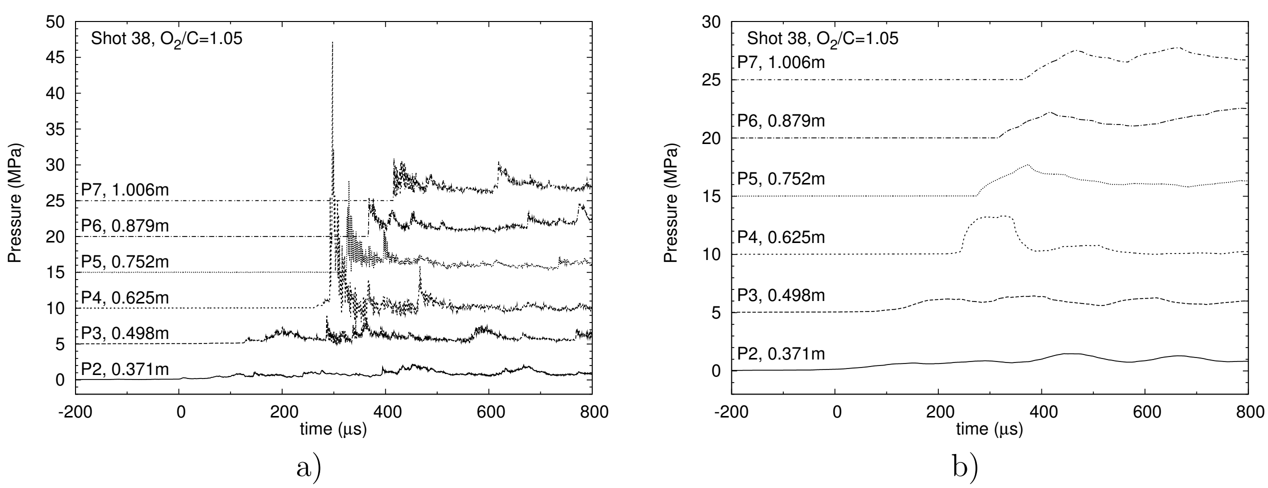

Figure 14: Original (a) and averaged (b) pressure signal. An equally weighted box-car average of width 100 μs was used for the low pass filtering.

the measured peak pressure gives an upper bound for the measured peak hoop stress. In order to estimate the pulse length of the peak pressures, the pressure signals were averaged over various time intervals. A running average (box-car-average) was used; an example of original and averaged pressure signals is shown in Fig. 14. When averaging the pressure signals over 100 μs, the peak pressure of the averaged signals were found to be close to the calculated CJ-pressure (Fig. 15a). This observation is valid only in the fast combustion regime when a detonation developed in the tube and the CJ-pressure is reached after the detonation onset. The pressure pulse caused by the DDT event and exceeding the CJ-pressure significantly has a maximum duration on the order of 100 μs.

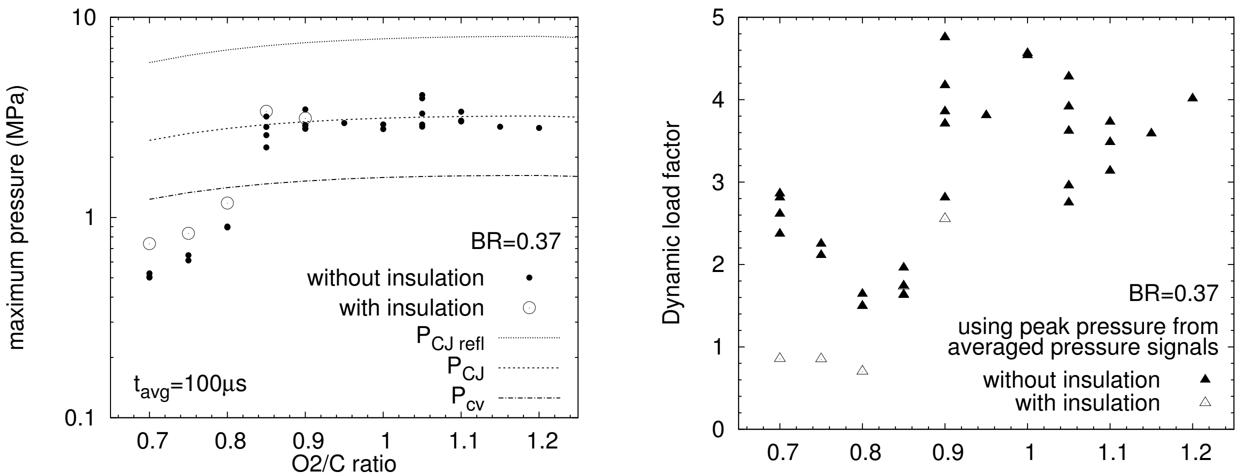

a) b)

Figure 15: a) Peak pressure of averaged pressure signals. Pressure signals were averaged with a 100 μs wide box-car average. b) Dynamic load factor based on the peak pressure of the averaged pressure signals.

Using the peak pressures of the filtered signals, the dynamic load factor is determined to be approximately 4–5 for the fast combustion regime (Fig. 15b). In case of a DDT event, the effective loading pressure can be estimated from the calculated CJ-pressure P_{CJ} and $\Phi = 4$. For the slow combustion regime, the loading on the tube can be bounded by the constant volume explosion pressure P_{CV} and $\Phi = 1$. For the slow combustion regime, the thermal stresses have to be taken into account separately.

5 Summary

Experiments were carried out in an obstacle laden tube and smooth tube to investigate the structural response to the loading by a DDT event. The setup was modified from previous investigations (Pintgen and Shepherd, 2003) and strain gauge measurements were obtained along the tube sidewalls. Pressure transducer ports were also added along the tube sidewall allowing for detailed tracking of the pressure loading. The transition from slow to fast combustion regimes was confirmed to be O_2/C=0.85 and O_2/C=1 for the setup with ($BR = 0.37$) and without ($BR = 0$) obstacles, respectively.

The highest peak pressure measured on the tube sidewalls is 60 MPa, which corresponds to 20 P_{CJ}. The peak pressures are lower than the one measured at the tube endwall in previous experiments (Pintgen and Shepherd, 2003), for which pressures up to 150 MPa were observed. The peak hoop strain was $\epsilon = 370\mu$, corresponding to a hoop stress of $\sigma = 77$ MPa in our experimental setup. The typical hoop strains measured for the fast combustion regimes were on the order of 250 μ. Based on the simultaneous strain and pressure measurements for the fast combustion regime, a static loading with four to five times the CJ-pressure (4–5 P_{CJ}) can be used to estimate the peak loading on the tube. For the slow combustion regime, the constant volume explosion pressure P_{CV} and a dynamic load factor $\Phi = 1$ can be used to estimate the peak loading on the structure. Note that in the slow combustion regime, besides the mechanical loading due to the pressure increase inside the tube, the thermal loading has to be considered. The thermal stresses in our setup increased the strain on the outside of the tube up to 125% and were measured and calculated to be on the order of 20 μ. In the fast combustion regime, the thermal stresses are negligible compared to the mechanical loading. Also, the characteristic time scale of the thermal loading (≈50 ms) is comparable only to the mechnical loading time scale in the slow combustion regime, since the pressure rise is slower in this regime. In conclusion, thermal effects influence only the strain measurements in the slow combustion regime.

Acknowledgments

The development and operation of the experimental facility used for the current study occupied staff and students of the Explosion Dynamics Laboratory at Caltech. The authors thank C. Krok and J. Karnesky for their contributions.

Bibliography

N. Noda, R.B. Hetnarski, and Y. Tanigawa. *Thermal Stresses*. Taylor and Francis, 2002. ISBN 1-56032-971-8. 10

OECD. Flame acceleration and deflagration to detonation transition in nuclear safety. Technical Report NEA/CSNI/R(2000)7, OECD Nuclear Energy Agency, 2000. State-of-the-Art Report by a Group of Experts, `http://www.galcit.caltech.edu/~jeshep/SOAR/index.html`. 5

F. Pintgen and J.E. Shepherd. Deflagration-to-detonation transition (DDT) in rich methane-oxygen mixtures. Technical Report FM2003-006, Graduate Aeronautical Laboratories California Institute of Technology, March 2003. 2, 3, 5, 13, 19

W.C. Reynolds. The element potential method for chemical equilibrium analysis: implementation in the interactive program STANJAN. Technical report, Mechanical Engineering Department, Stanford University, 1986. 11

A Shotlist

shot	O2/C	BR	$\mathbf{P}_{max}$ (MPa)	$\mathbf{S}_{max}$ (μstrain)
2	0.8	0.37	0.93	36
3	0.8	0.37	0.92	36
4	0.85	0.37	5.04	91
5	0.85	0.37	3.52	95
6	0.9	0.37	9.26	241
7	0.9	0.37	13.86	223
8	0.85	0.37	4.28	101
9	0.8	0.37	0.94	32
10	0.85	0.37	6.83	122
11	0.9	0.37	6.45	252
12	0.9	0.37	8.69	211
13	0.95	0.37	14.21	245
14	1	0.37	13.21	289
15	1.05	0.37	11.56	371
16	1.1	0.37	13.64	245
17	1.1	0.37	8.70	208
18	1.2	0.37	14.08	244
19	1.05	0	6.04	140
20	1	0	1.78	55
21	1	0	2.05	71
22	1.1	0	5.45	159
23	1.15	0	7.23	230

shot	O2/C	BR	$\mathbf{P}_{max}$ (MPa)	$\mathbf{S}_{max}$ (μstrain)
24	1.2	0	8.86	193
25	1.25	0	8.70	208
26	1.35	0	14.21	264
27	1.3	0	8.26	228
28	1.35	0	24.78	248
29	1.4	0	8.64	249
30	0.95	0.37	12.09	215
31	0.9	0.37	12.87	299
32	1.1	0.37	6.97	256
33	1.15	0.37	11.78	221
34	1.05	0.37	13.86	228
35	1.05	0.37	43.86	242
36	1	0.37	16.97	273
37	1.05	0.37	56.92	244
38	1.05	0.37	37.19	212
39	0.75	0.37	0.62	33
40	0.7	0.37	0.51	32
41	0.7	0.37	0.51	34
42	0.7	0.37	0.53	29
43	0.7	0.37	0.51	34
44	0.75	0.37	0.65	33

Table 3: Summary of shots without thermal insulation.

shot	O2/C	BR	$\mathbf{P}_{max}$ (MPa)	$\mathbf{S}_{max}$ (μstrain)
45	0.75	0.37	0.84	19
46	0.7	0.37	0.76	17
47	0.8	0.37	1.22	27
48	0.85	0.37	5.39	127
49	0.9	0.37	13.50	173

Table 4: Summary of shots with thermal insulation.

B Summary Plots

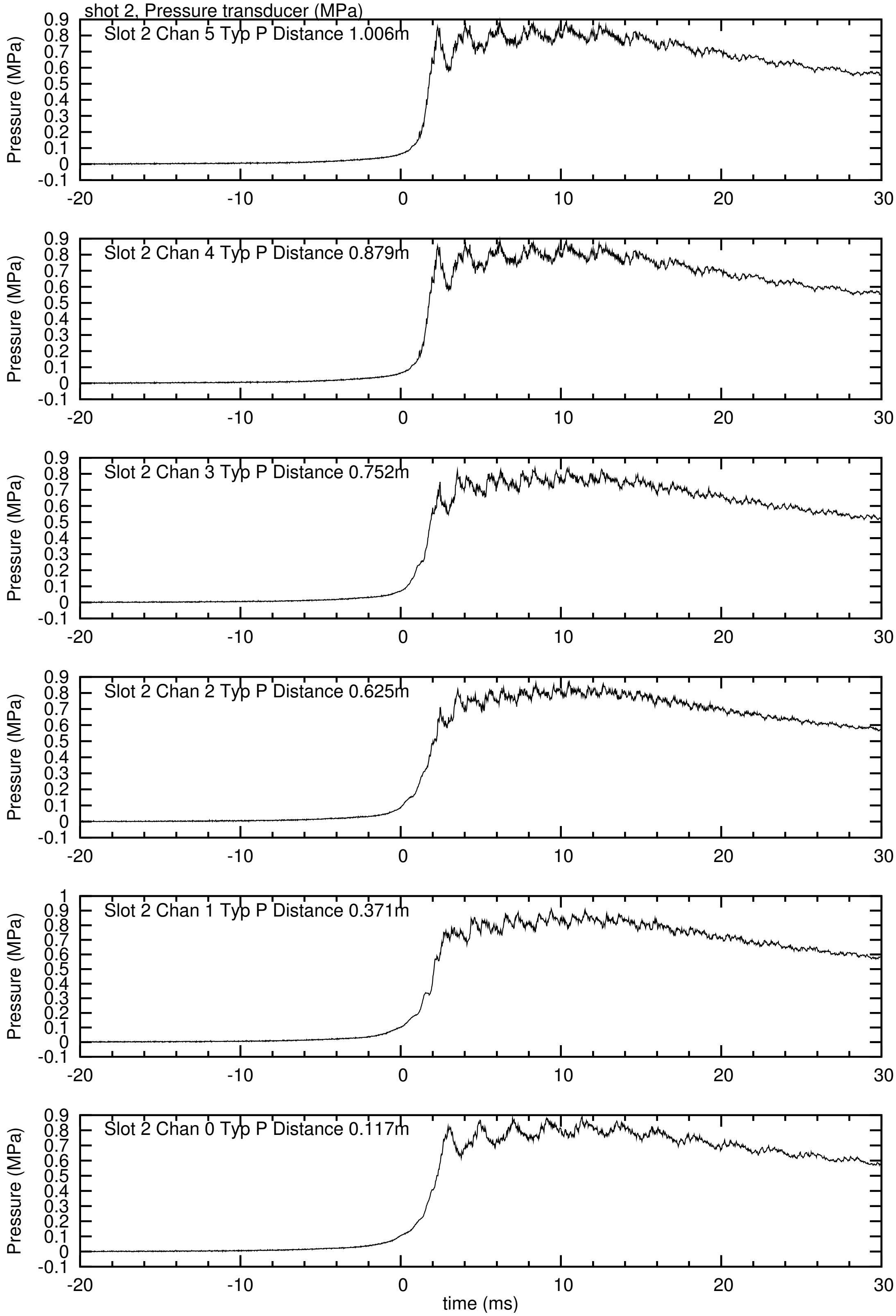

Figure 16: **Pressure transducers, shot 2**, BR=0.37, O_2/C=0.8, P_{CJ}=2.79 MPa, P_{CV}=1.41 MPa.

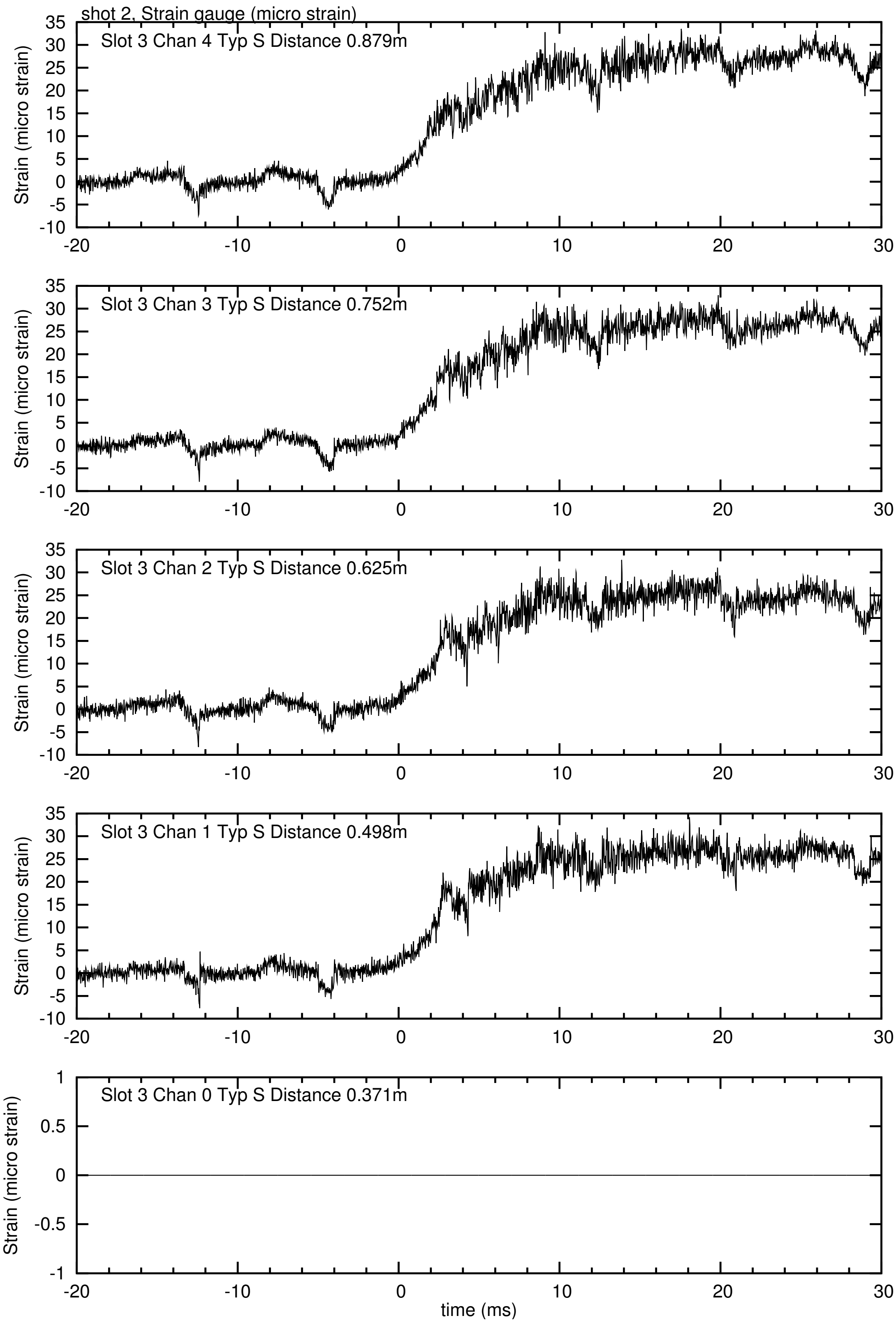

Figure 17: **Strain gauges, shot 2**, BR=0.37, O_2/C=0.8, P_{CJ}=2.79 MPa, P_{CV}=1.41 MPa.

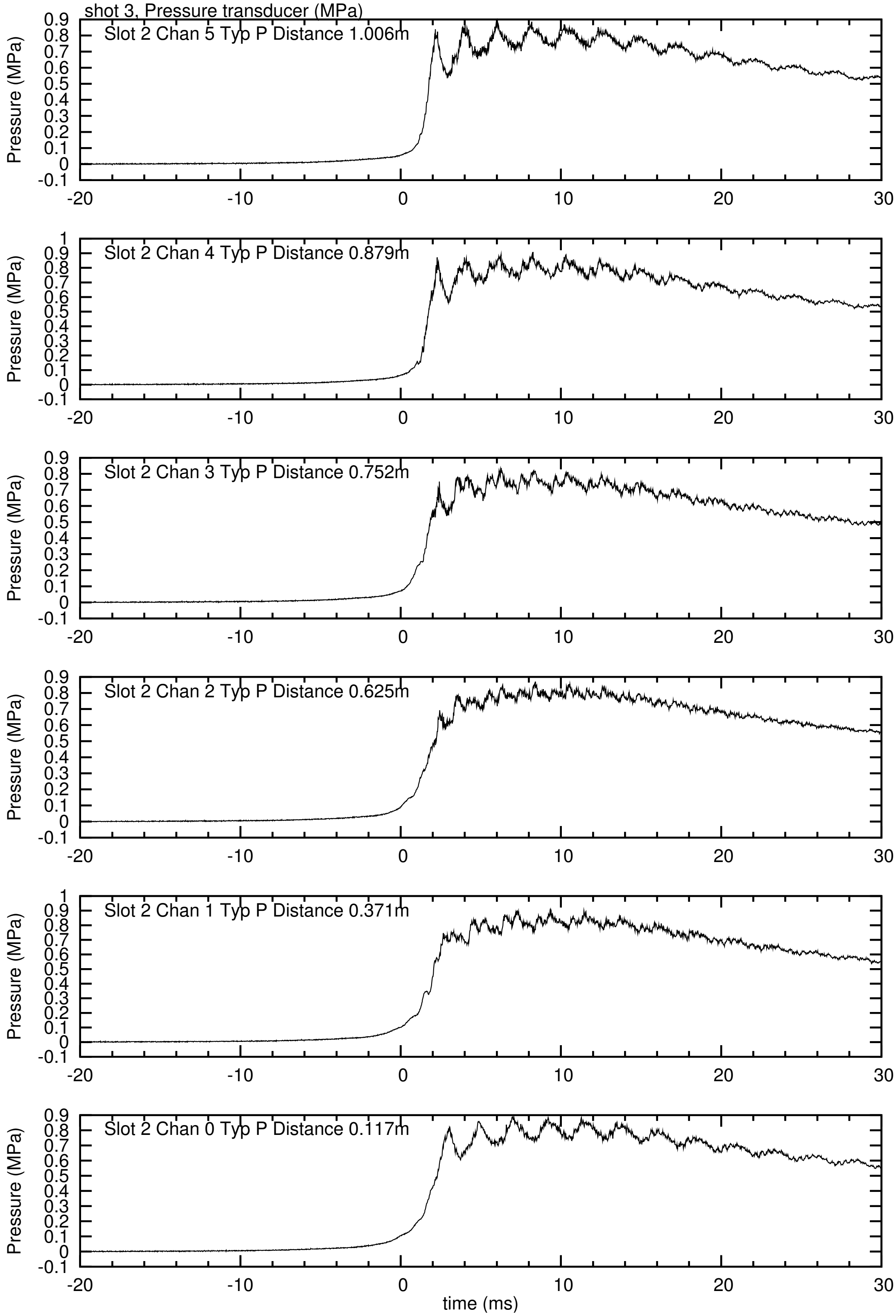

Figure 18: **Pressure transducers, shot 3**, BR=0.37, O_2/C=0.8, P_{CJ}=2.79 MPa, P_{CV}=1.41 MPa.

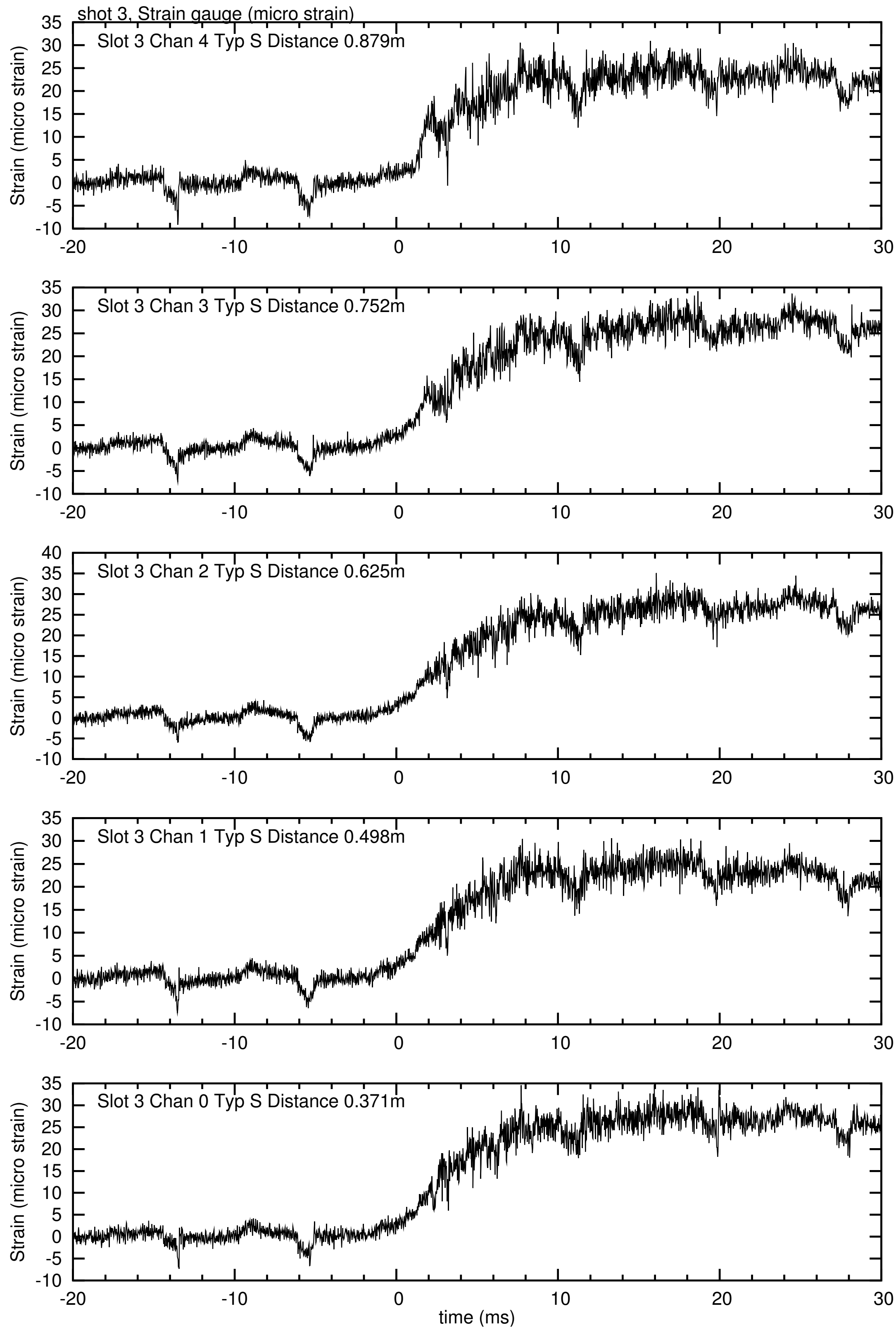

Figure 19: **Strain gauges, shot 3**, BR=0.37, O_2/C=0.8, P_{CJ}=2.79 MPa, P_{CV}=1.41 MPa.

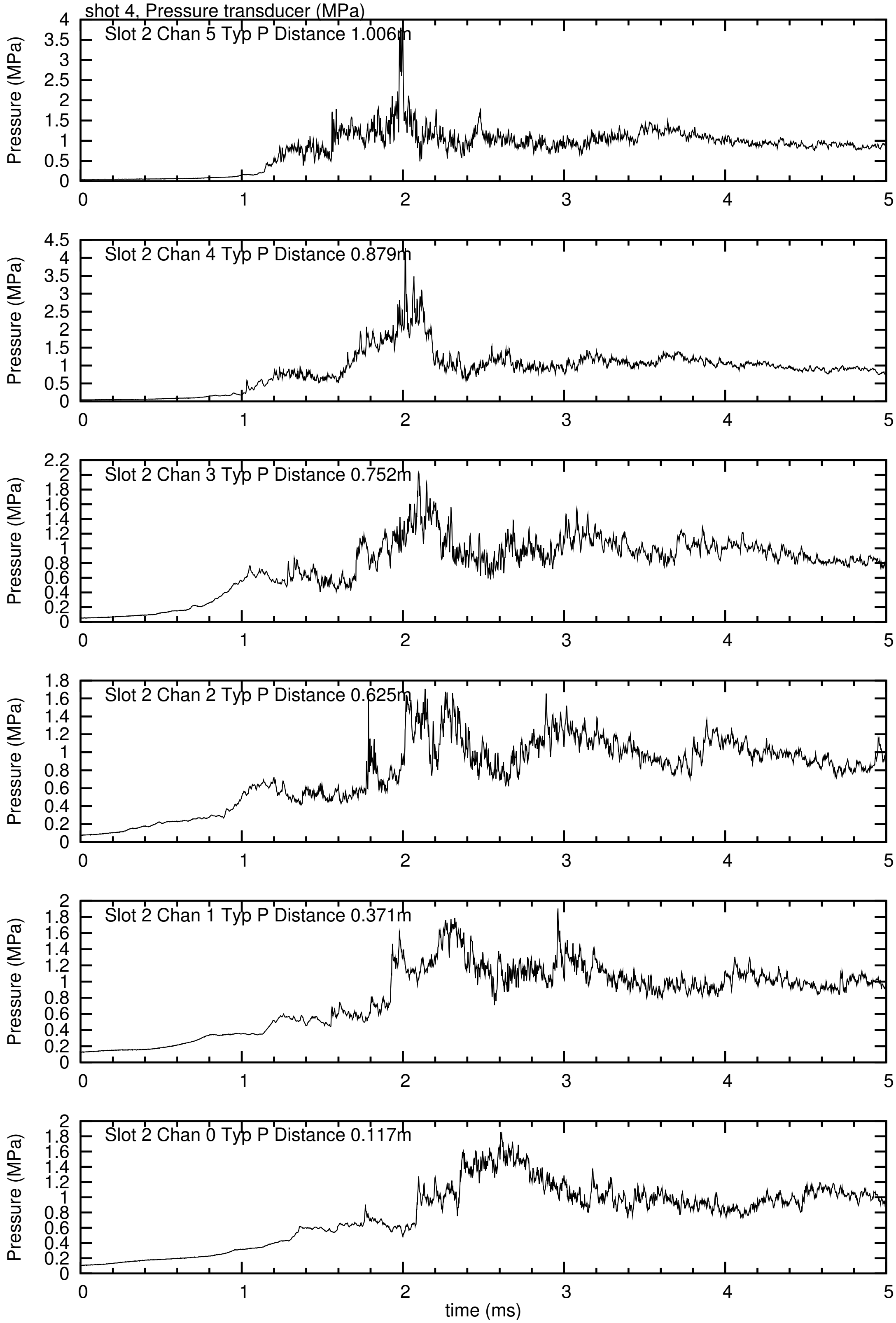

Figure 20: **Pressure transducers, shot 4**, BR=0.37, O_2/C=0.85, P_{CJ}=2.91 MPa, P_{CV}=1.47 MPa.

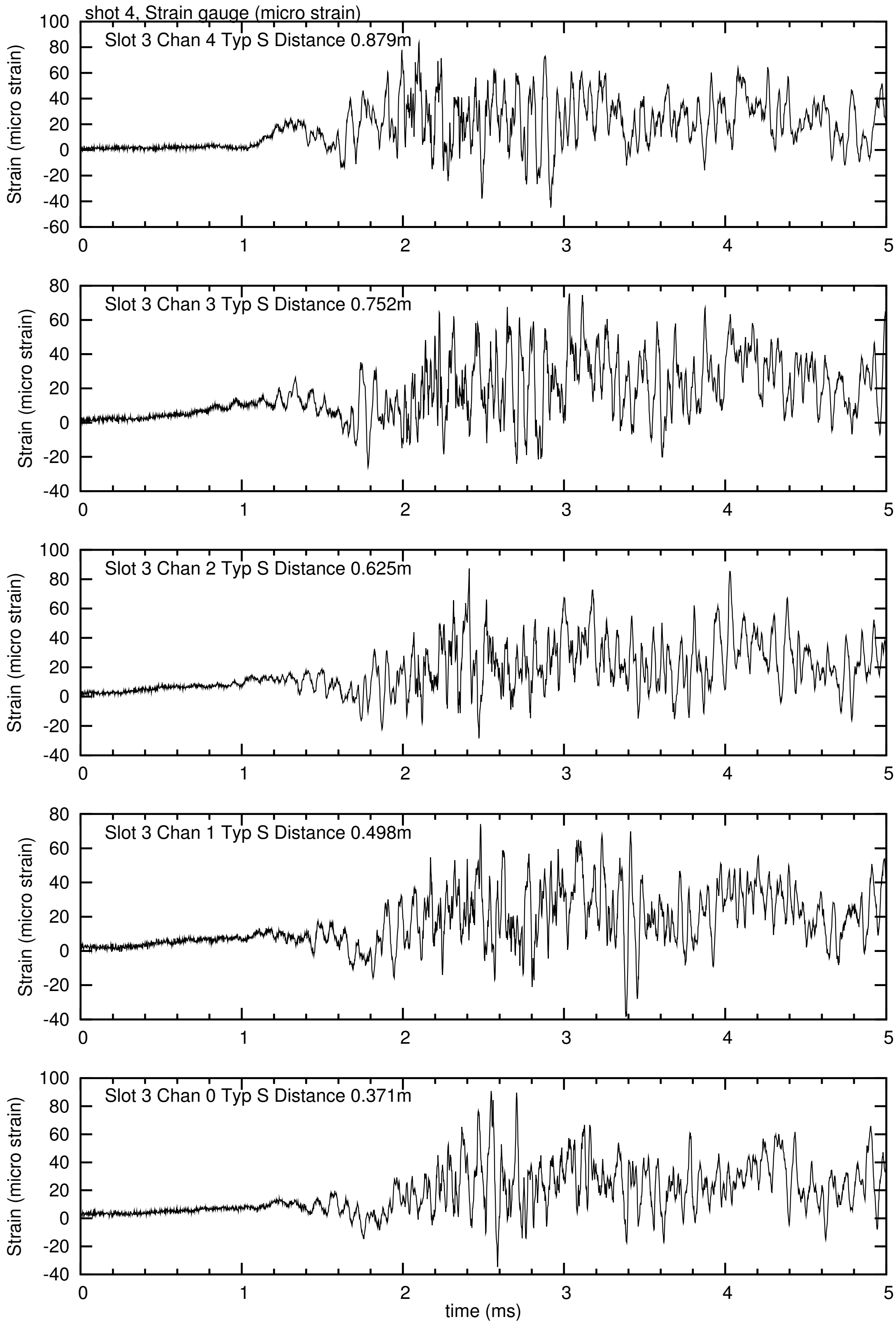

Figure 21: **Strain gauges, shot 4**, BR=0.37, O_2/C=0.85, P_{CJ}=2.91 MPa, P_{CV}=1.47 MPa.

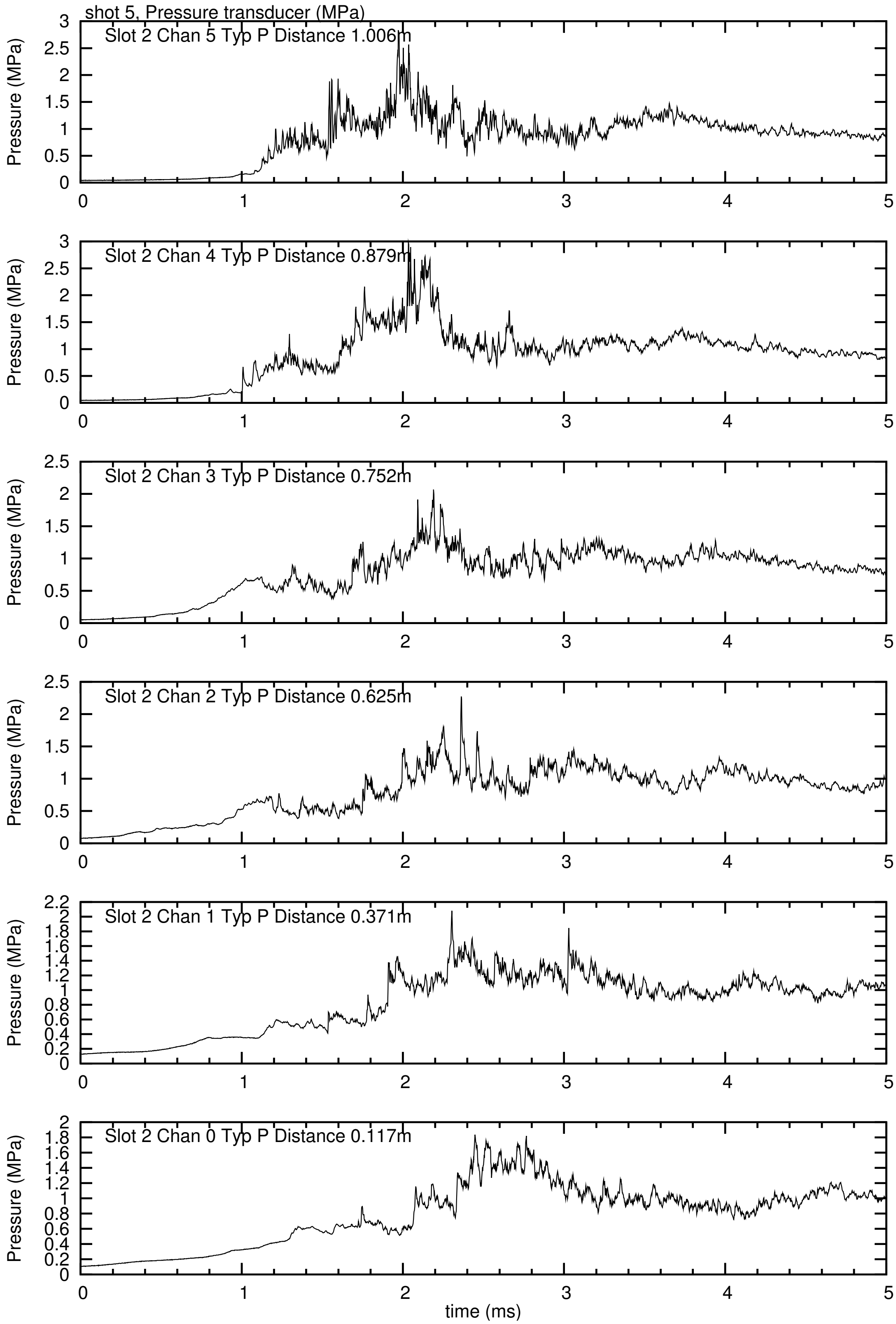

Figure 22: **Pressure transducers, shot 5**, BR=0.37, O_2/C=0.85, P_{CJ}=2.91 MPa, P_{CV}=1.47 MPa.

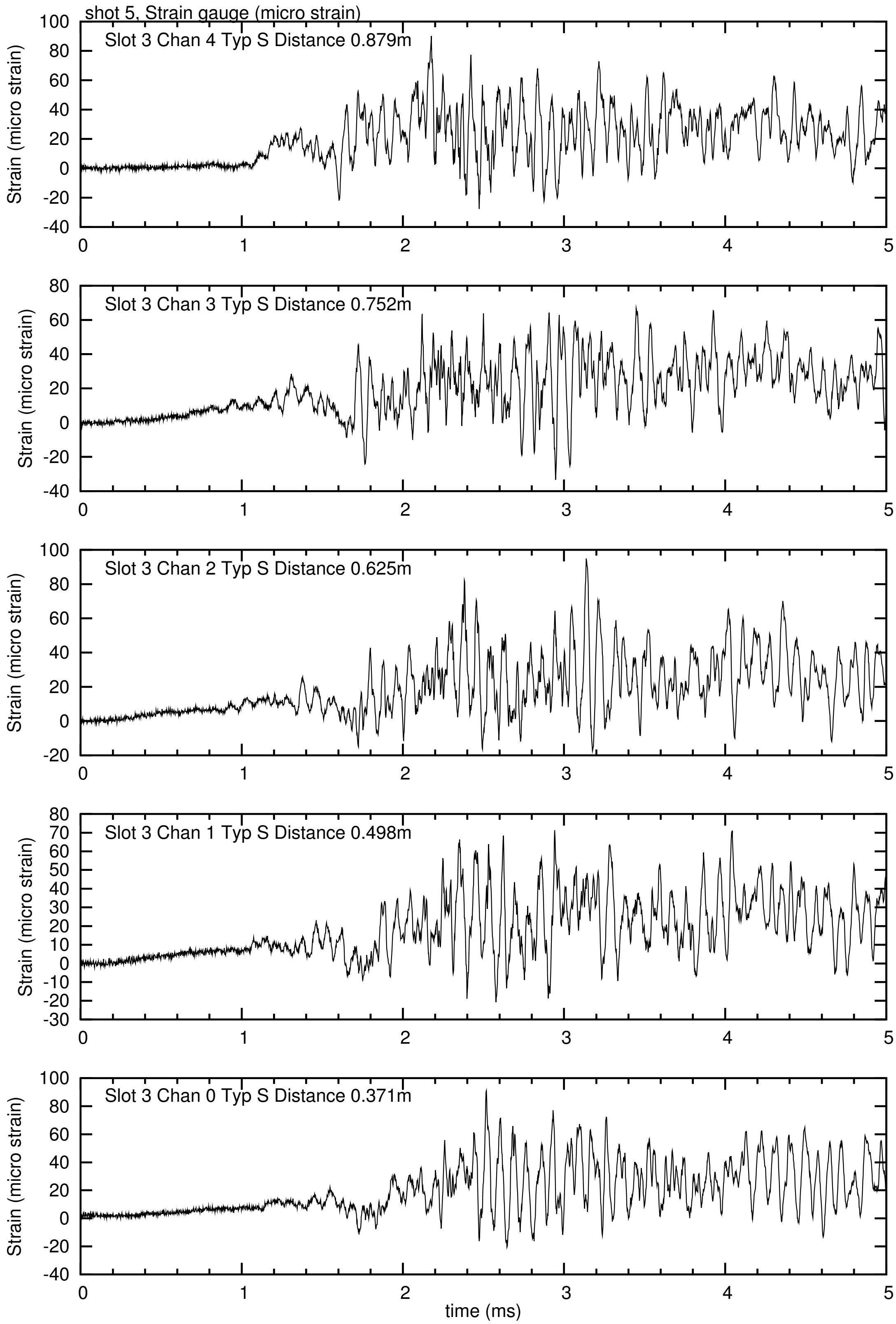

Figure 23: **Strain gauges, shot 5**, BR=0.37, O_2/C=0.85, P_{CJ}=2.91 MPa, P_{CV}=1.47 MPa.

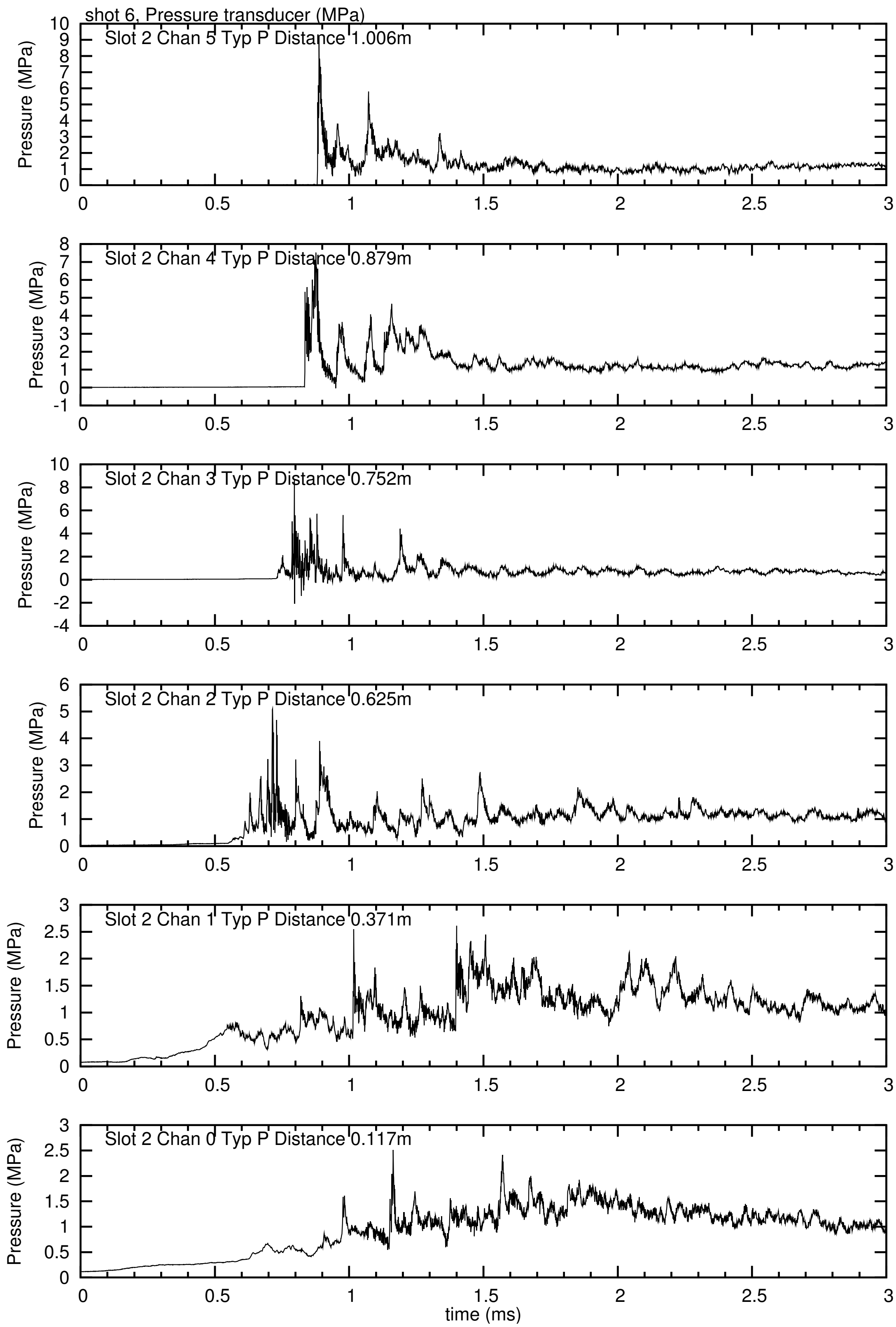

Figure 24: **Pressure transducers, shot 6**, BR=0.37, O_2/C=0.9, P_{CJ}=3.01 MPa, P_{CV}=1.52 MPa.

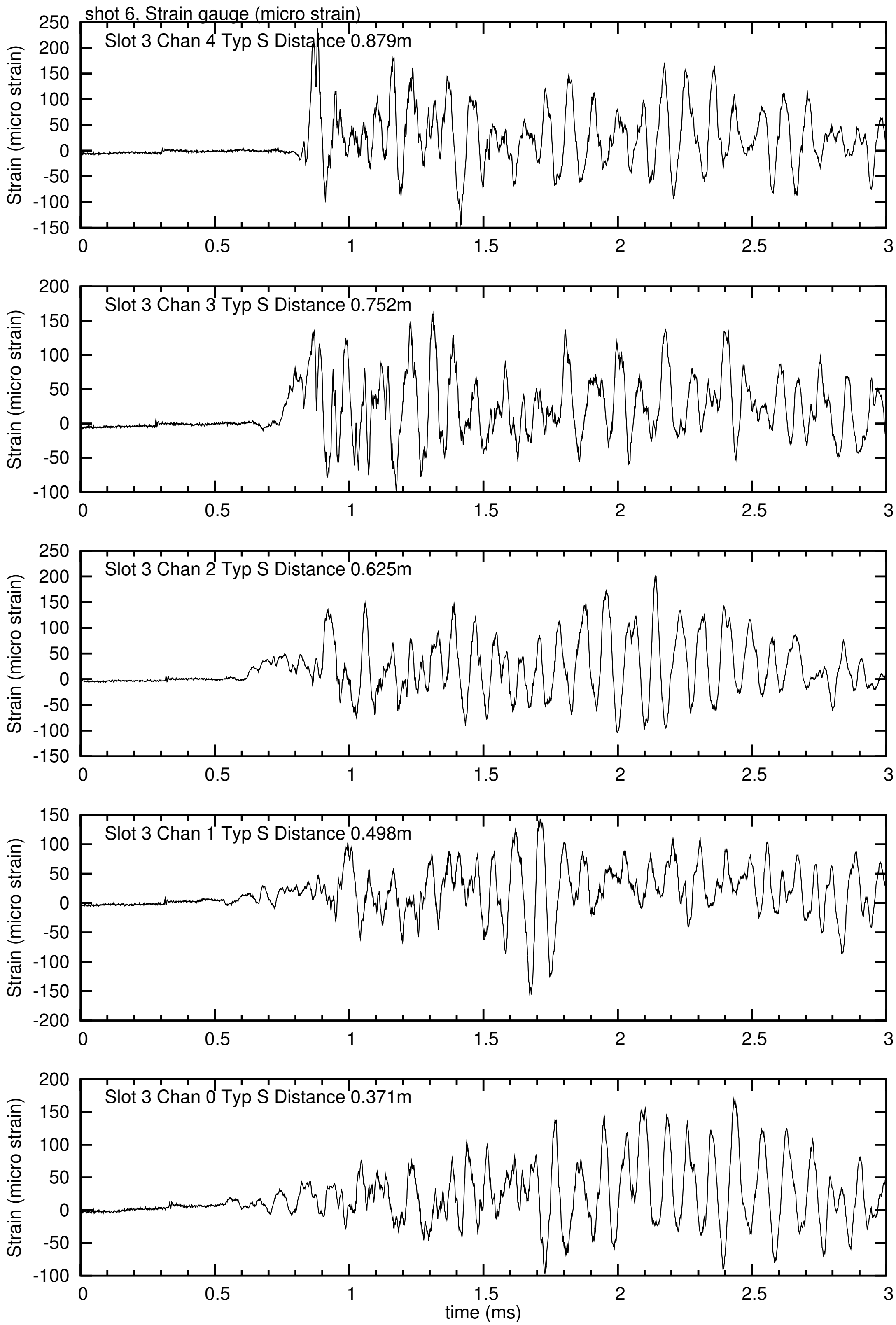

Figure 25: **Strain gauges, shot 6**, BR=0.37, O_2/C=0.9, P_{CJ}=3.01 MPa, P_{CV}=1.52 MPa.

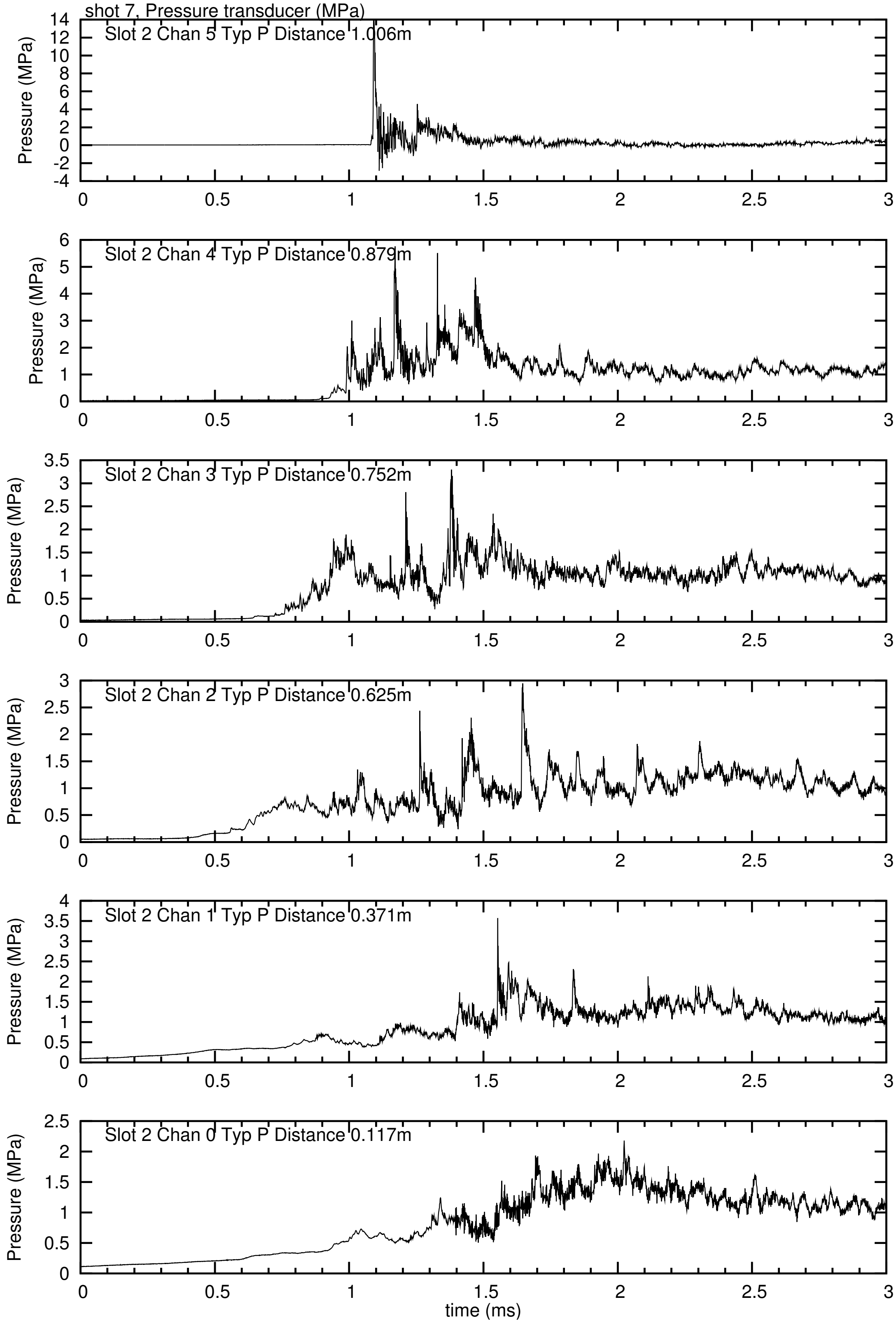

Figure 26: **Pressure transducers, shot 7**, BR=0.37, O_2/C=0.9, P_{CJ}=3.01 MPa, P_{CV}=1.52 MPa.

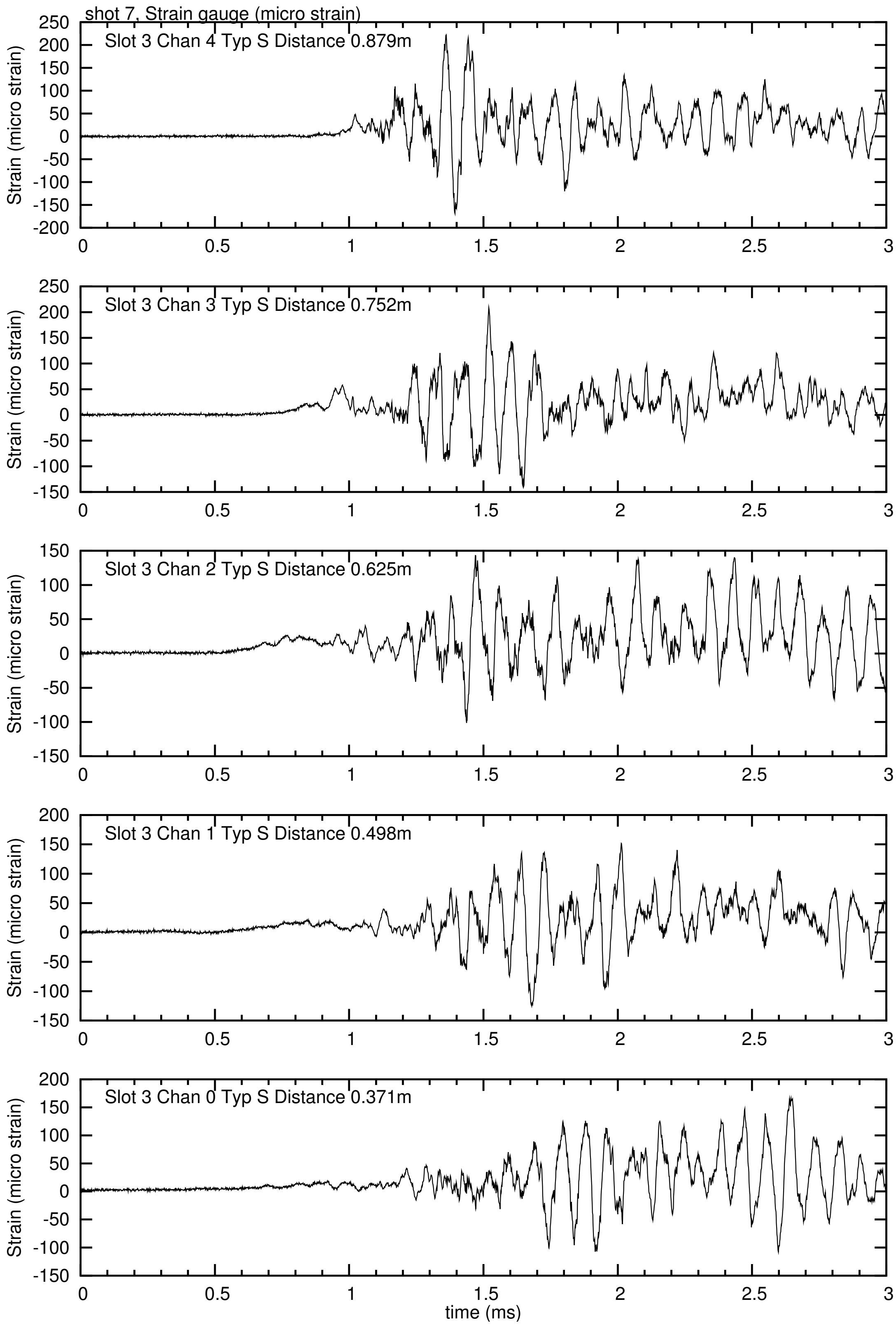

Figure 27: **Strain gauges, shot 7**, BR=0.37, O_2/C=0.9, P_{CJ}=3.01 MPa, P_{CV}=1.52 MPa.

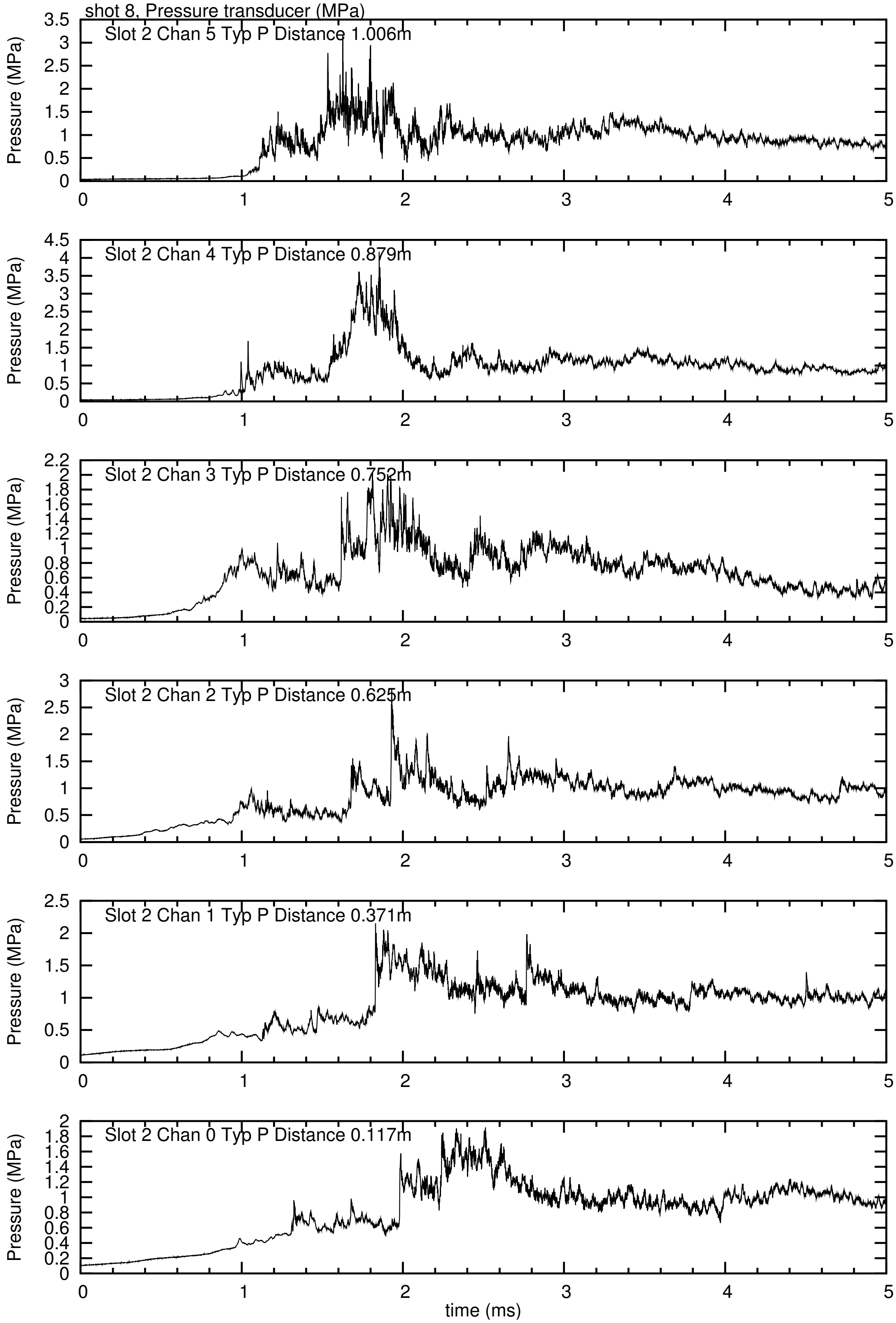

Figure 28: **Pressure transducers, shot 8**, BR=0.37, O_2/C=0.85, P_{CJ}=2.91 MPa, P_{CV}=1.47 MPa.

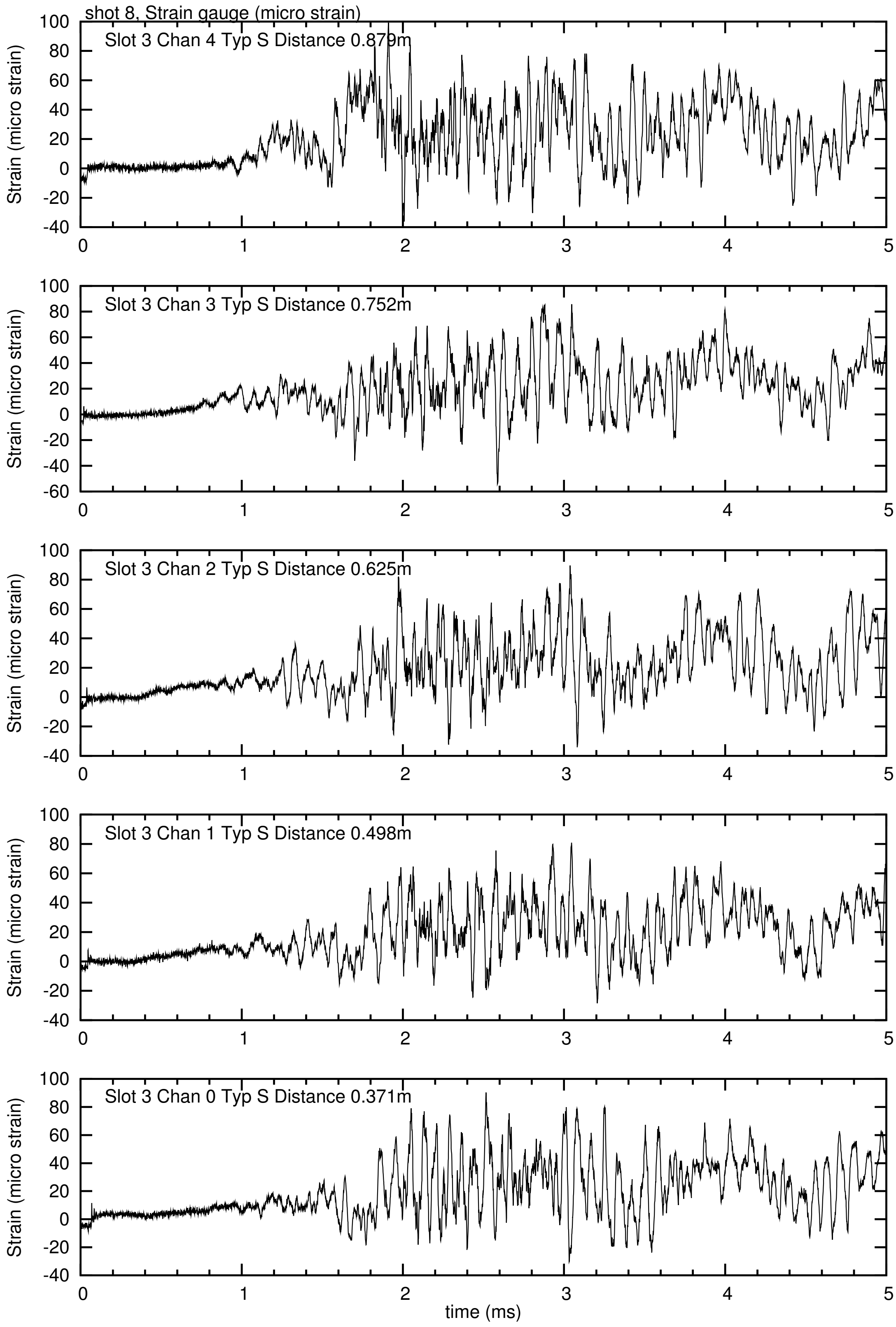

Figure 29: **Strain gauges, shot 8**, BR=0.37, O_2/C=0.85, P_{CJ}=2.91 MPa, P_{CV}=1.47 MPa.

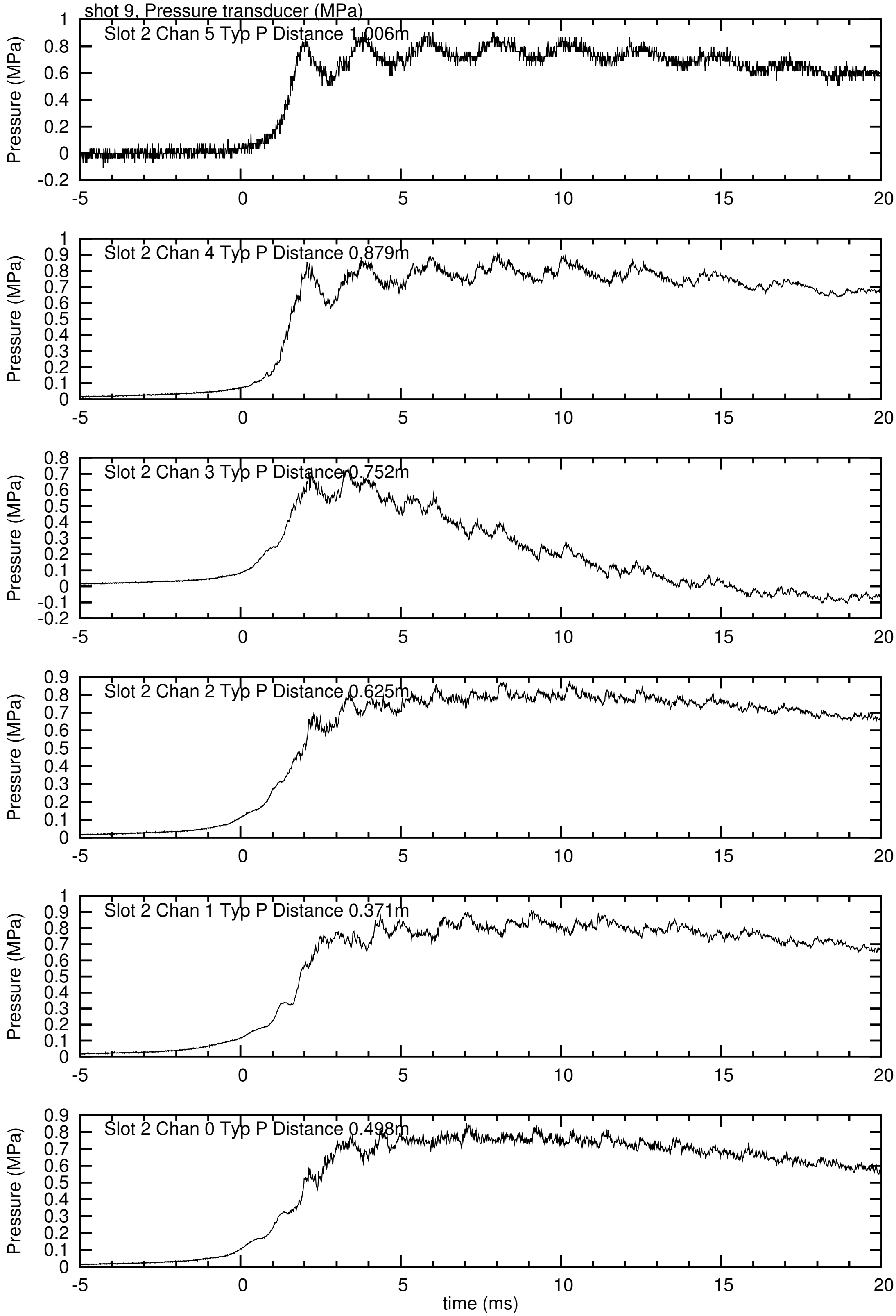

Figure 30: **Pressure transducers, shot 9**, BR=0.37, O_2/C=0.8, P_{CJ}=2.79 MPa, P_{CV}=1.41 MPa.

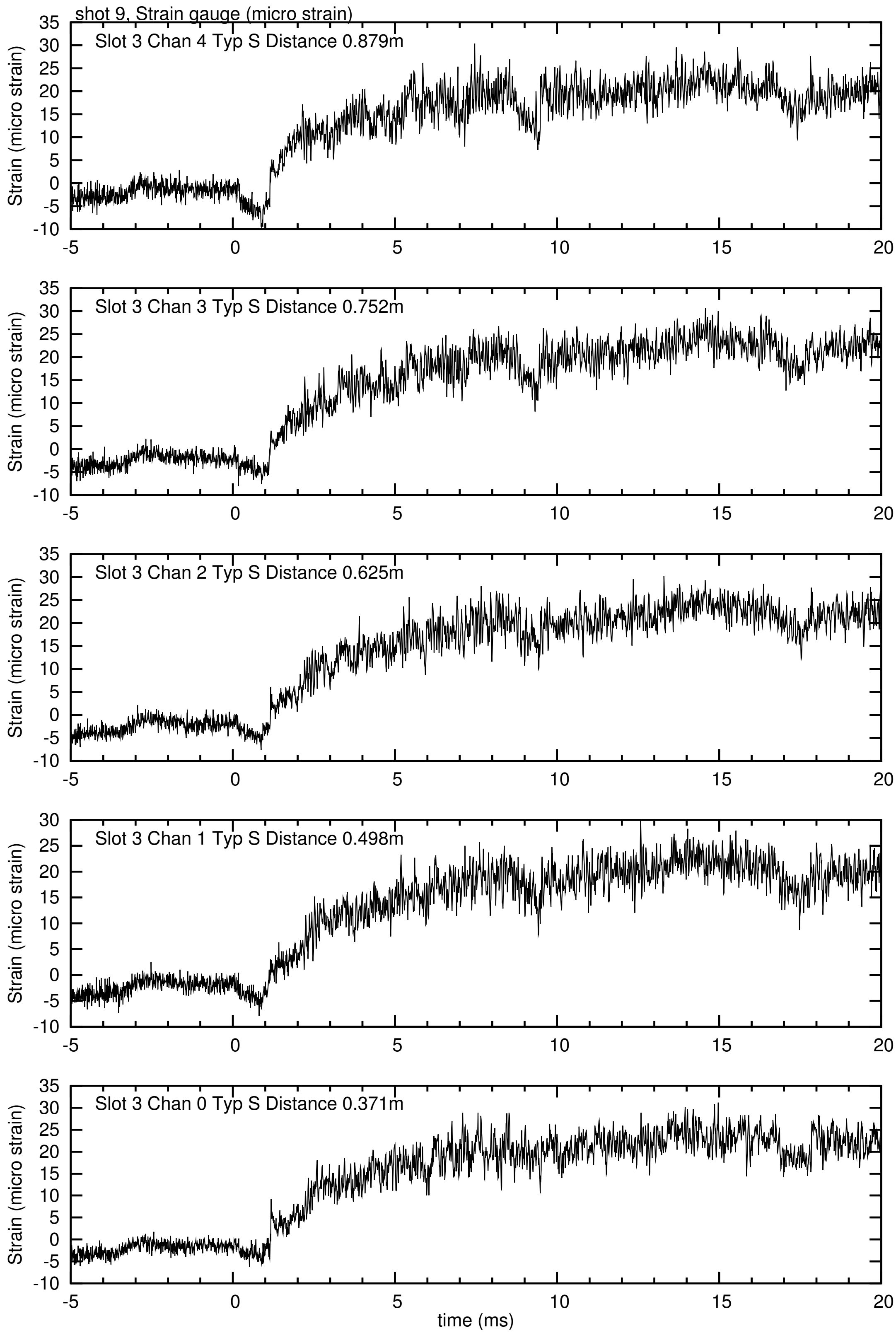

Figure 31: **Strain gauges, shot 9**, BR=0.37, O_2/C=0.8, P_{CJ}=2.79 MPa, P_{CV}=1.41 MPa.

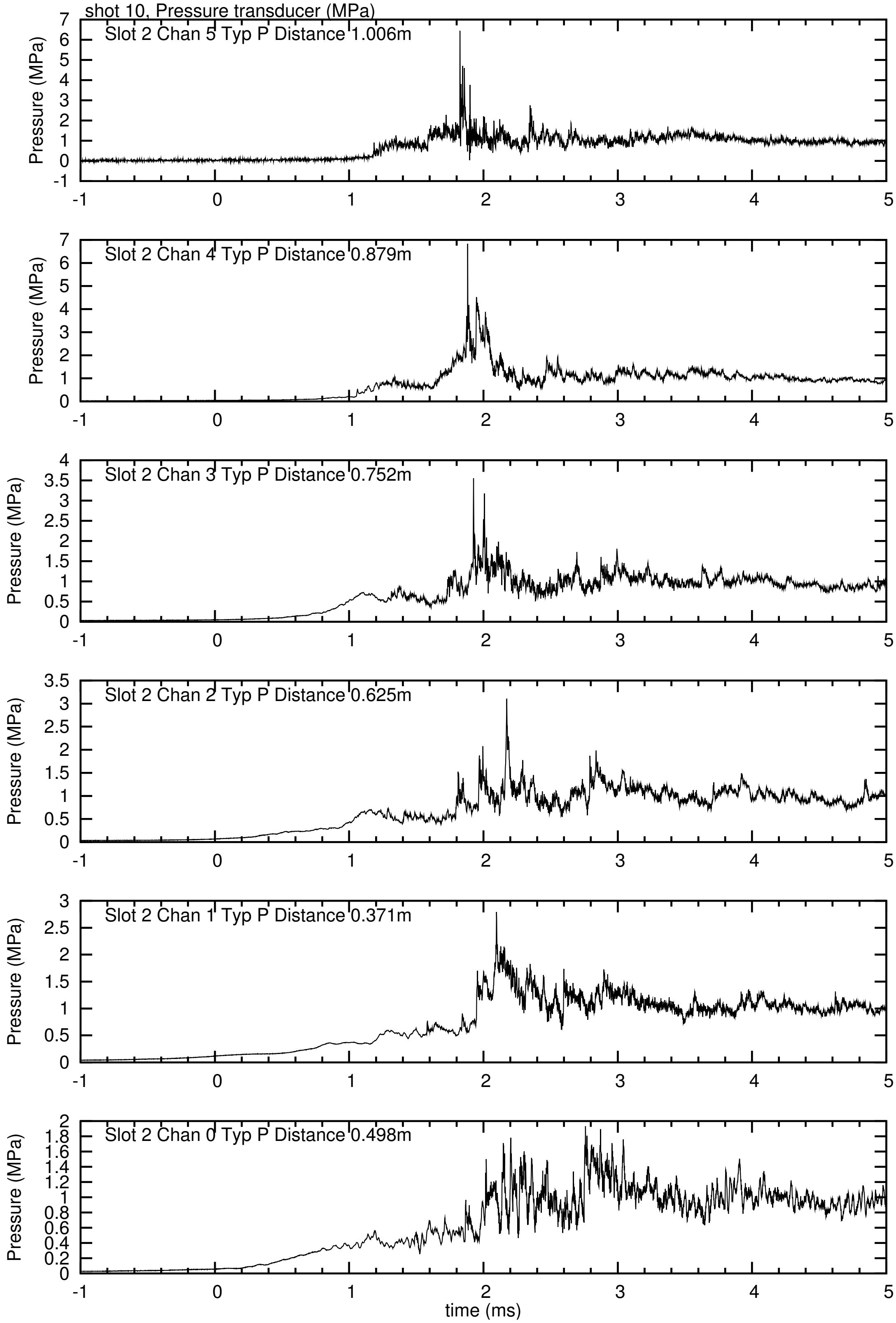

Figure 32: **Pressure transducers, shot 10**, BR=0.37, O_2/C=0.85, P_{CJ}=2.91 MPa, P_{CV}=1.47 MPa.

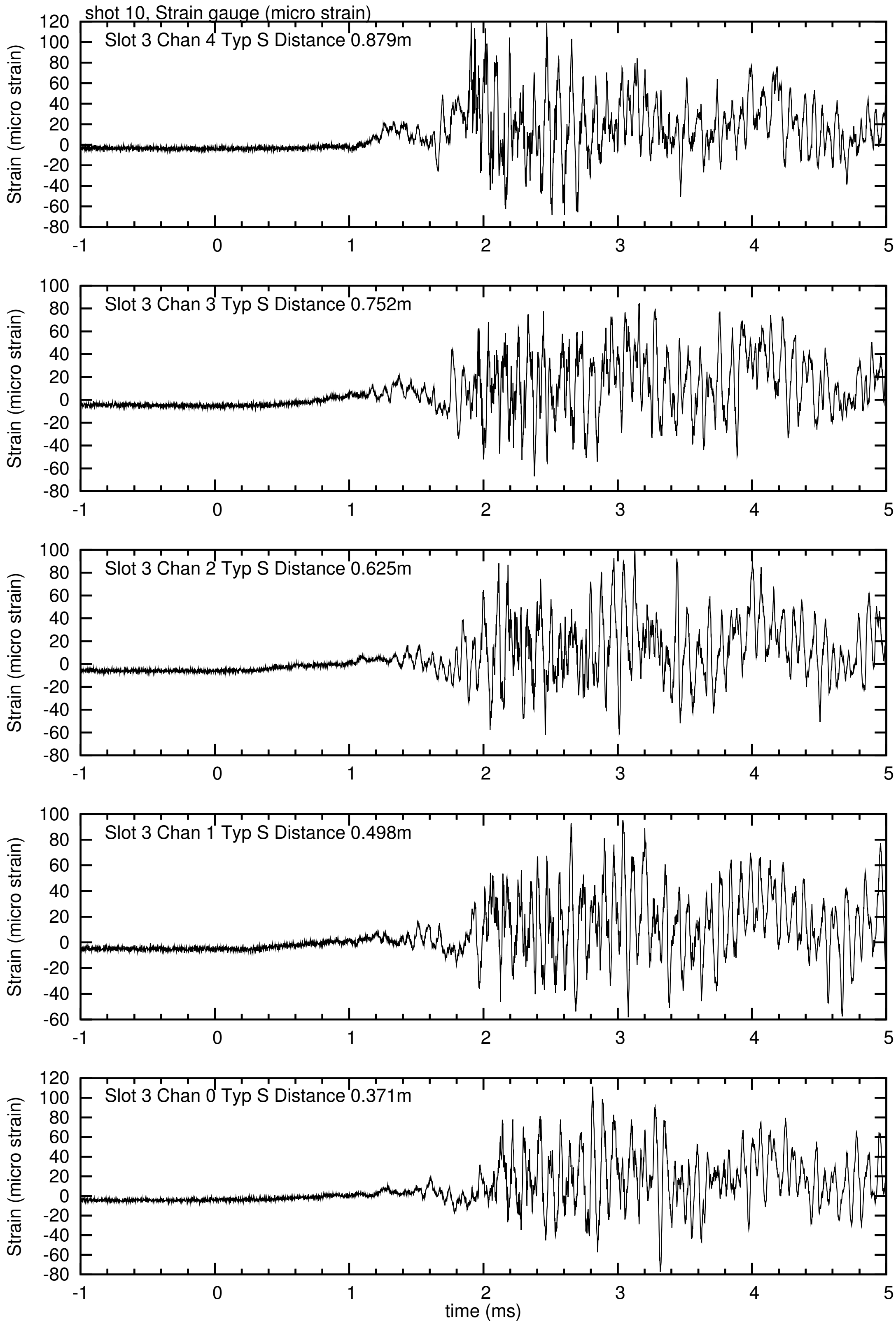

Figure 33: **Strain gauges, shot 10**, BR=0.37, O_2/C=0.85, P_{CJ}=2.91 MPa, P_{CV}=1.47 MPa.

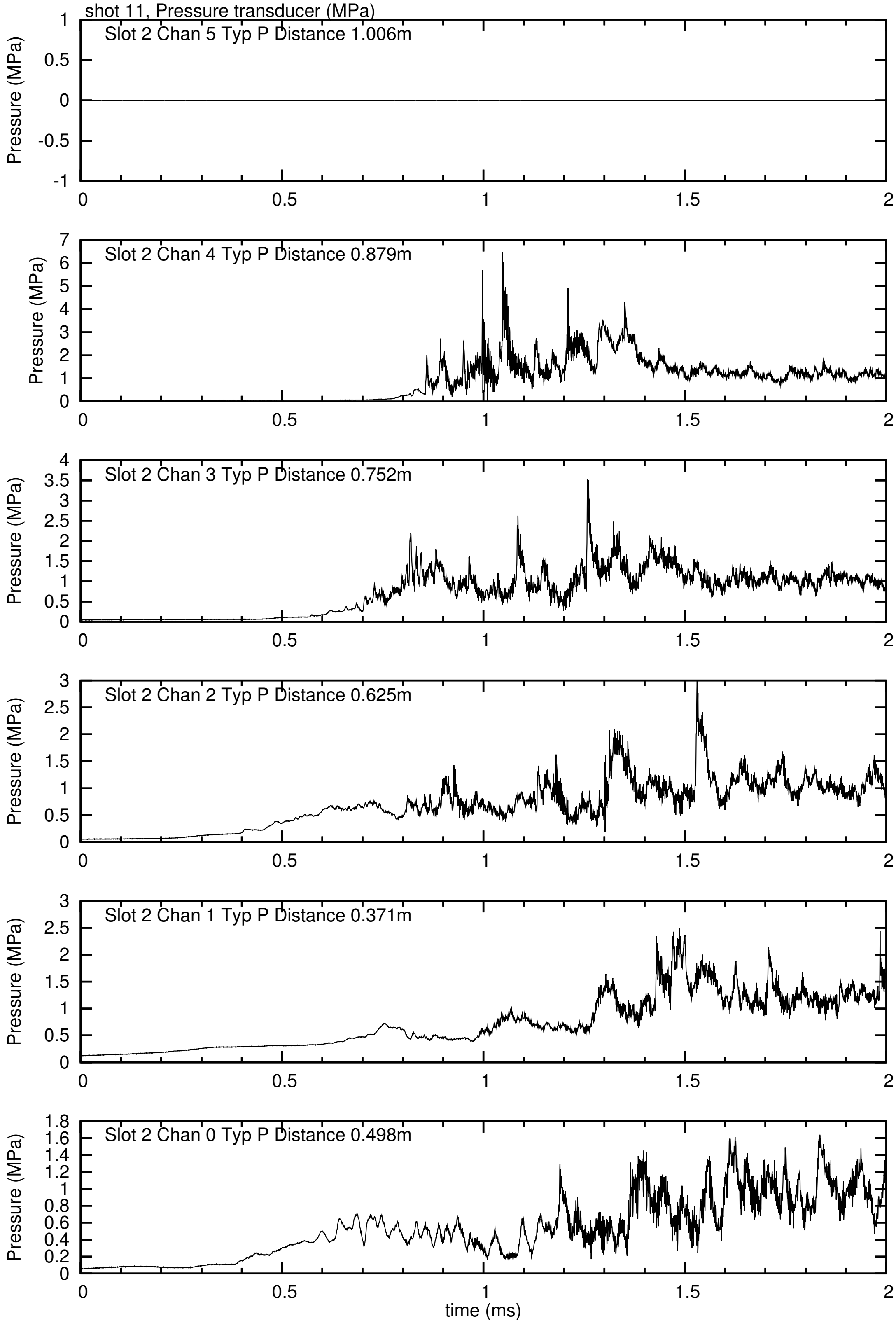

Figure 34: **Pressure transducers, shot 11**, BR=0.37, O_2/C=0.9, P_{CJ}=3.01 MPa, P_{CV}=1.52 MPa.

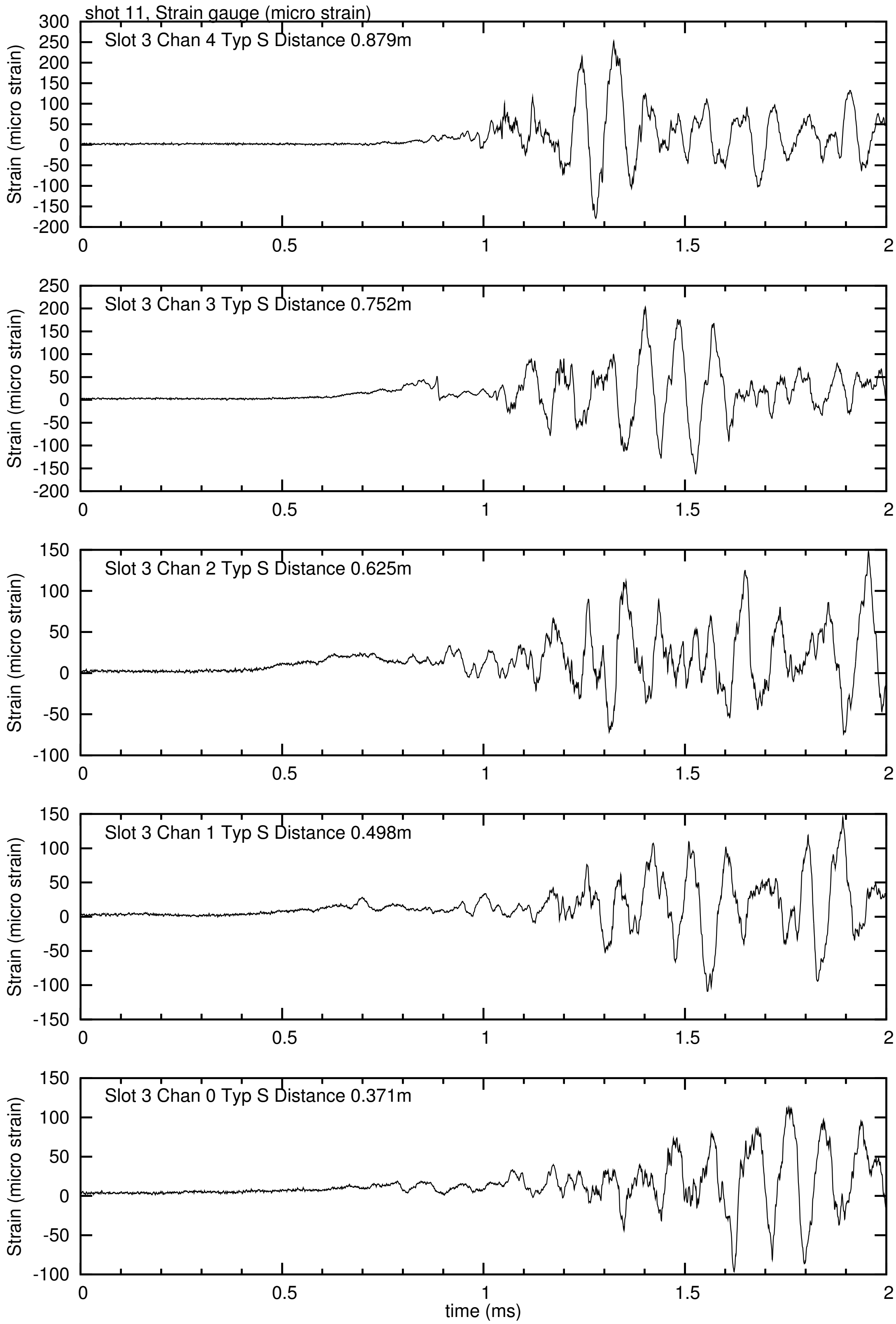

Figure 35: **Strain gauges, shot 11**, BR=0.37, O_2/C=0.9, P_{CJ}=3.01 MPa, P_{CV}=1.52 MPa.

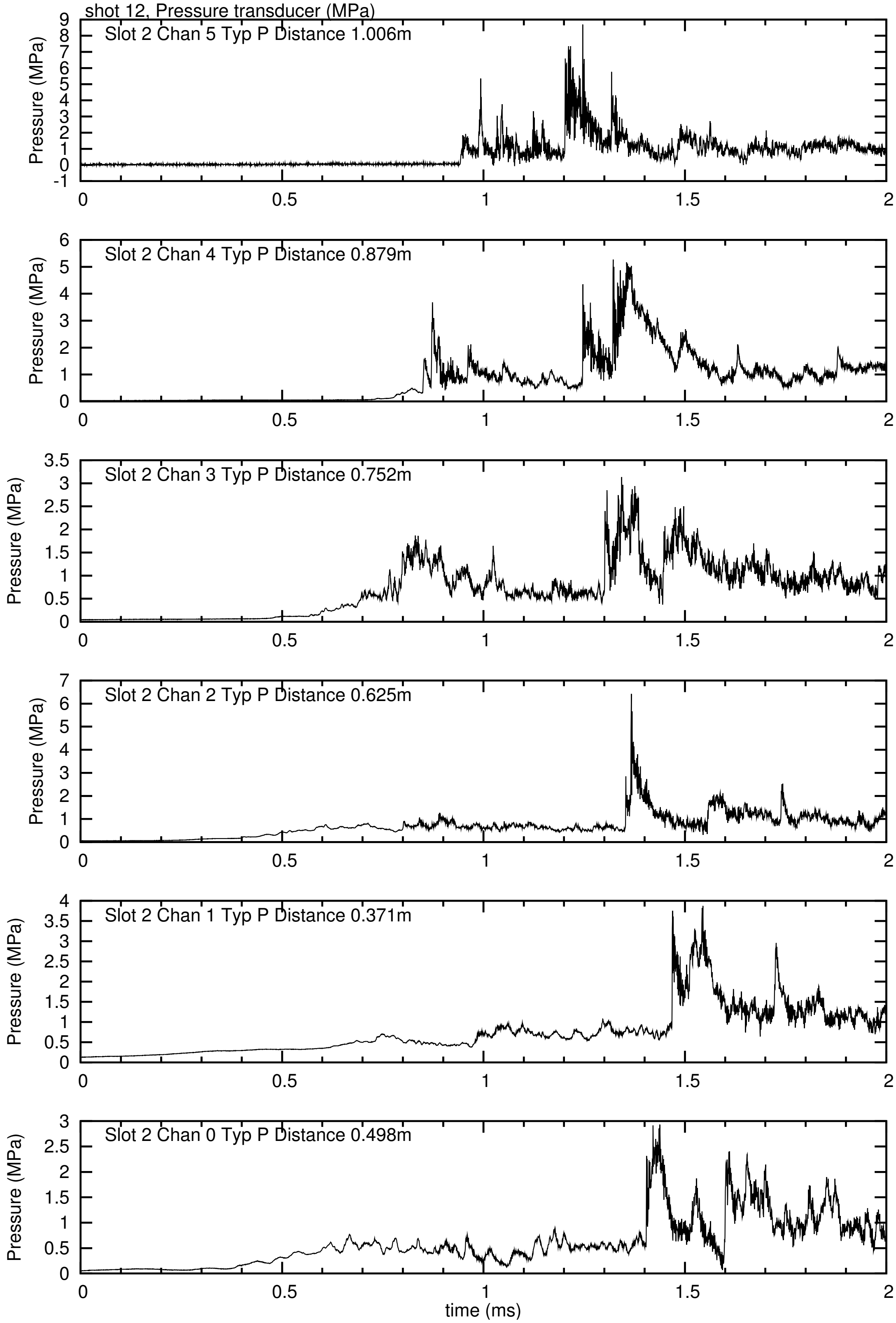

Figure 36: **Pressure transducers, shot 12**, BR=0.37, O_2/C=0.9, P_{CJ}=3.01 MPa, P_{CV}=1.52 MPa.

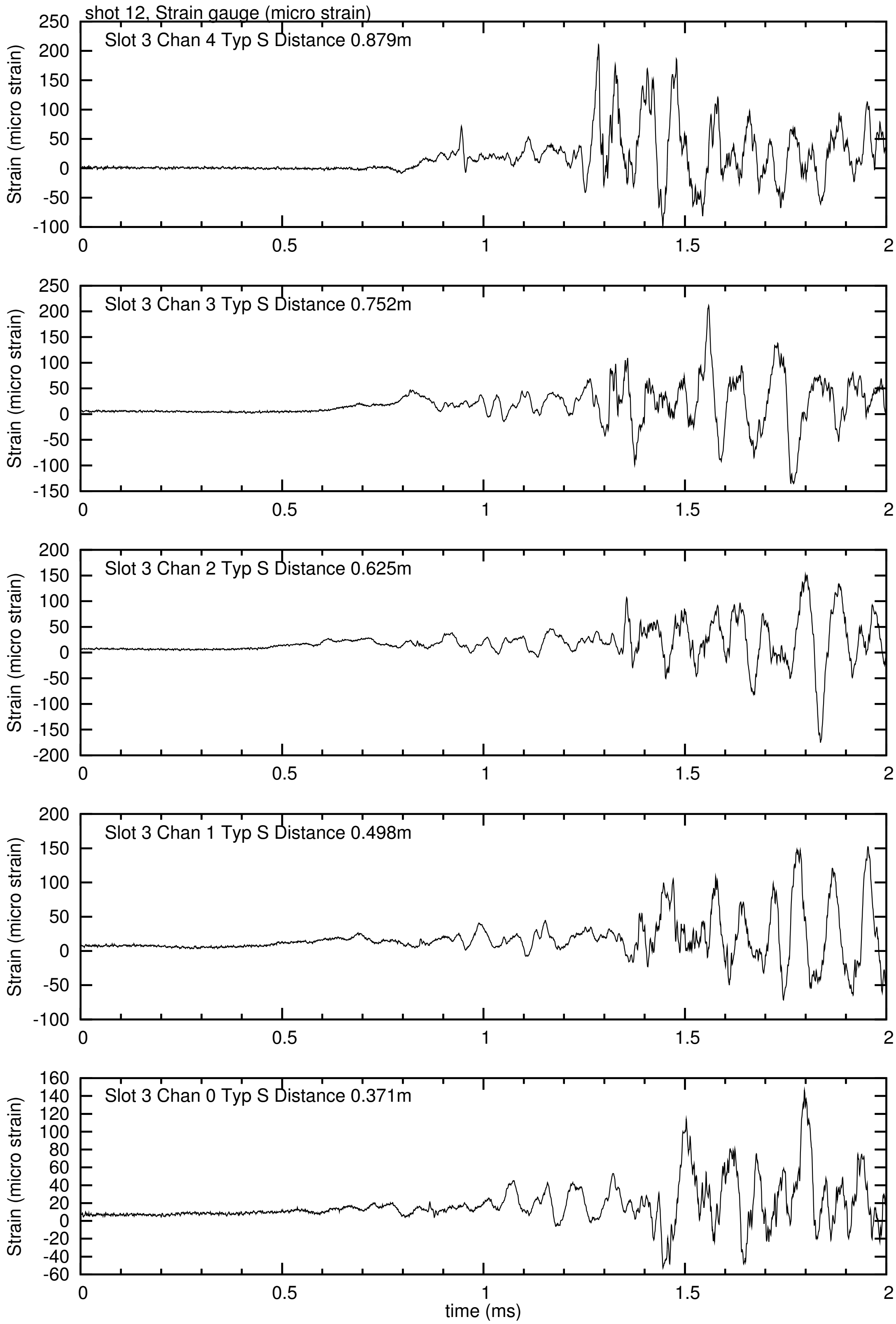

Figure 37: **Strain gauges, shot 12**, BR=0.37, O_2/C=0.9, P_{CJ}=3.01 MPa, P_{CV}=1.52 MPa.

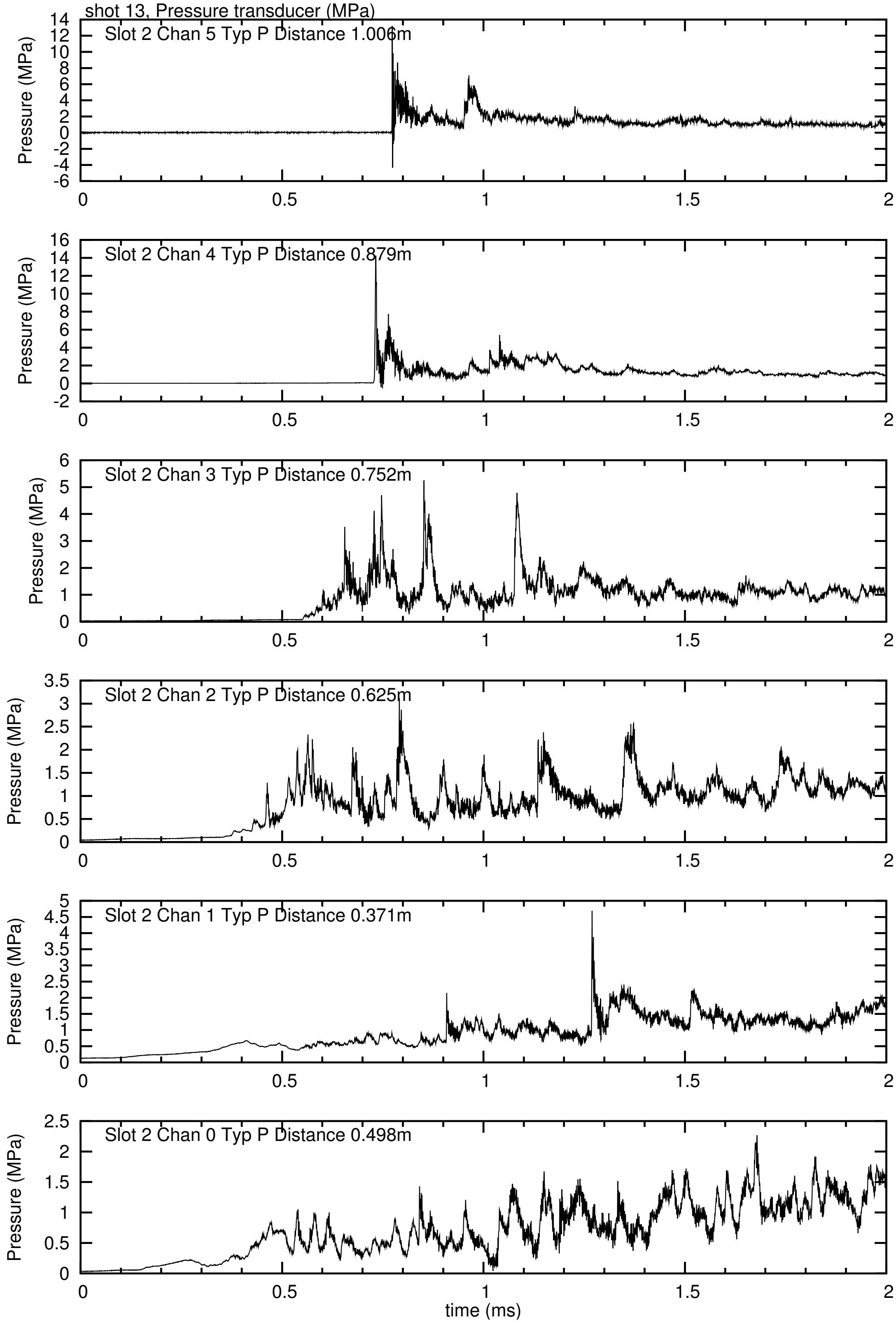

Figure 38: **Pressure transducers, shot 13**, BR=0.37, O_2/C=0.95, P_{CJ}=3.08 MPa, P_{CV}=1.56 MPa.

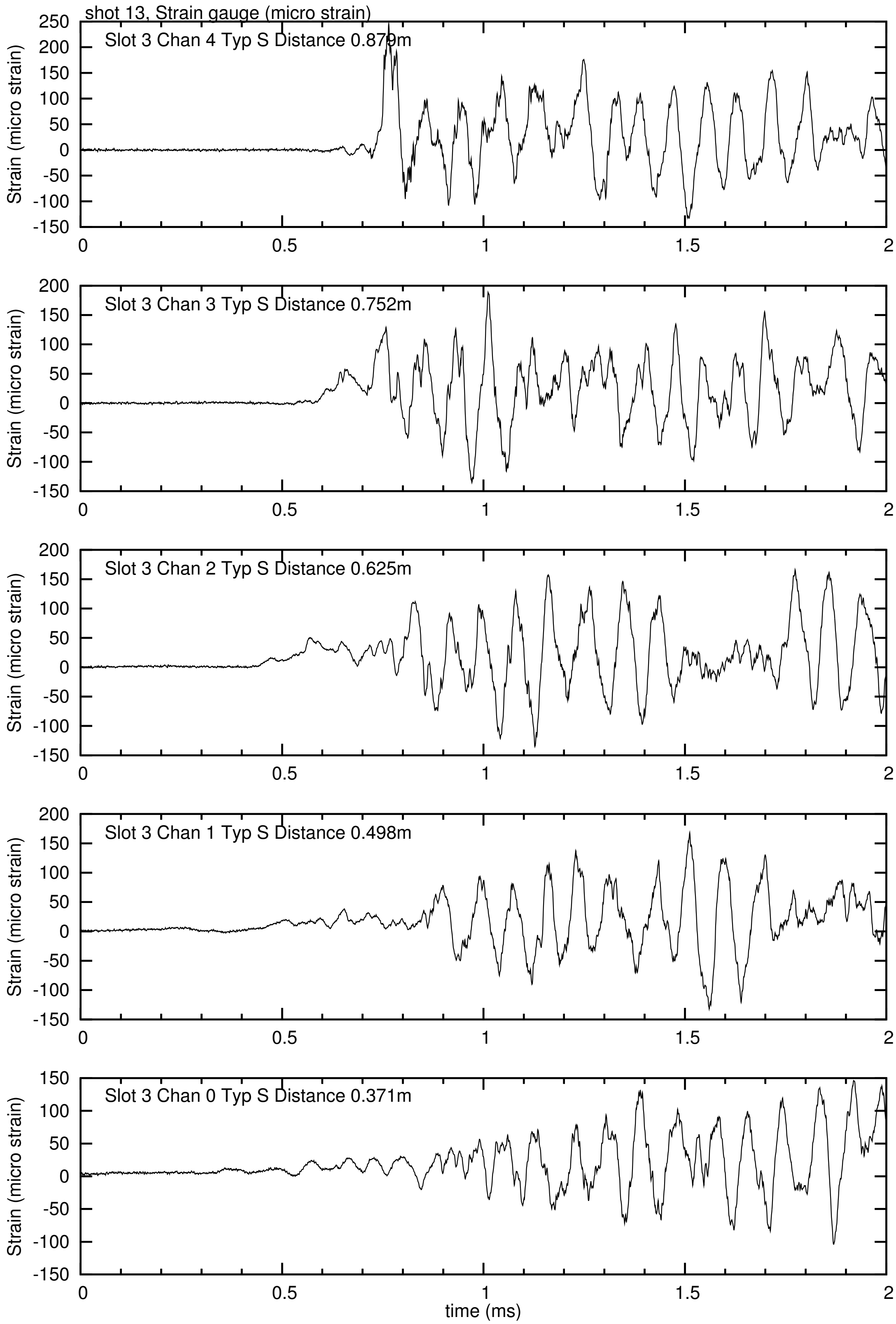

Figure 39: **Strain gauges, shot 13**, BR=0.37, O_2/C=0.95, P_{CJ}=3.08 MPa, P_{CV}=1.56 MPa.

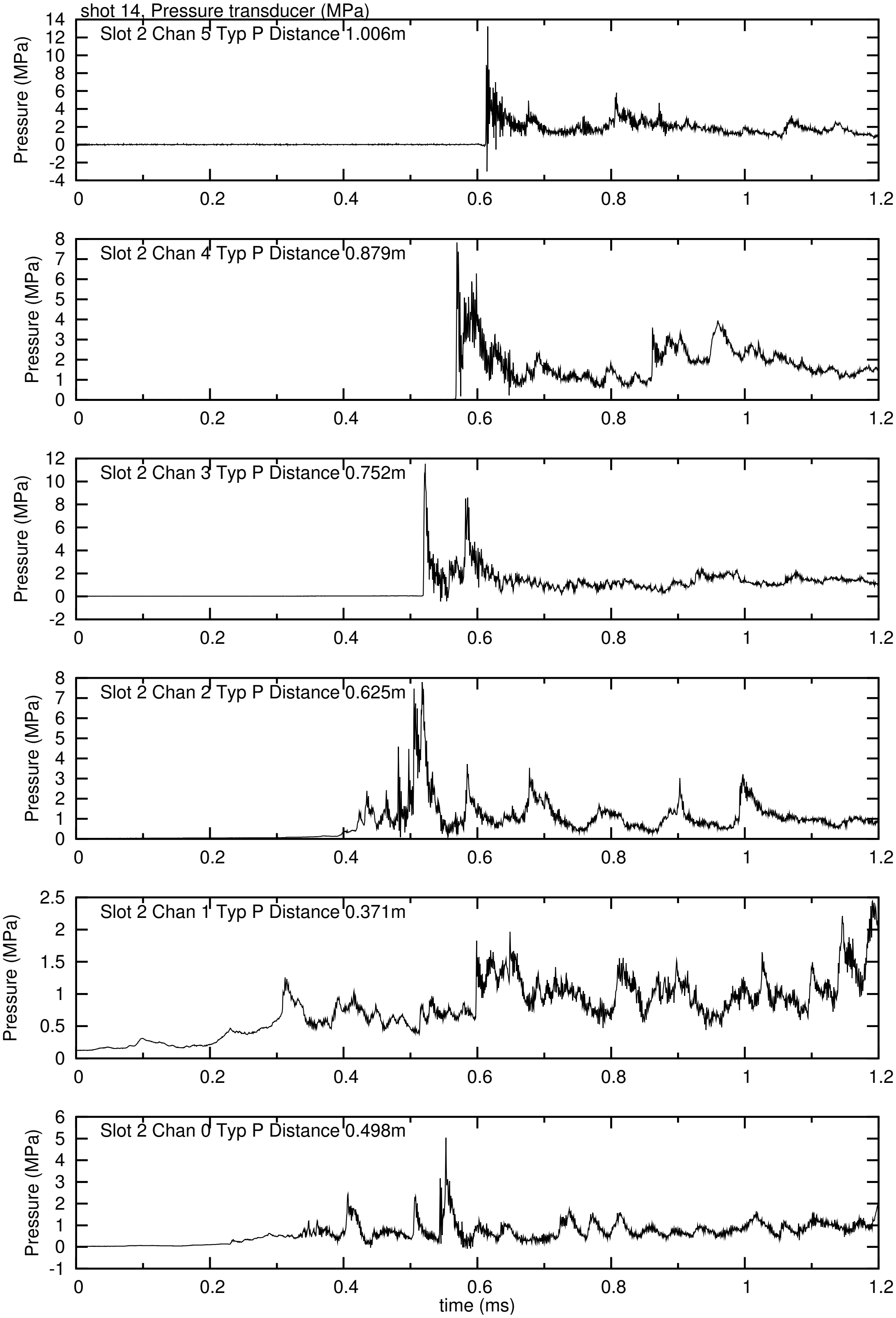

Figure 40: **Pressure transducers, shot 14**, BR=0.37, O_2/C=1, P_{CJ}=3.13 MPa, P_{CV}=1.58 MPa.

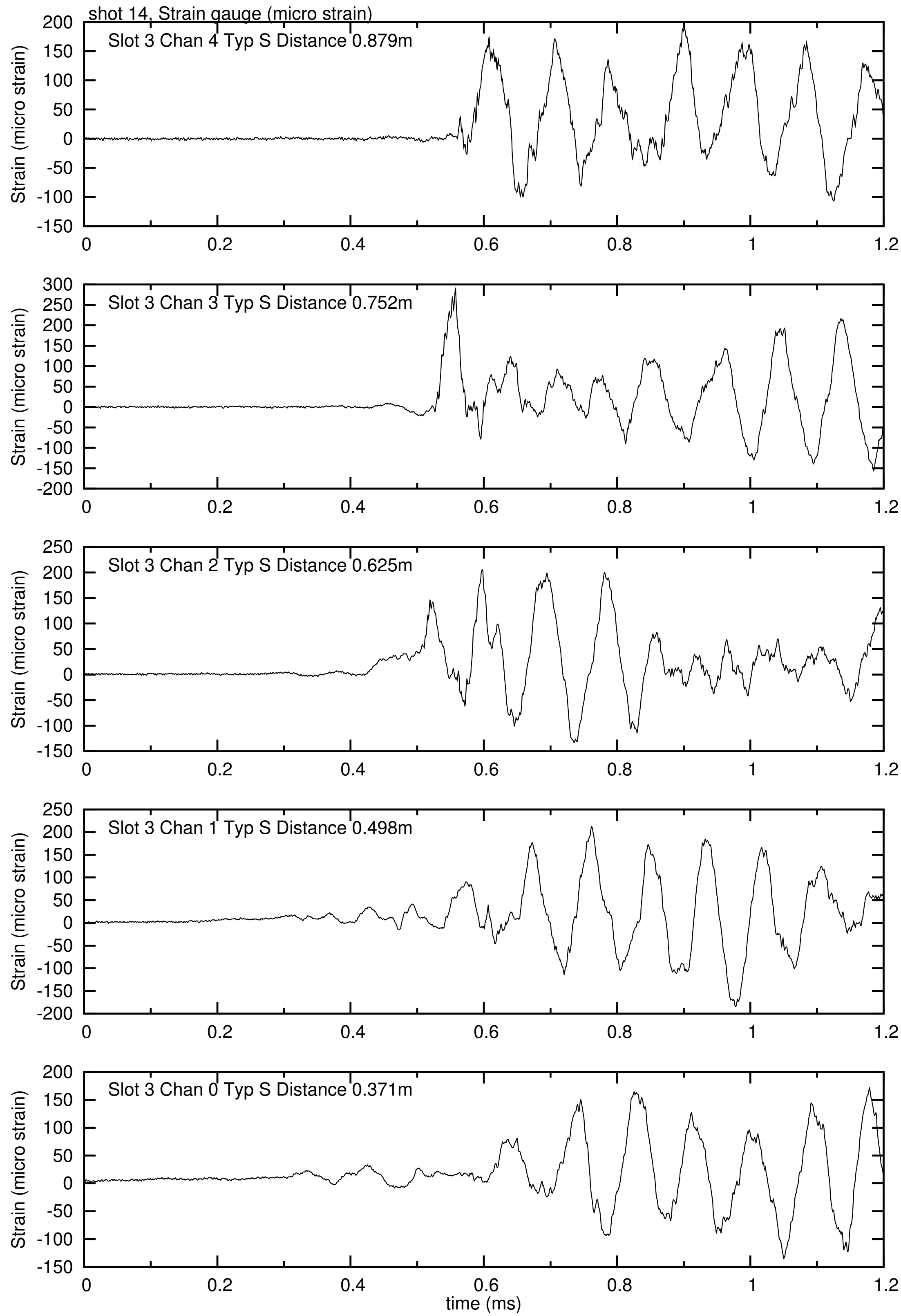

Figure 41: **Strain gauges, shot 14**, BR=0.37, O_2/C=1, P_{CJ}=3.13 MPa, P_{CV}=1.58 MPa.

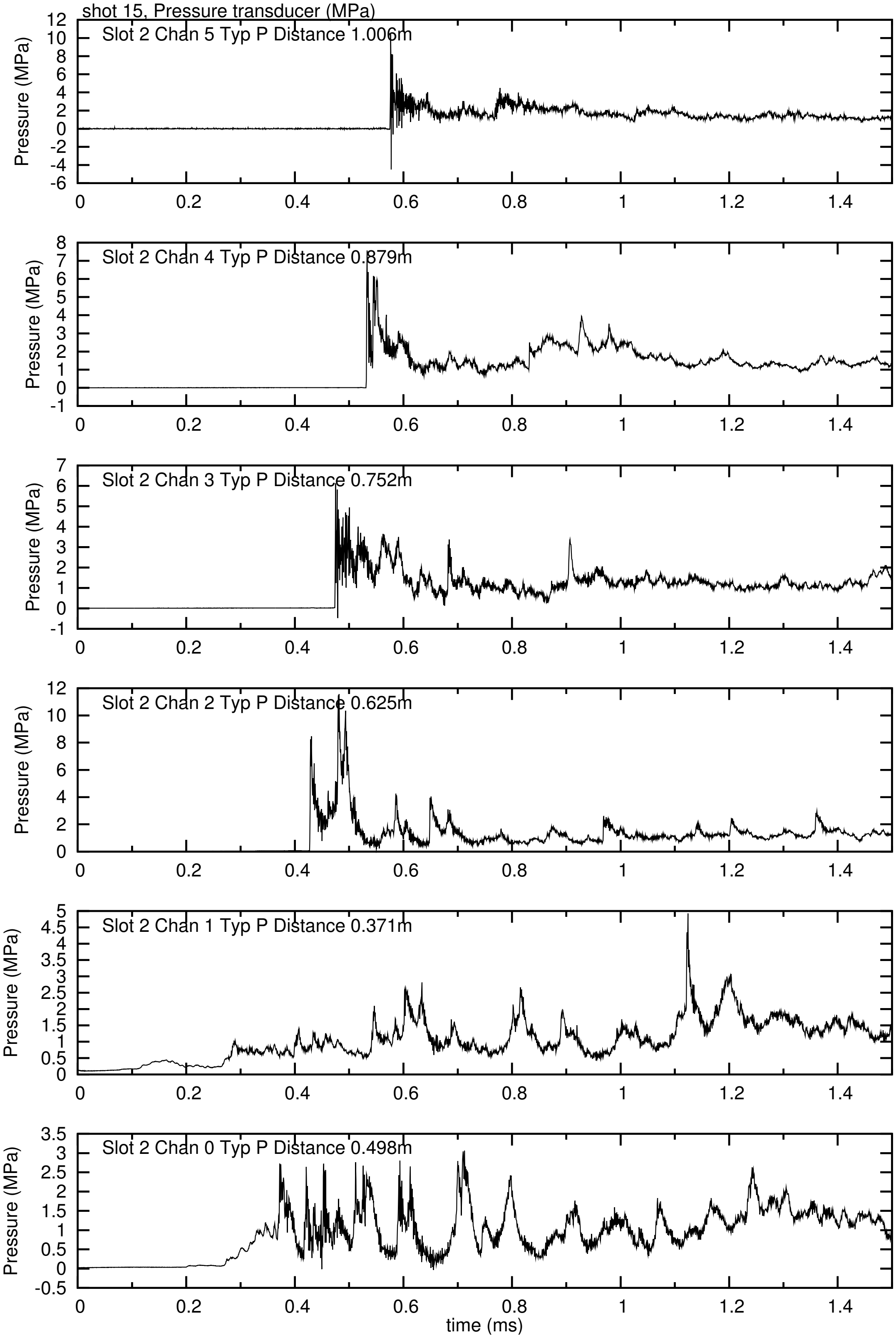

Figure 42: **Pressure transducers, shot 15**, BR=0.37, O_2/C=1.05, P_{CJ}=3.17 MPa, P_{CV}=1.60 MPa.

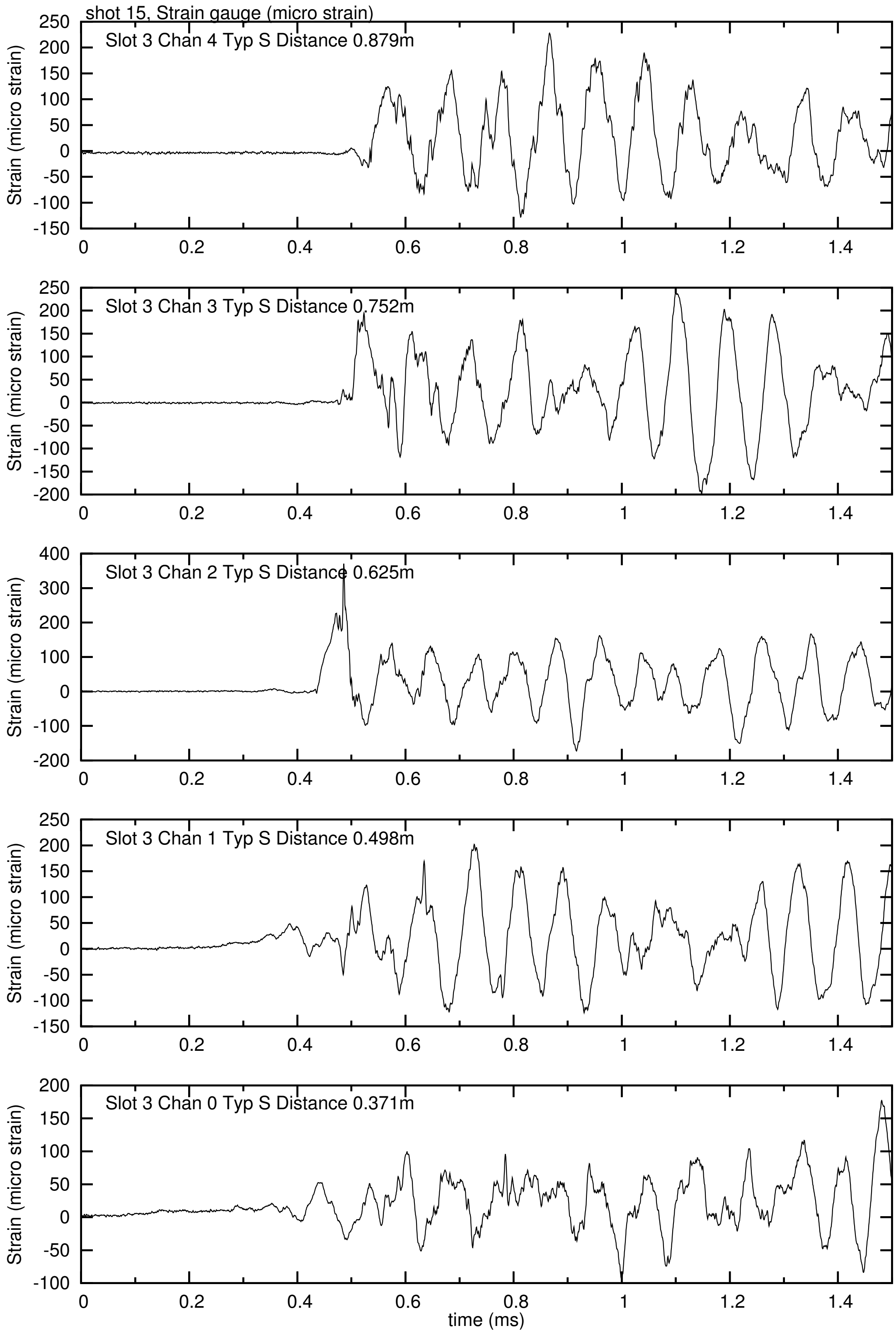

Figure 43: **Strain gauges, shot 15**, BR=0.37, O_2/C=1.05, P_{CJ}=3.17 MPa, P_{CV}=1.60 MPa.

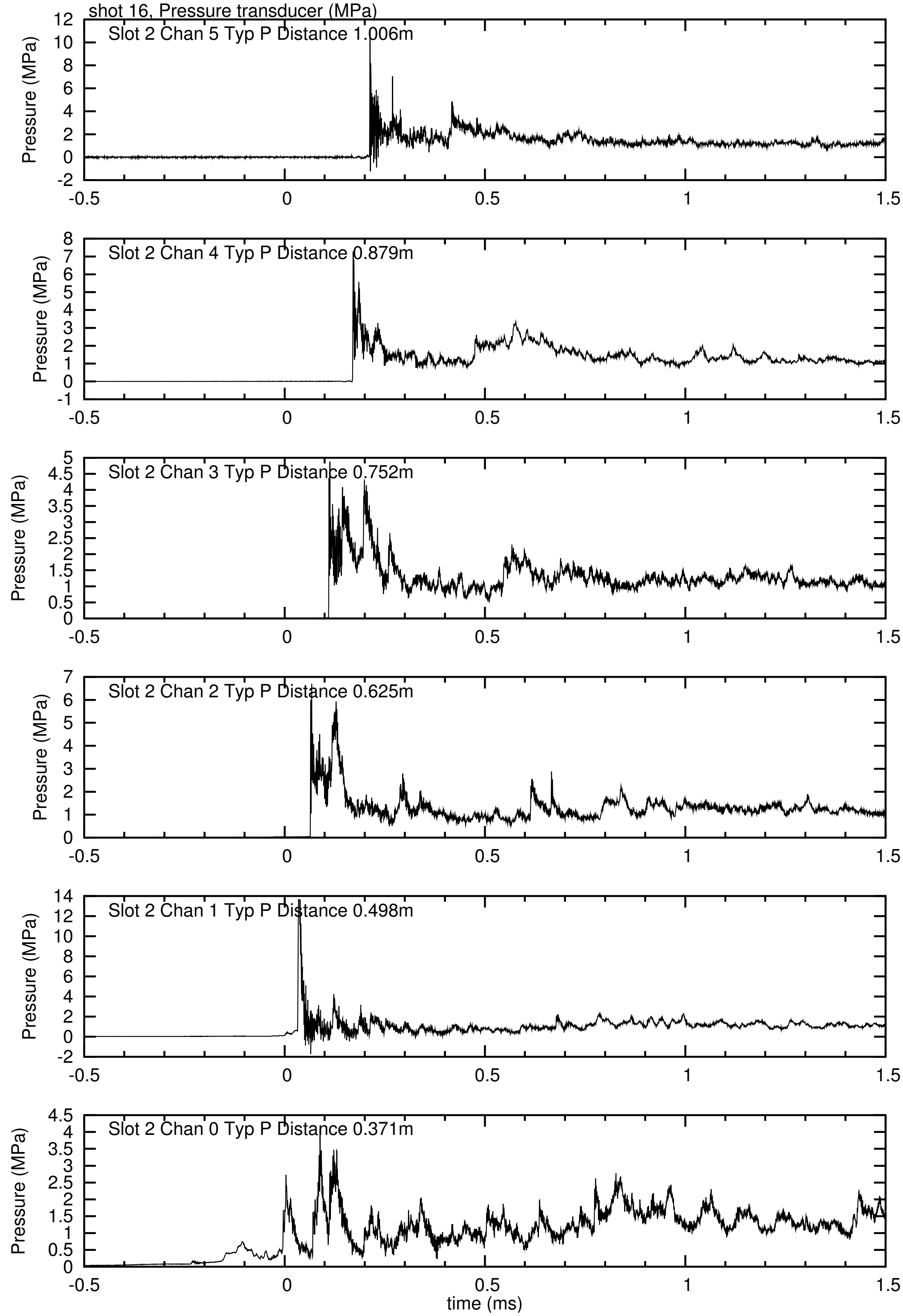

Figure 44: **Pressure transducers, shot 16**, BR=0.37, O_2/C=1.1, P_{CJ}=3.19 MPa, P_{CV}=1.61 MPa.

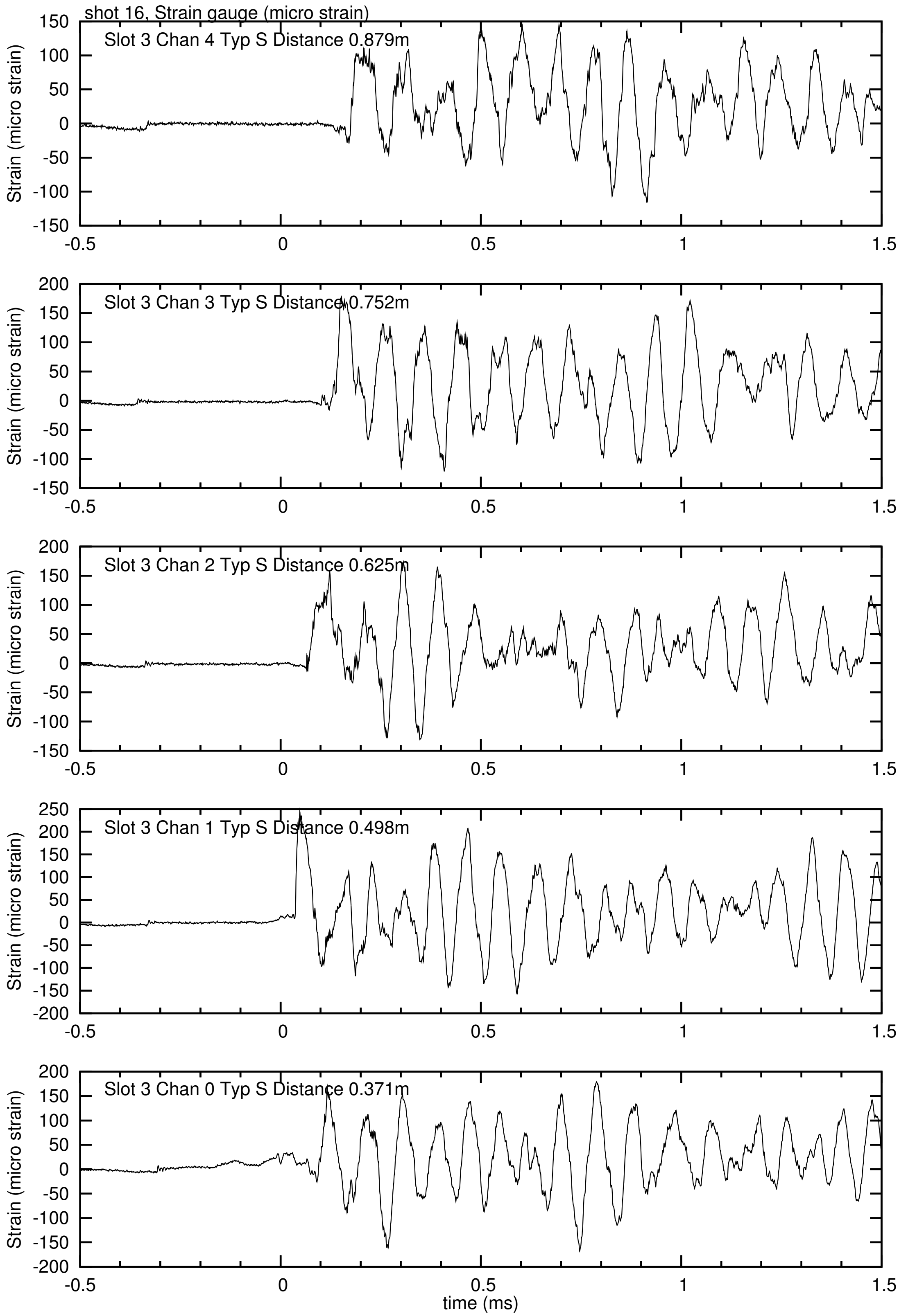

Figure 45: **Strain gauges, shot 16**, BR=0.37, O_2/C=1.1, P_{CJ}=3.19 MPa, P_{CV}=1.61 MPa.

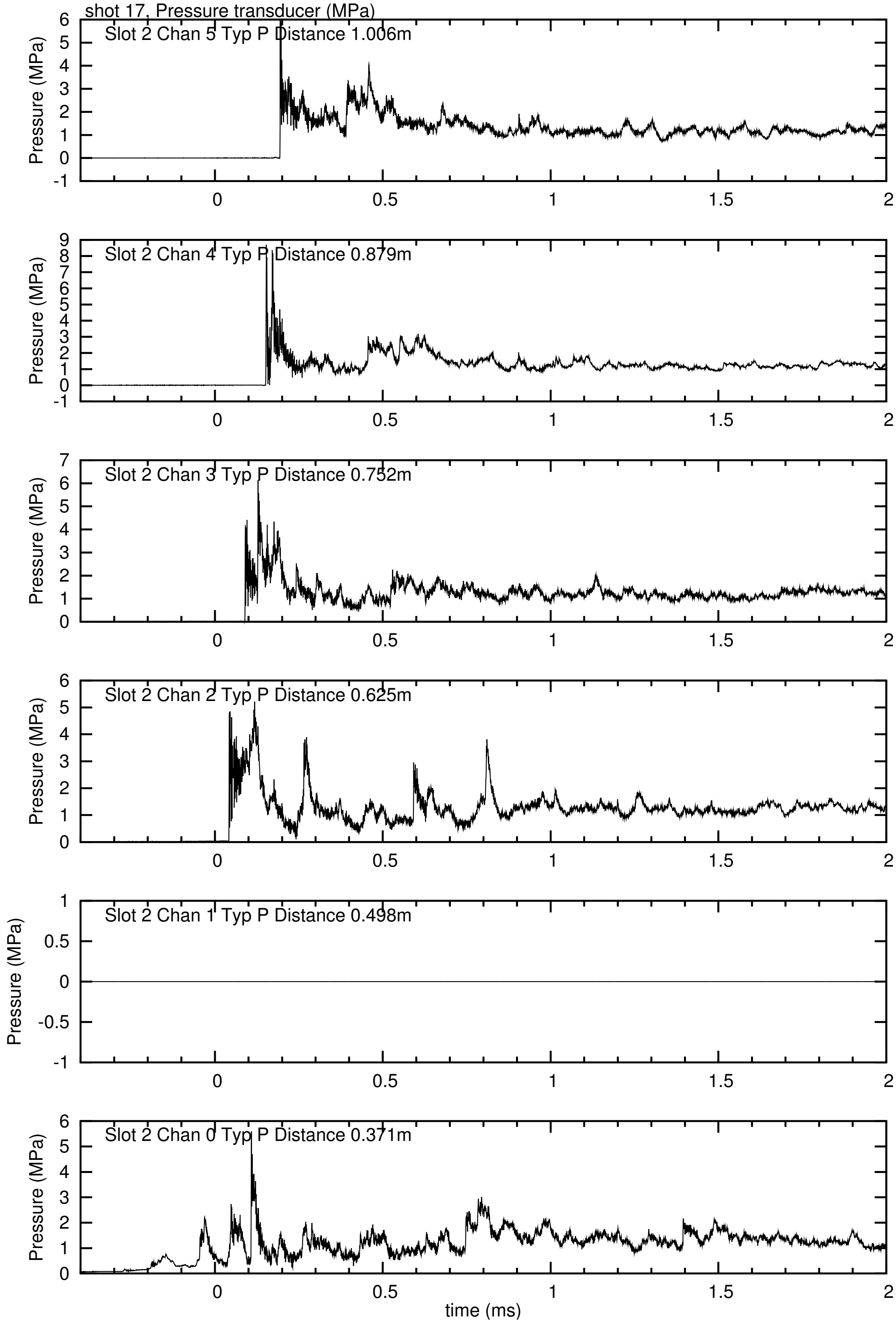

Figure 46: **Pressure transducers, shot 17**, BR=0.37, O_2/C=1.1, P_{CJ}=3.19 MPa, P_{CV}=1.61 MPa.

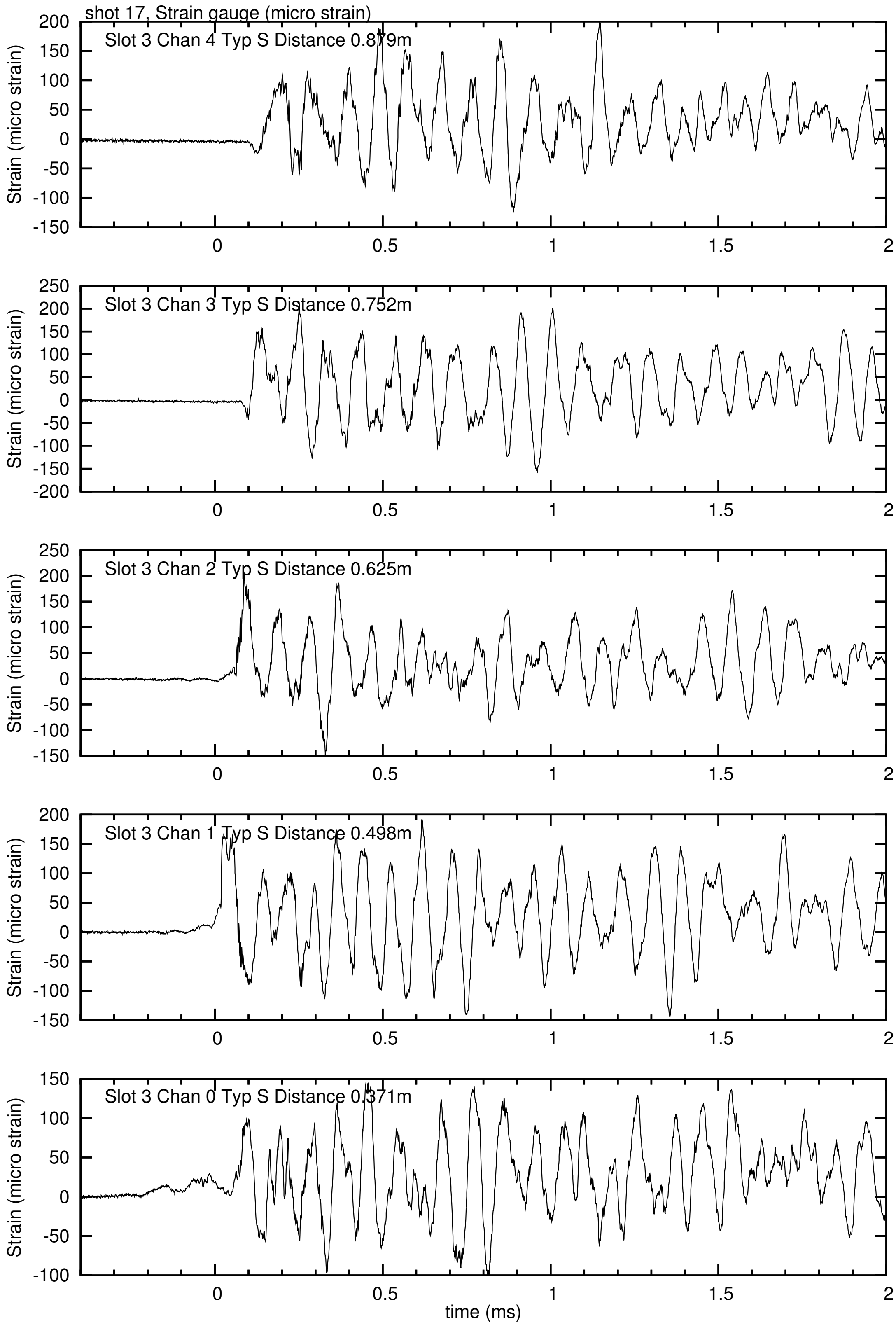

Figure 47: **Strain gauges, shot 17**, BR=0.37, O_2/C=1.1, P_{CJ}=3.19 MPa, P_{CV}=1.61 MPa.

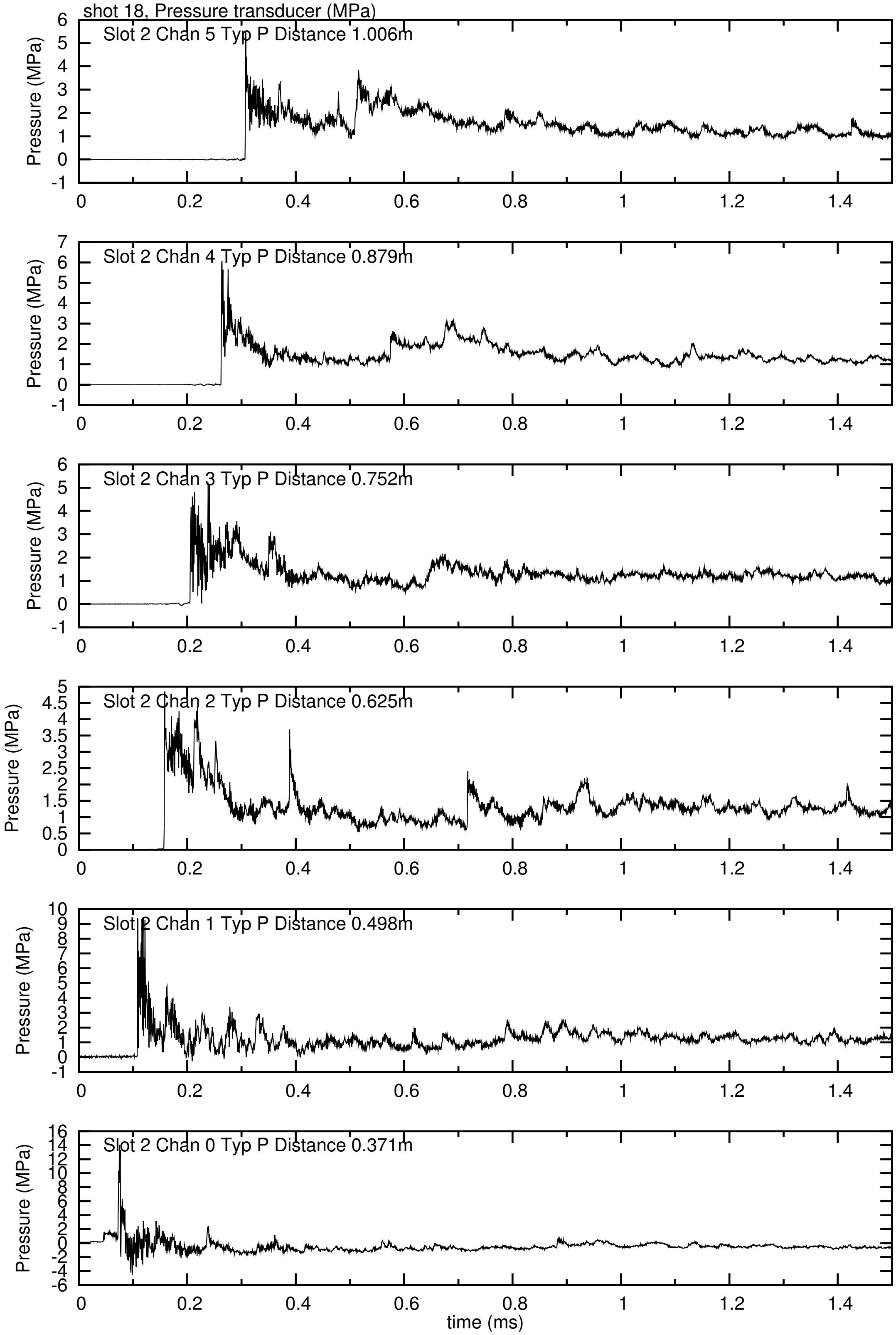

Figure 48: **Pressure transducers, shot 18**, BR=0.37, O_2/C=1.2, P_{CJ}=3.21 MPa, P_{CV}=1.62 MPa.

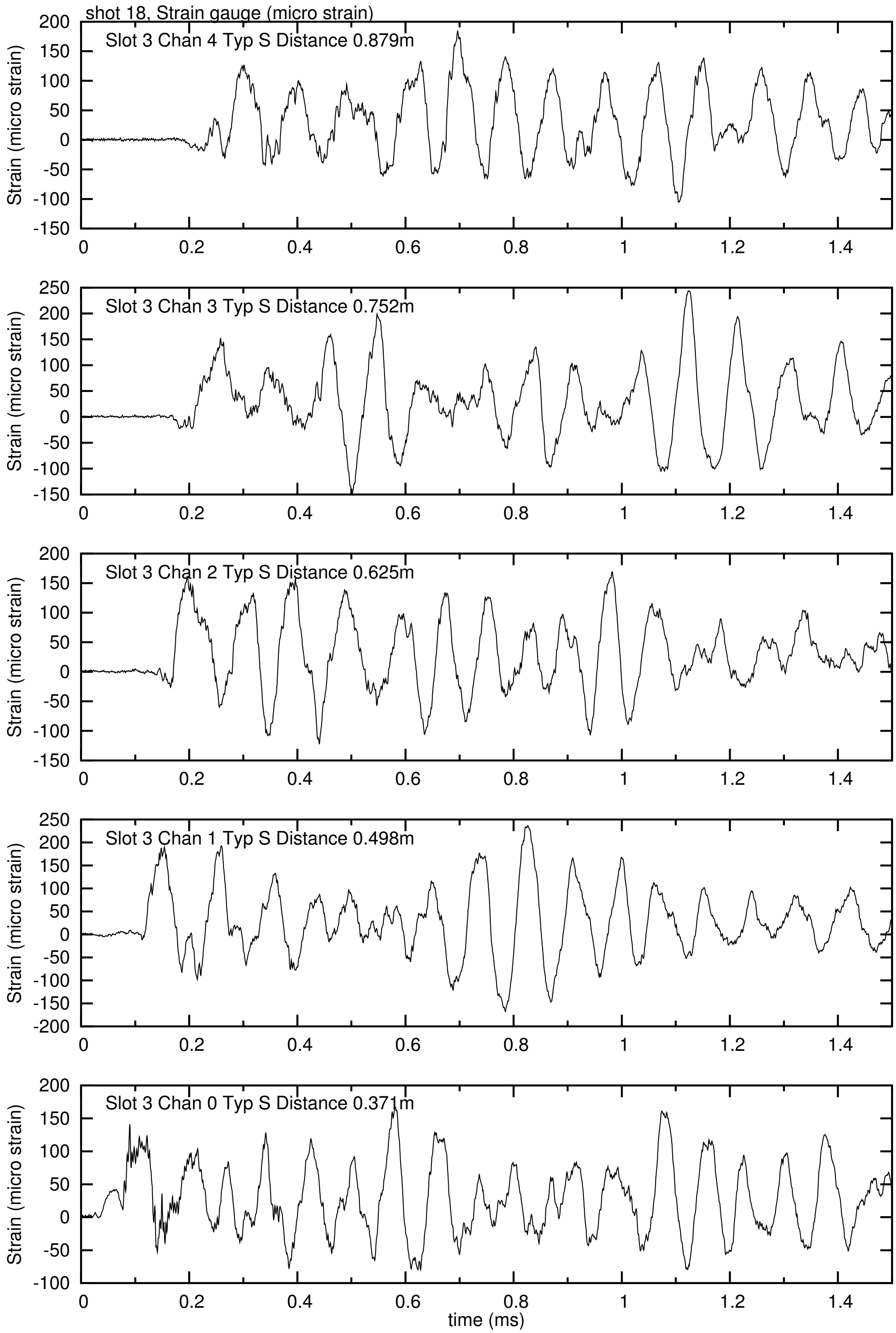

Figure 49: **Strain gauges, shot 18**, BR=0.37, O_2/C=1.2, P_{CJ}=3.21 MPa, P_{CV}=1.62 MPa.

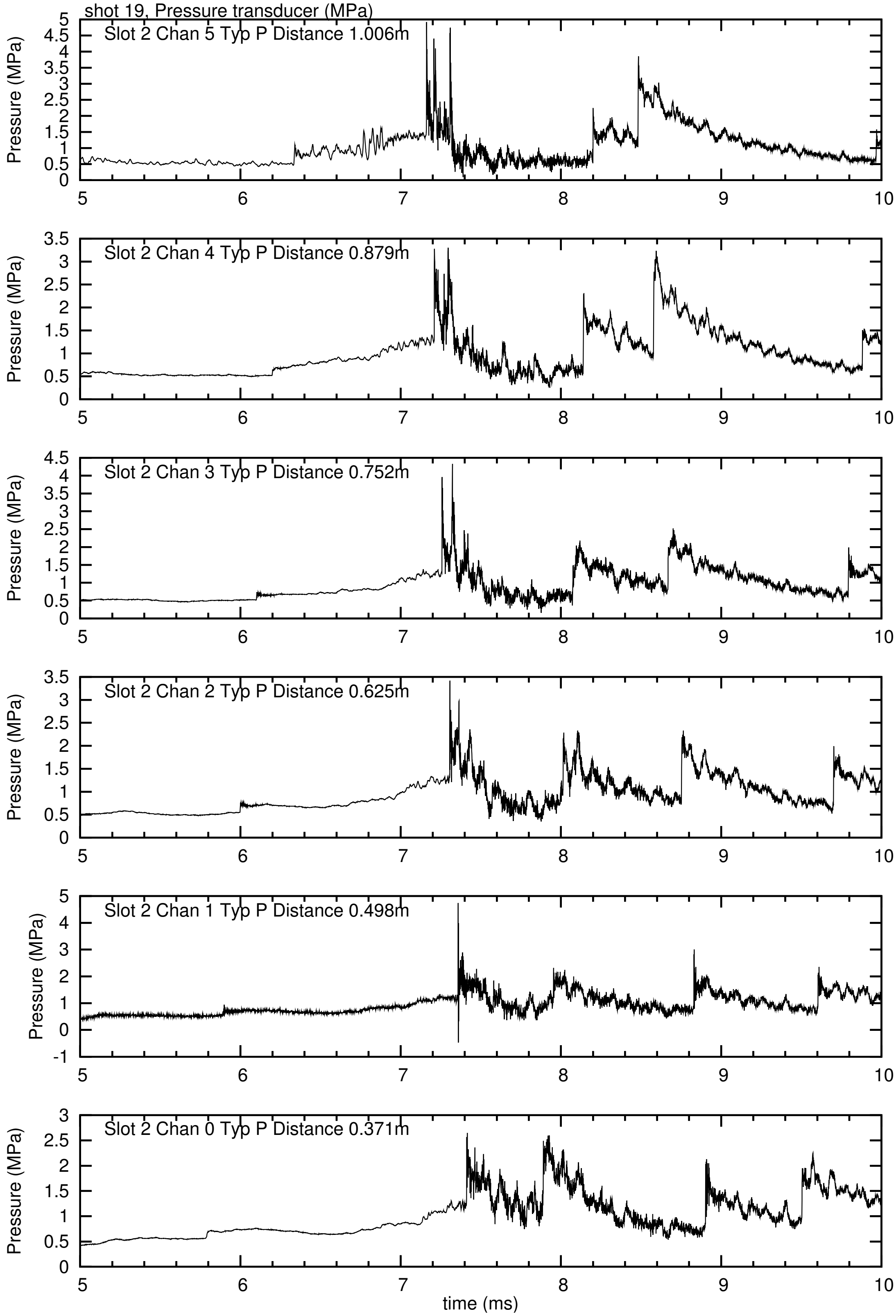

Figure 50: **Pressure transducers, shot 19**, BR=0, O_2/C=1.05, P_{CJ}=3.17 MPa, P_{CV}=1.60 MPa.

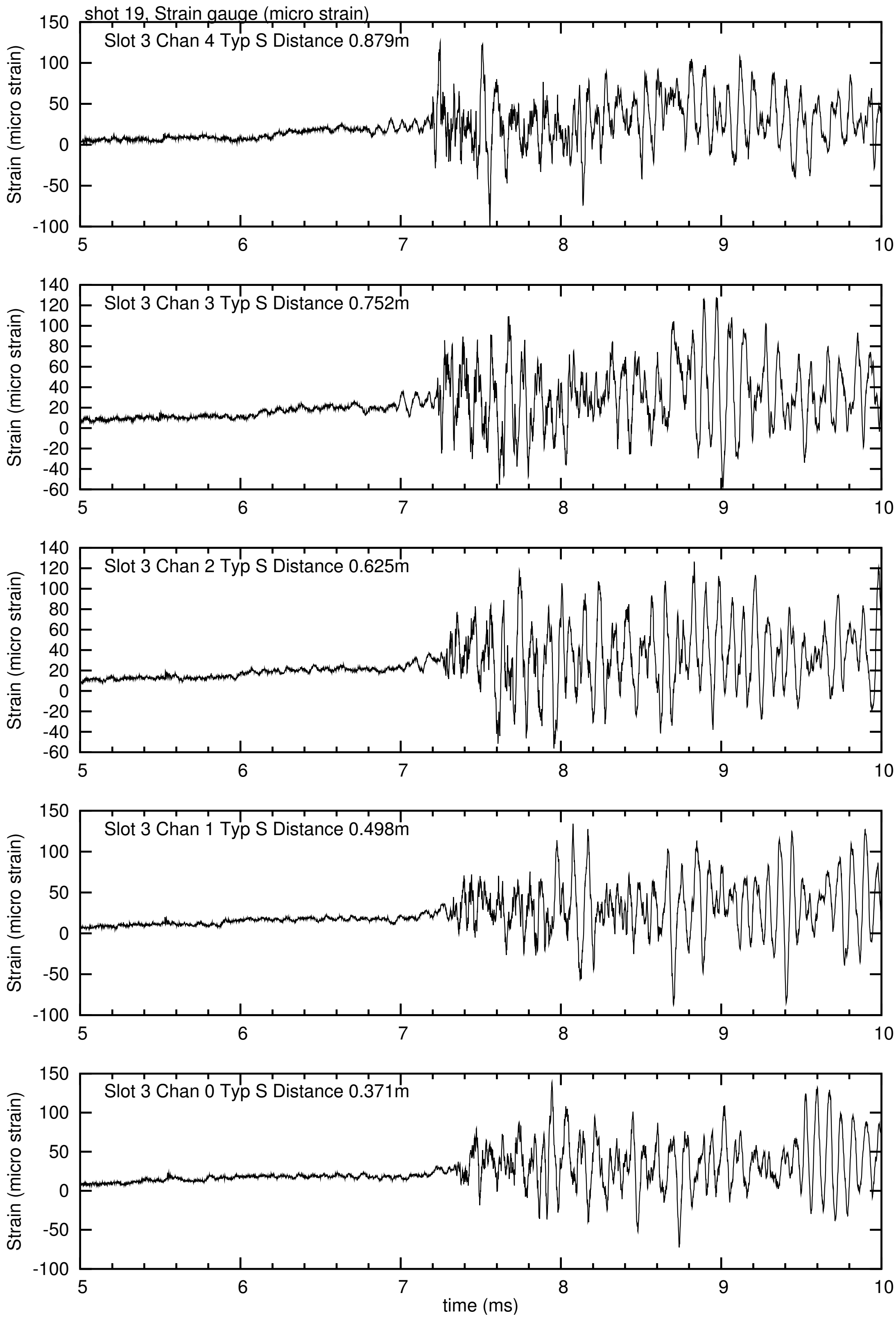

Figure 51: **Strain gauges, shot 19**, BR=0, O_2/C=1.05, P_{CJ}=3.17 MPa, P_{CV}=1.60 MPa.

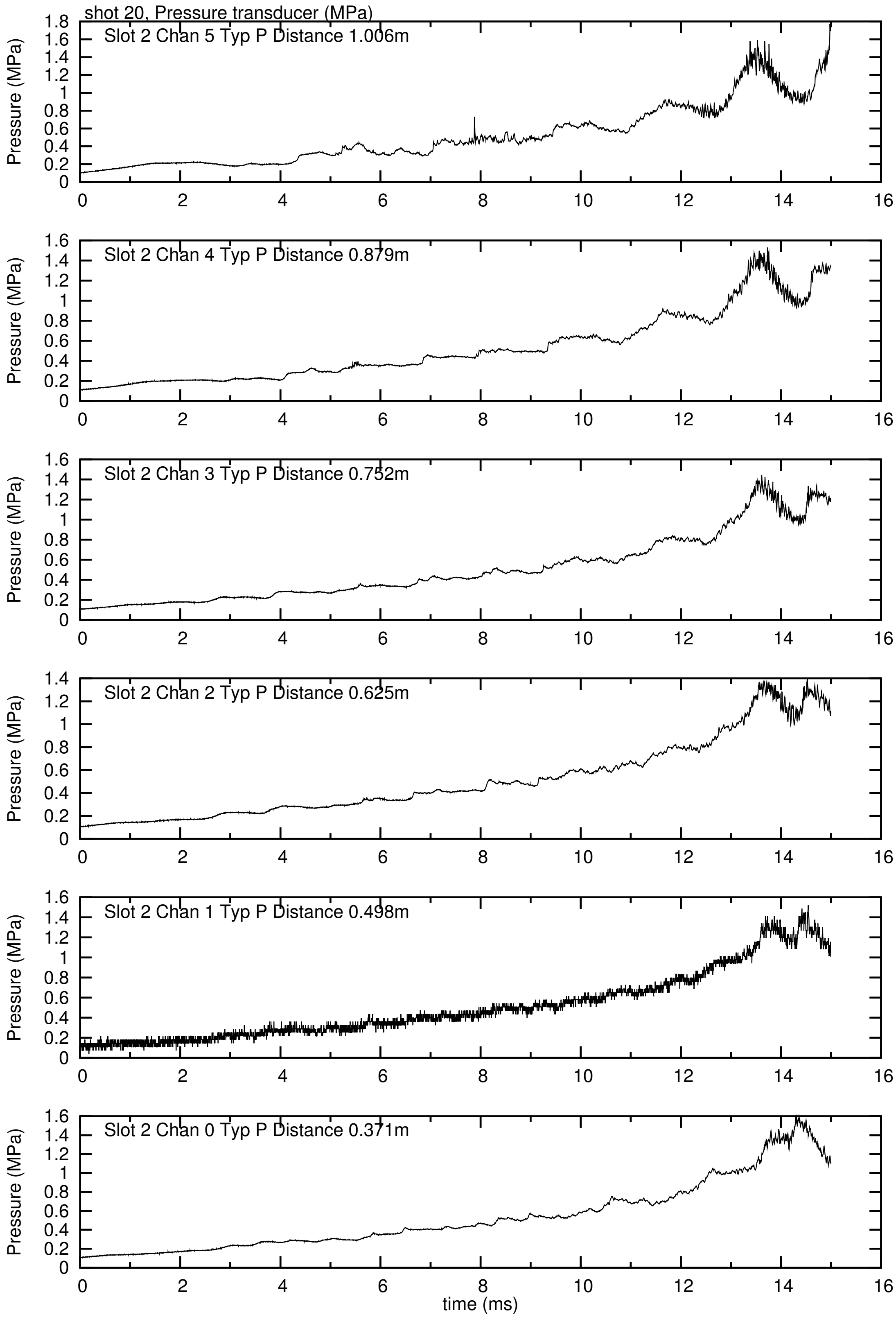

Figure 52: **Pressure transducers, shot 20**, BR=0, O_2/C=1, P_{CJ}=3.13 MPa, P_{CV}=1.58 MPa.

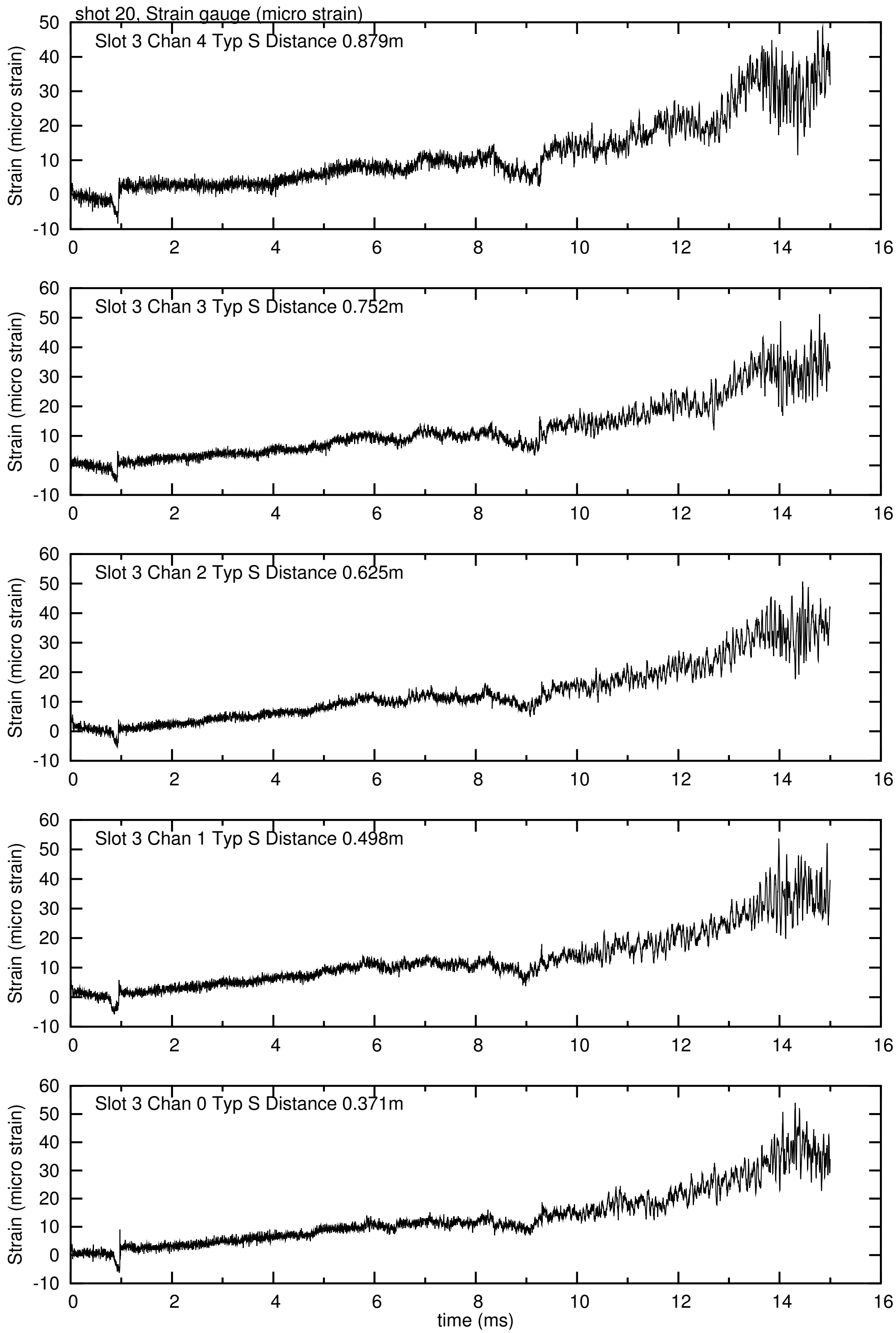

Figure 53: **Strain gauges, shot 20**, BR=0, O_2/C=1, P_{CJ}=3.13 MPa, P_{CV}=1.58 MPa.

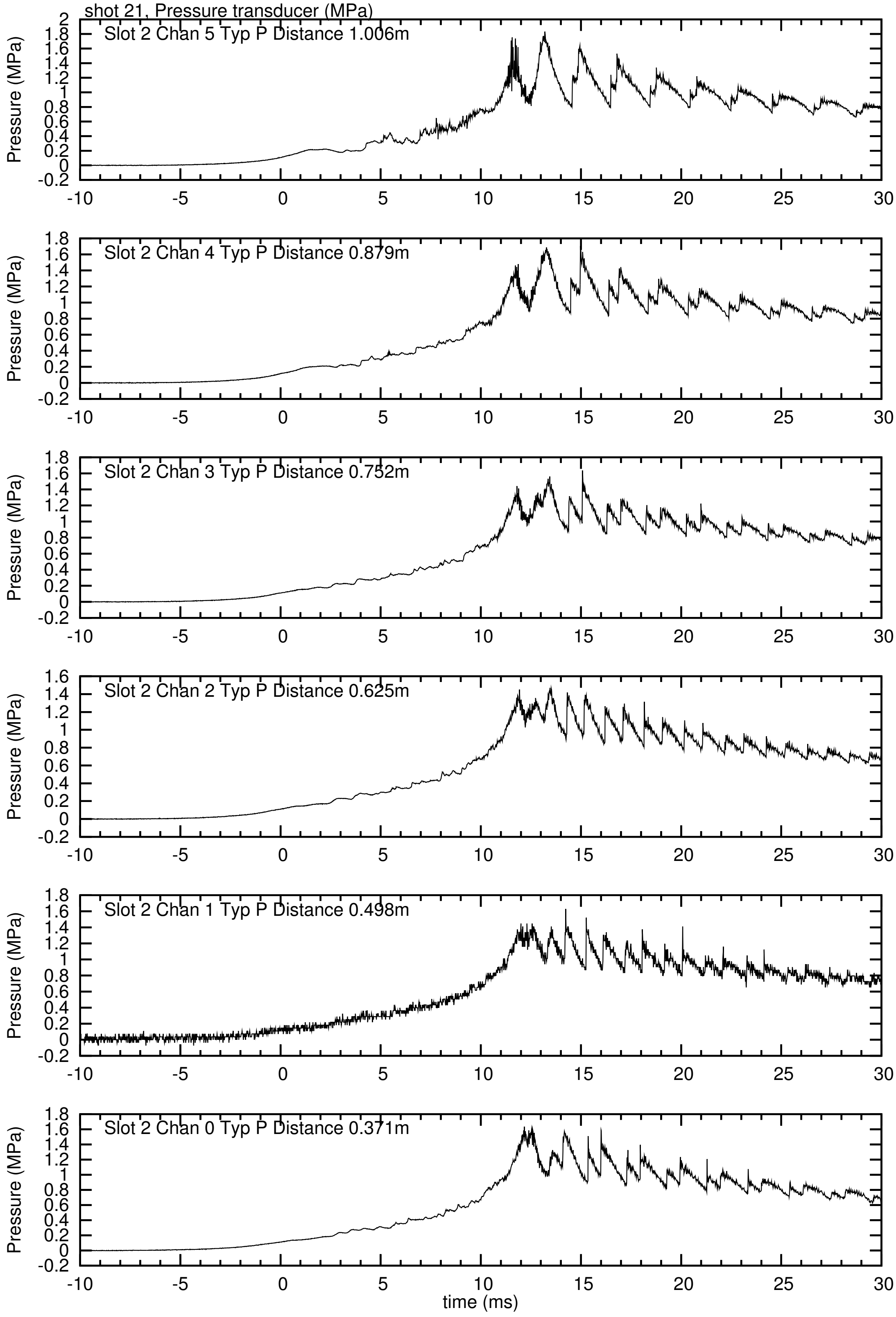

Figure 54: **Pressure transducers, shot 21**, BR=0, O_2/C=1, P_{CJ}=3.13 MPa, P_{CV}=1.58 MPa.

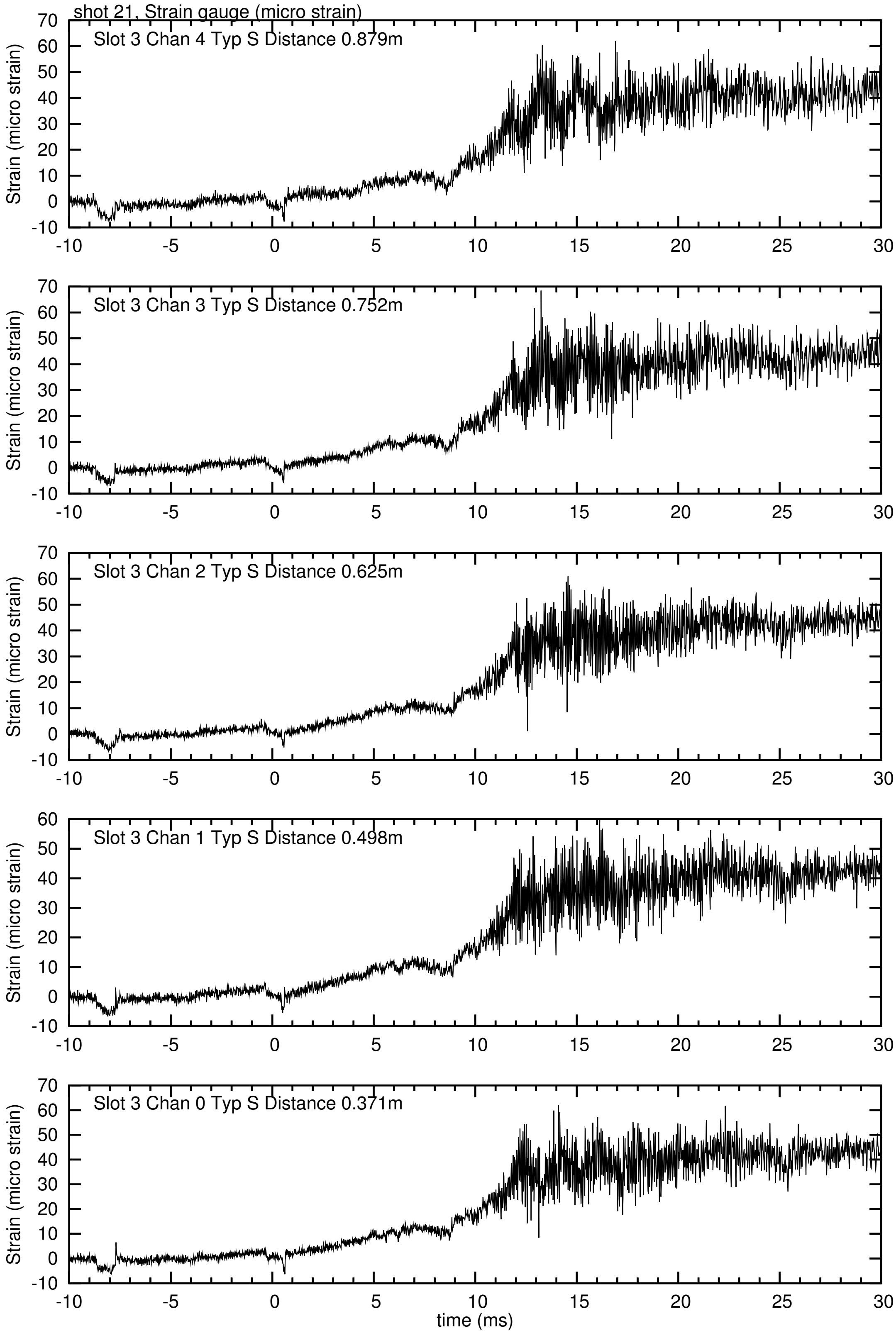

Figure 55: **Strain gauges, shot 21**, BR=0, O_2/C=1, P_{CJ}=3.13 MPa, P_{CV}=1.58 MPa.

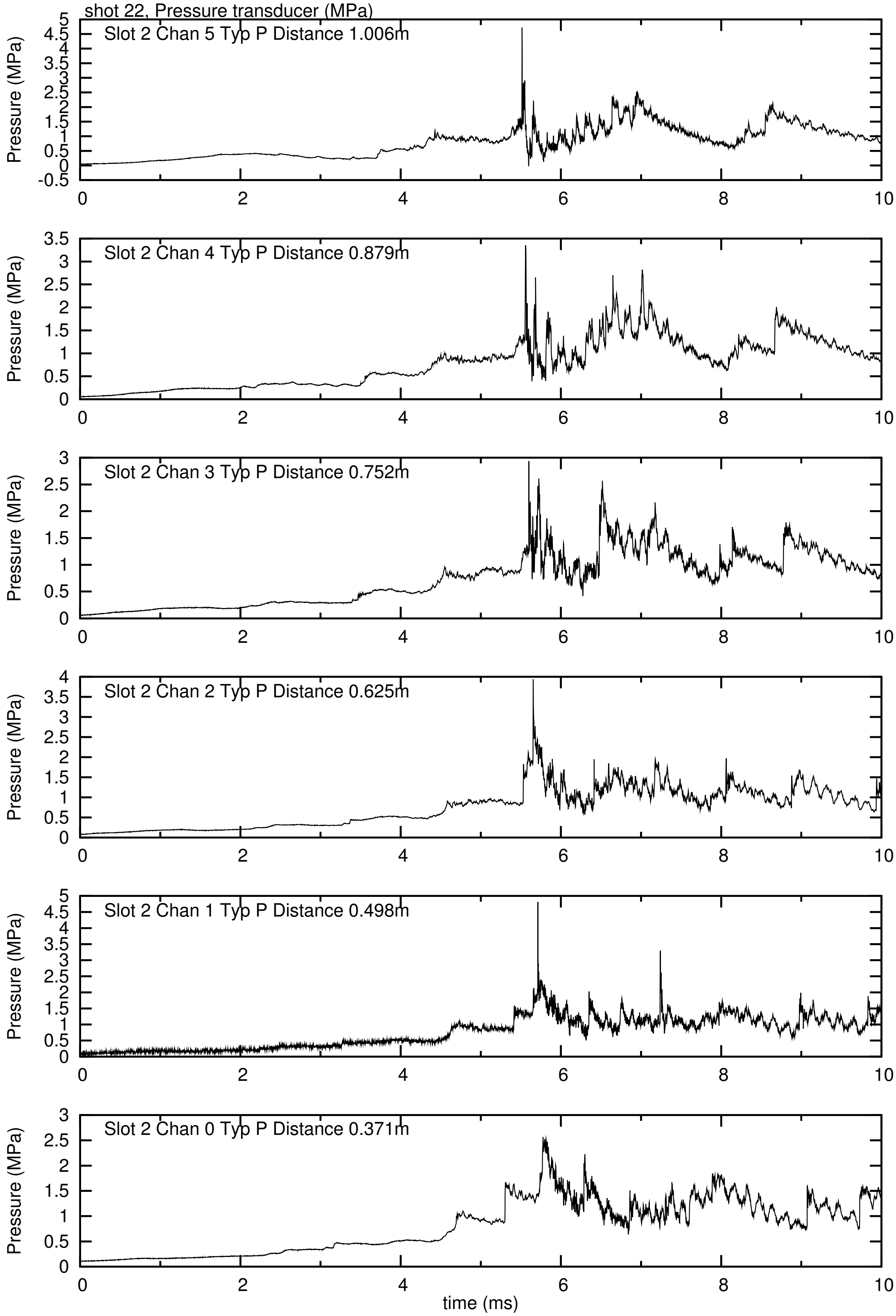

Figure 56: **Pressure transducers, shot 22**, BR=0, O_2/C=1.1, P_{CJ}=3.19 MPa, P_{CV}=1.61 MPa.

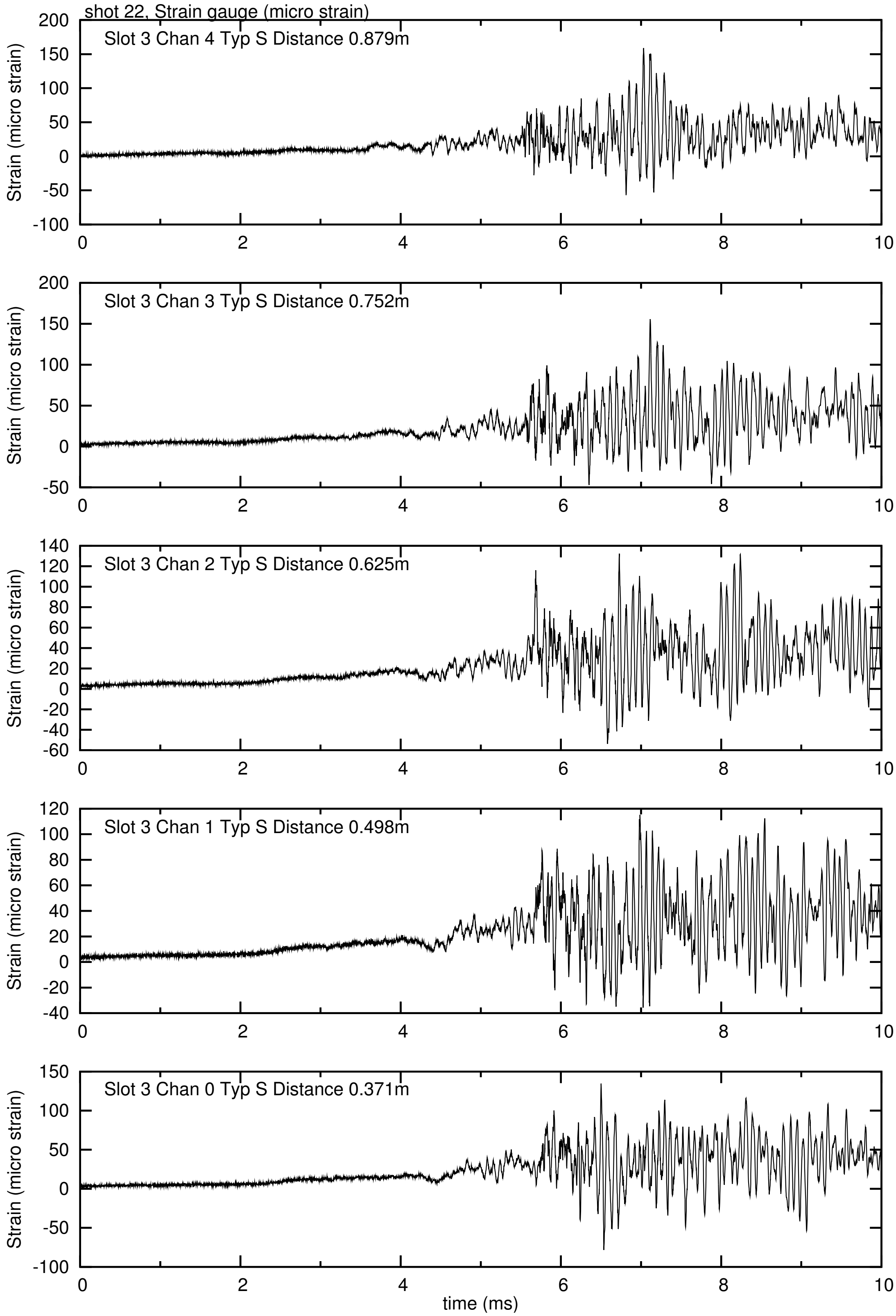

Figure 57: **Strain gauges, shot 22**, BR=0, O_2/C=1.1, P_{CJ}=3.19 MPa, P_{CV}=1.61 MPa.

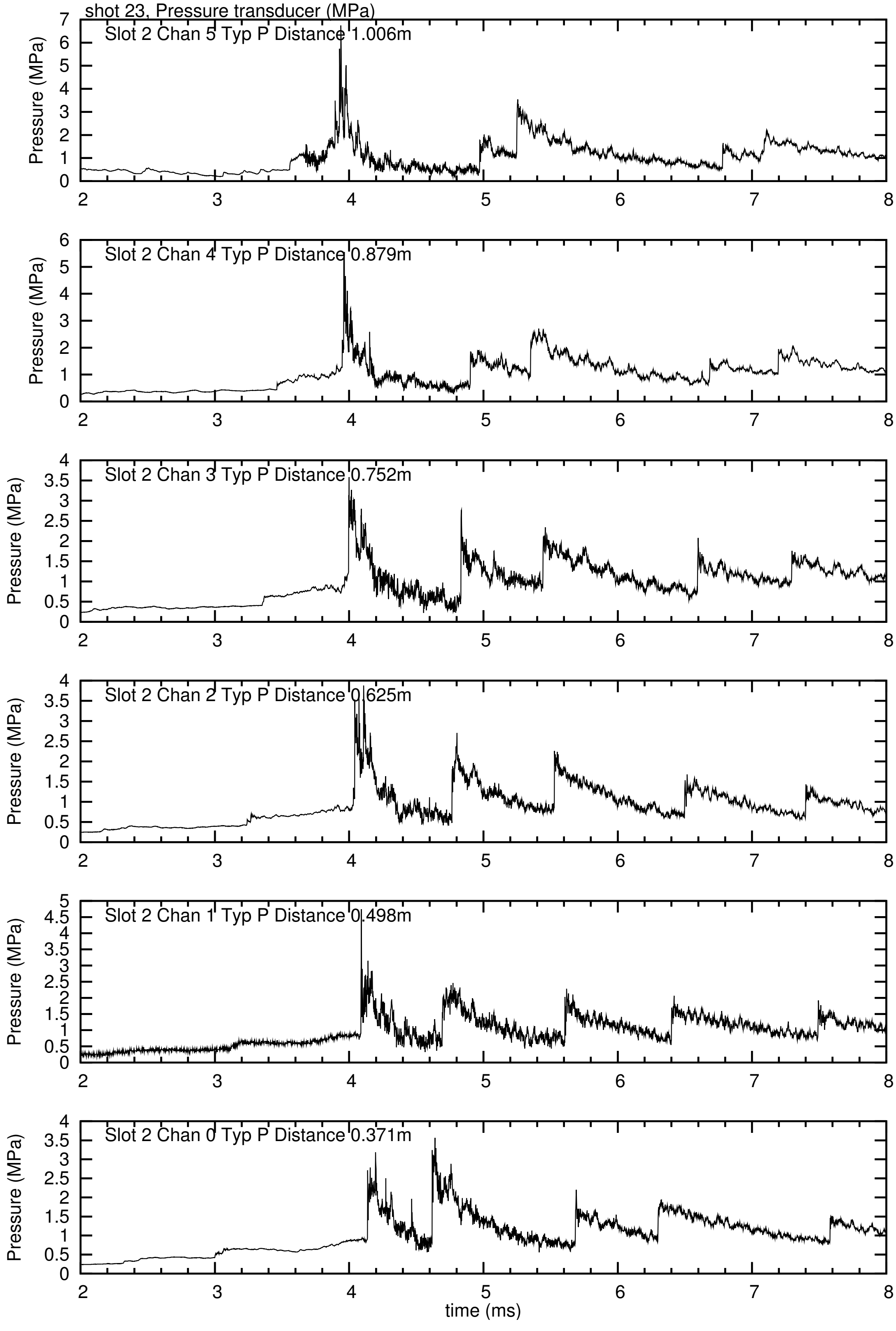

Figure 58: **Pressure transducers, shot 23**, BR=0, O_2/C=1.15, P_{CJ}=3.21 MPa, P_{CV}=1.62 MPa.

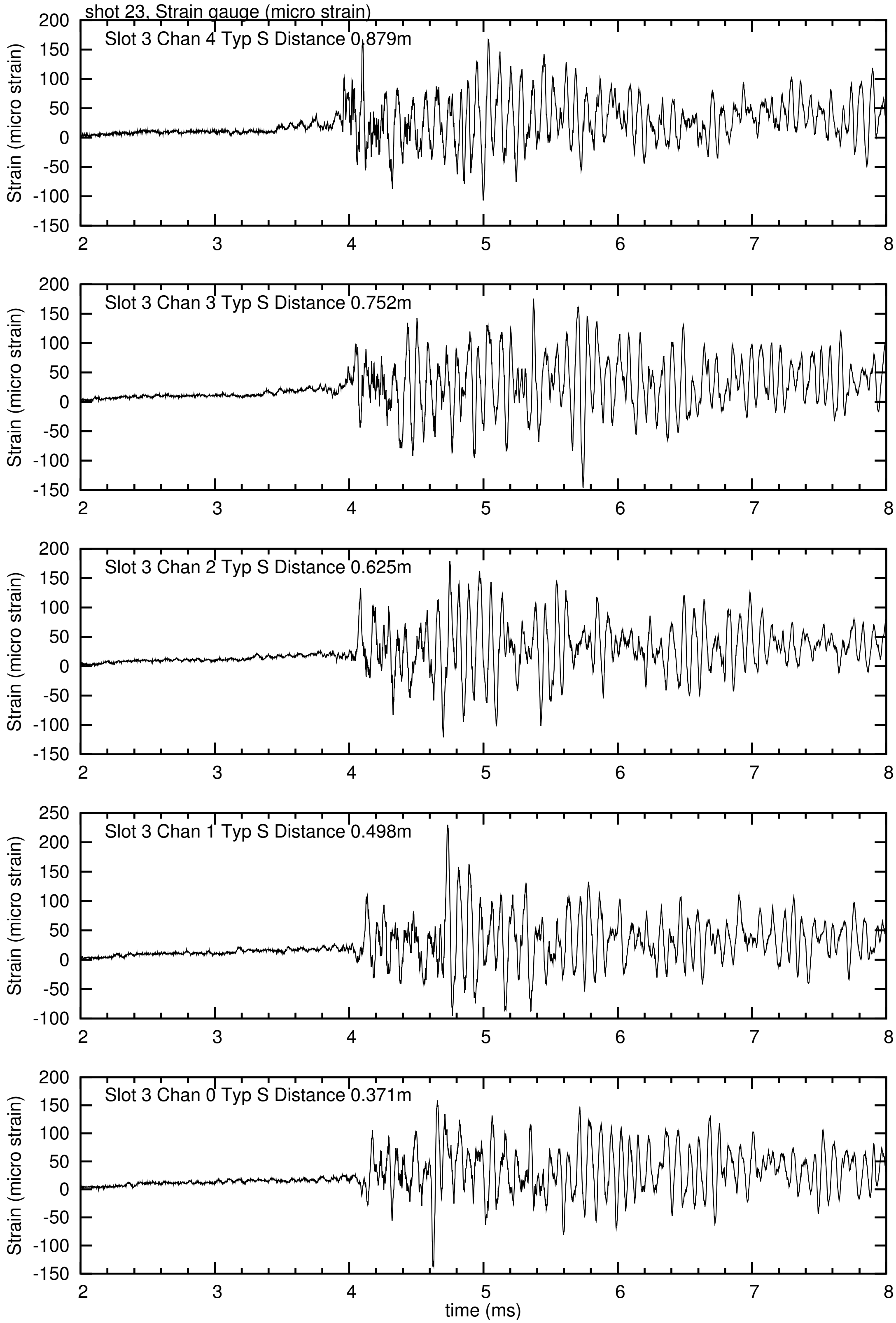

Figure 59: **Strain gauges, shot 23**, BR=0, O_2/C=1.15, P_{CJ}=3.21 MPa, P_{CV}=1.62 MPa.

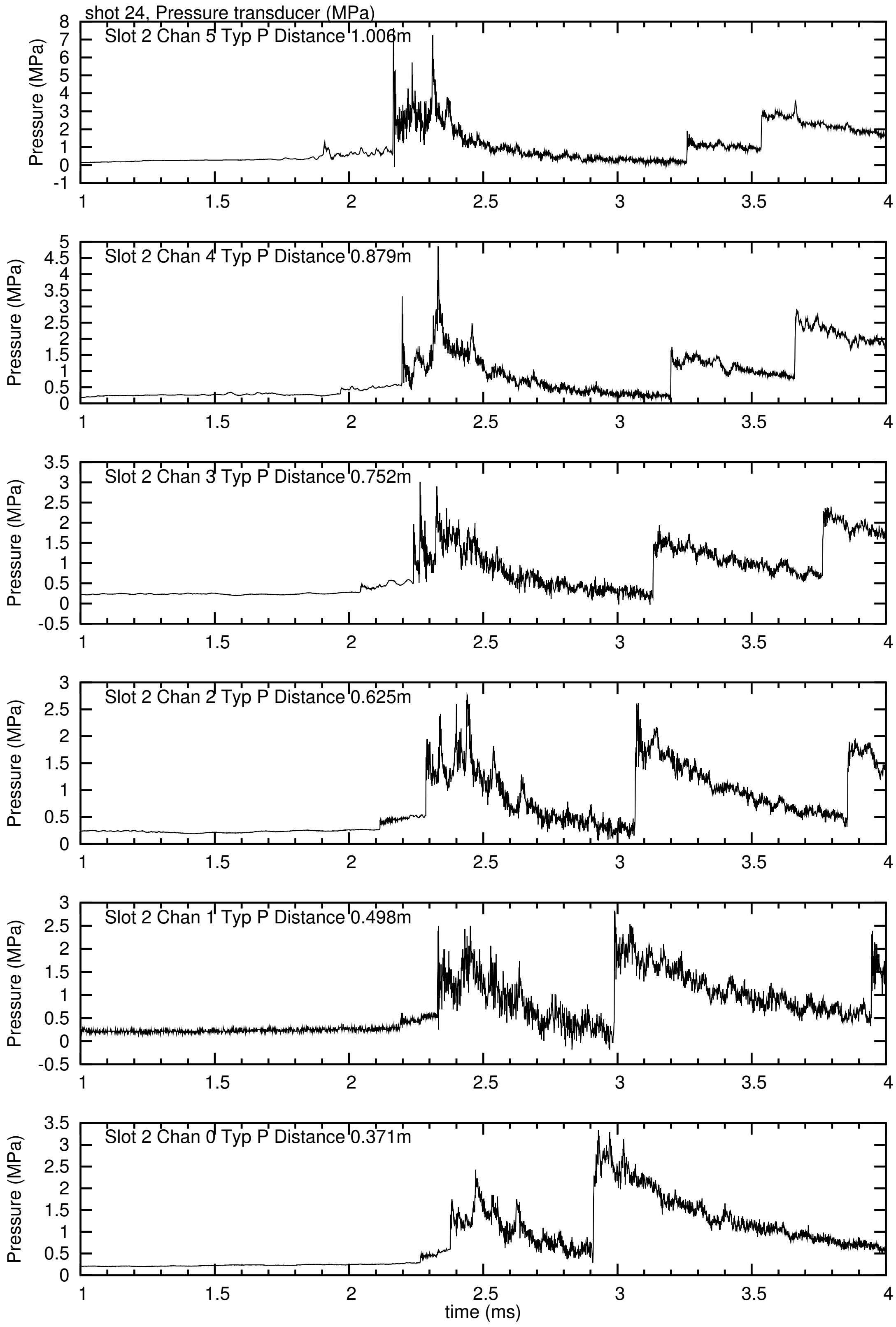

Figure 60: **Pressure transducers, shot 24**, BR=0, O_2/C=1.2, P_{CJ}=3.21 MPa, P_{CV}=1.62 MPa.

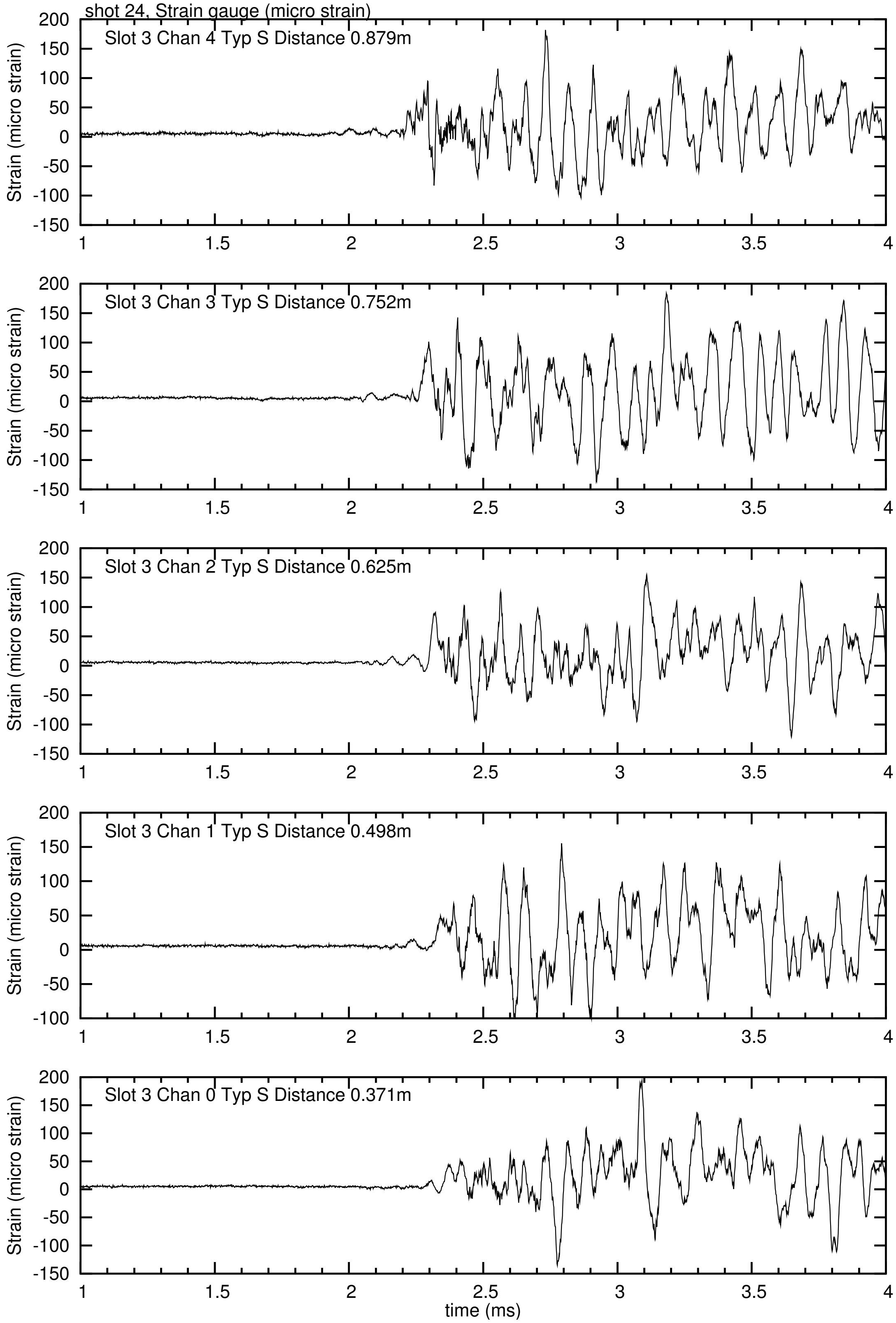

Figure 61: **Strain gauges, shot 24**, BR=0, O_2/C=1.2, P_{CJ}=3.21 MPa, P_{CV}=1.62 MPa.

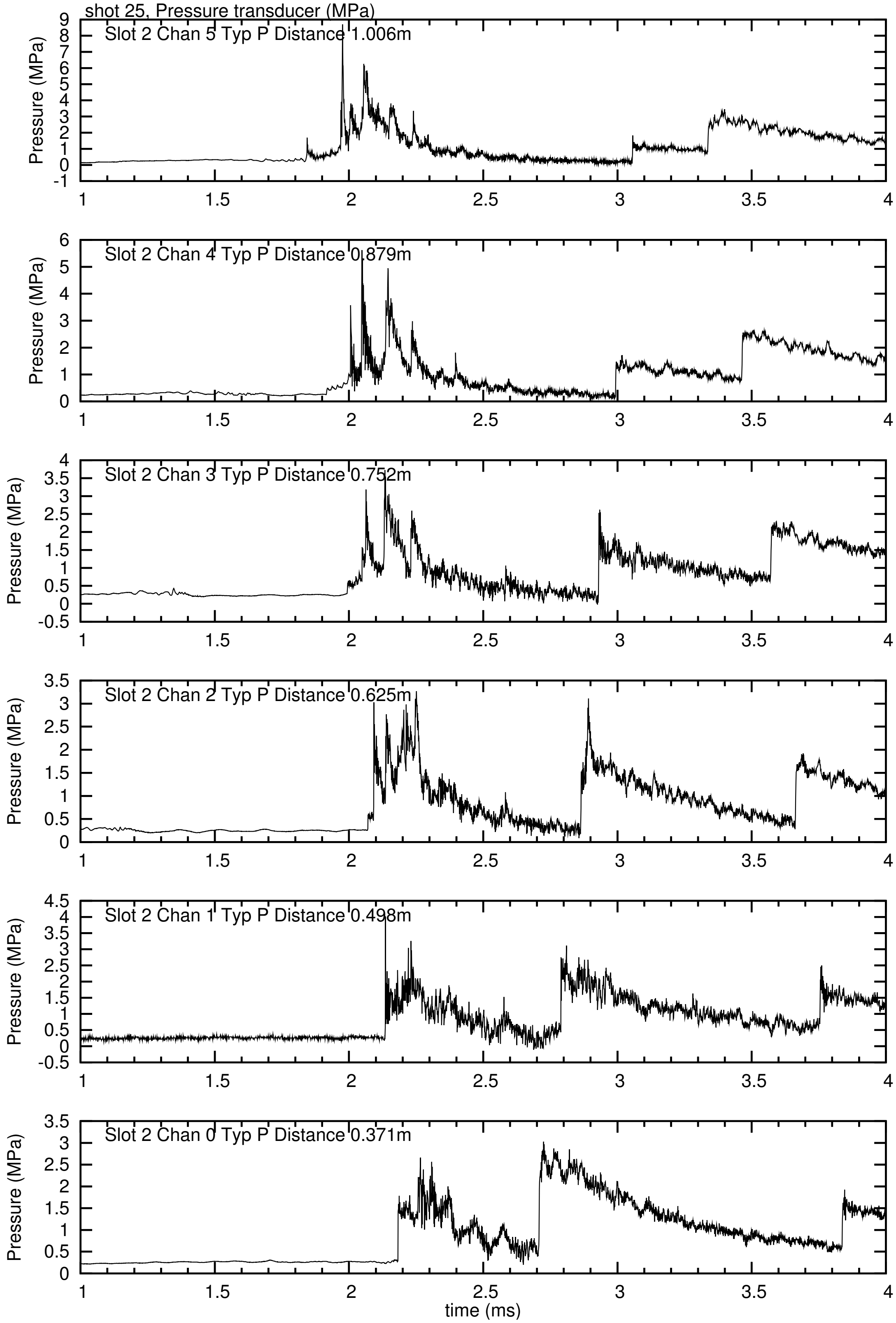

Figure 62: **Pressure transducers, shot 25**, BR=0, O_2/C=1.25, P_{CJ}=3.21 MPa, P_{CV}=1.62 MPa.

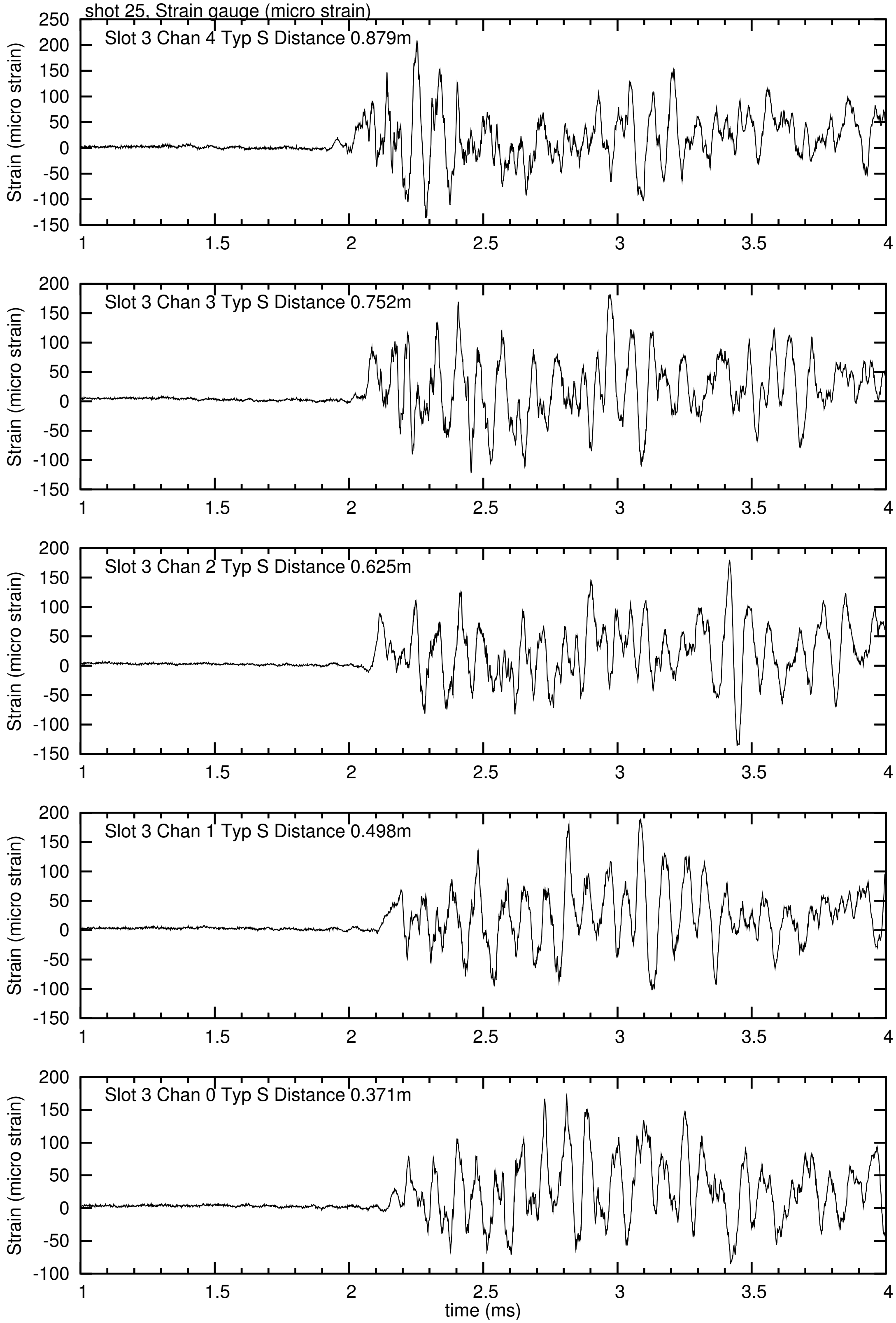

Figure 63: **Strain gauges, shot 25**, BR=0, O_2/C=1.25, P_{CJ}=3.21 MPa, P_{CV}=1.62 MPa.

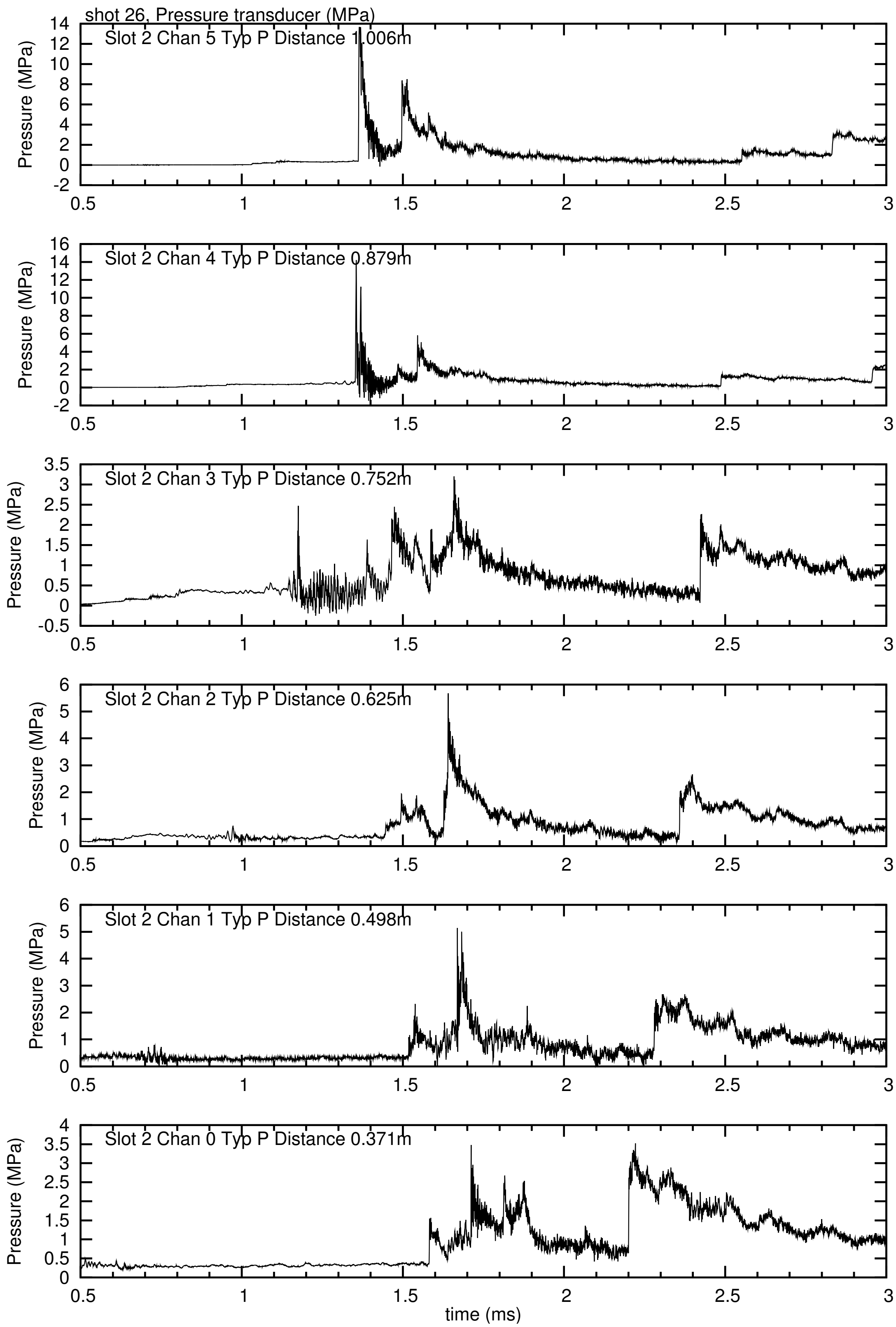

Figure 64: **Pressure transducers, shot 26**, BR=0, O_2/C=1.35, P_{CJ}=3.19 MPa, P_{CV}=1.61 MPa.

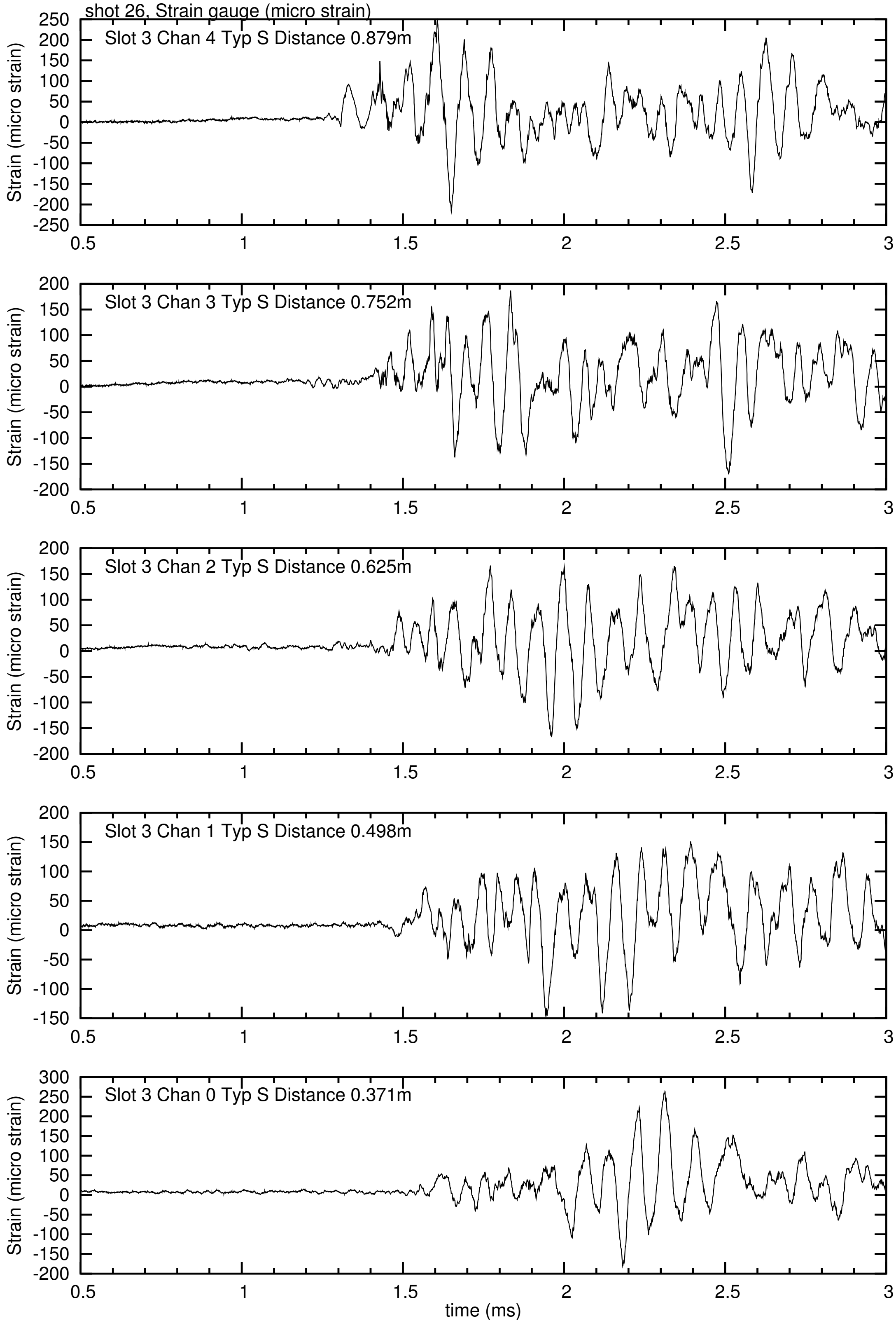

Figure 65: **Strain gauges, shot 26**, BR=0, O_2/C=1.35, P_{CJ}=3.19 MPa, P_{CV}=1.61 MPa.

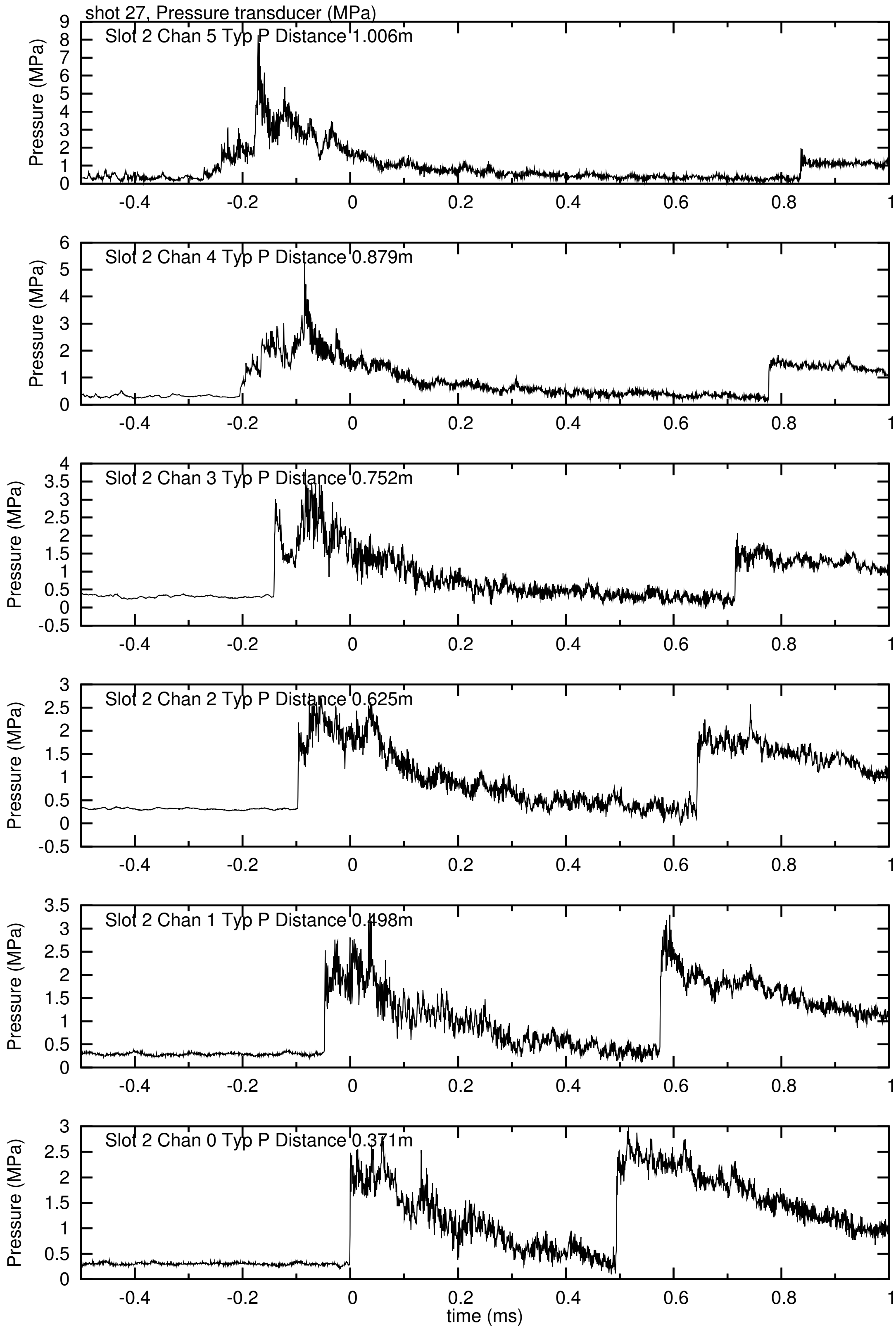

Figure 66: **Pressure transducers, shot 27**, BR=0, O_2/C=1.3, P_{CJ}=3.20 MPa, P_{CV}=1.62 MPa.

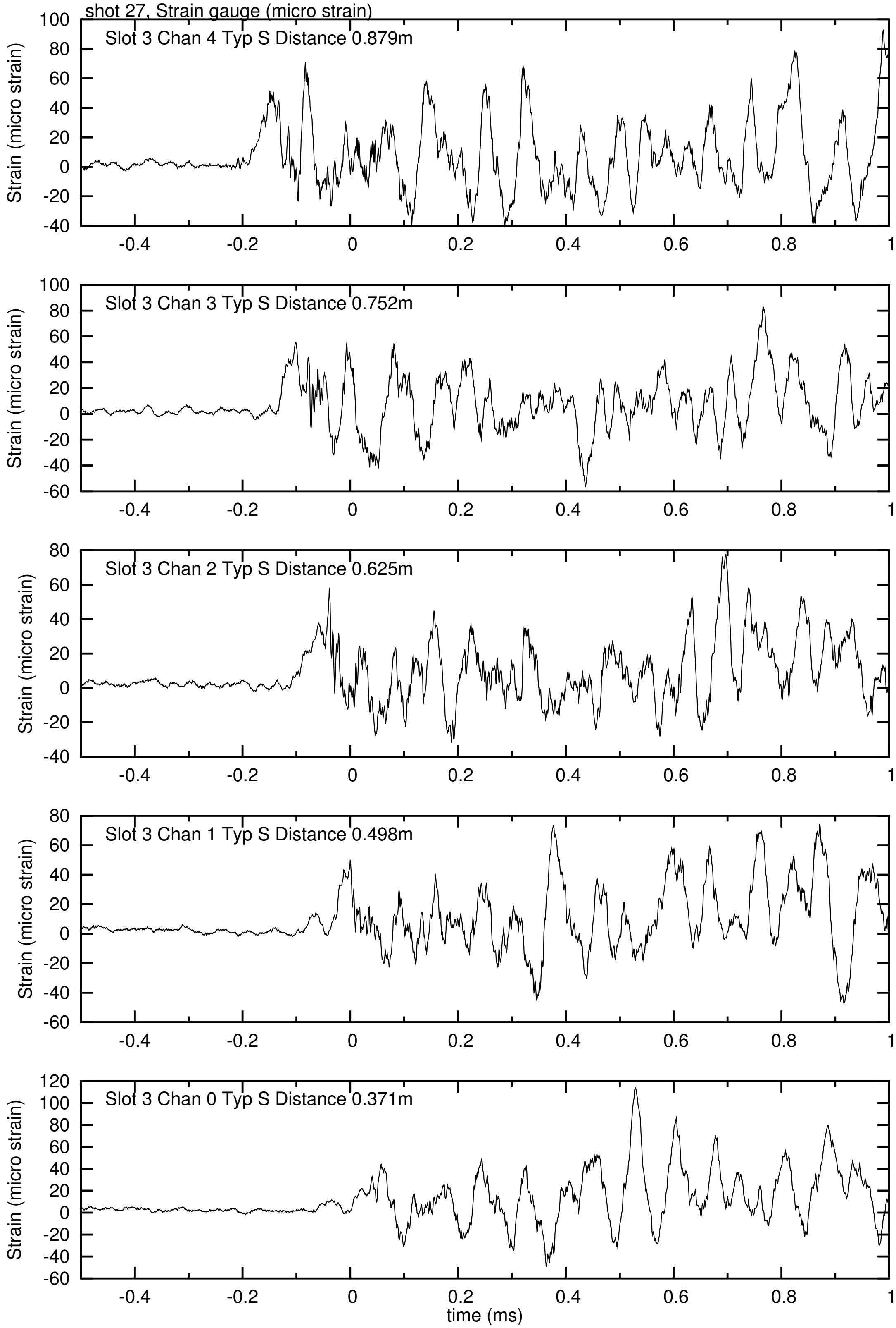

Figure 67: **Strain gauges, shot 27**, BR=0, O_2/C=1.3, P_{CJ}=3.20 MPa, P_{CV}=1.62 MPa.

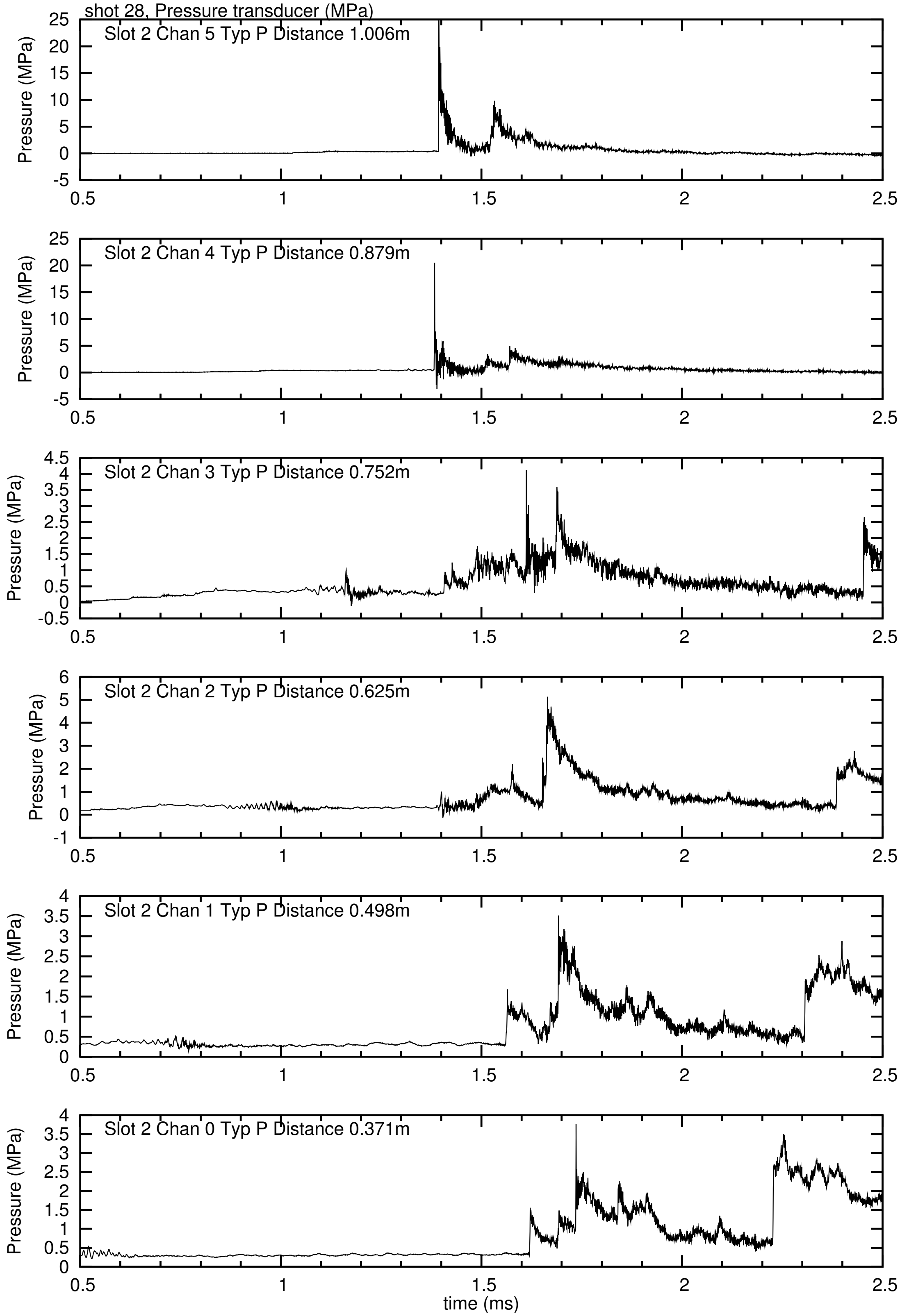

Figure 68: **Pressure transducers, shot 28**, BR=0, O_2/C=1.35, P_{CJ}=3.19 MPa, P_{CV}=1.61 MPa.

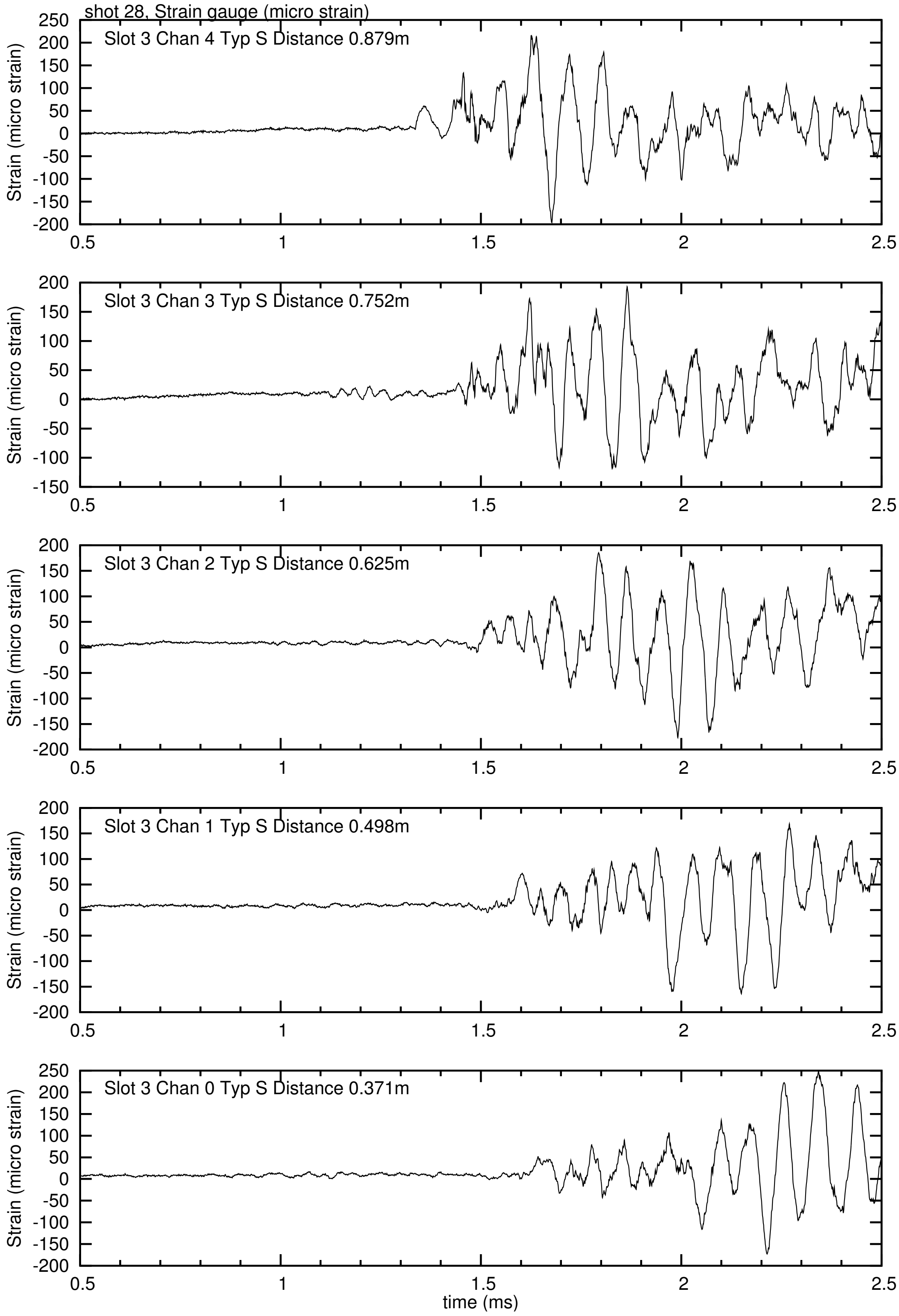

Figure 69: **Strain gauges, shot 28**, BR=0, O_2/C=1.35, P_{CJ}=3.19 MPa, P_{CV}=1.61 MPa.

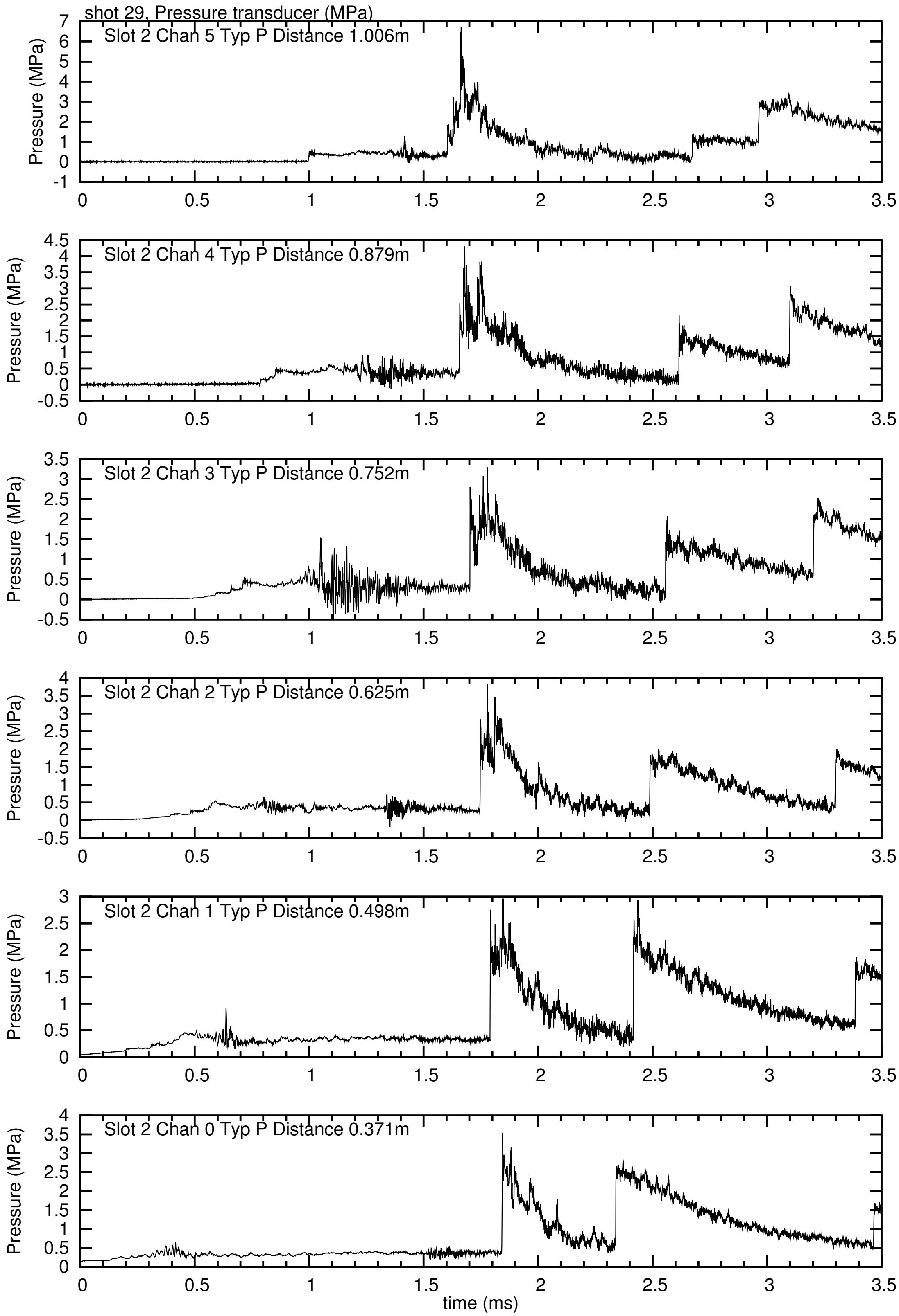

Figure 70: **Pressure transducers, shot 29**, BR=0, O_2/C=1.4, P_{CJ}=3.17 MPa, P_{CV}=1.60 MPa.

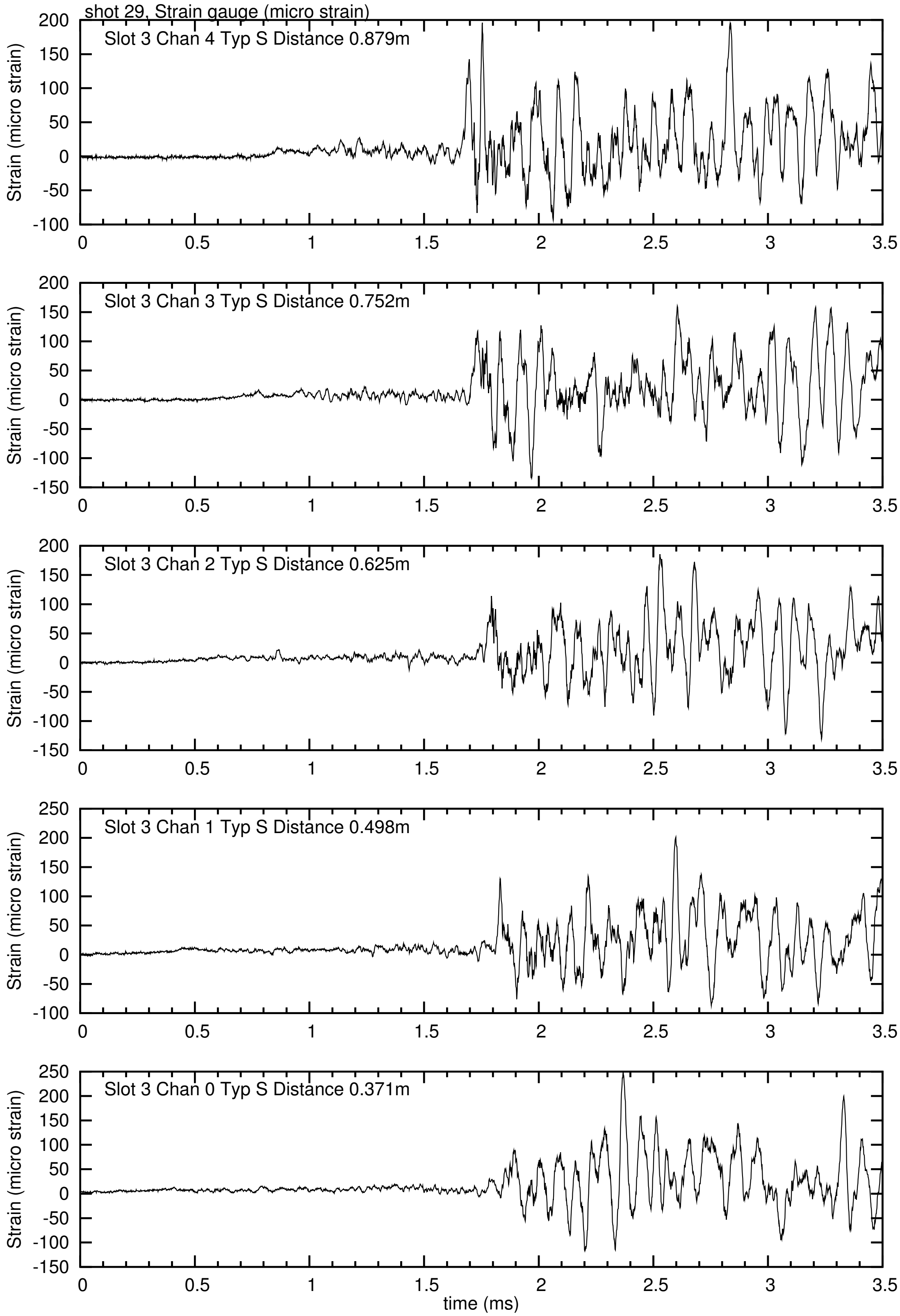

Figure 71: **Strain gauges, shot 29**, BR=0, O_2/C=1.4, P_{CJ}=3.17 MPa, P_{CV}=1.60 MPa.

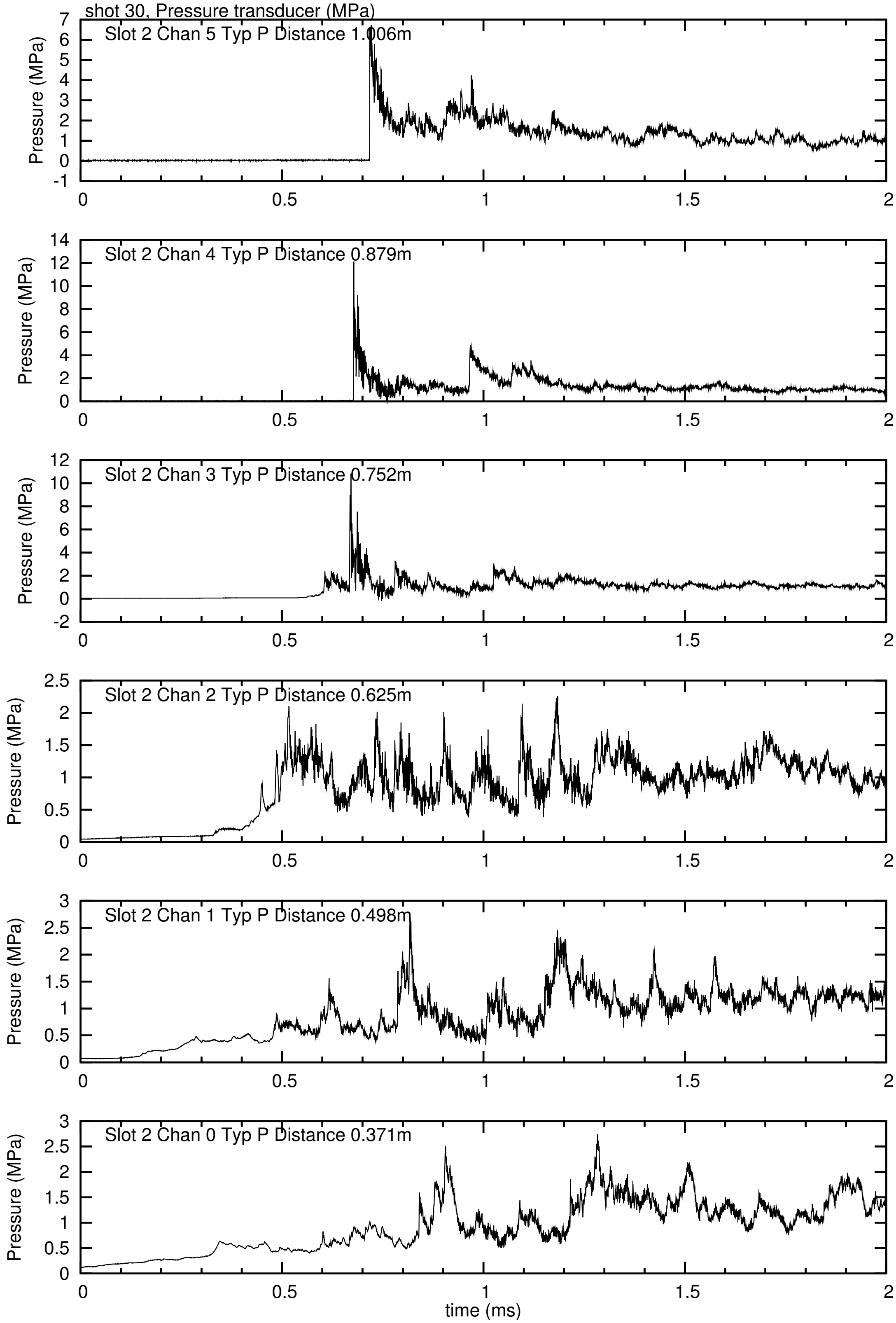

Figure 72: **Pressure transducers, shot 30**, BR=0.37, O_2/C=0.95, P_{CJ}=3.08 MPa, P_{CV}=1.56 MPa.

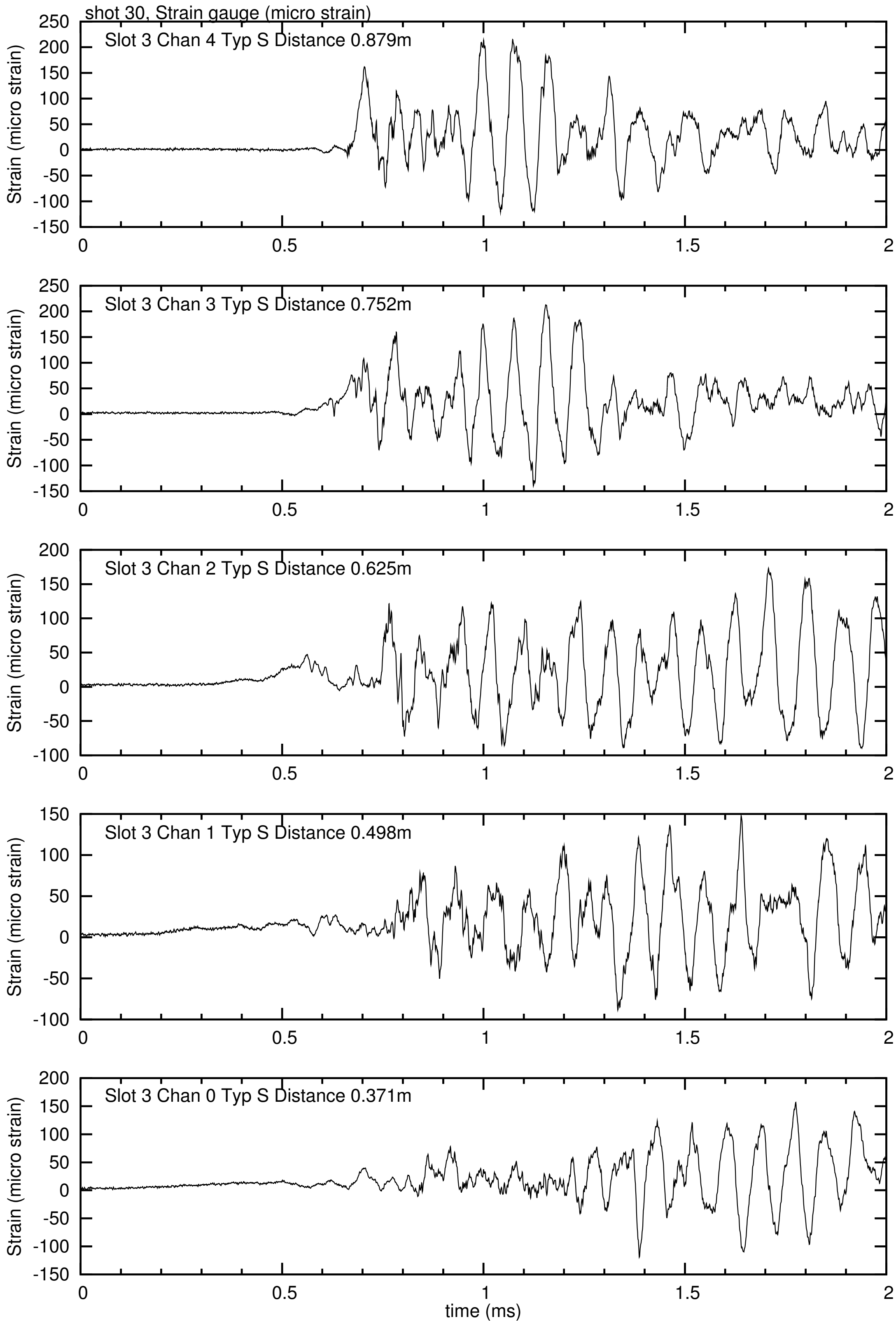

Figure 73: **Strain gauges, shot 30**, BR=0.37, O_2/C=0.95, P_{CJ}=3.08 MPa, P_{CV}=1.56 MPa.

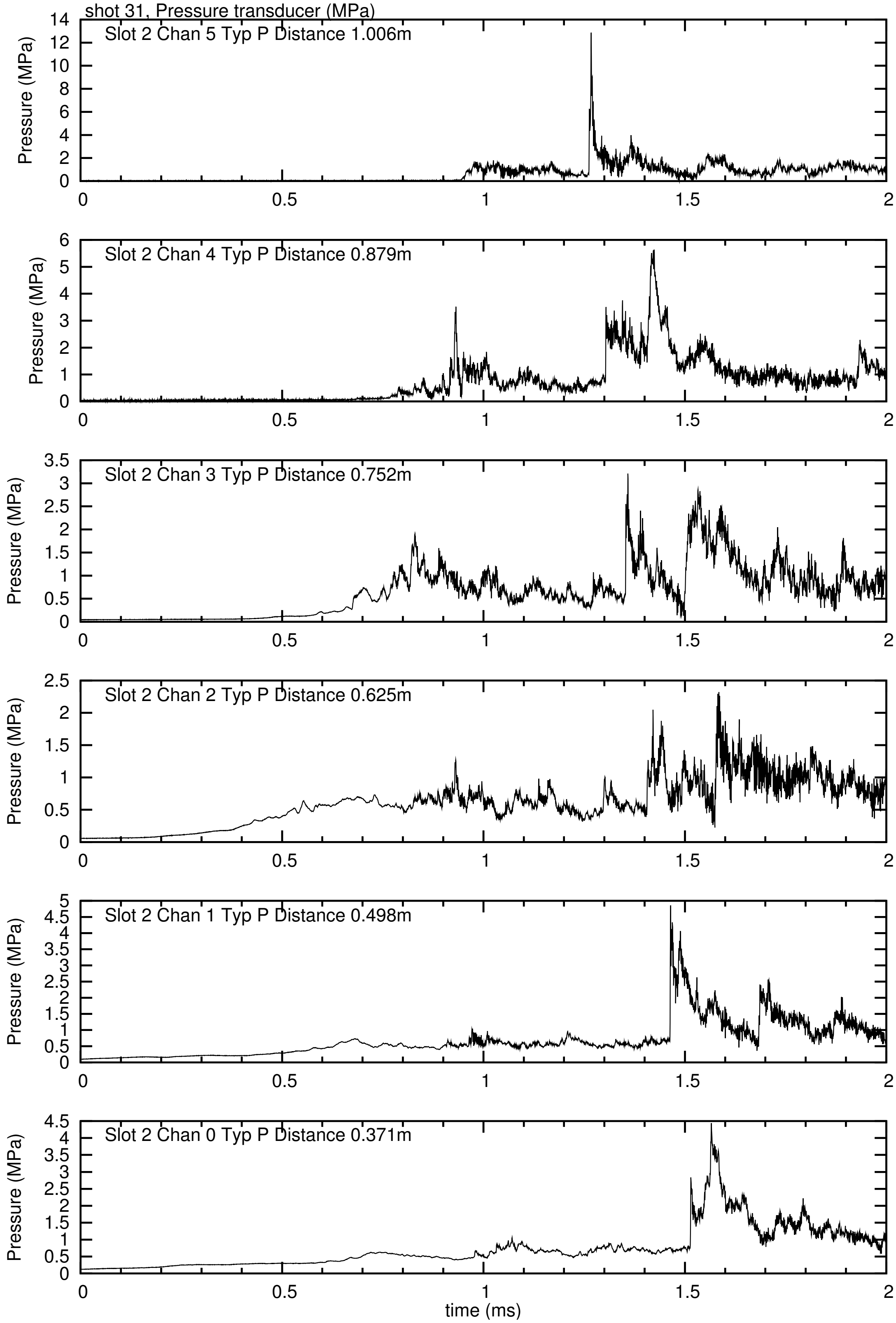

Figure 74: **Pressure transducers, shot 31**, BR=0.37, O_2/C=0.9, P_{CJ}=3.01 MPa, P_{CV}=1.52 MPa.

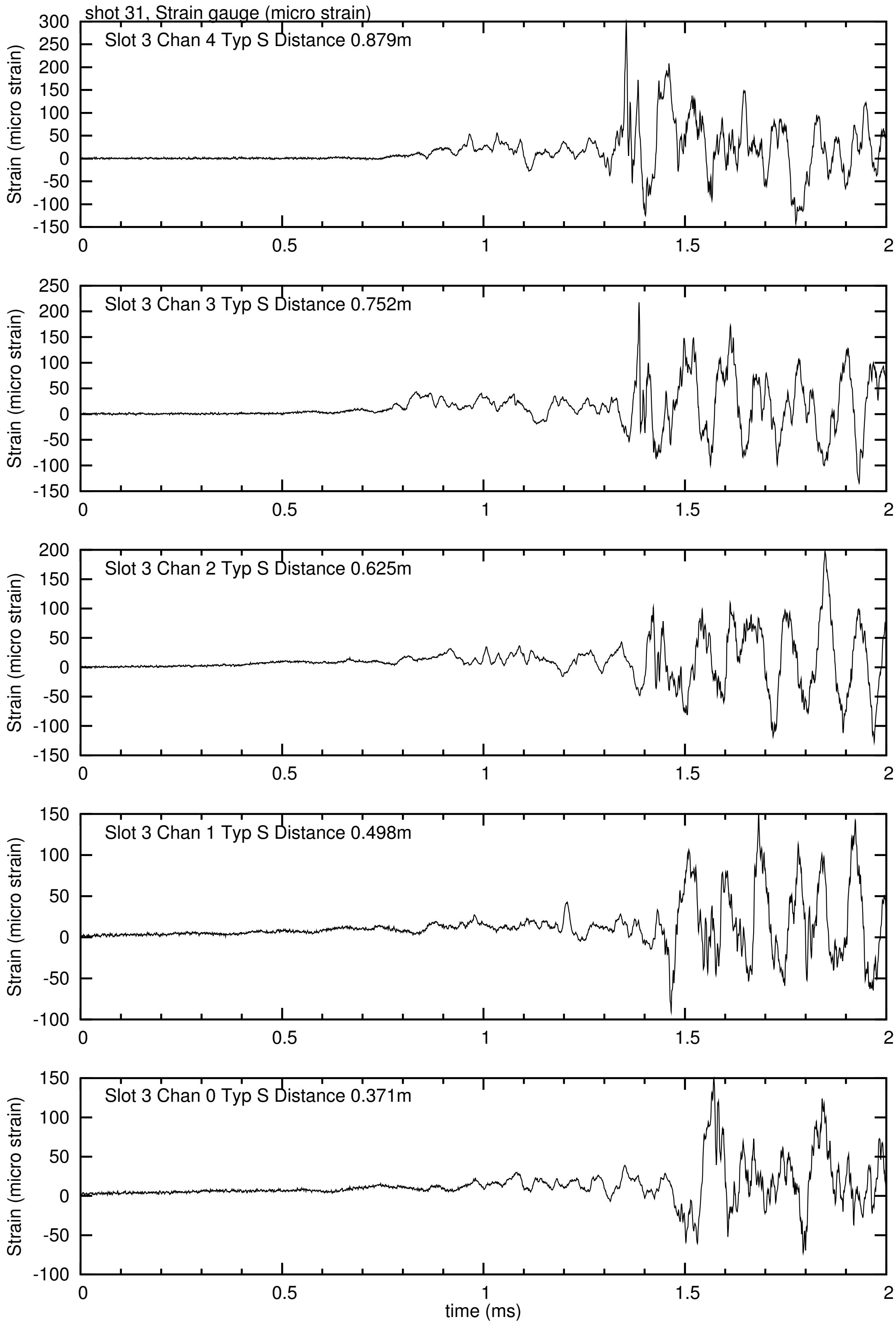

Figure 75: **Strain gauges, shot 31**, BR=0.37, O_2/C=0.9, P_{CJ}=3.01 MPa, P_{CV}=1.52 MPa.

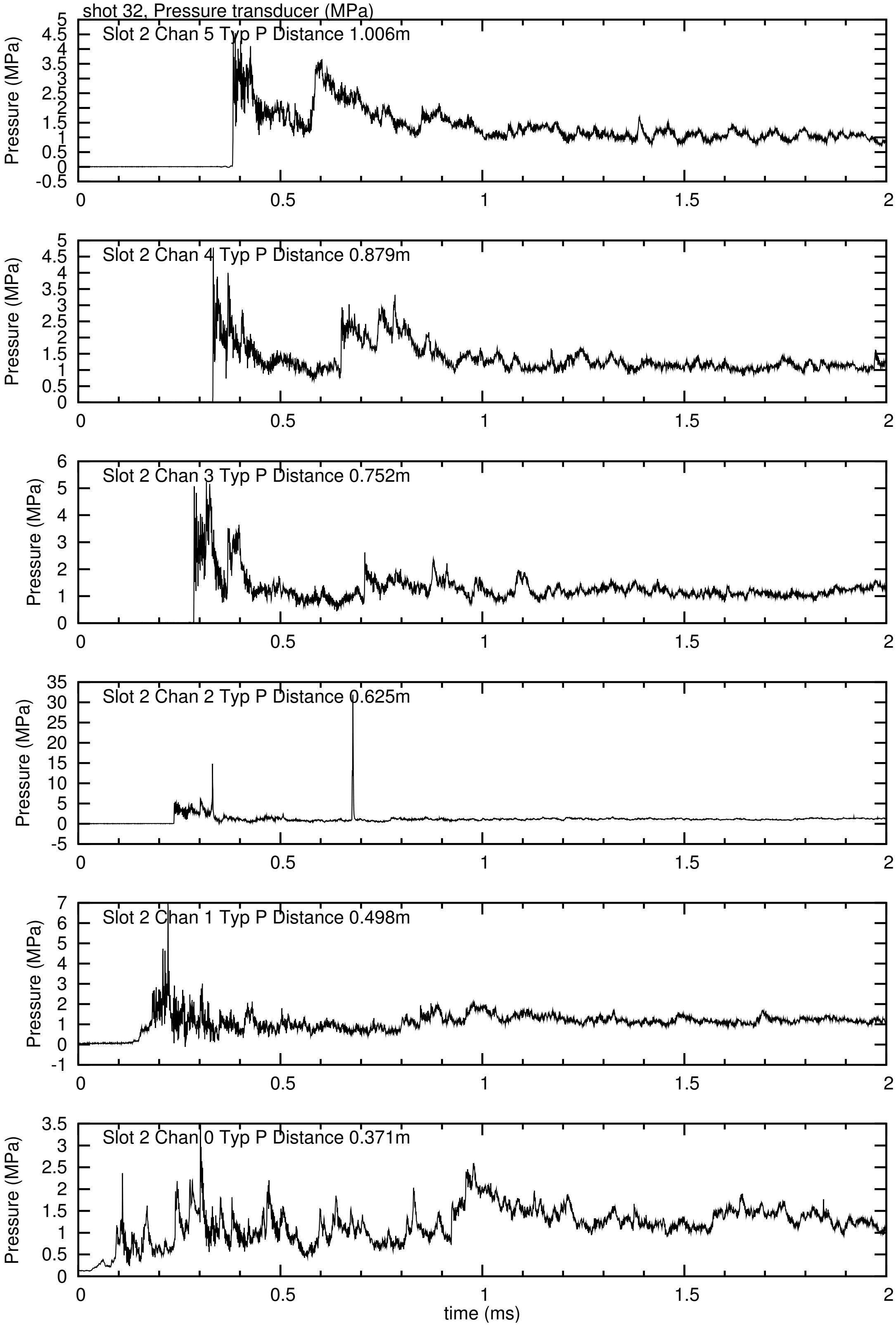

Figure 76: **Pressure transducers, shot 32**, BR=0.37, O_2/C=1.1, P_{CJ}=3.19 MPa, P_{CV}=1.61 MPa.

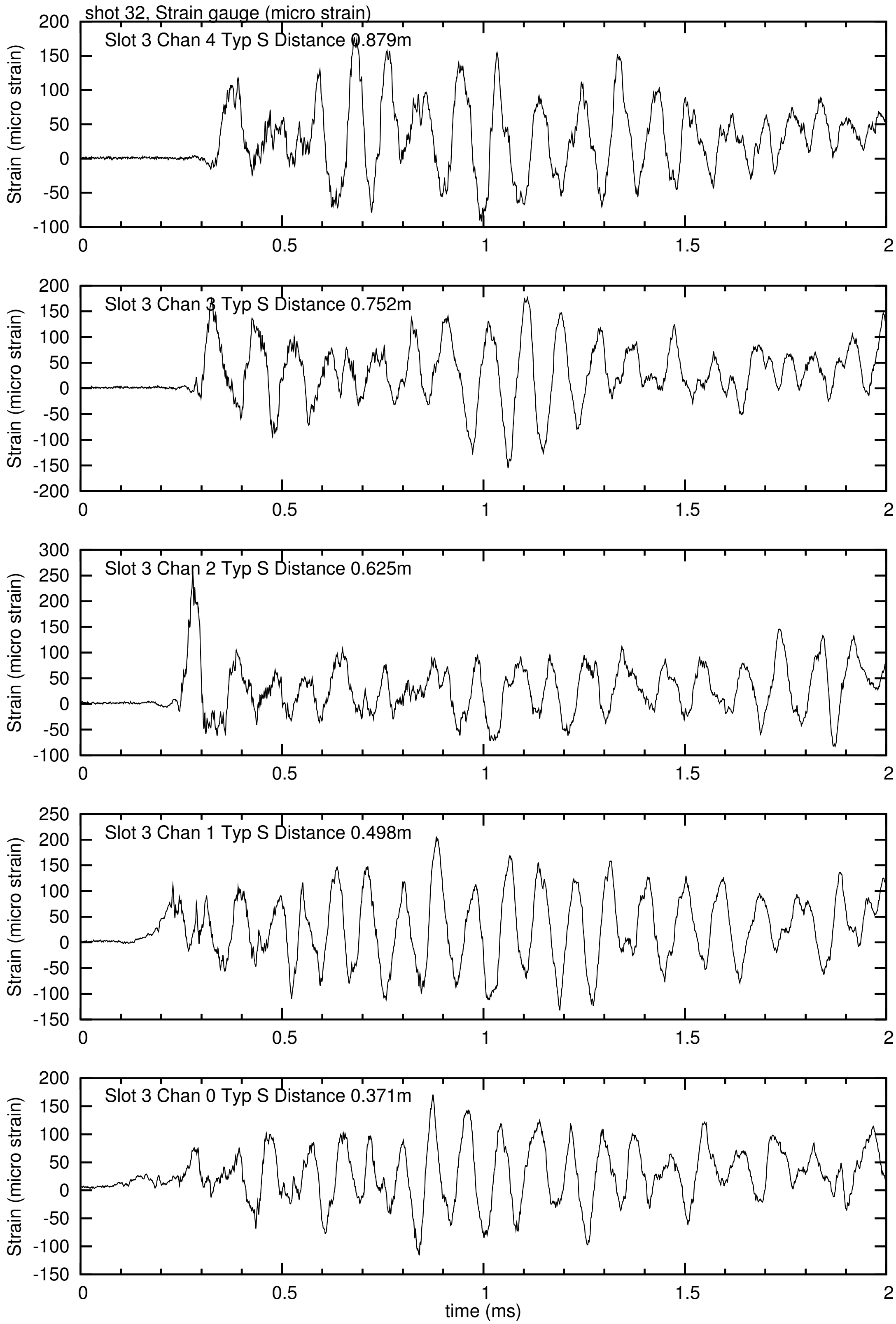

Figure 77: **Strain gauges, shot 32**, BR=0.37, O_2/C=1.1, P_{CJ}=3.19 MPa, P_{CV}=1.61 MPa.

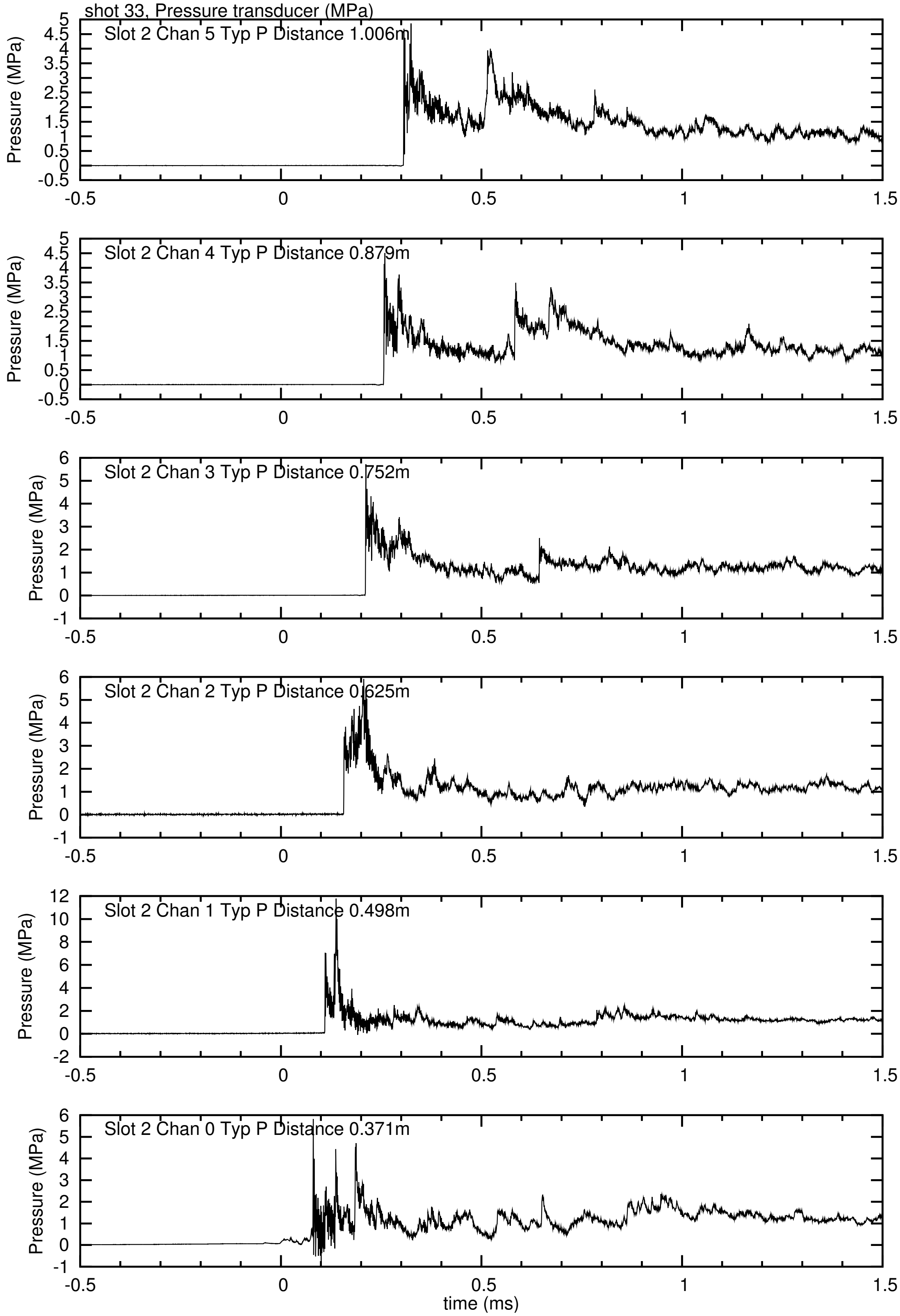

Figure 78: **Pressure transducers, shot 33**, BR=0.37, O_2/C=1.15, P_{CJ}=3.21 MPa, P_{CV}=1.62 MPa.

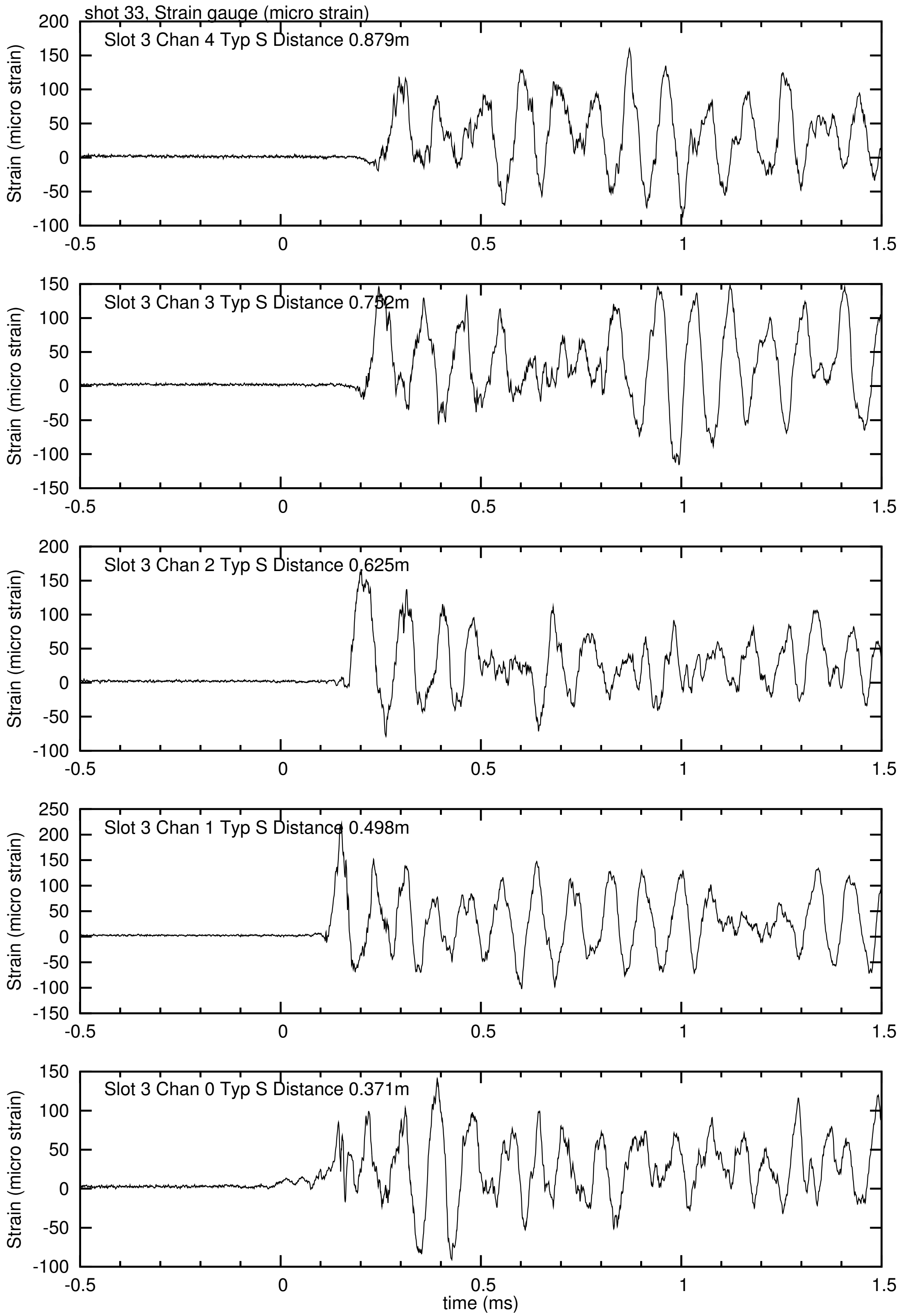

Figure 79: **Strain gauges, shot 33**, BR=0.37, O_2/C=1.15, P_{CJ}=3.21 MPa, P_{CV}=1.62 MPa.

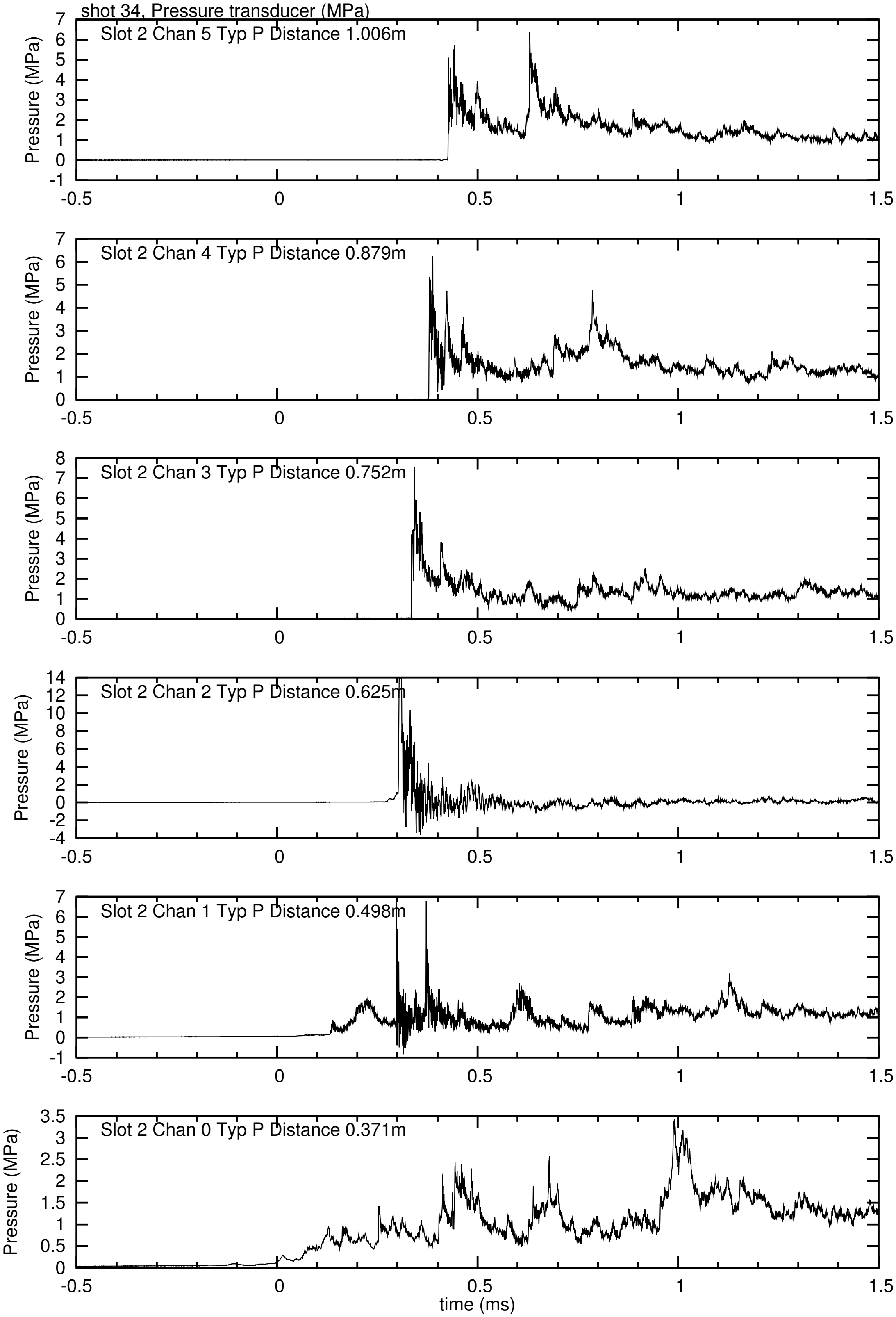

Figure 80: **Pressure transducers, shot 34**, BR=0.37, O_2/C=1.05, P_{CJ}=3.17 MPa, P_{CV}=1.60 MPa.

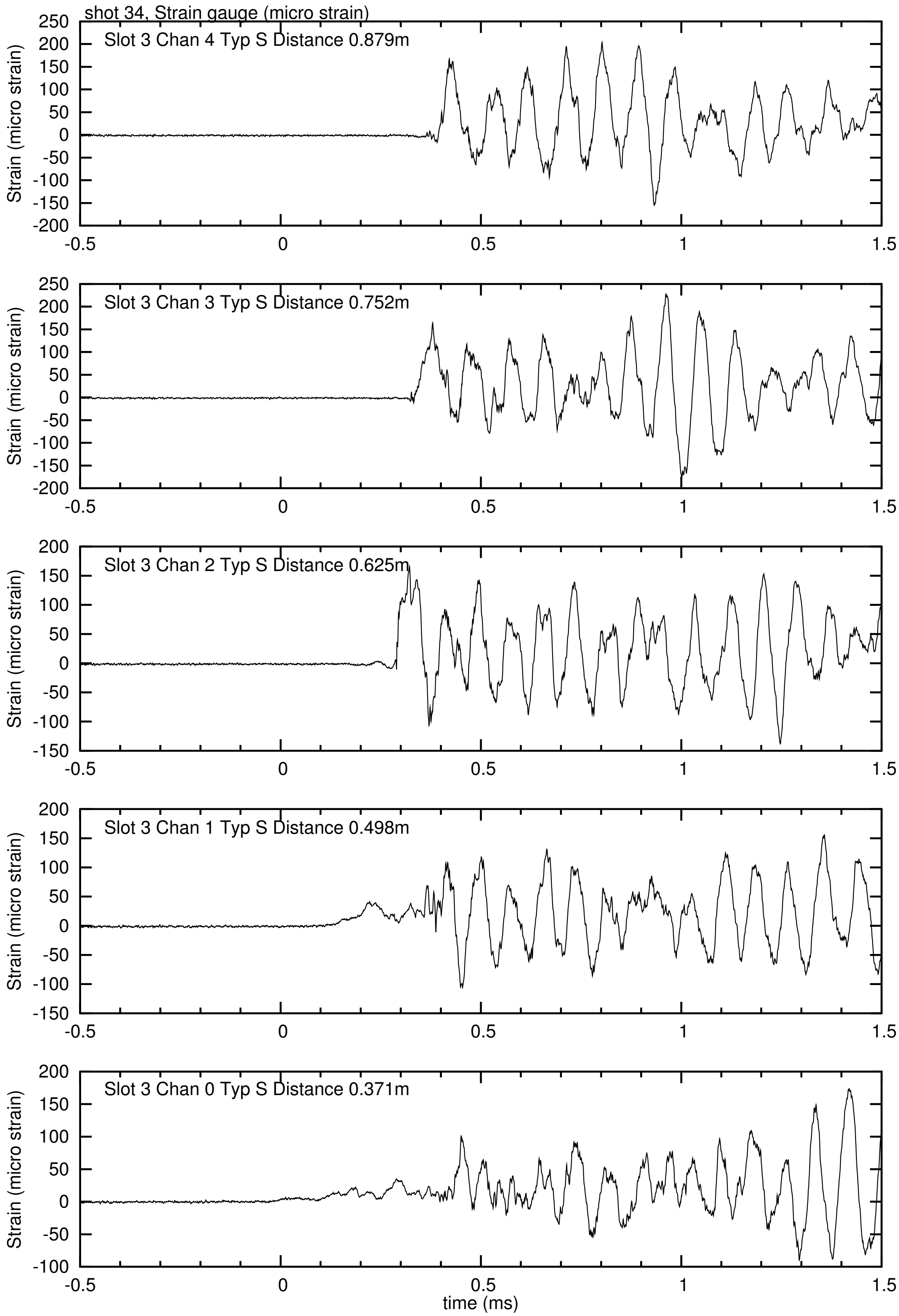

Figure 81: **Strain gauges, shot 34**, BR=0.37, O_2/C=1.05, P_{CJ}=3.17 MPa, P_{CV}=1.60 MPa.

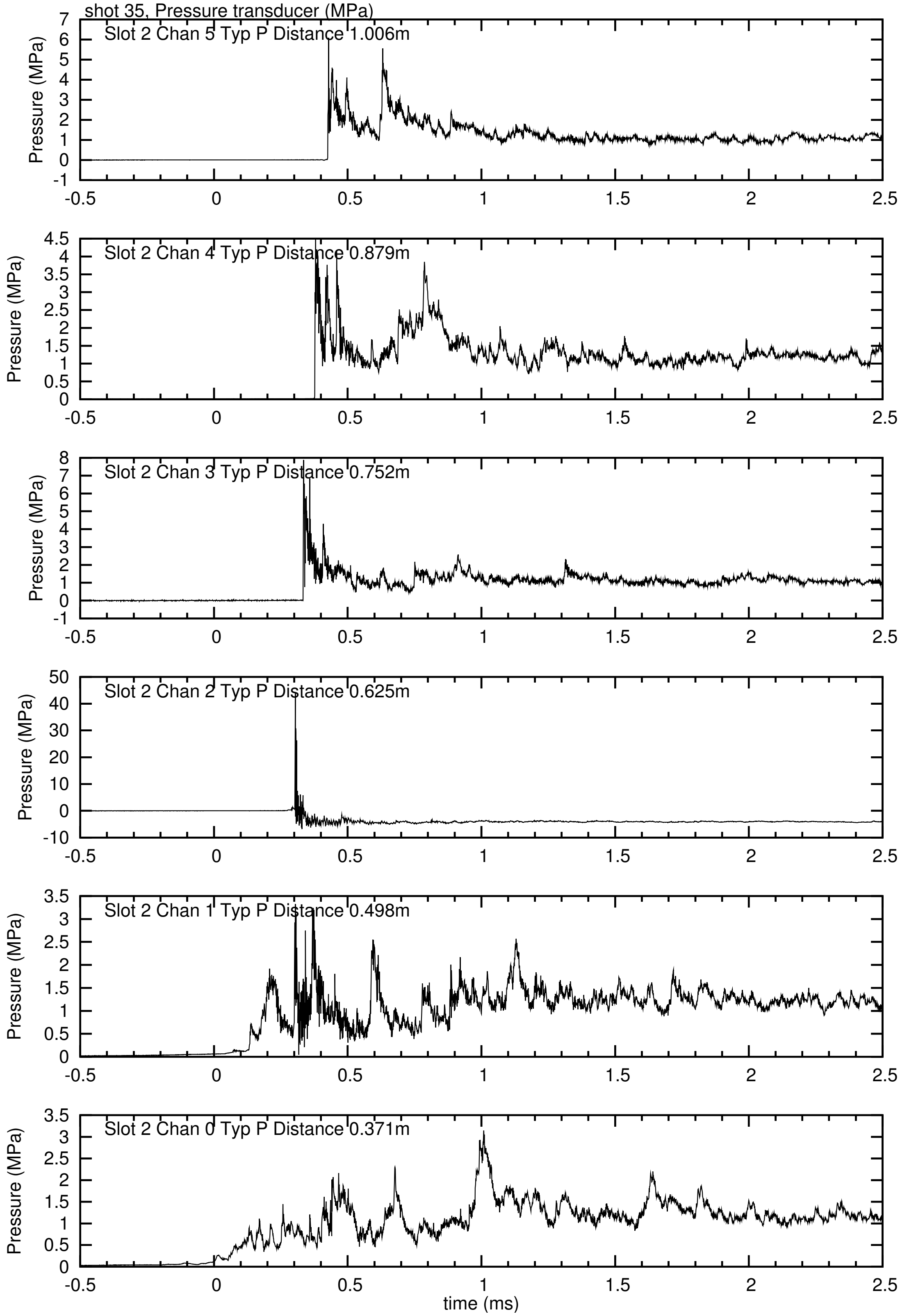

Figure 82: **Pressure transducers, shot 35**, BR=0.37, O_2/C=1.05, P_{CJ}=3.17 MPa, P_{CV}=1.60 MPa.

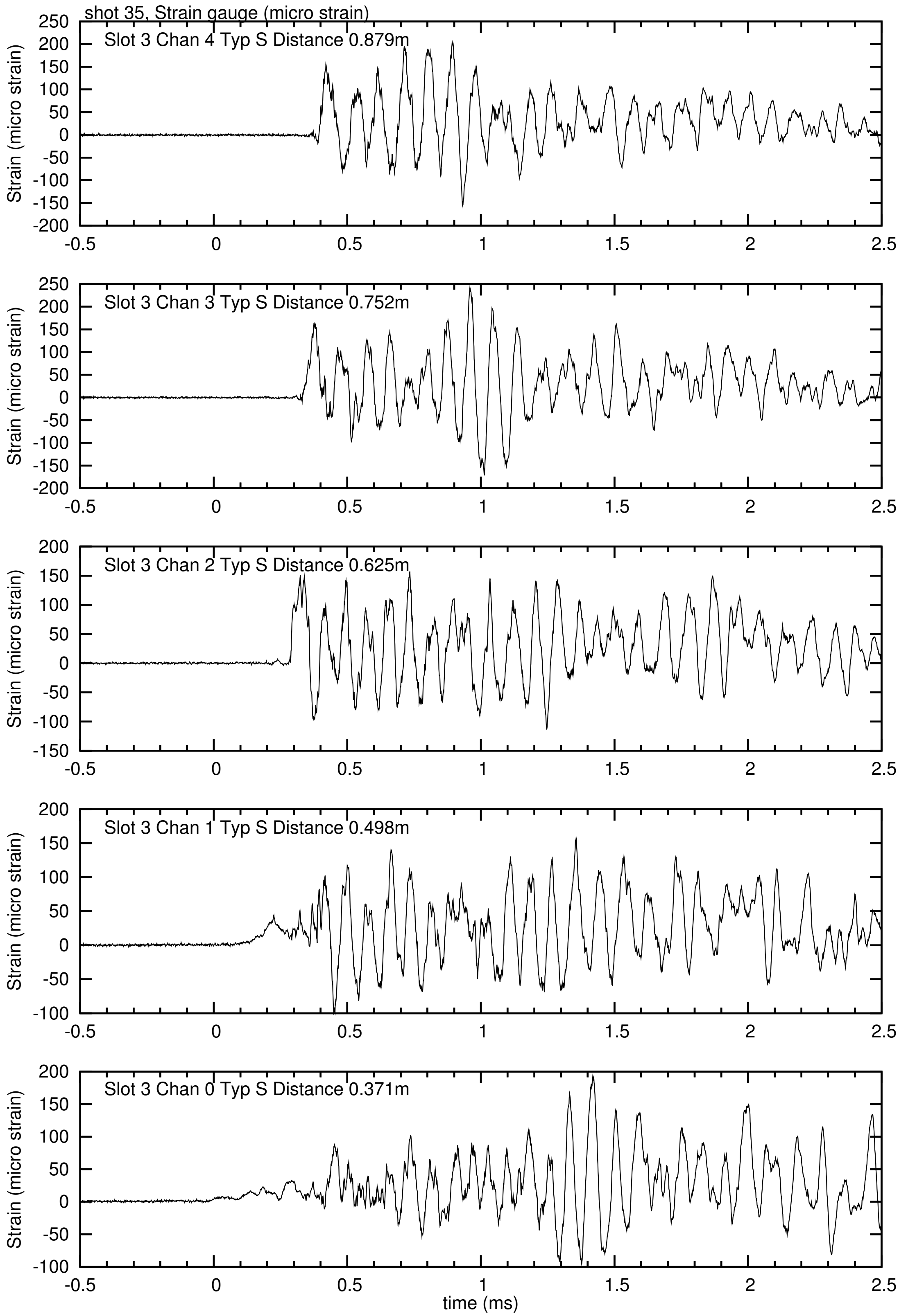

Figure 83: **Strain gauges, shot 35**, BR=0.37, O_2/C=1.05, P_{CJ}=3.17 MPa, P_{CV}=1.60 MPa.

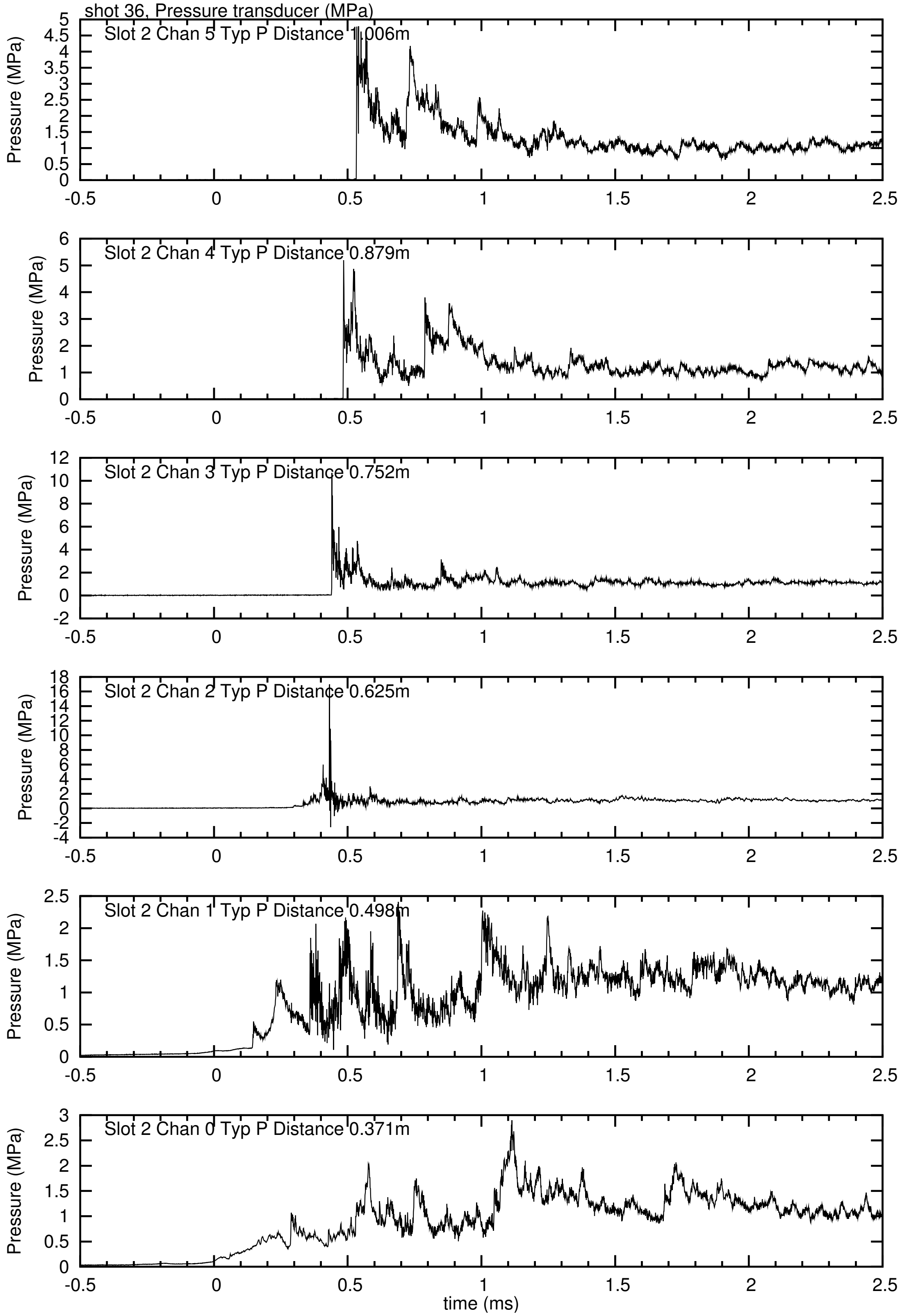

Figure 84: **Pressure transducers, shot 36**, BR=0.37, O_2/C=1, P_{CJ}=3.13 MPa, P_{CV}=1.58 MPa.

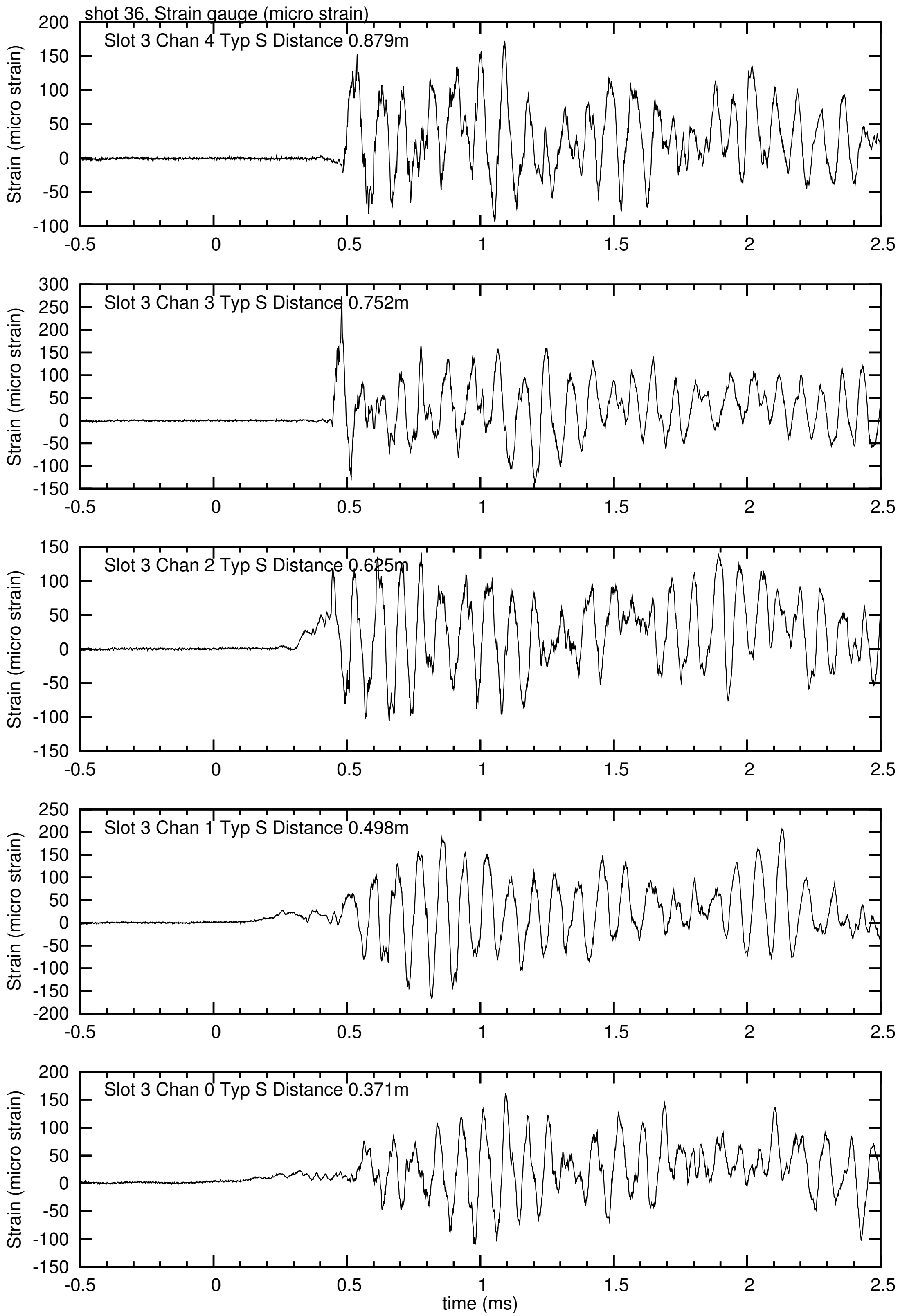

Figure 85: **Strain gauges, shot 36**, BR=0.37, $O_2/C=1$, P_{CJ}=3.13 MPa, P_{CV}=1.58 MPa.

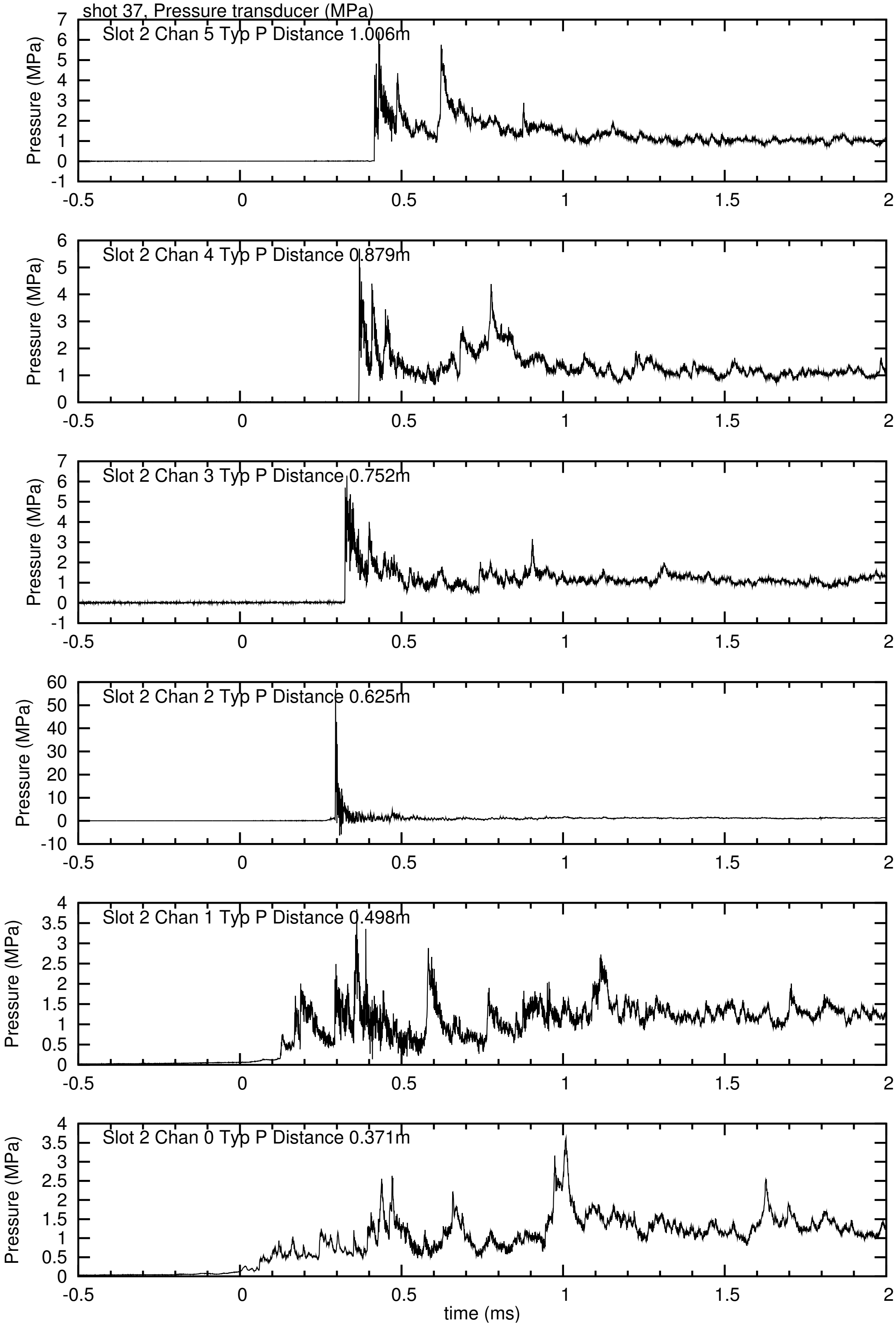

Figure 86: **Pressure transducers, shot 37**, BR=0.37, O_2/C=1.05, P_{CJ}=3.17 MPa, P_{CV}=1.60 MPa.

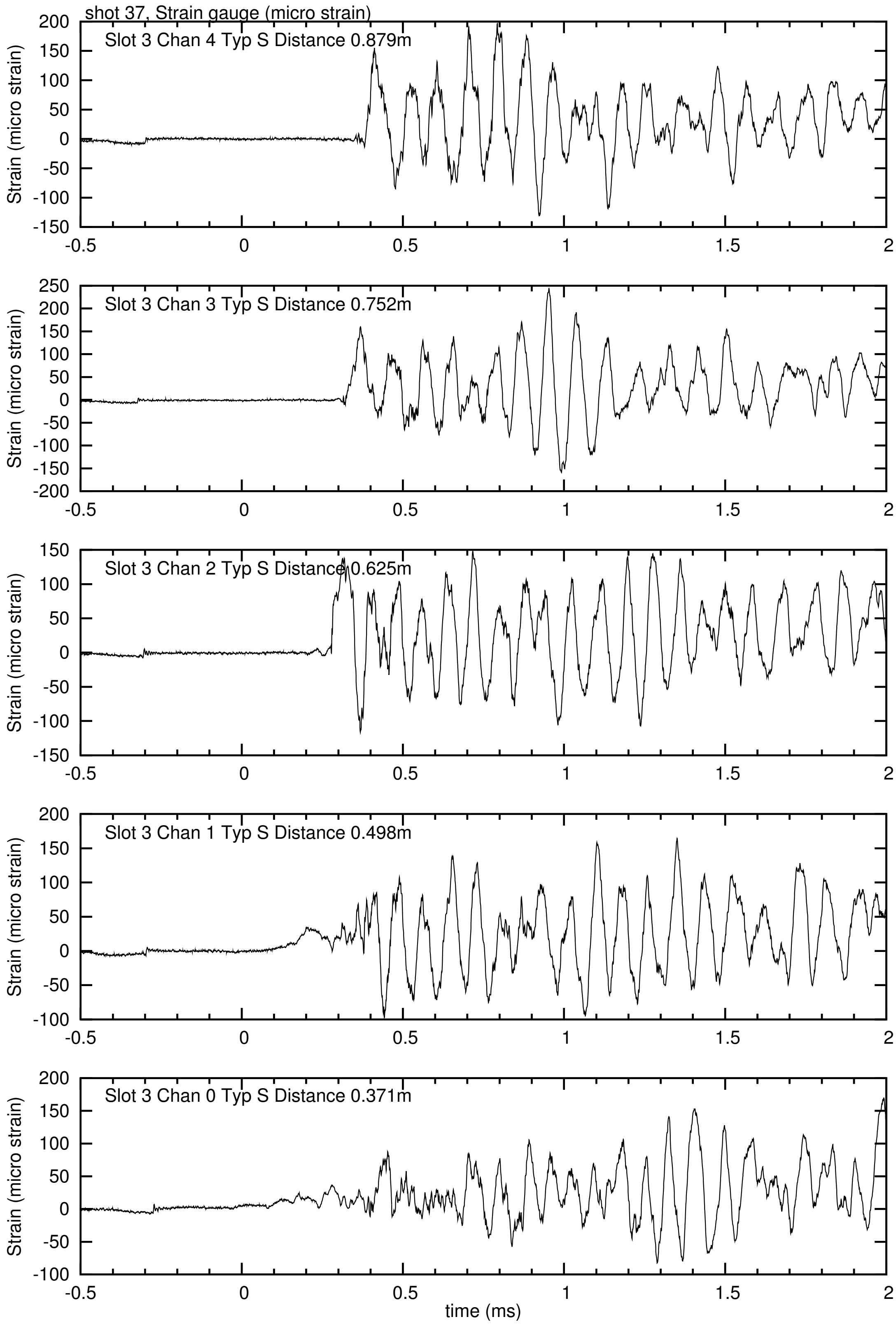

Figure 87: **Strain gauges, shot 37**, BR=0.37, O_2/C=1.05, P_{CJ}=3.17 MPa, P_{CV}=1.60 MPa.

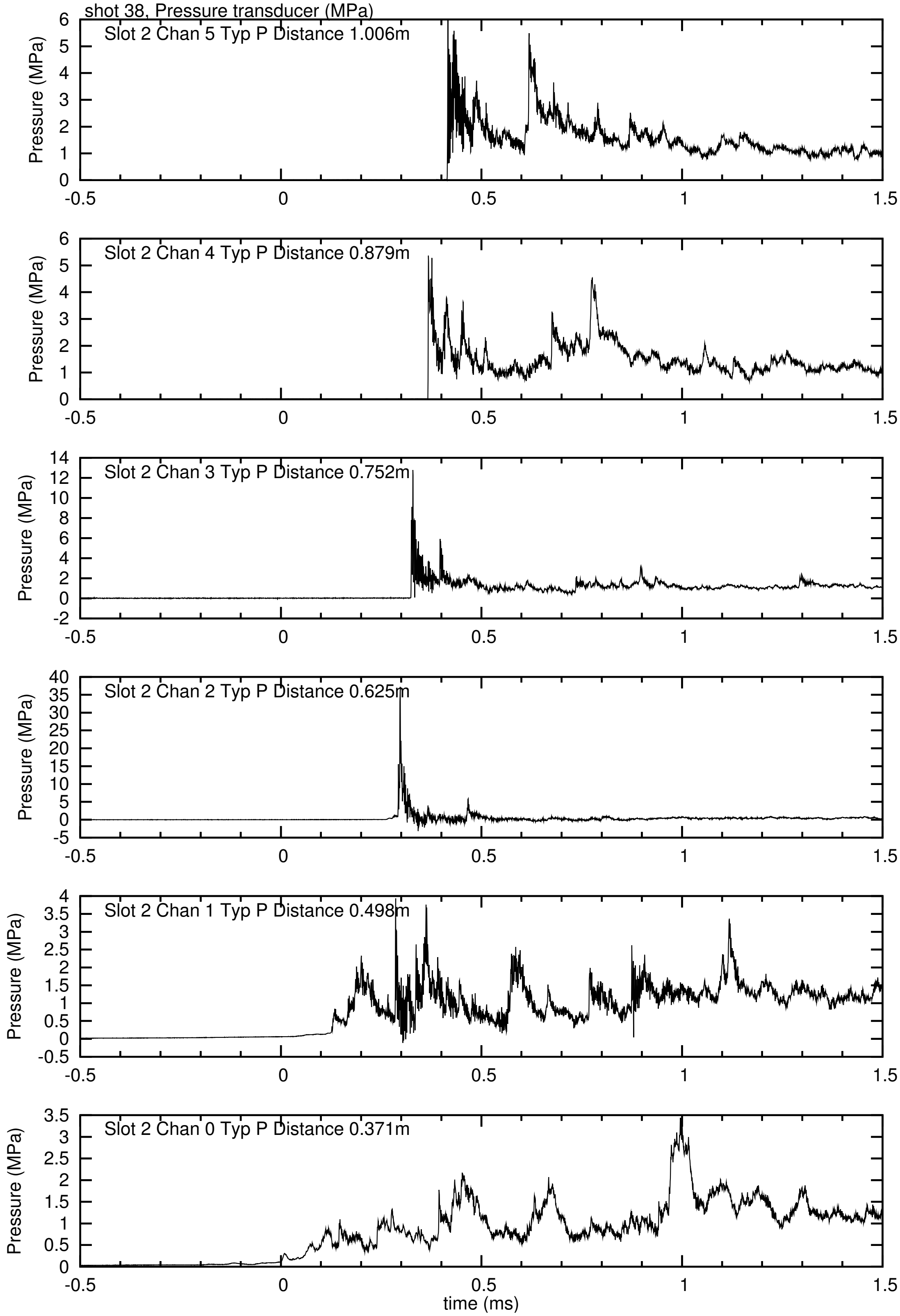

Figure 88: **Pressure transducers, shot 38**, BR=0.37, O_2/C=1.05, P_{CJ}=3.17 MPa, P_{CV}=1.60 MPa.

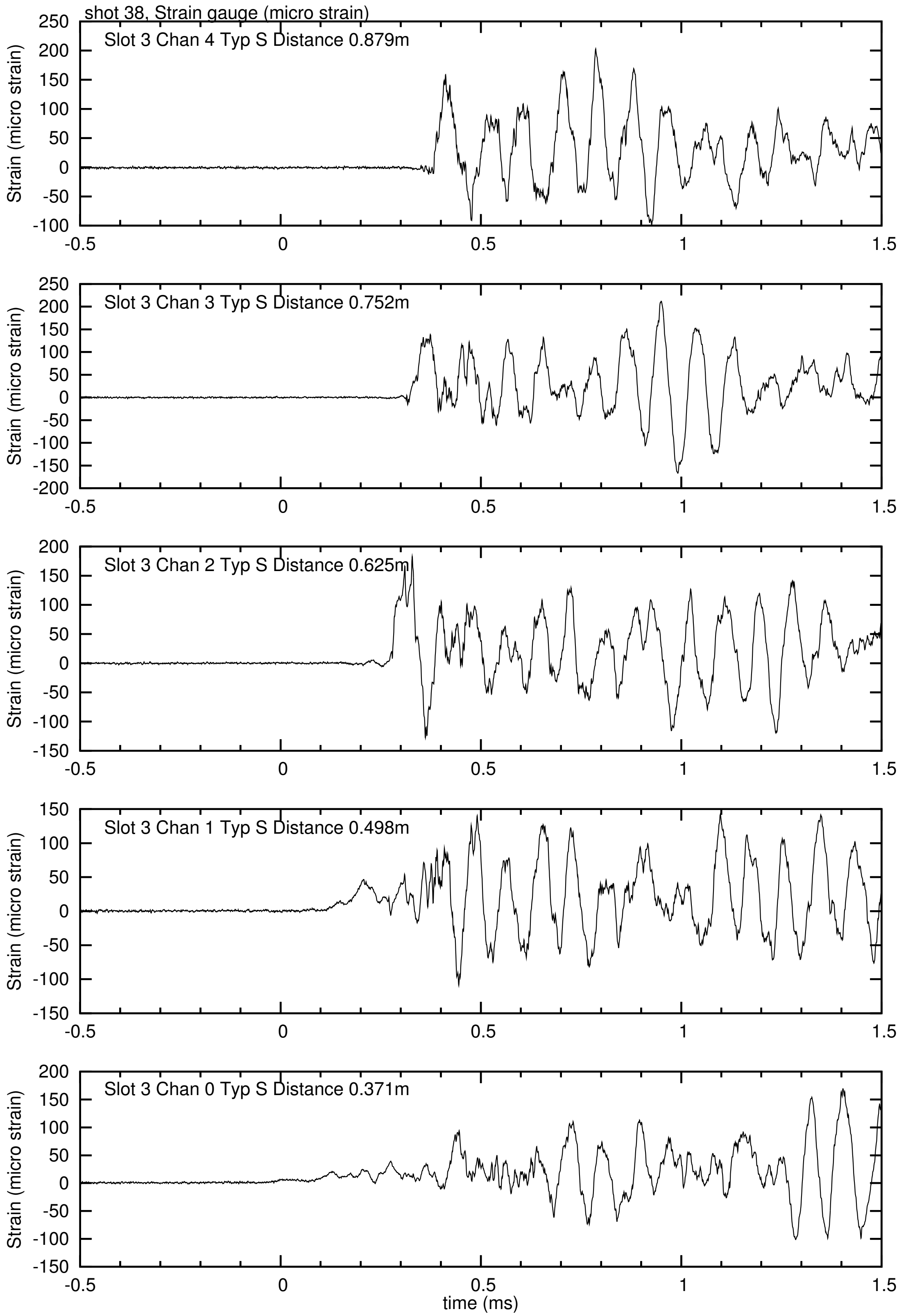

Figure 89: **Strain gauges, shot 38**, BR=0.37, O_2/C=1.05, P_{CJ}=3.17 MPa, P_{CV}=1.60 MPa.

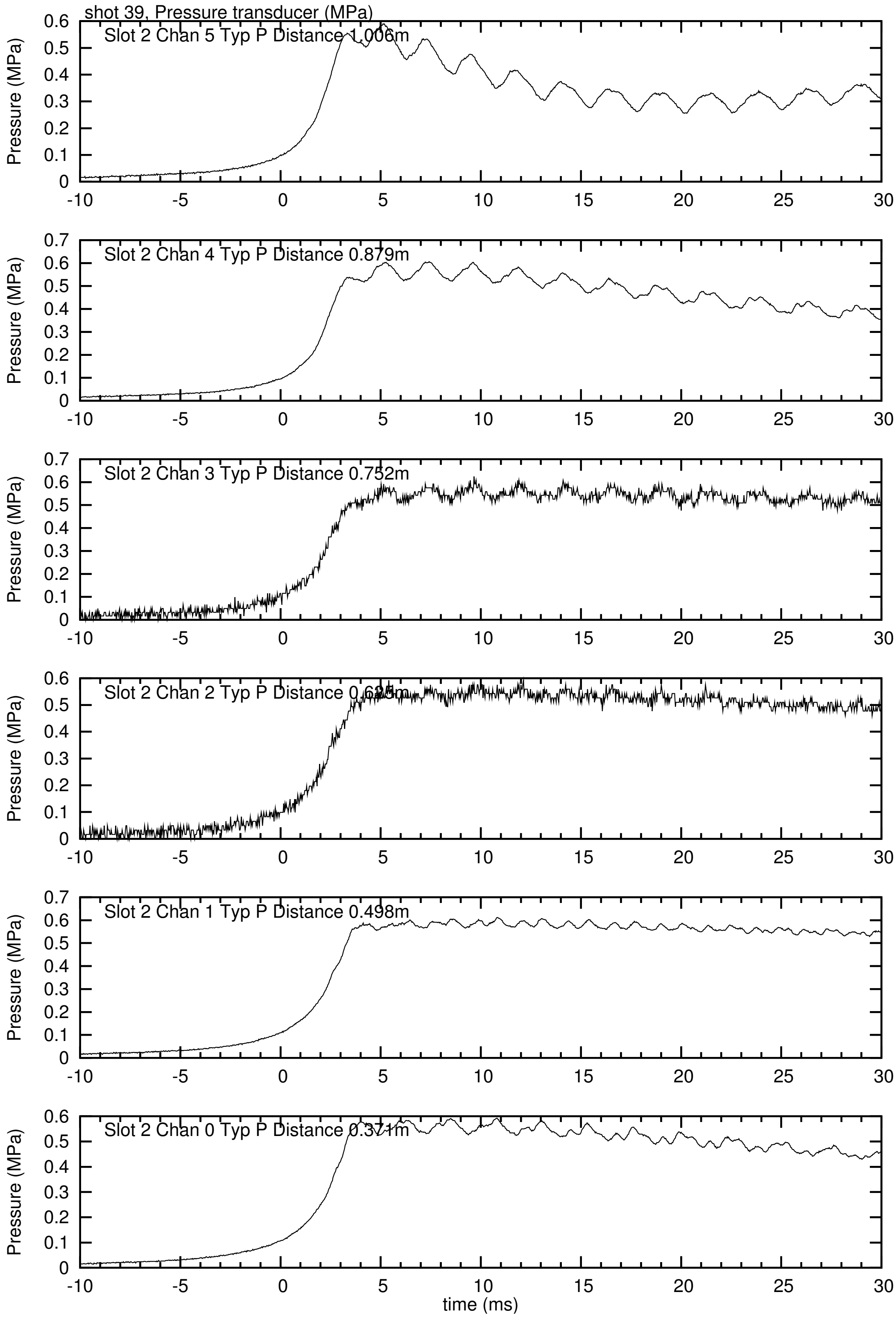

Figure 90: **Pressure transducers, shot 39**, BR=0.37, O_2/C=0.75, P_{CJ}=2.63 MPa, P_{CV}=1.33 MPa.

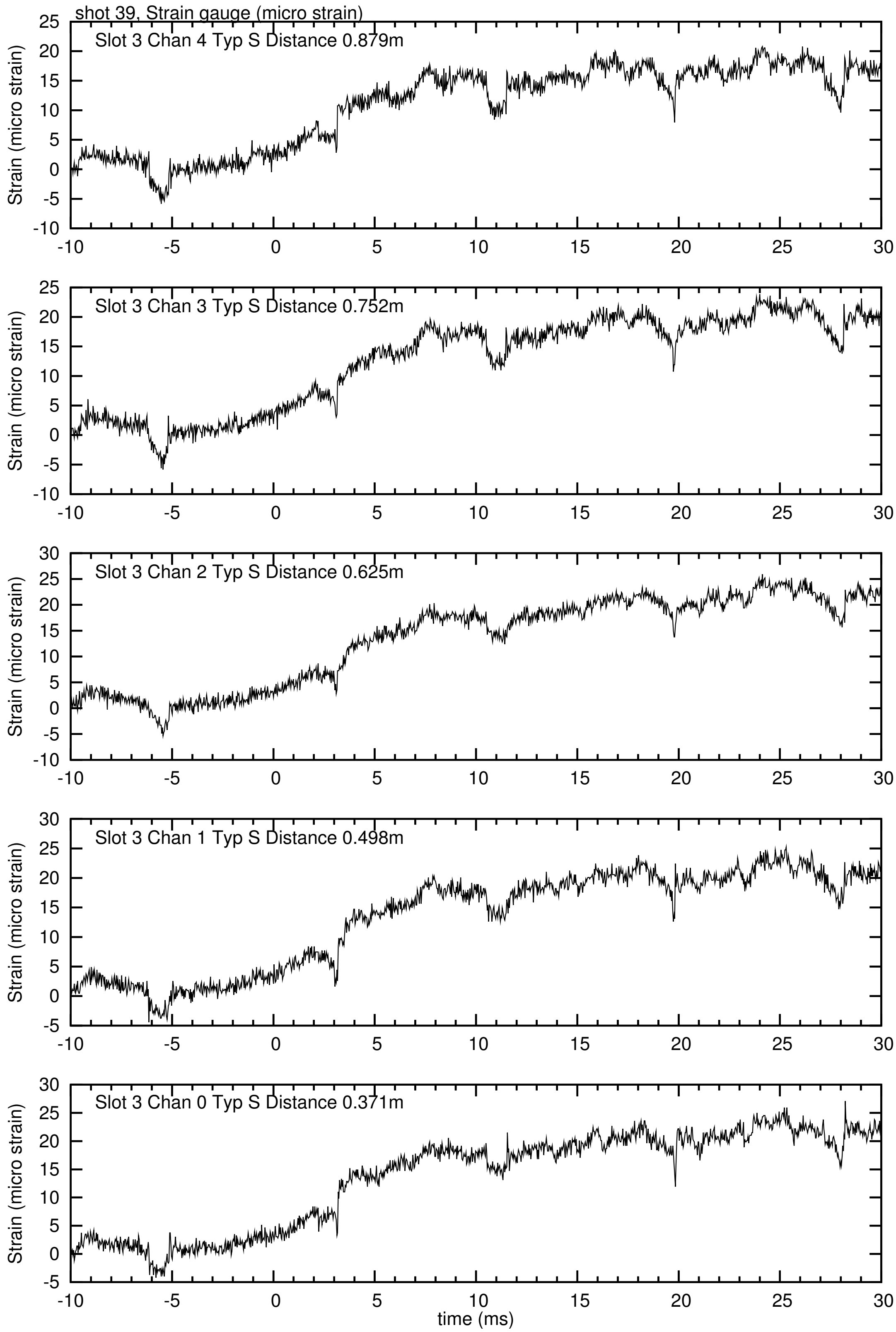

Figure 91: **Strain gauges, shot 39**, BR=0.37, O_2/C=0.75, P_{CJ}=2.63 MPa, P_{CV}=1.33 MPa.

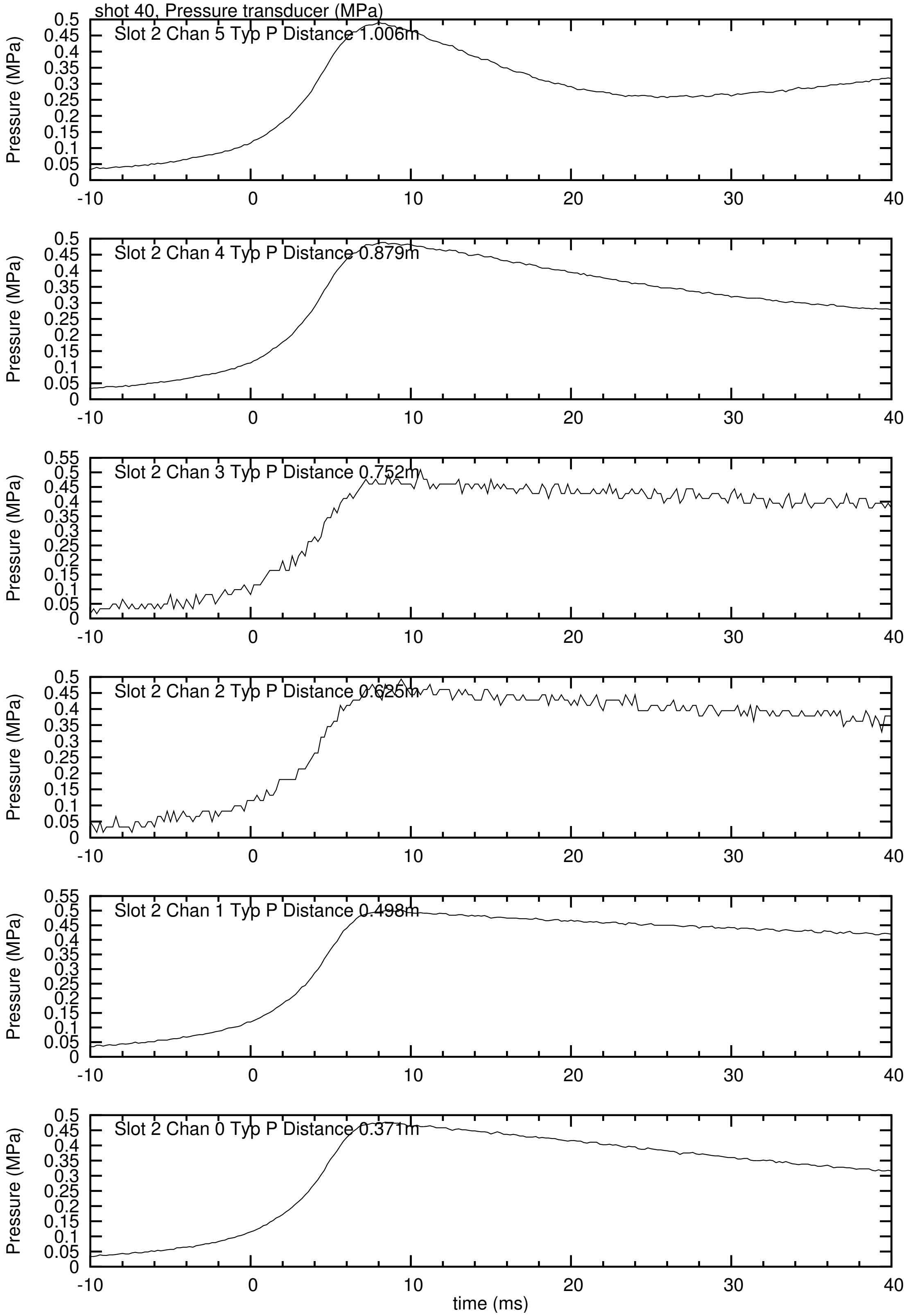

Figure 92: **Pressure transducers, shot 40**, BR=0.37, O_2/C=0.7, P_{CJ}=2.43 MPa, P_{CV}=1.23 MPa.

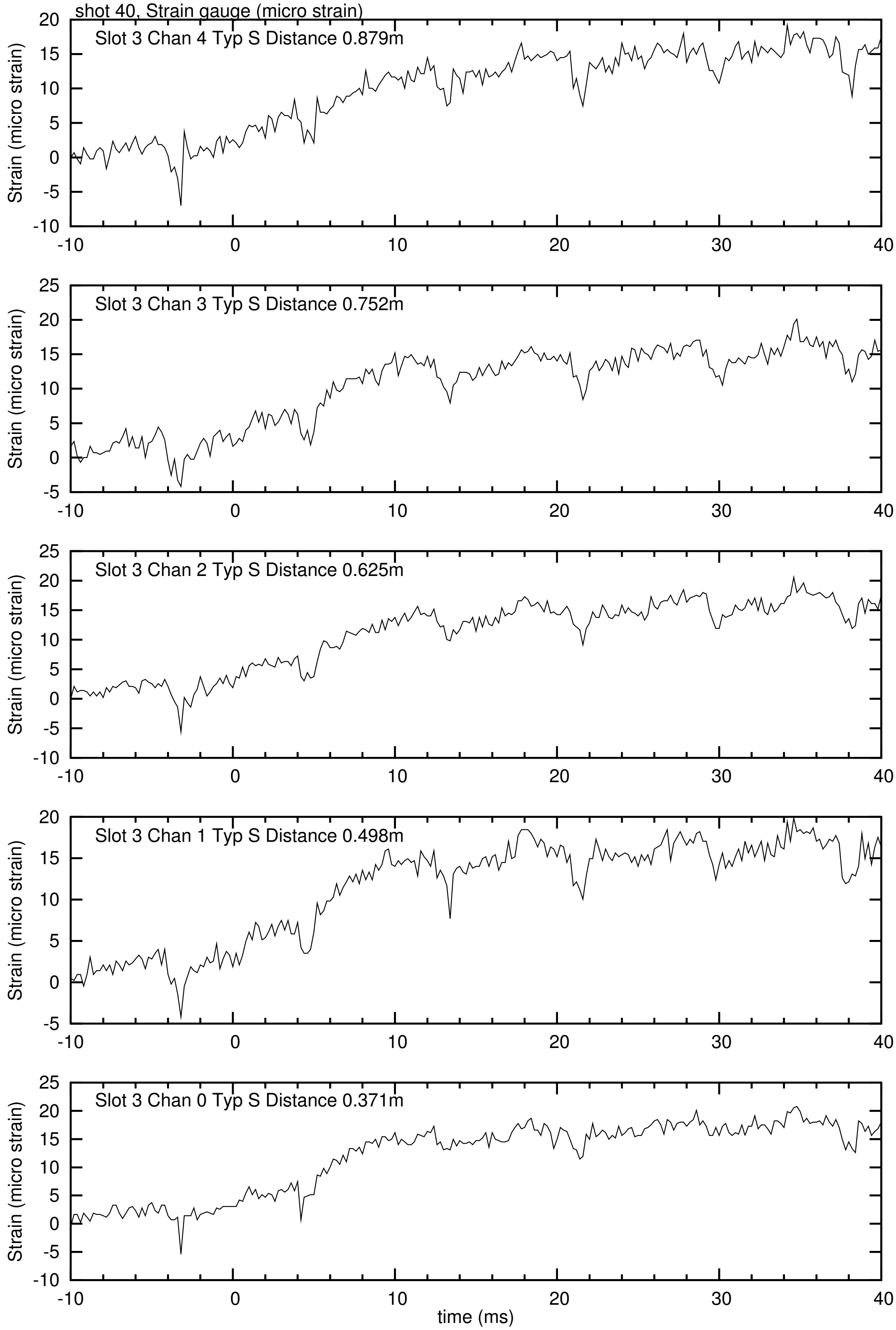

Figure 93: **Strain gauges, shot 40**, BR=0.37, O_2/C=0.7, P_{CJ}=2.43 MPa, P_{CV}=1.23 MPa.

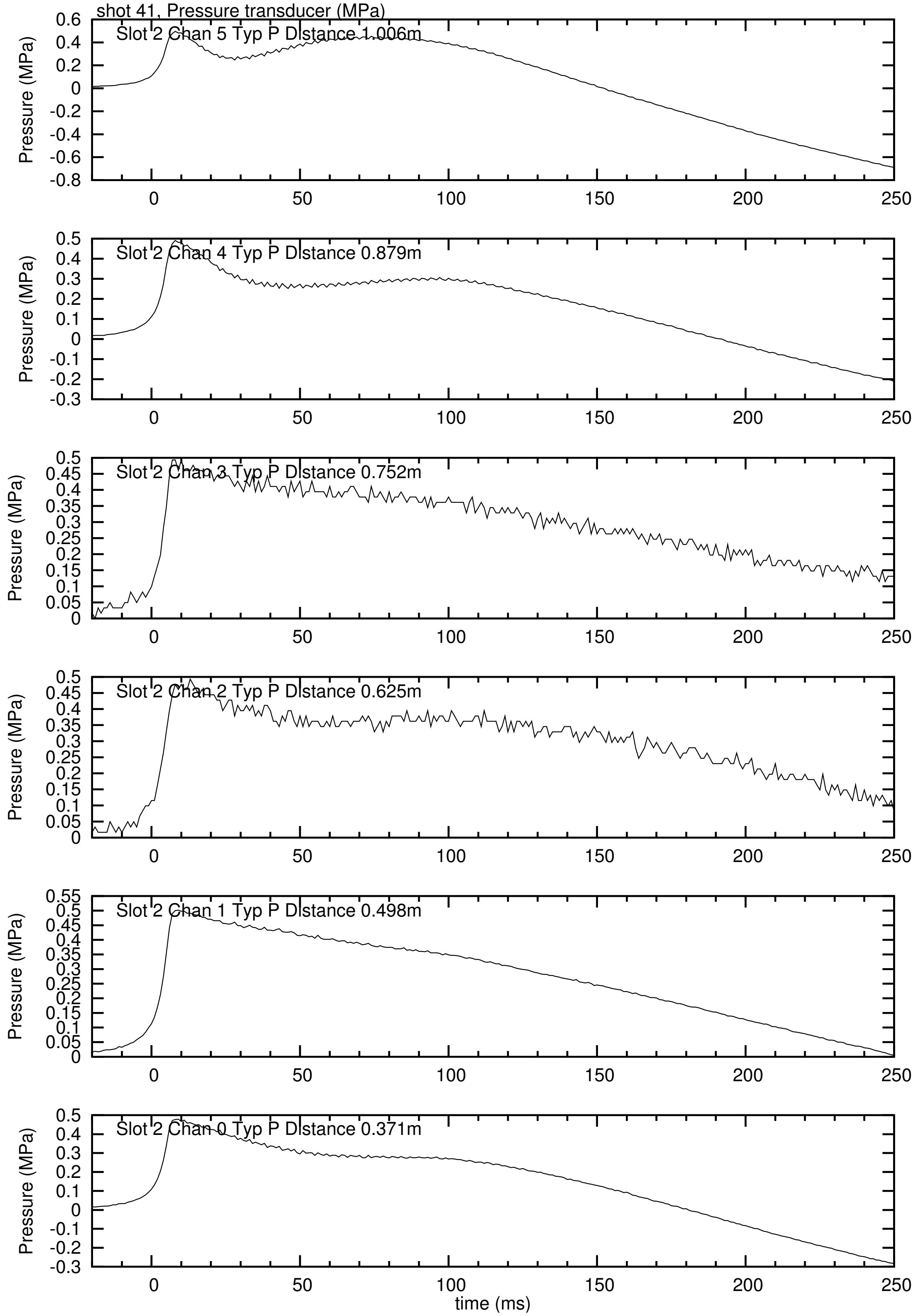

Figure 94: **Pressure transducers, shot 41**, BR=0.37, O_2/C=0.7, P_{CJ}=2.43 MPa, P_{CV}=1.23 MPa.

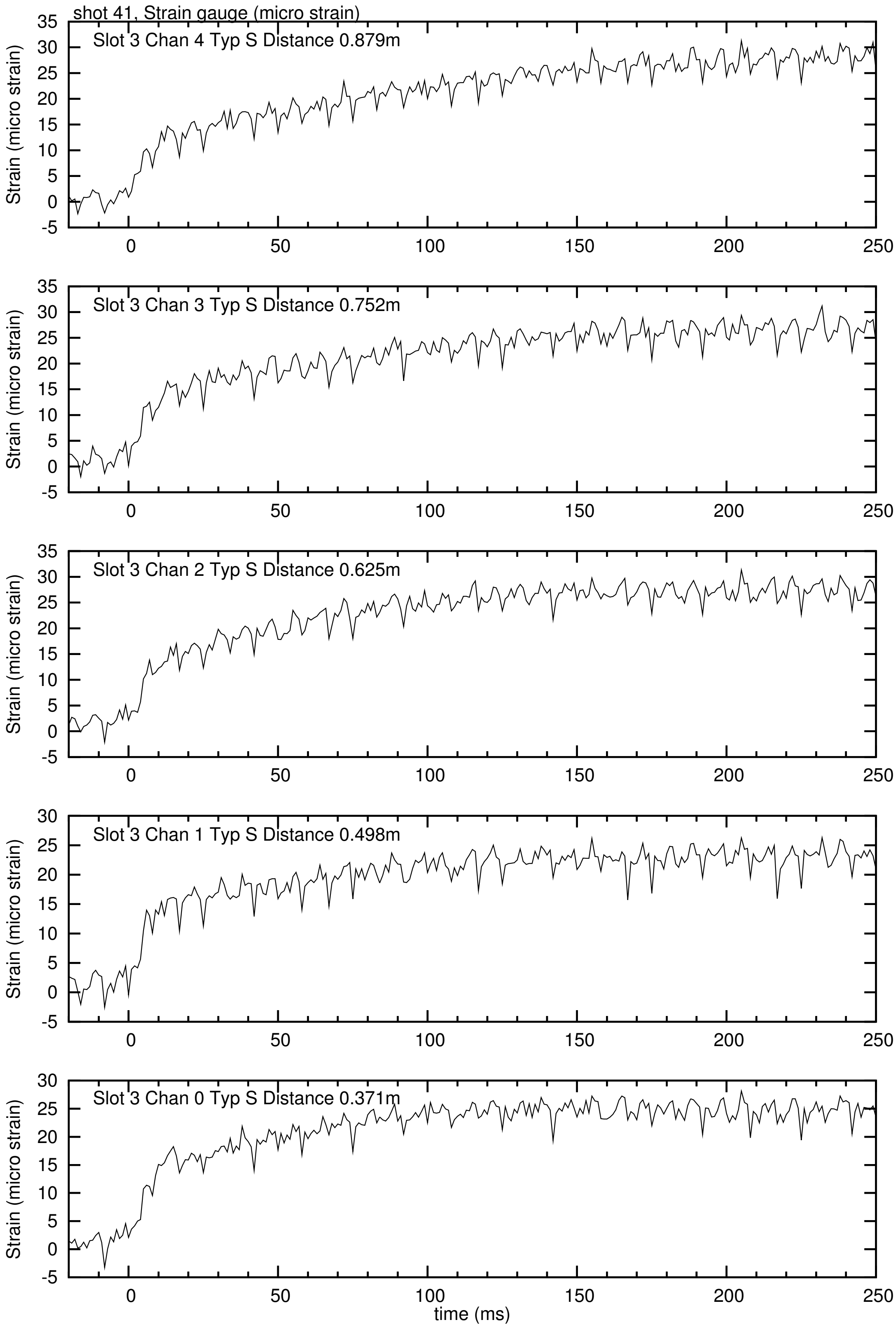

Figure 95: **Strain gauges, shot 41**, BR=0.37, O_2/C=0.7, P_{CJ}=2.43 MPa, P_{CV}=1.23 MPa.

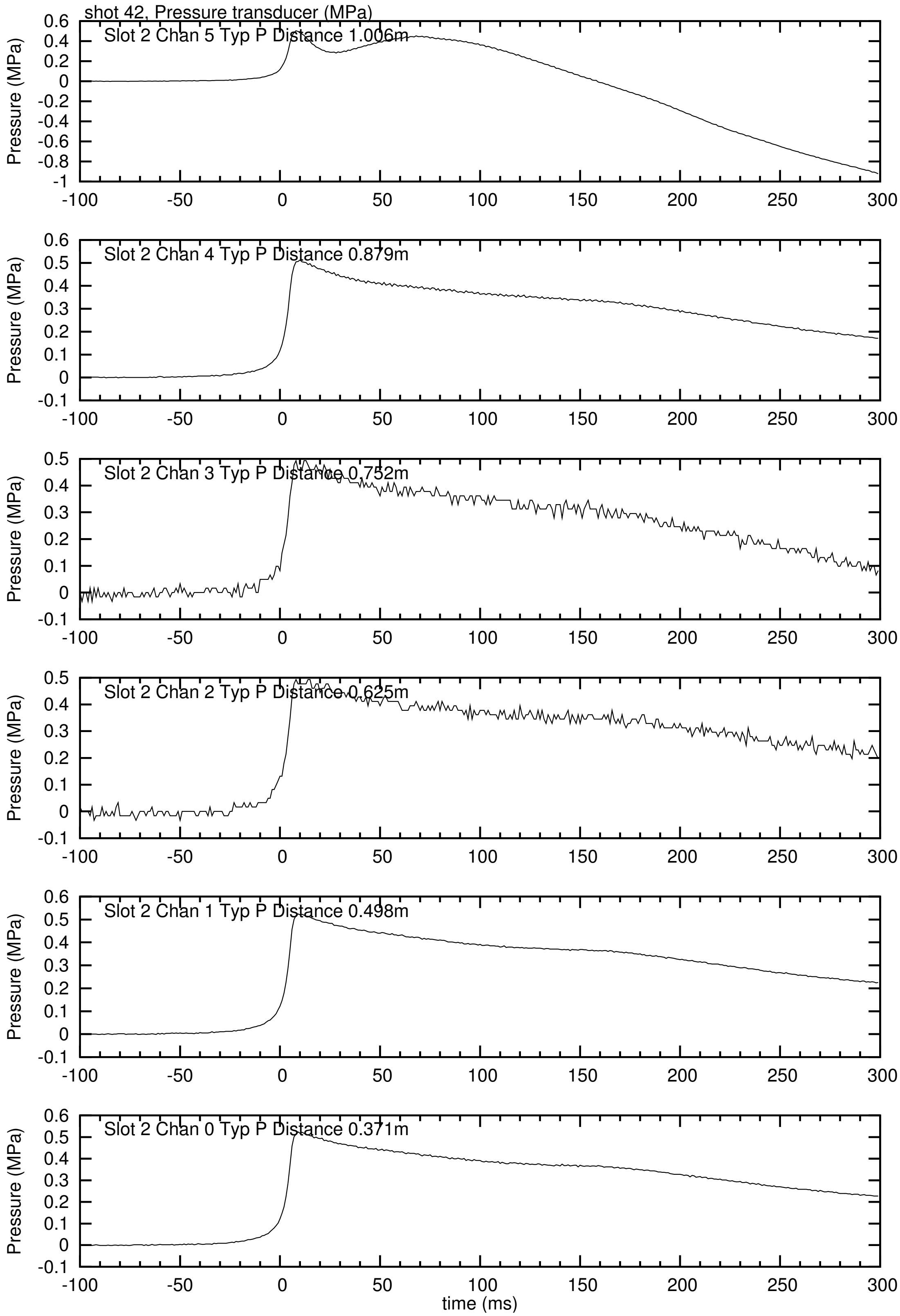

Figure 96: **Pressure transducers, shot 42**, BR=0.37, O_2/C=0.7, P_{CJ}=2.43 MPa, P_{CV}=1.23 MPa.

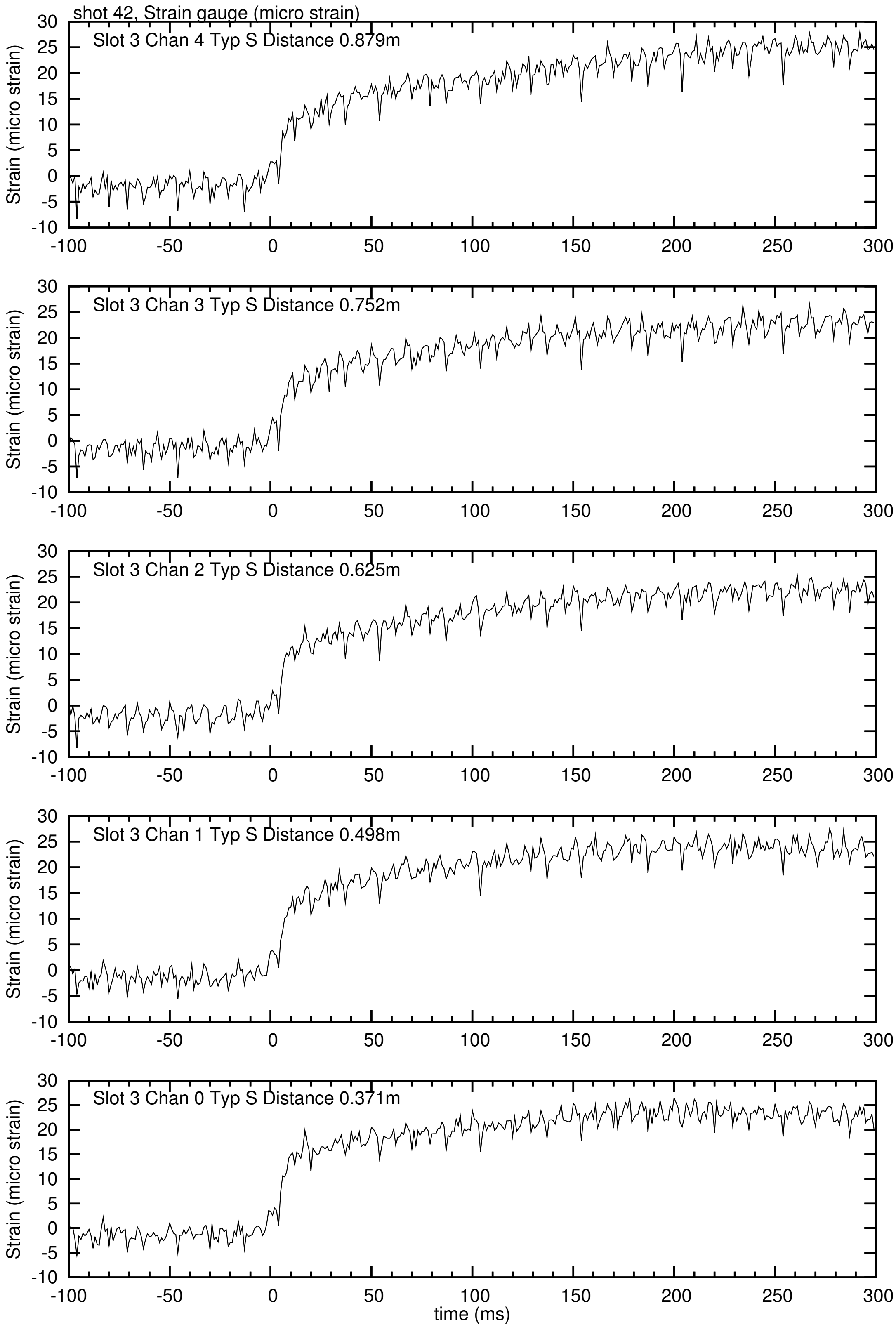

Figure 97: **Strain gauges, shot 42**, BR=0.37, O_2/C=0.7, P_{CJ}=2.43 MPa, P_{CV}=1.23 MPa.

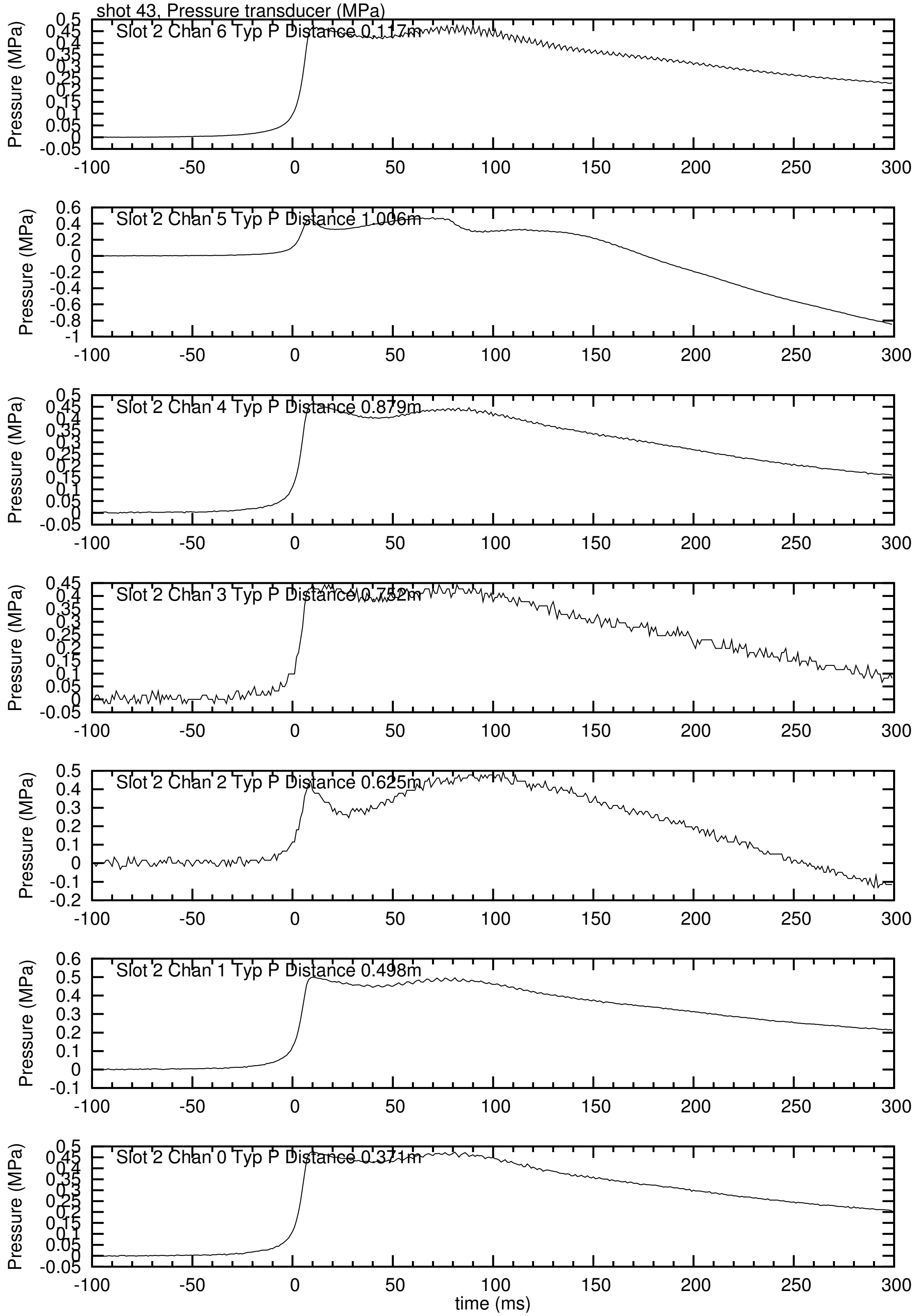

Figure 98: **Pressure transducers, shot 43**, BR=0.37, O_2/C=0.7, P_{CJ}=2.43 MPa, P_{CV}=1.23 MPa.

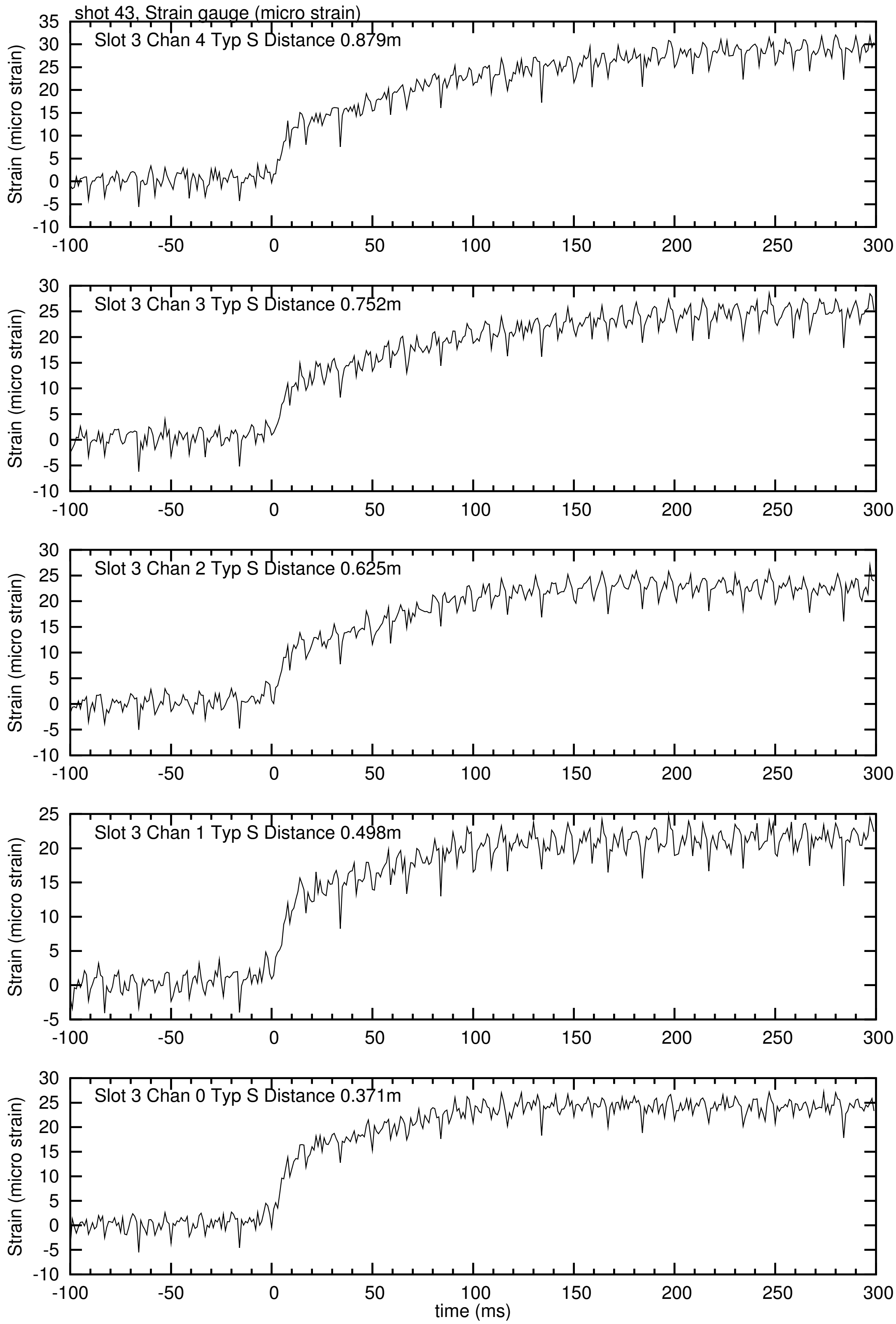

Figure 99: **Strain gauges, shot 43**, BR=0.37, O_2/C=0.7, P_{CJ}=2.43 MPa, P_{CV}=1.23 MPa.

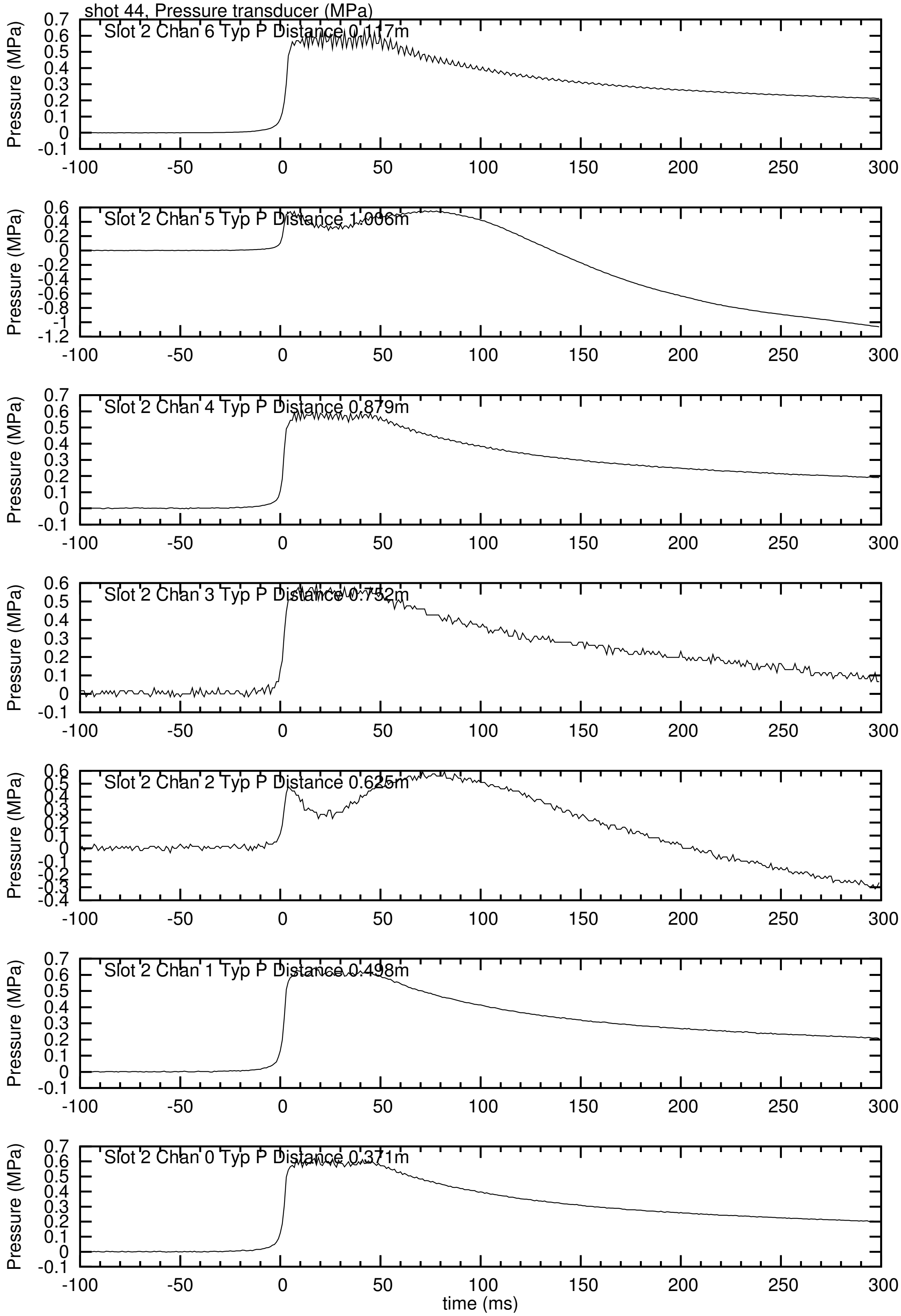

Figure 100: **Pressure transducers, shot 44**, BR=0.37, O_2/C=0.75, P_{CJ}=2.63 MPa, P_{CV}=1.33 MPa.

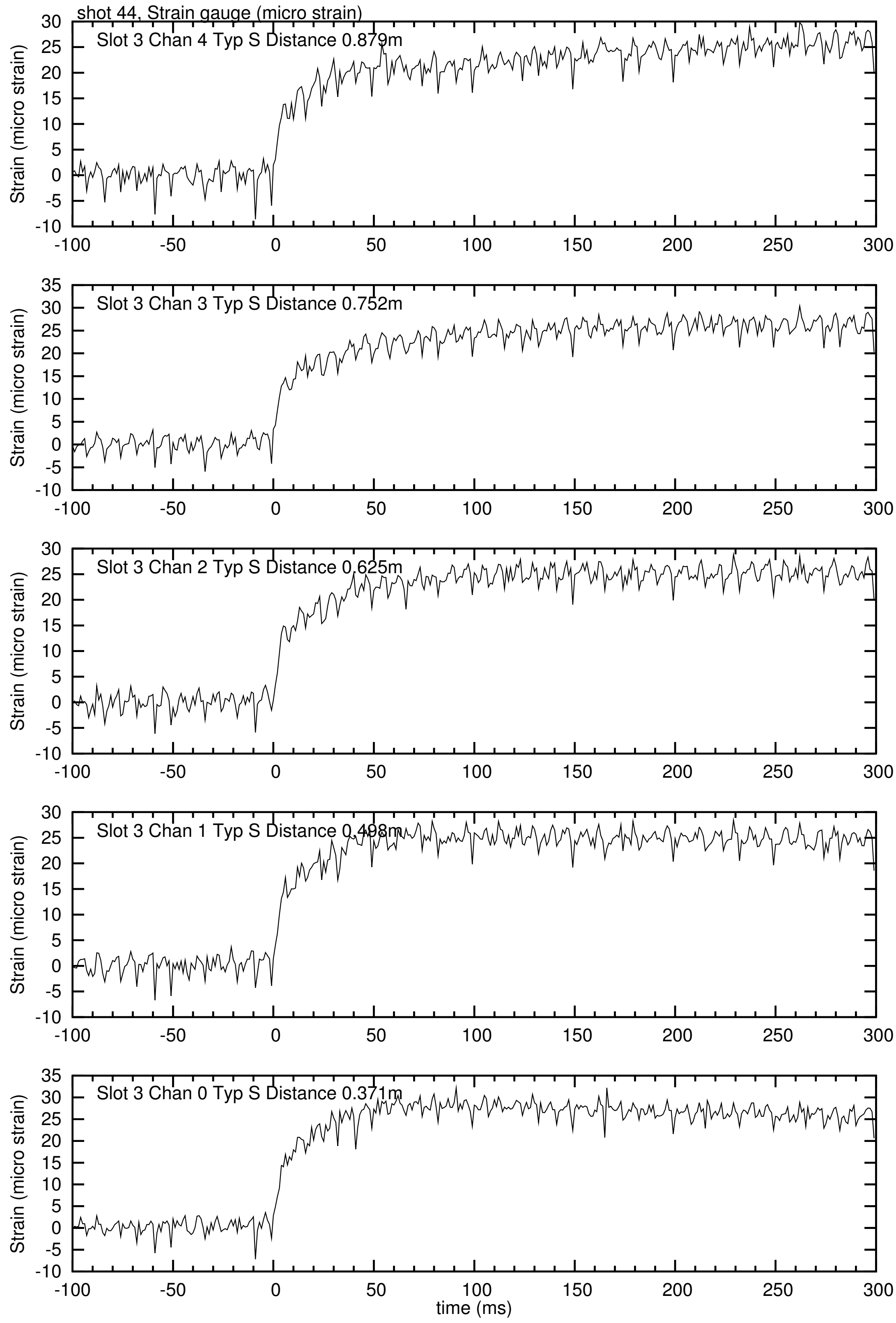

Figure 101: **Strain gauges, shot 44**, BR=0.37, O_2/C=0.75, P_{CJ}=2.63 MPa, P_{CV}=1.33 MPa.

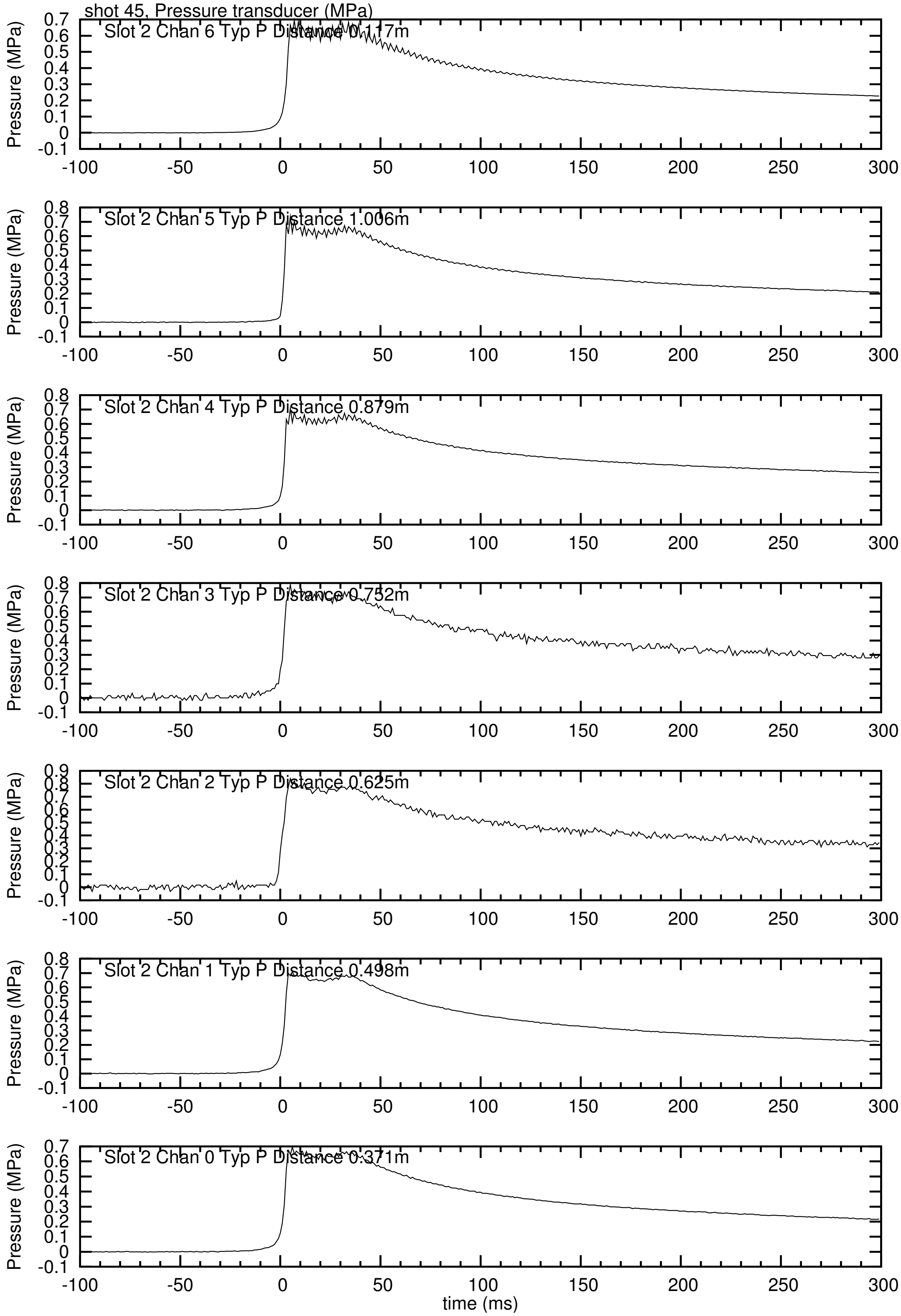

Figure 102: **Pressure transducers, shot 45**, BR=0.37, O_2/C=0.75, P_{CJ}=2.63 MPa, P_{CV}=1.33 MPa.

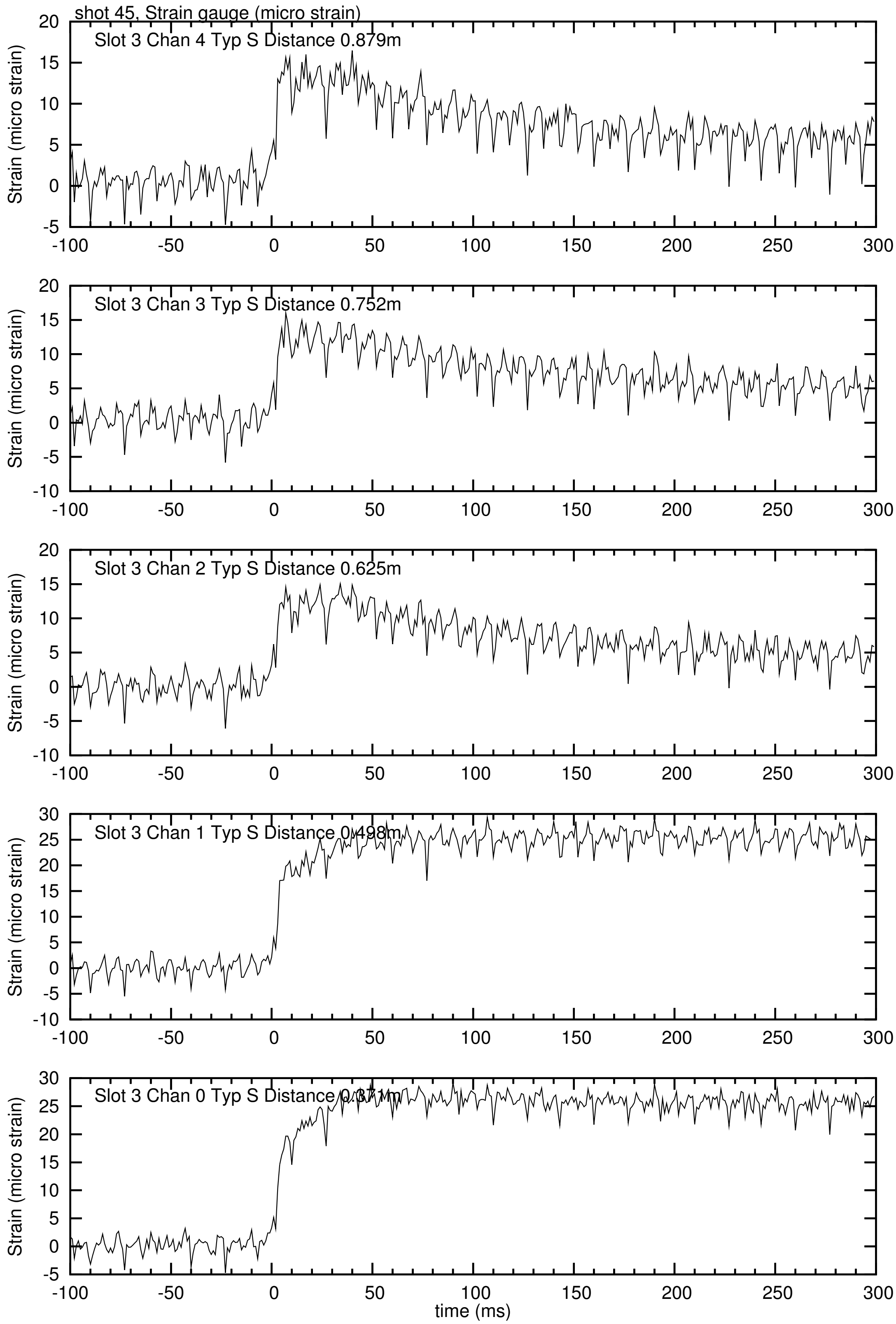

Figure 103: **Strain gauges, shot 45**, BR=0.37, O_2/C=0.75, P_{CJ}=2.63 MPa, P_{CV}=1.33 MPa.

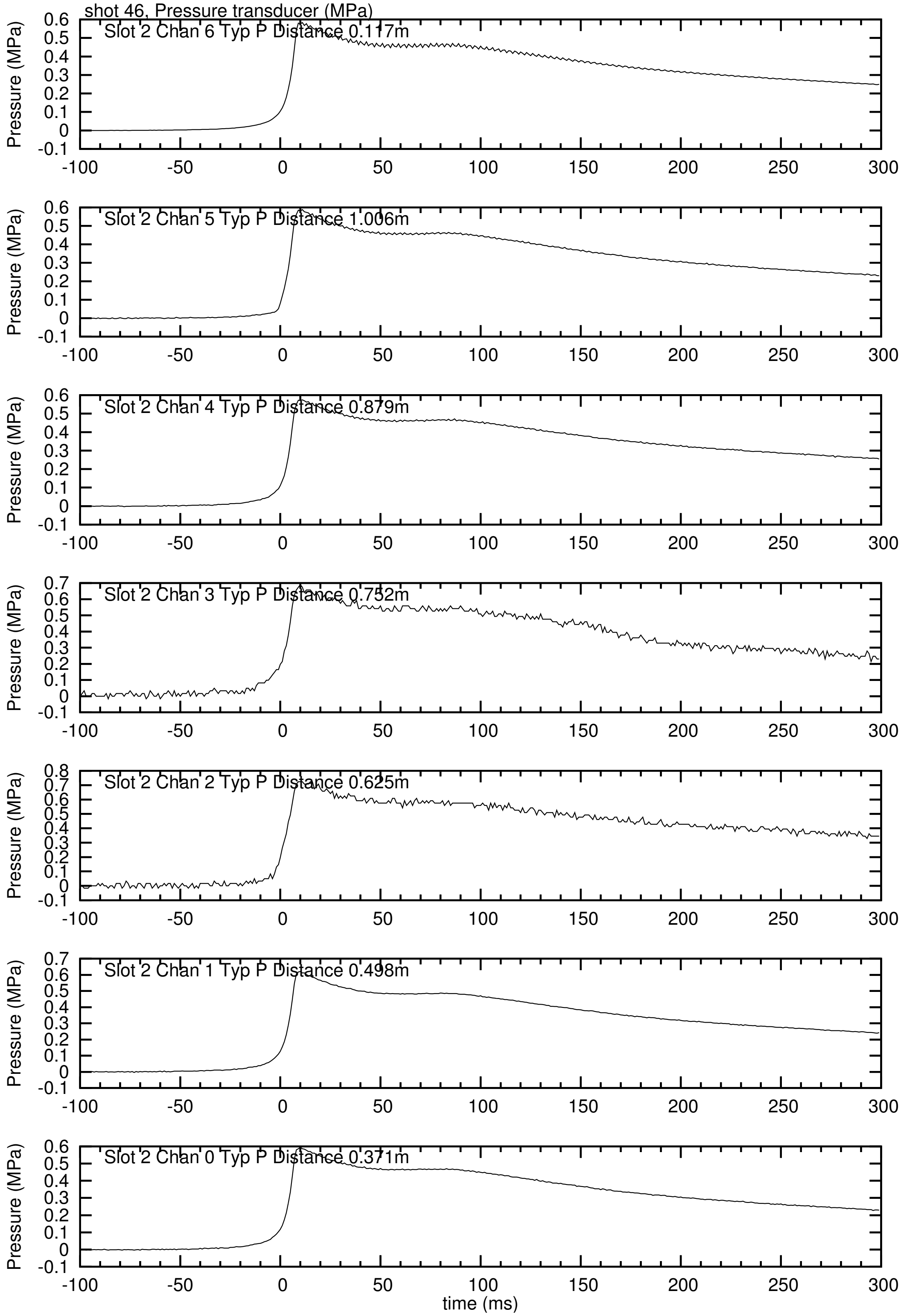

Figure 104: **Pressure transducers, shot 46**, BR=0.37, O_2/C=0.7, P_{CJ}=2.43 MPa, P_{CV}=1.23 MPa.

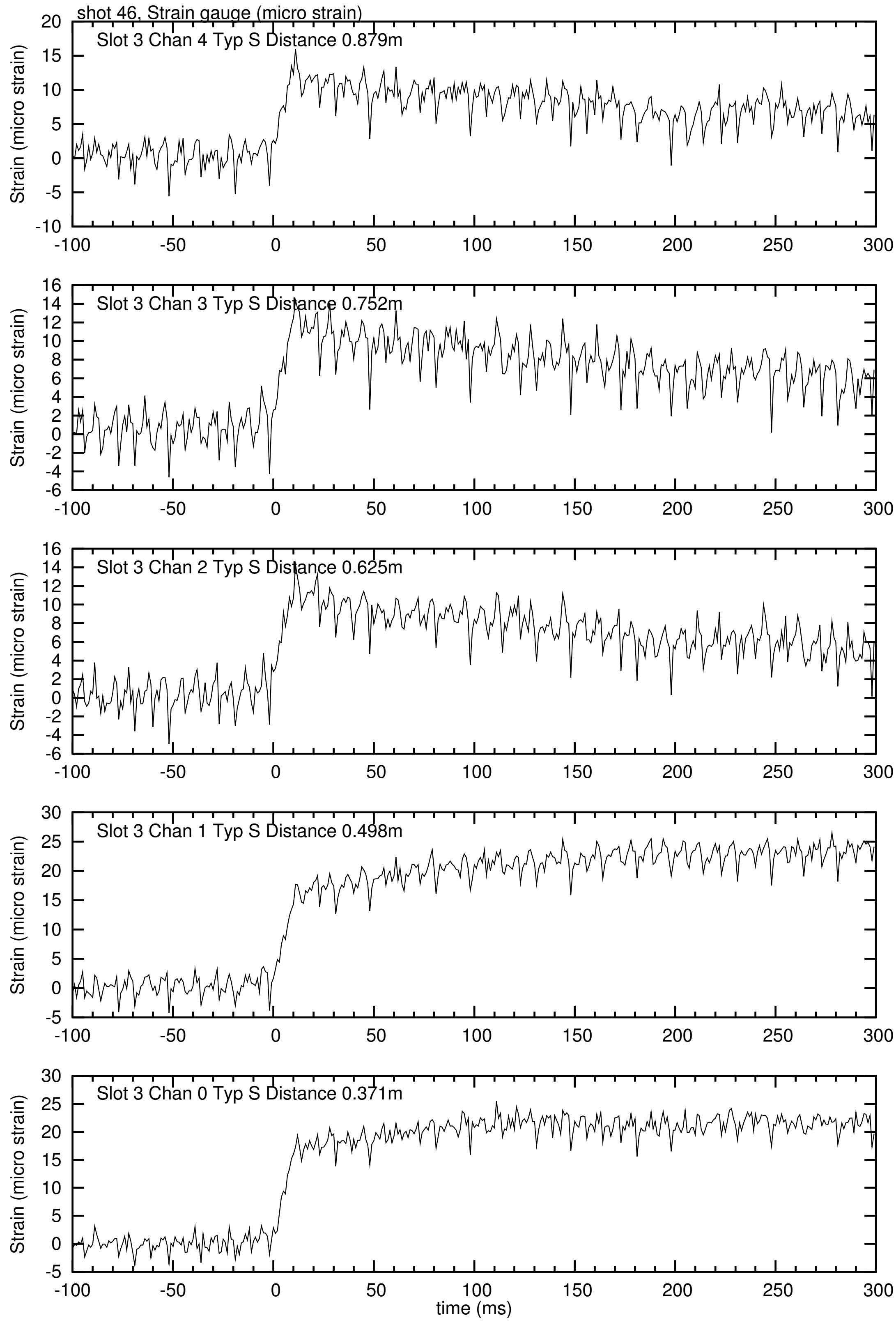

Figure 105: **Strain gauges, shot 46**, BR=0.37, O_2/C=0.7, P_{CJ}=2.43 MPa, P_{CV}=1.23 MPa.

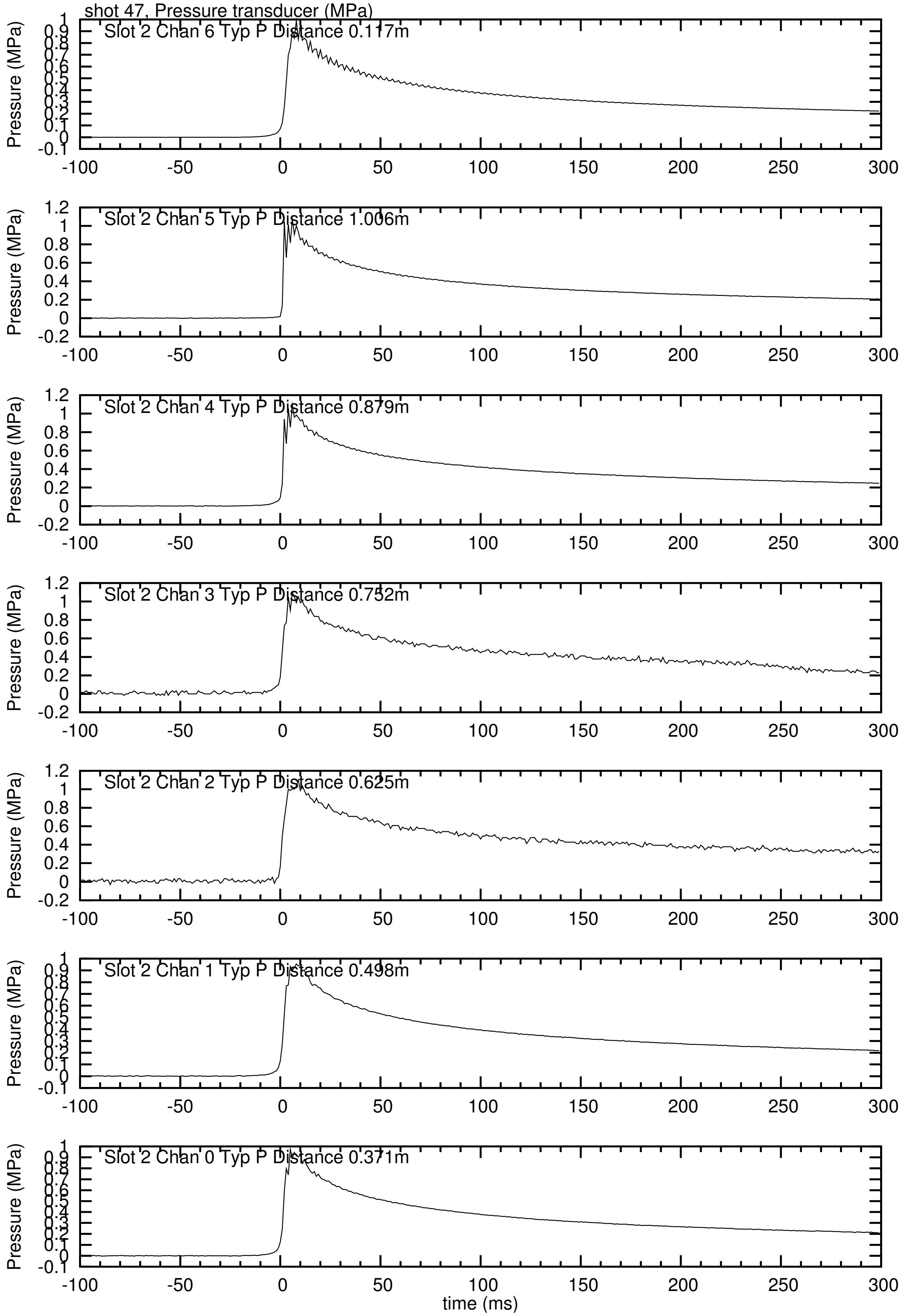

Figure 106: **Pressure transducers, shot 47**, BR=0.37, O_2/C=0.8, P_{CJ}=2.79 MPa, P_{CV}=1.41 MPa.

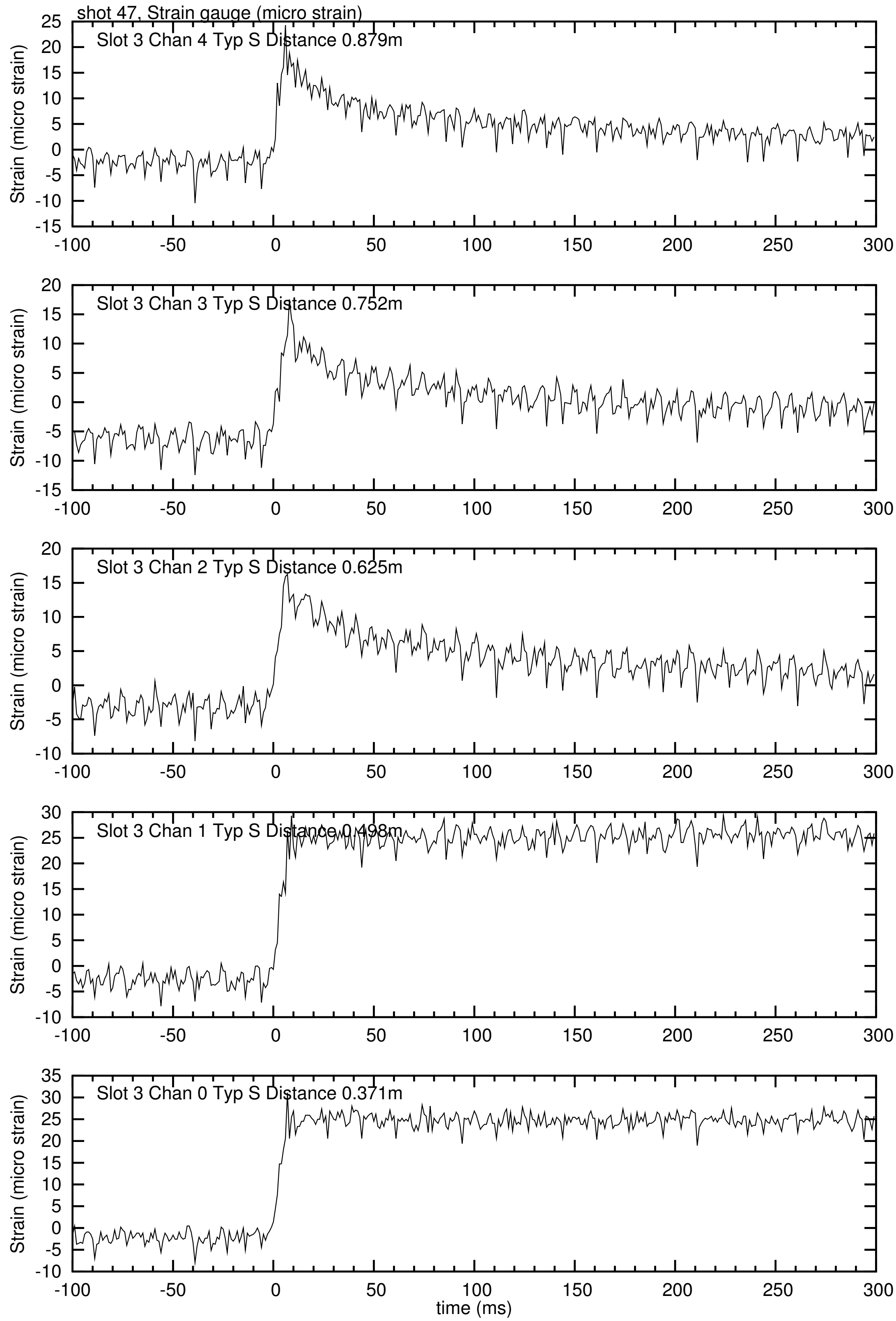

Figure 107: **Strain gauges, shot 47**, BR=0.37, O_2/C=0.8, P_{CJ}=2.79 MPa, P_{CV}=1.41 MPa.

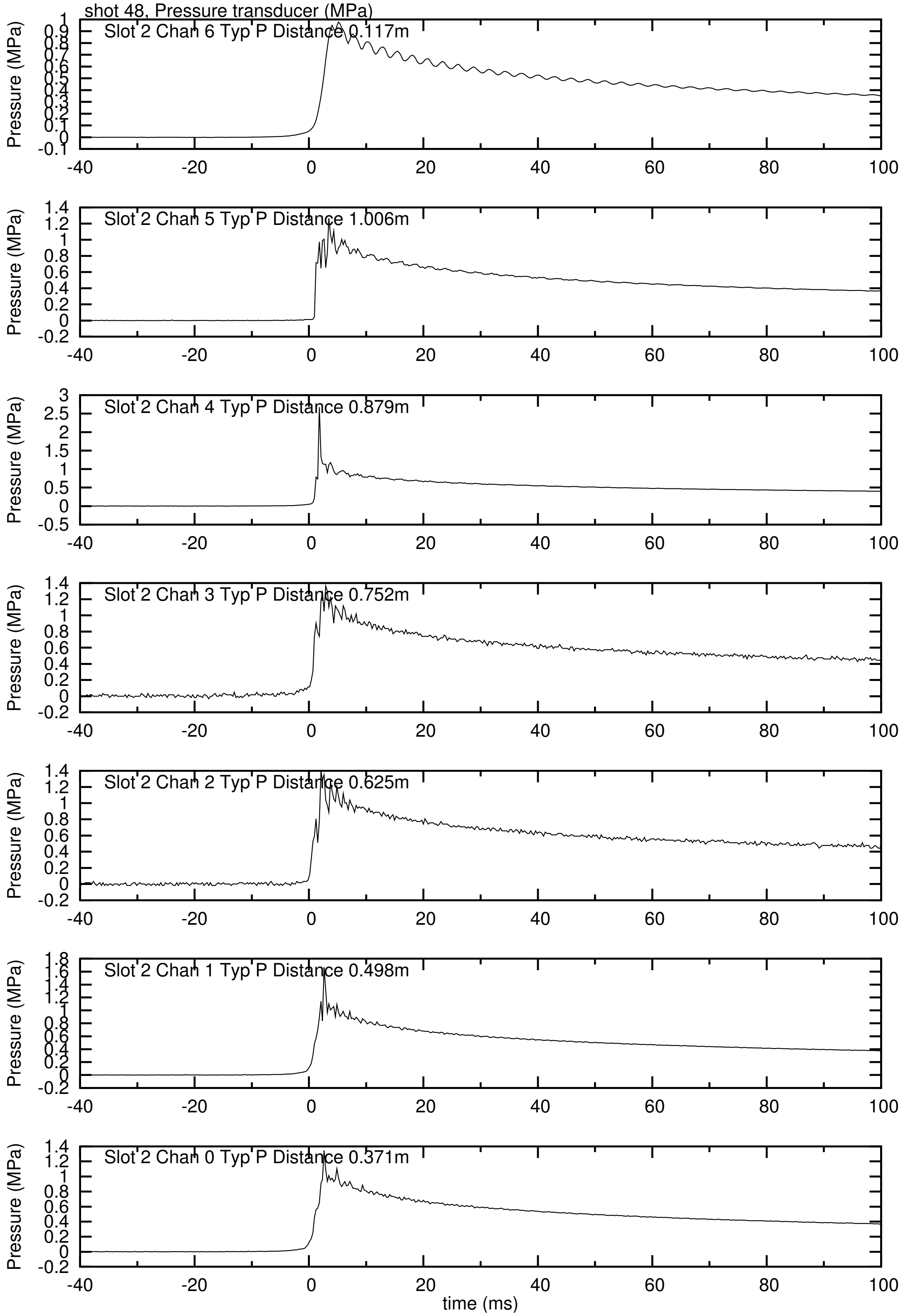

Figure 108: **Pressure transducers, shot 48**, BR=0.37, O_2/C=0.85, P_{CJ}=2.91 MPa, P_{CV}=1.47 MPa.

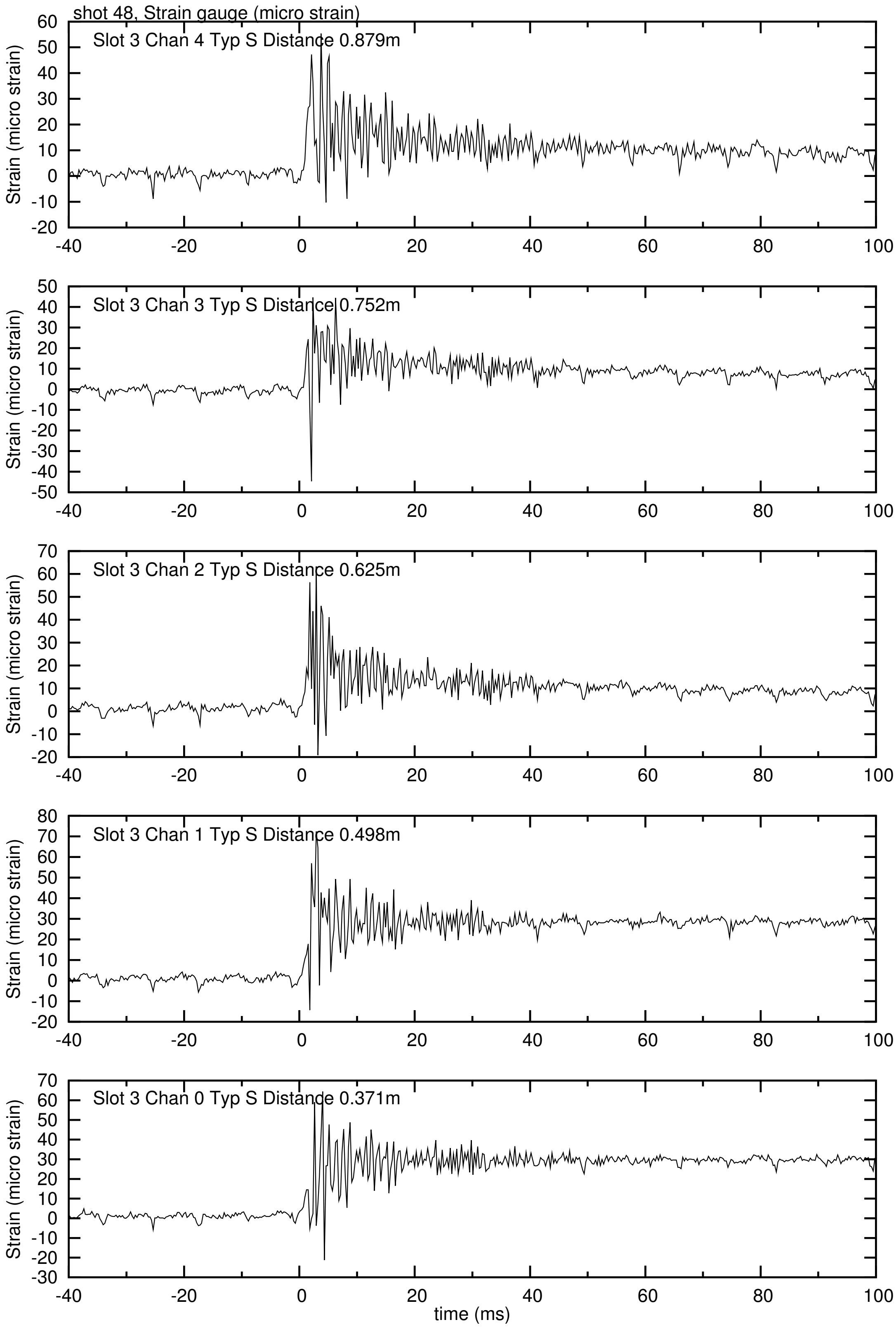

Figure 109: **Strain gauges, shot 48**, BR=0.37, O_2/C=0.85, P_{CJ}=2.91 MPa, P_{CV}=1.47 MPa.

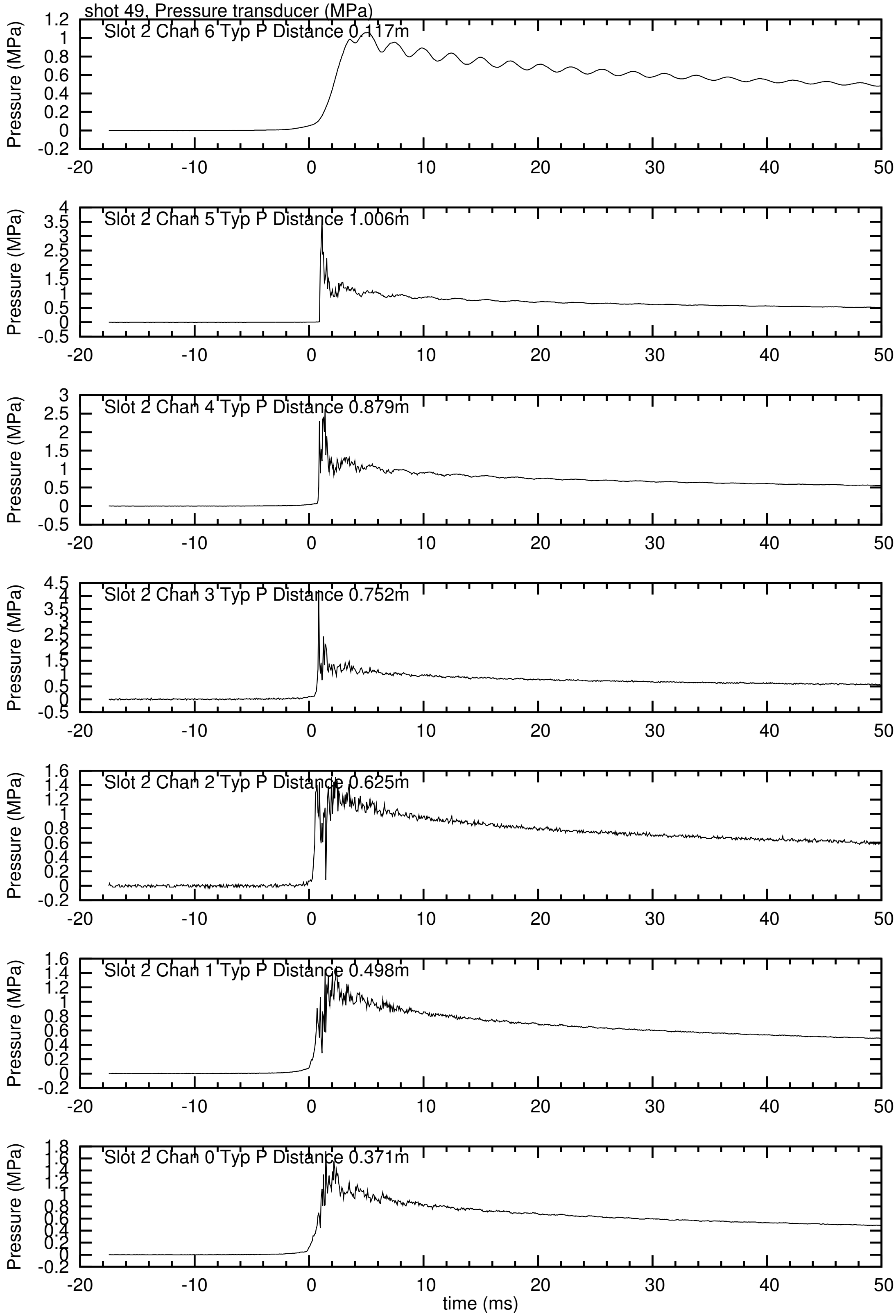

Figure 110: **Pressure transducers, shot 49**, BR=0.37, O_2/C=0.9, P_{CJ}=3.01 MPa, P_{CV}=1.52 MPa.

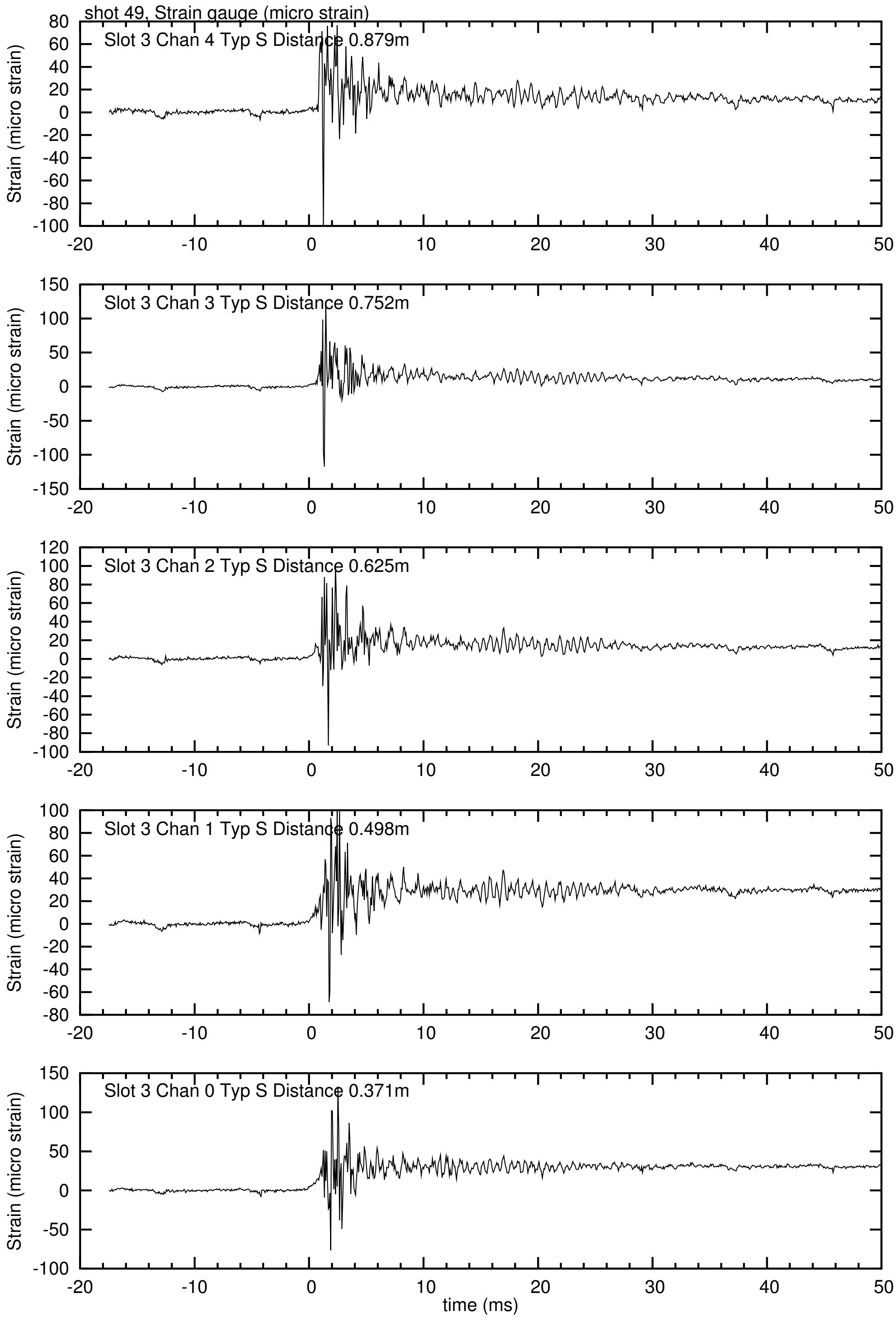

Figure 111: **Strain gauges, shot 49**, BR=0.37, O_2/C=0.9, P_{CJ}=3.01 MPa, P_{CV}=1.52 MPa.

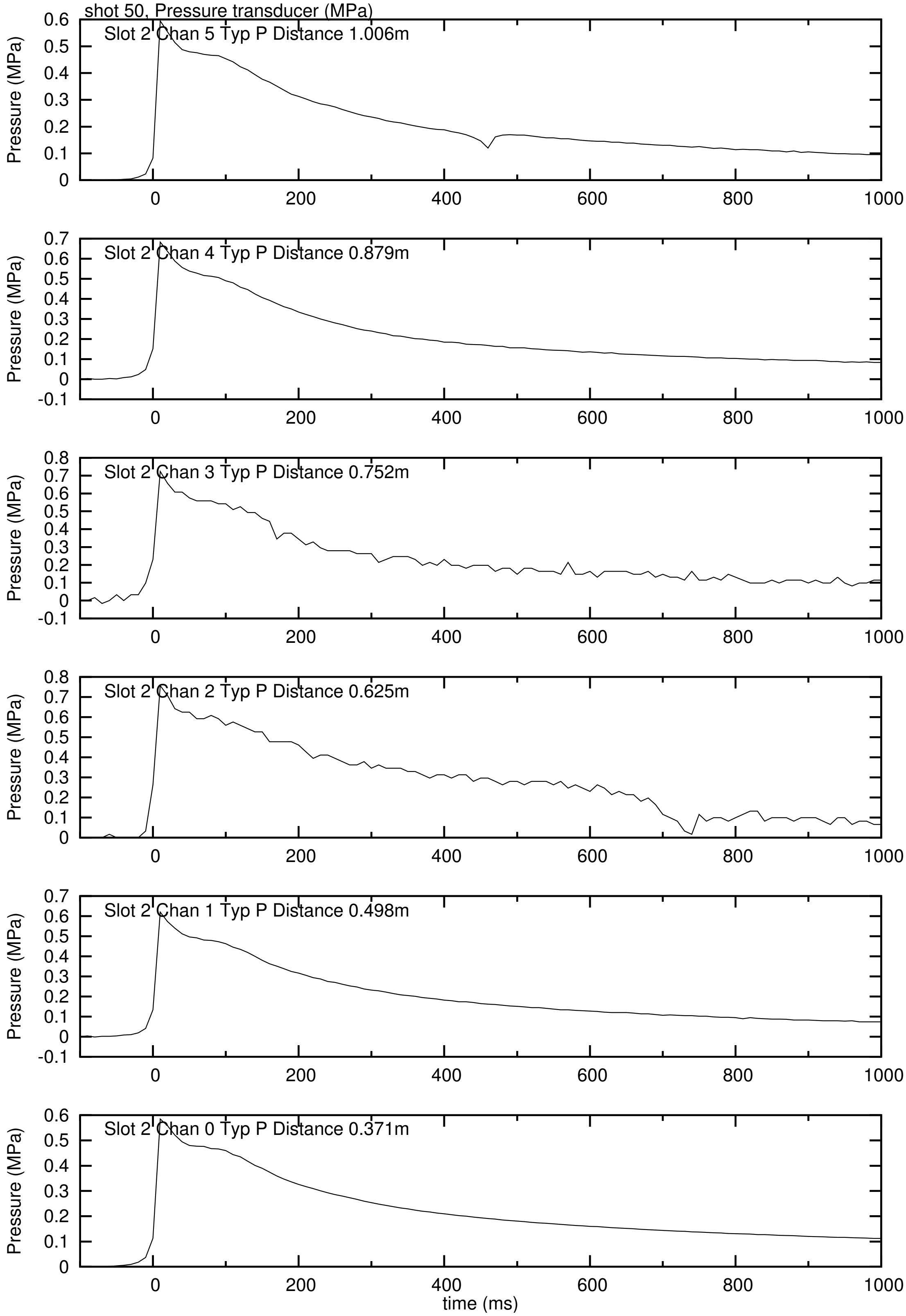

Figure 112: **Pressure transducers, shot 50**, BR=0.37, O_2/C=0.7, P_{CJ}=2.43 MPa, P_{CV}=1.23 MPa.

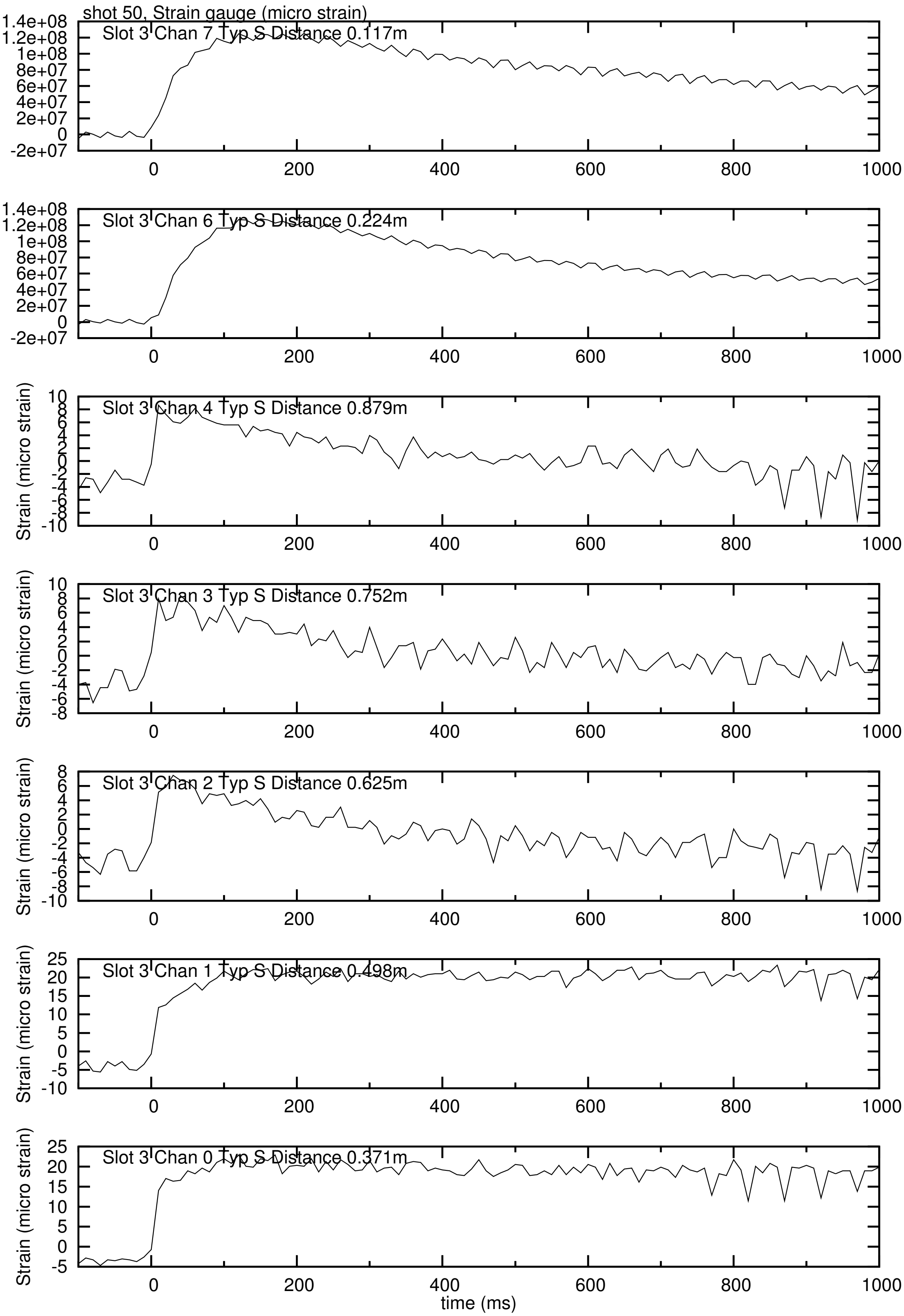

Figure 113: **Strain gauges, shot 50**, BR=0.37, O_2/C=0.7, P_{CJ}=2.43 MPa, P_{CV}=1.23 MPa.

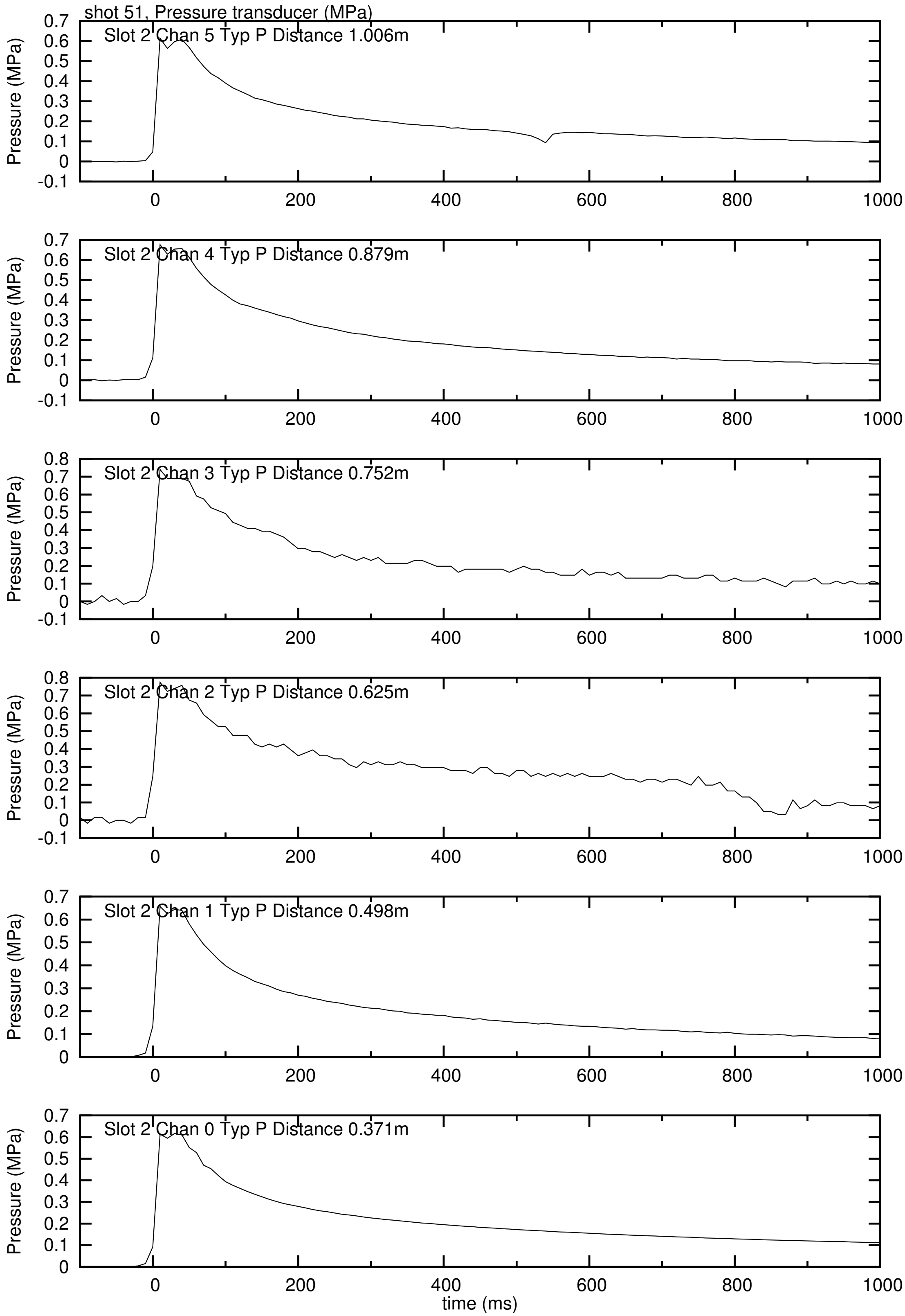

Figure 114: **Pressure transducers, shot 51**, BR=0.37, O_2/C=0.75, P_{CJ}=2.63 MPa, P_{CV}=1.33 MPa.

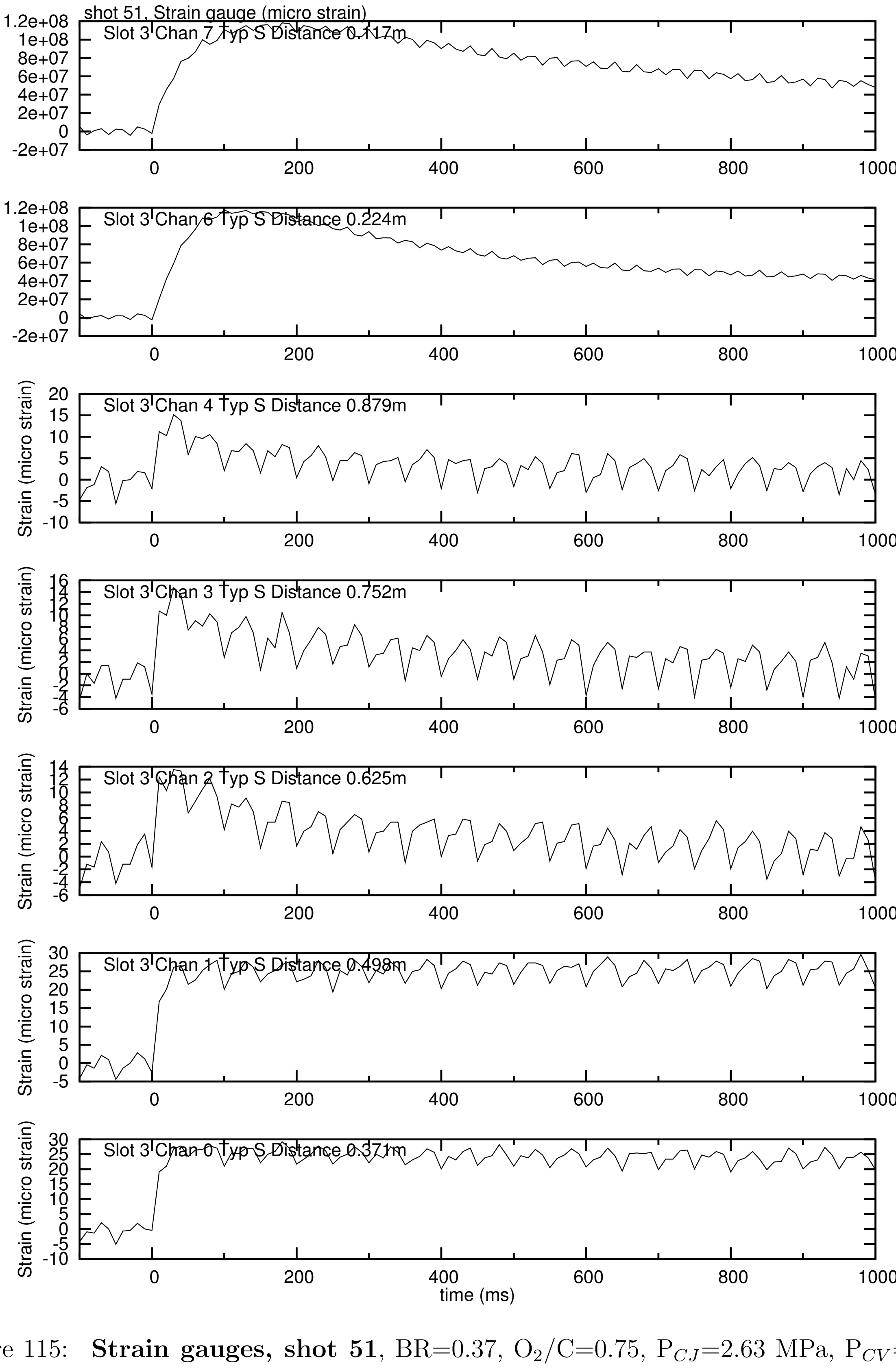

Figure 115: **Strain gauges, shot 51**, BR=0.37, O_2/C=0.75, P_{CJ}=2.63 MPa, P_{CV}=1.33 MPa.